LOUGHBOROUGH UNIVERSITY

Numerical and analytical study of the convective Cahn-Hilliard equation

by

Meshari Alesemi

A DOCTORAL THESIS
Submitted in partial fulfillment of the requirements
for the award of
Doctor of Philosophy of Loughborough University

in the

School of Science
Department of Mathematical Sciences

June 2016

Declaration of Authorship

I, Meshari Alesemi, declare that this thesis titled, **"Numerical and analytical study of the convective Cahn-Hilliard equation"** and the work presented in it are my own. I confirm that:

- This work was done wholly or mainly while in candidature for a research degree at this University.
- Where any part of this thesis has previously been submitted for a degree or any other qualification at this University or any other institution, this has been clearly stated.
- Where I have consulted the published work of others, this is always clearly attributed.
- Where I have quoted from the work of others, the source is always given. With the exception of such quotations, this thesis is entirely my own work.
- I have acknowledged all main sources of help.
- Where the thesis is based on work done by myself jointly with others, I have made clear exactly what was done by others and what I have contributed myself.

Signed: _____

Date: **June 2016** _____

LOUGHBOROUGH UNIVERSITY

Abstract

School of Science
Department of Mathematical Sciences

Doctor of Philosophy

by Meshari Alesemi

We consider the convective Cahn-Hilliard equation that is used as a model of coarsening dynamics in driven systems and that in two spatial dimensions (x, y) has the form

$$u_t + Duu_x + \nabla^2(u - u^3 + \nabla^2 u) = 0.$$

Here t denotes time, $u = u(x, y, t)$ is the order parameter and D is the parameter measuring the strength of driving. We primarily consider the case of one spatial dimension, when there is no y-dependence. For the case of no driving, when $D = 0$, the standard Cahn-Hilliard equation is recovered, and it is known that solutions to this equation are characterised by an initial stage of phase separation into regions of one phase surrounded by the other phase (i.e., clusters or droplets/holes or islands are obtained) followed by the coarsening process, where the average size of the clusters grows in time and the number of the clusters decreases. Moreover, two main coarsening mechanisms have been identified in the literature, namely, coarsening due to volume and translational modes. On the other hand, for the case of strong driving, when $D \to \infty$, the well-known Kuramoto-Sivashinsky equation is recovered, solutions of which are characterised by complicated chaotic oscillations in both space and time. The primary aim of the present thesis is to perform a detailed and systematic investigation of the transitions in the solutions of the convective Cahn-Hilliard equation for a wide range of parameter values as the driving-force parameter is increased, and, in particular, to understand in detail how the coarsening dynamics is affected by driving. We find that one of the coarsening modes is stabilised at relatively small values of D, and the type of the unstable coarsening mode may change as D increases. In addition, we find that there may be intervals in the driving-force parameter D where coarsening is completely stabilised. On the other hand, there may be intervals where two-mode solutions are unstable and the solutions can evolve, for example, into one-droplet/hole solutions, symmetry-broken two-droplet/hole solutions or time-periodic solutions. We present detailed stability diagrams for 2-mode solutions in the parameter planes and corroborate our findings by time-dependent simulations. Finally, we present preliminary results for the case of the (convective) Cahn-Hilliard equation in two spatial dimensions.

In this thesis:

Chapters 5 and 6 of this thesis are based on a manuscript intended to be submitted in summer 2016.

Acknowledgements

Praise be to ALLAH, the Almighty, with whose gracious help it made it easy to accomplish successfully this report. Foremost I would like to express my deep thanks and appreciation to my supervisors, Professor Uwe Thiele and Dr Dmitri Tseluiko whose support, constant guidance and continuous encouragements made my dissertation work possible. They have always been available to advise me. I wish to thank them for their understanding, patience, motivation, enthusiasm and their immense knowledge. I owe them lots of gratitude for having shown to me this way of research. They could not even realise how much I have learned from them.

I am greatly indebted to my mother, brothers, sisters and the rest of my family for encouragement, prayers and support they have provided me during my studies. My sincere thanks are due to my wife, Noor, who has managed patiently to look after our kids, Leen and Dina, so that I could concentrate on my studies. May ALLAH bless them all.

My great pleasure and appreciations go to my friends Mariano Galvagno and Desislava Todorova, for their moral support and encouragement throughout my studies.

Finally, I would like to thank the Saudi Arabian Cultural Bureau and the Department of Mathematics at Jazan University for their financial support.

Meshari Alesemi.

Contents

List of Figures

List of Tables

Chapter 1

Introduction

In recent years, there has been a renewed interest in the convective Cahn-Hilliard equation as a model of coarsening dynamics in driven systems, see, for example, Emmott and Bray [36], Golovin et al. [45–47], Watson [117], Watson et al. [119], Zaks et al. [123]. Related models have also been derived, for instance, in the context of epitaxial growth (Šmilauer et al. [58]) and thin liquid films on inclined planes (Thiele and Knobloch [105, 106], Thiele [102]).

The convective Cahn-Hilliard equation is a semilinear parabolic equation of fourth order. In the absence of driving, the convective Cahn-Hilliard equation reduces to the standard Cahn-Hilliard equation, that was proposed as a model to describe phase separation (or spinodal decomposition) of two-component mixtures (see, for instance, Cahn [16–18], Cahn and Hilliard [19, 20]). The initial dynamics of the solutions of the standard Cahn-Hilliard equation from a perturbed homogeneous state is characterised by separation into regions corresponding to different components, i.e., clusters (droplets or islands) of one phase surrounded by the other phase. However, after this initial stage of evolution, these clusters slowly grow in size and the number of the clusters decreases, i.e., the clusters coarsen. There have been identified two main mechanisms of coarsening, namely, coarsening by the volume and translational modes. In coarsening by the volume mode (which is also known as Ostwald ripening [84]), the centres of the clusters remain fixed in space, while the sizes of the clusters change – some of the clusters grow in time, while other clusters decrease in size and, eventually, disappear. In coarsening by the translational mode, the centres of the clusters are not fixed anymore, and the coarsening happens due to the movement and joining of the clusters. The coarsening

process continues until a single large-size cluster is obtained. For a more detailed discussion of coarsening see, for example, Onuki [83], Desai [27], Pototsky et al. [91]).

In the convective Cahn-Hilliard equation, an additional nonlinear term of Burgers type (multiplied by a driving-force parameter) is introduced. In the limit of strong driving, the convective Cahn-Hilliard equation reduces to the well-known Kuramoto-Sivashinsky equation (see, for example, Golovin et al. [47]). In contrast to the solutions of the Cahn-Hilliard equation, the large-time dynamics of the solutions of the Kuramoto-Sivashinsky equation is characterised by complicated chaotic oscillations in both space and time. We note also that for the Kuramoto-Sivashinsky equation, viewed as an infinite-dimensional dynamical system on an appropriate function space, there has been established the existence of a finite-dimensional inertial manifold, see, e.g., Collet et al. [23, 24], Goodman [49], Hyman et al. [57], Jolly et al. [61], Il'yashenko [59], Otto [85]. We can conclude that, as the driving force is increased from zero to large values, there must appear transitions leading from the coarsening dynamics typical of the standard Cahn-Hilliard equations to complicated chaotic oscillations typical of the Kuramoto-Sivashinsky equation. The main aim of the present thesis is to perform a detailed and systematic investigation of the transitions in the solutions of the convective Cahn-Hilliard equation for a wide range of parameter values as the driving force parameter is increased. We note that coarsening dynamics for the convective Cahn-Hilliard equation has been studied in the limit of a weak driving force numerically by Emmott and Bray [36] and Golovin et al. [47] and analytically by Watson et al. [119]. Zaks et al. [123] reported that driving can be used to stop coarsening for certain parameter values. Some stationary solutions of the convective Cahn-Hilliard equation have been analysed by Korzec et al. [68]. We also note that Eden and Kalantarov [33] demonstrated the existence of a finite-dimensional inertial manifold for the convective Cahn-Hilliard equation.

The thesis is organised as follows. In Chapter 2, we discuss the theoretical and numerical background for the present study. We first introduce the standard Cahn-Hilliard equation and discuss some important concepts and ideas related to this equation. In particular, we show that the free energy functional for this equation is a Lyapunov functional so that time evolution tends to minimise it. We also discuss stability of homogeneous solutions and introduce the concepts of spinodal and binodal curves. Next, we discuss the two main mechanisms of coarsening for the standard Cahn-Hilliard equation, namely, coarsening by translational and volume modes. We then introduce the

convective Cahn-Hilliard equation and briefly review some known results for this equation. After that, we discuss the numerical background needed for the present study, namely, we briefly explain time-dependent solution by Fourier spectral methods and numerical continuation and bifurcation techniques.

In Chapter 3, we discuss temporal and spatial linear stability analyses of homogenous solutions of the one-dimensional standard and convective Cahn-Hilliard equations. We also discuss the connection of the spatial linear stability analysis to the existence of single- and double-interface solutions (i.e., fronts and droplets/holes). We additionally corroborate the theoretical predictions by time-dependent computations.

Chapter 4 presents the results of numerical continuation of single- and double-interface solutions (i.e., fronts and droplets/holes). First, we discuss the results of numerical continuation with respect to the domain size for the standard Cahn-Hilliard equation for several values of the mean solution thickness obtaining different types of the primary bifurcations (supercritical and subcritical) from the branch of homogeneous solutions and metastability in the absence of a primary bifurcation. Next, we analyse how the driving force affects inhomogeneous solutions of the Cahn-Hilliard equation. We first discuss double-interface solutions (i.e., fronts and droplets/holes) and then discuss single-interface solutions (i.e., kinks and anti-kinks). Finally, in this Chapter, we discuss the weakly nonlinear analysis that can be used to analyse the nature of primary bifurcations from branches of homogeneous solutions.

In Chapter 5, we present a systematic study of the linear stability properties of various spatially periodic traveling solutions of the convective Cahn-Hilliard equation. Our main focus is on the analysis of the stability of double-droplet/hole solutions. We identify coarsening modes of such solutions, and we also obtain intervals in the driving force, where there are no unstable eigenvalues so that coarsening is stopped by driving. We also compute and analyse the stability of side branches of symmetry-broken solutions. To obtain more complete bifurcation diagrams, we, in addition, compute branches of time-periodic solutions. Finally, at the end of this Chapter, we produce detailed stability diagrams in parameter planes. We note that the predictions from the numerical continuation results are supported by time-dependent simulations for the convective Cahn-Hilliard equation.

Chapter 6 presents some preliminary results on the computation of solutions of the two-dimensional standard and convective Cahn-Hilliard equations. Bifurcation diagrams for two-droplet/hole solutions are presented showing primary branches of solutions with a discrete translational symmetry and side branches of symmetry broken solutions. Conclusions and outlook are discussed in Chapter 7.

Chapter 2

Theoretical and numerical background

2.1 Introduction

In this Chapter, we introduce the theoretical and numerical background that is needed in the present thesis. In Section 2.2, we discuss the standard Cahn-Hilliard equation as a model for phase separation introducing it first in a general gradient-dynamics formulation. We also discuss the determination of spinodal and binodal lines separating the regions of linear stability, metastability and linear instability for homogeneous solutions in a parameter plane. Next, in Section 2.3, we discuss the coarsening dynamics for large-amplitude clusters (droplets or islands) for the standard Cahn-Hilliard equation, which is the process where the average size of the clusters grows in time and the number of the clusters decreases. We introduce the two main mechanisms of coarsening, the volume and translational modes, and present time-dependent simulations to illustrate coarsening. In Section 2.4, we introduce the convective Cahn-Hilliard equation, which is the main object of our research. We additionally discuss two alternative scalings for the convective Cahn-Hilliard equation. In the first scaling, that we mainly use in this thesis, there is only one dimensionless parameter, the dimensionless driving force D. For an alternative scaling, we fix the domain size and obtain two dimensionless parameters, the dimensionless driving force and a dimensionless parameter controlling the shape of the free energy. In Section 2.5, we discuss the Fourier spectral numerical method that we use for time-dependent simulations for the convective Cahn-Hilliard equation. Finally, in Section 2.6, we briefly discuss numerical continuation and bifurcation techniques that we use in the present thesis to obtain detailed information on long-time behaviour of the solutions of the convective Cahn-Hilliard equation.

2.2 The Cahn-Hilliard equation

The Cahn-Hilliard equation was developed by Cahn and Hilliard, who proposed a phenomenological model for phase separation (see, for example, Cahn [16–18], Cahn and Hilliard [19, 20], Cook [25], Hilliard [55]). Phase separation or spinodal decomposition is a process when a homogeneous mixture of two components A and B in one thermodynamic phase (whether it is a solid or a liquid phase) suddenly separates into regions consisting of different components (i.e., two different phases), i.e., A-rich regions and B-rich regions. The phase separation mechanism of spinodal decomposition is different from the nucleation mechanism where the homogeneous state is stable to small local fluctuations in the composition but is unstable to sufficiently large fluctuations so that phase separation starts at discrete nucleations sites, see, for example, Goldenfeld [44] and Onuki [83]. Normally, the phenomenon of spinodal decomposition takes place when a mixture of two different components, for instance A and B, making up a single homogeneous phase at a temperature T which is higher than the critical temperature T_{crit}, is quickly cooled (quenched) to a temperature where the homogeneous state is unstable. The resultant inherent instability leads to composition fluctuations, and eventually to immediate phase separation. Primarily, the theory of spinodal decomposition has been developed by Hillert [54], Cahn [16, 17] and Hilliard [55], and can be described by the Cahn-Hilliard equation. A review of different derivations of the Cahn-Hilliard equation can be found, for example, in Lee et al. [73]. See also Cahn and Hilliard [19], Gaskell [40], Porter and Easterling [89].

The Cahn-Hilliard equation can be written in the following general form:

$$\partial_t u = \nabla \cdot \left\{ Q(u) \nabla \left(\frac{\delta F[u]}{\delta u} \right) \right\}. \tag{2.1}$$

For the case of a phase-separating binary system consisting of components A and B, u may be defined to be

$$u = u_A - u_B, \tag{2.2}$$

where u_A and u_B are the local concentrations of components A and B, respectively, scaled so that $u_A + u_B = 1$, see, for instance, Alt and Pawlow [35] and Elliott and French [3]. Note that equations of the form (2.1) also arise in other contexts, for example, in the study of thin liquid films (see, e.g., Thiele [102, 103], Thiele and Knobloch [106]), phase separation of binary and ternary liquid mixtures (see Anders and Weinberg [4] and Park et al. [87]), multi-phase flows (see Boyer [12], Khatavkar

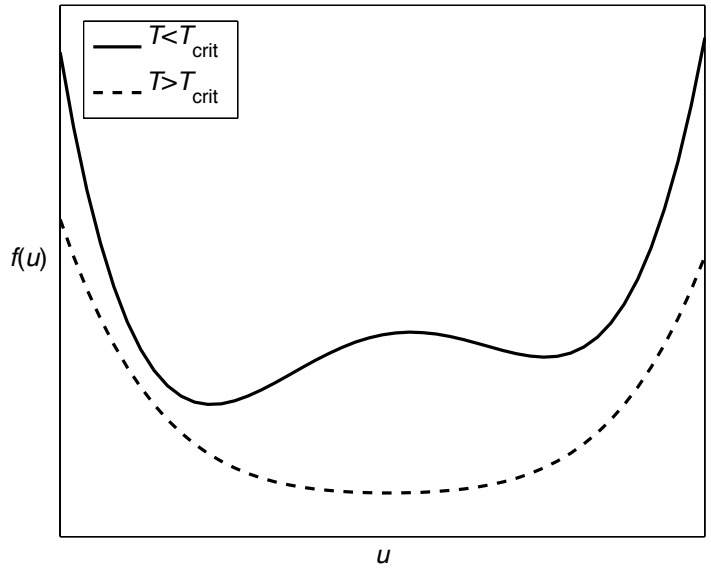

Figure 2.1: Schematic representation of the local free energy $f(u)$ for $T > T_{\text{crit}}$ (dashed line) and $T < T_{\text{crit}}$ (solid line).

et al. [64] and Kim [65]), two-layer flows in channels with topographical features (see Zhou and Kumar [124]), tumour growth (see Cristini et al. [26] and Wise et al. [121]). Function $Q(u)$ is the so-called mobility, and $F[u]$ is the Helmholtz free energy, which is assumed to have the form

$$F[u] = \int \varphi(u, \nabla u) dx, \tag{2.3}$$

where $\varphi(u, \nabla u)$ is the energy density, which is assumed to be of the form

$$\varphi(u, \nabla u) = f(u) + \frac{\gamma}{2}|\nabla u|^2. \tag{2.4}$$

Here $f(u)$ is the local free energy and the second term is the gradient term with γ being the interfacial energy coefficient.

The form of the local free energy may depend on some parameter, e.g., temperature, T. For example, for large values of T, $f(u)$ may have a single minimum, whereas for T below some critical value, T_{crit}, $f(u)$ may have a double-well form with two local minima. A schematic representation is shown in Fig. 2.1.

For the standard Cahn-Hilliard equation,

$$Q(u) \equiv 1, \quad f(u) = \frac{\alpha}{4}(u^2 + \beta)^2. \tag{2.5}$$

Note that the variables can be rescaled so that $\alpha = 1$ and $\gamma = 1$. Parameter β can then be interpreted as a parameter that increases as temperature increases. For $\beta > 0$, $f(u)$ has a single minimum at $u = 0$. For $\beta < 0$, $f(u)$ has two minima, at $u = -1/\sqrt{-\beta}$ and at $u = 1/\sqrt{-\beta}$.

Note that in one dimension, equation (2.1) becomes

$$\partial_t u = \partial_x \left\{ Q(u) \partial_x \left(\frac{\delta F[u]}{\delta u} \right) \right\}, \tag{2.6}$$

where

$$F[u] = \int \varphi(u, u_x) dx \tag{2.7}$$

with

$$\varphi(u, u_x) = f(u) + \frac{1}{2} u_x^2. \tag{2.8}$$

For the standard Cahn-Hilliard equation with $\alpha = \gamma = 1$ (and choosing $\beta = -1$), we obtain

$$f(u) = \frac{1}{4}(u^2 - 1)^2, \tag{2.9}$$

or, equivalently, we can use

$$f(u) = \frac{1}{4} u^4 - \frac{1}{2} u^2. \tag{2.10}$$

Then, we obtain

$$u_t + (u - u^3 + u_{xx})_{xx} = 0. \tag{2.11}$$

Lyapunov functional $F[u]$. Next, let us show that $F[u]$ is a Lyapunov functional for equation (2.6). In general, $\delta F[u]/\delta u$ is functional (or variational) derivative such that

$$F[u + v] = F[u] + \int \frac{\delta F[u]}{\delta u} v \, dx + O(v^2) \tag{2.12}$$

when $|v| \ll 1$. We obtain

$$\begin{aligned} \frac{dF[u]}{dt} &= \lim_{\Delta t \to 0} \frac{F[u(t + \Delta t, \cdot)] - F[u(t, \cdot)]}{\Delta t} \\ &= \lim_{\Delta t \to 0} \frac{1}{\Delta t} \left\{ F[u(t, \cdot) + \Delta t u_t(t, \cdot) + O(\Delta t^2)] - F[u(t, \cdot)] \right\} \\ &= \lim_{\Delta t \to 0} \frac{1}{\Delta t} \left\{ F[u(t, \cdot)] + \Delta t \int \frac{\delta F[u]}{\delta u} u_t dx + O(\Delta t^2) - F[u(t, \cdot)] \right\} \\ &= \int \frac{\delta F[u]}{\delta u} u_t \, dx. \end{aligned} \tag{2.13}$$

Substituting equation (2.6) in equation (2.13), we find

$$\frac{dF[u]}{dt} = \int \frac{\delta F[u]}{\delta u} \partial_x \left\{ Q(u) \partial_x \frac{\delta F[u]}{\delta u} \right\} dx. \tag{2.14}$$

Integrating by parts and assuming appropriate boundary conditions (e.g., periodic or zero-flux boundary conditions), we get

$$\frac{dF[u]}{dt} = - \int Q(u) \left\{ \partial_x \frac{\delta F[u]}{\delta u} \right\}^2 dx \leq 0, \tag{2.15}$$

assuming that $Q(u) \geq 0$. We conclude that $F[u]$ is a Lyapunov functional. Therefore, the dynamics minimises $F[u]$ subject to the constraint that $\int u\, dx$ is fixed and equal to a given value.

Next, a steady-state solution $u_0(x)$ of equation (2.6) satisfies

$$\left. \frac{\delta F[u]}{\delta u} \right|_{u=u_0} = C_1, \tag{2.16}$$

where C_1 is a constant of integration that can be fixed by, for example, requiring that $\int u\, dx$ is fixed and equal to a given value. Equation (2.16) can be formulated as a variational problem with C_1 having the meaning of a Lagrange multiplier. Indeed, let us consider the problem of minimising $F[u]$ with the constraint $\int (u - \bar{u}) dx = 0$ (i.e., $\bar{u}$ is the mean value of u). This problem is equivalent to minimising the functional

$$\begin{aligned} G[u] &= F[u] - C_1 \int (u - \bar{u}) dx, \\ &= \int \underbrace{\left(\varphi(u, u_x) - C_1 (u - \bar{u}) \right)}_{\psi(u, u_x)} dx, \end{aligned} \tag{2.17}$$

where $C_1 = \partial_u f|_{u=\bar{u}}$. The corresponding Euler-Lagrange equation for u_0 is

$$\left. \frac{\delta F[u]}{\delta u} \right|_{u=u_0} = C_1 \qquad \Leftrightarrow \qquad f'(u_0) - u_{0xx} = C_1. \tag{2.18}$$

We note that C_1 has the meaning of the chemical potential. Indeed, it is the first variation of the free-energy functional (or the derivative of the volumetric free energy with respect to u). (To be more precise, C_1 is the difference of the chemical potentials of components A and B, $C_1 = C_A - C_B$.) Note that $G[u]$ is also a Lyapunov functional for equation (2.6).

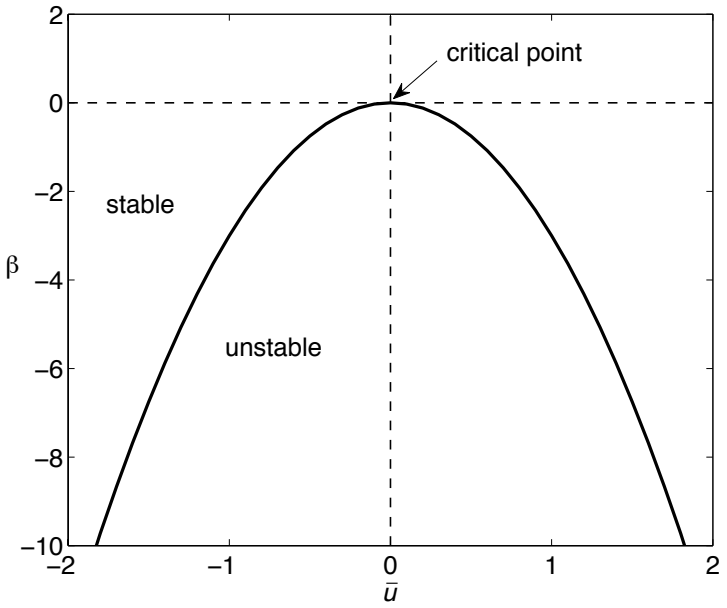

Figure 2.2: The spinodal line in the $(\bar{u}, \beta)$-plane for the standard Cahn-Hilliard equation separating the plane into the regions of linear stability and instability. The critical point is also shown.

Linear stability analysis. Next, we analyse the linear stability of homogeneous solutions of the Cahn-Hilliard equation (2.6). To do this, we first linearise equation (2.6) by substituting $u = \bar{u} + \epsilon\tilde{u}$ in this equation, where $\bar{u}$ is a constant and $\epsilon \ll 1$. At first order in ϵ, we obtain the equation

$$\tilde{u}_t = f''(u_0)\tilde{u}_{xx} - \tilde{u}_{xxxx}. \tag{2.19}$$

Next, we assume the ansatz $\tilde{u} = \exp(ikx + st)$ and obtain

$$\tilde{u}_t = se^{ikx+st}, \quad \tilde{u}_{xx} = -k^2e^{ikx+st}, \quad \tilde{u}_{xxxx} = k^4e^{ikx+st}. \tag{2.20}$$

Substituting expressions (2.20) into (2.19), we find the dispersion relation

$$s = -f''(\bar{u})k^2 - k^4. \tag{2.21}$$

If $f''(\bar{u}) > 0$, then the constant solution $u = \bar{u}$ is linearly stable. Otherwise, if $f''(\bar{u}) < 0$, the constant solution $u = \bar{u}$ is linearly unstable. Thus, the spinodal line is given by the equation $f''(\bar{u}) = 0$ in the $(\bar{u}, T)$-plane (or $(\bar{u}, \beta)$-plane). For the standard Cahn-Hilliard equation, when $f(u)$ is given by (2.5), we obtain the following equation for the spinodal line:

$$3\bar{u}^2 + \beta = 0, \tag{2.22}$$

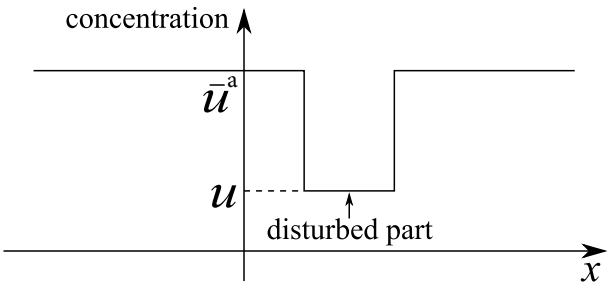

Figure 2.3: Constant solution with a disturbed part.

which is a parabola in the $(\bar{u}, \beta)$-plane, see Fig. 2.2. The point $\bar{u} = 0$, $\beta = 0$ is the critical point. It is the point where a substance moves into the spinodal region of the phase diagram and spinodal decomposition is occurring, see, e.g., Jones [62]. We denote the critical value of β by β_c and the corresponding critical value of temperature by T_c.

Note that in the region of linear instability, $f''(\bar{u}) < 0$, i.e., the graph of $f(\bar{u})$ is concave down. This implies that locally the free energy of the decomposed state with λ amount of $\bar{u}^a < \bar{u}$ and $(1-\lambda)$ amount of $\bar{u}^b > \bar{u}$, where $\lambda \in (0,1)$, is lower than the energy of the mixed state. Indeed, for a function that is concave down, we have

$$f(\bar{u}) = f\big(\lambda\bar{u}^a + (1-\lambda)\bar{u}^b\big) > \lambda f(\bar{u}^a) + (1-\lambda) f(\bar{u}^b), \tag{2.23}$$

i.e., indeed, the mixed state is locally unstable.

Determination of the binodal line. Let $u(x) = \bar{u}^a$ be a constant solutions, i.e., a solution satisfying

$$\left.\frac{\delta F[u]}{\delta u}\right|_{u=\bar{u}^a} = C_1. \tag{2.24}$$

Such a solution is considered to be stable (in the sense of classical thermodynamics), if there does not exist a two-phase configuration whose total free energy (without the gradient terms) is lower than the total free energy of the homogenous solution. Otherwise, the solution is metastable. One way to analyse metastability is to look at the constant solution $\bar{u}^a$ with a disturbed part, see Fig. 2.3. The energy per unit volume of the disturbed part is $g(u) = f(u) - C_1(u - \bar{u}^a)$. Then, $\bar{u}^a$ is the stationary value of the functional $G[u]$ and it is a stationary value of the function $g(u)$. Let us assume that it is a local minimum. If $\bar{u}^a$ is the global minimum, then this constant solution is stable. Otherwise, we obtain metastability. Assuming that $g(u)$ has two local minima, the binodal line is then determined by the points $(\bar{u}^a, \beta)$ in the $(\bar{u}, T)$-plane (or, equivalently, $(\bar{u}, \beta)$-plane) for which there exists $\bar{u}^b$ such that $\partial_u g|_{u=\bar{u}^b} = 0$ (i.e., $\bar{u}^b$ is

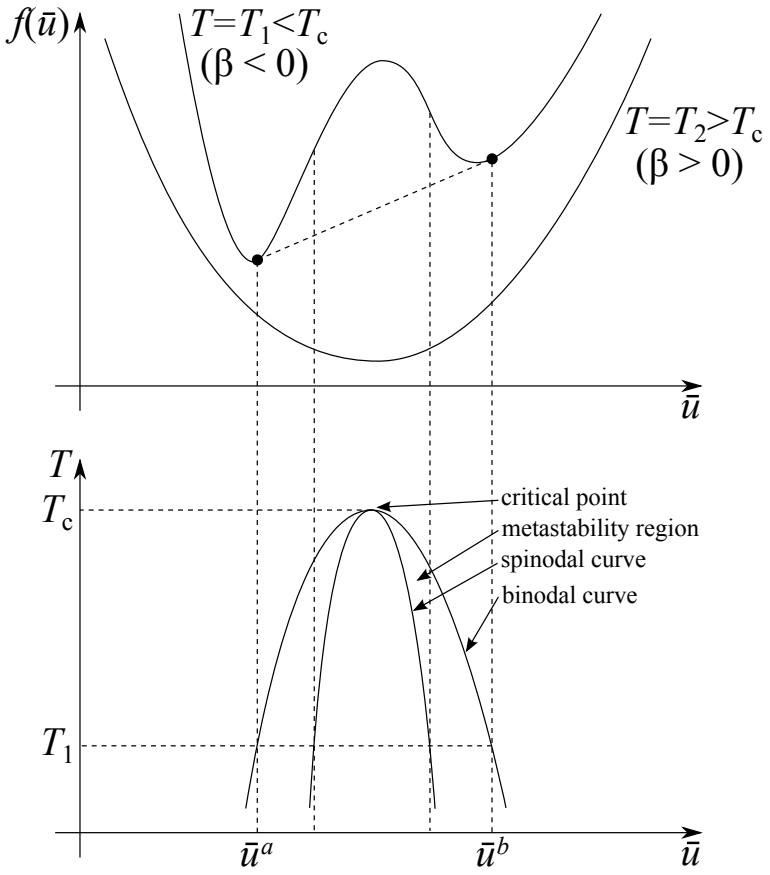

Figure 2.4: Free energy f as a function of $\bar{u}$ at temperatures $T = T_1 < T_c$, and $T = T_2 > T_c$. Underneath is the phase diagram in the $(\bar{u}, T)$-plane.

another local minimum) and $g(\bar{u}^b) = g(\bar{u}^a)$. Since $g(u) = f(u) - C_1(u - \bar{u}^a)$, we find $g'(u) = f'(u) - C_1 = f'(u) - f'(\bar{u}^a)$ (because $f'(\bar{u}^a) = C_1$). We, therefore, obtain the following two conditions:

$$f'(\bar{u}^b) = f'(\bar{u}^a), \tag{2.25}$$

$$\frac{f(\bar{u}^b) - f(\bar{u}^a)}{\bar{u}^b - \bar{u}^a} = C_1 \equiv f'(\bar{u}^a). \tag{2.26}$$

Equations (2.25) and (2.26) imply that $\bar{u}^a$ and $\bar{u}^b$ are the points at which the common tangent to the graph of $f(\bar{u})$ touches this graph. These points determine the binodal curve (coexistence curve) in the $(\bar{u}, T)$-plane (or, equivalently, $(\bar{u}, \beta)$-plane). Thus, we get the phase diagram shown in Fig 2.4, see also Alt and Pawlow [3].

Note that in the region of metastability, $f''(\bar{u}) > 0$, i.e., the graph of $f(\bar{u})$ is concave up. This implies that locally the free energy of the decomposed state with λ amount of $\bar{u}^a < \bar{u}$ and $(1 - \lambda)$ amount of $\bar{u}^b > \bar{u}$, where $\lambda \in (0, 1)$, is higher than the energy of

the mixed state. Indeed, for a function that is concave up, we have

$$f(\bar{u}) = f\big(\lambda\bar{u}^a + (1-\lambda)\bar{u}^b\big) < \lambda f(\bar{u}^a) + (1-\lambda) f(\bar{u}^b), \tag{2.27}$$

if both $\bar{u}^a$ and $\bar{u}^b$ are sufficiently close to $\bar{u}$. Therefore, indeed, the mixed state is locally stable. However, globally, there exists a decomposed state with lower energy.

2.3 Coarsening

After the initiation of spinodal decomposition, the late-stage dynamics is characterised by larger clusters (droplets or islands) of one phase surrounded by the other phase. However, these clusters are unstable to perturbations of larger length scales, and, over time, the average size of the clusters grows and the number of the clusters decreases. This process is called coarsening, see, for example, Onuki [83], Desai [27], Pototsky et al. [91].

Coarsening for the standard Cahn-Hilliard equation (2.11) is demonstrated in the time-dependent simulations in Figs. 2.5–2.7. The simulations have been performed using the Fourier spectral method described in Section 2.5. The equation is solved on a periodic domain of length 70 for $\bar{u} = 0.4$. The initial condition is $u(x,0) = 0.4 + \eta(x)$, where $\eta(x)$ is a randomly generated noise of small amplitude. Figs. 2.5(a)–(c), 2.6(a)–(c), 2.7(a)–(c) correspond to the evolution of the solution in the time intervals $[0, 300]$, $[300, 3500]$ and $[3500, 5000]$, respectively. Panels (a) of the figures show the time evolution of the solution in the indicated time intervals. Panels (b) show the time evolution of the energy $F[u]$ of the solution. Finally, panels (c) show the time evolution of the norm of the solution.

In Fig. 2.5(a), we can observe that the solution initially evolves into a superposition of 6 droplets (we enumerate them by $1, \ldots, 6$ starting from the left). At the same time, the energy and norm evolve to certain levels, as can be seen in panels (b) and (c). At around $t = 50$, droplets 5 and 6 start to merge into one larger droplet. The energy decreases and approaches another plateau. We can also observe that the norm of the solution increases and approaches another constant value. We can also observe that at a slightly later time, droplets 2 and 3 also start to merge, and the merging process for these two droplets takes slightly longer than for droplets 5 and 6, up to $t \approx 150$. The energy again monotonically decreases and approaches another steady value. Similarly,

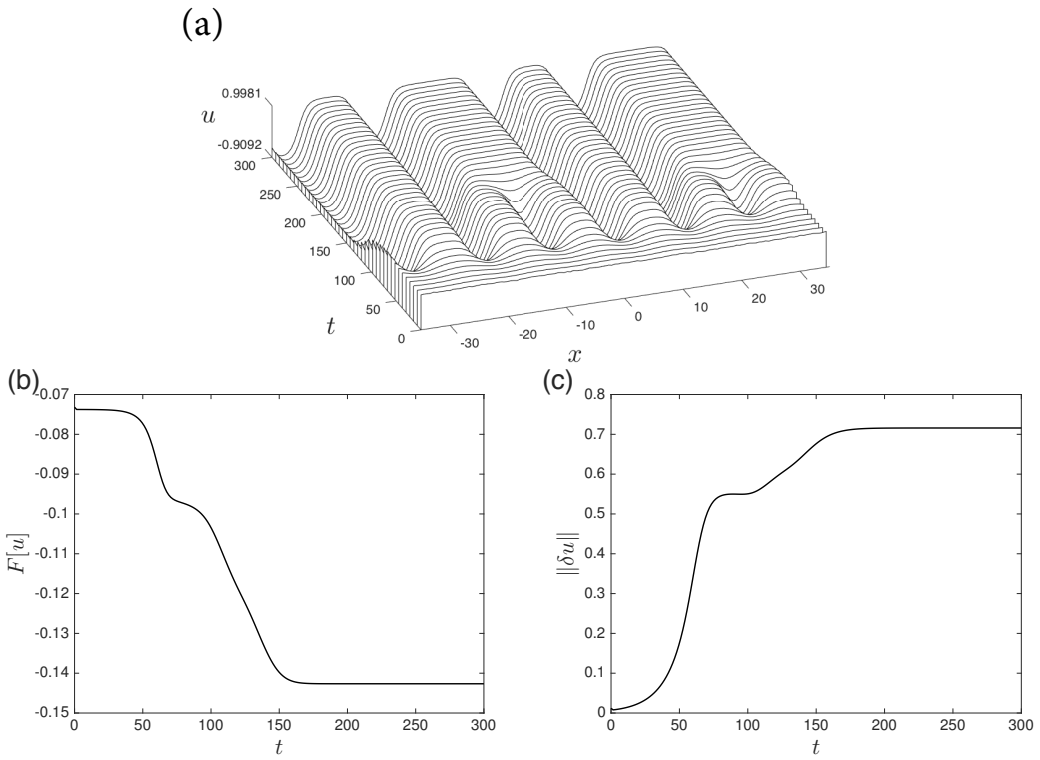

Figure 2.5: Numerical solution of the standard Cahn-Hilliard equation (2.11) on the periodic domain $[-35, 35]$ for $\bar{u} = 0.4$. Panel (a) shows the time evolution of the solution for $t \in [0, 300]$. Panel (b) shows the time evolution of the energy of the solution. Panel (c) shows the time evolution of the norm of the solution. The initial condition is 0.4 superimposed with a small-amplitude noise.

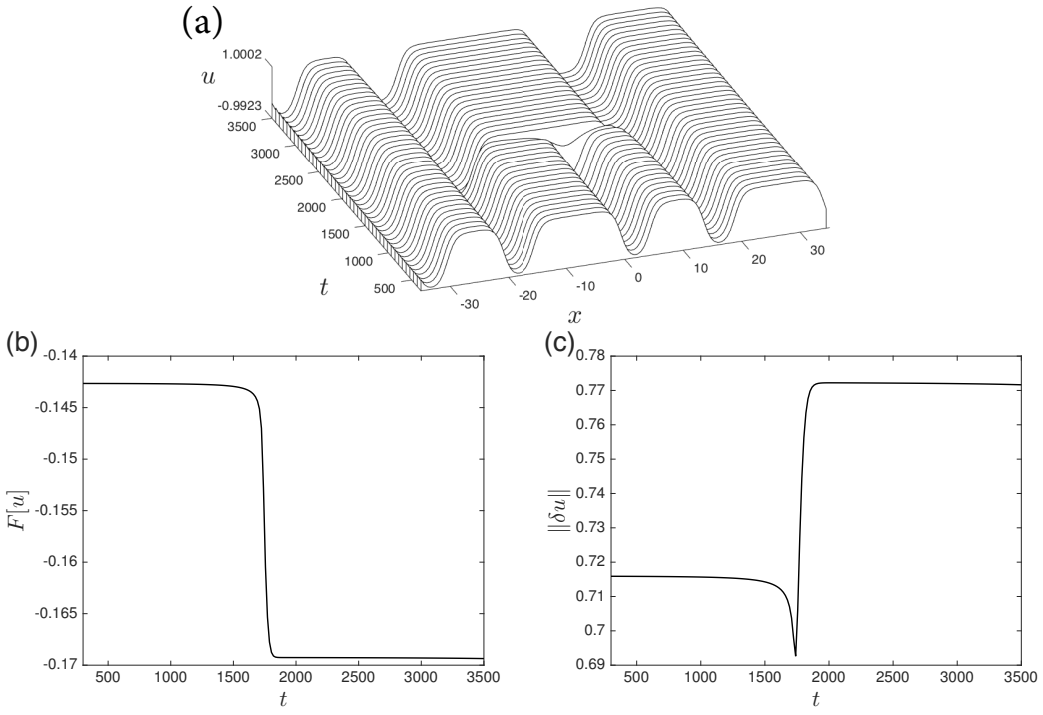

Figure 2.6: Numerical solution of the standard Cahn-Hilliard equation (2.11) on the periodic domain $[-35, 35]$ for $\bar{u} = 0.4$. Panel (a) shows the time evolution of the solution for $t \in [300, 3500]$. Panel (b) shows the time evolution of the energy of the solution. Panel (c) shows the time evolution of the norm of the solution.

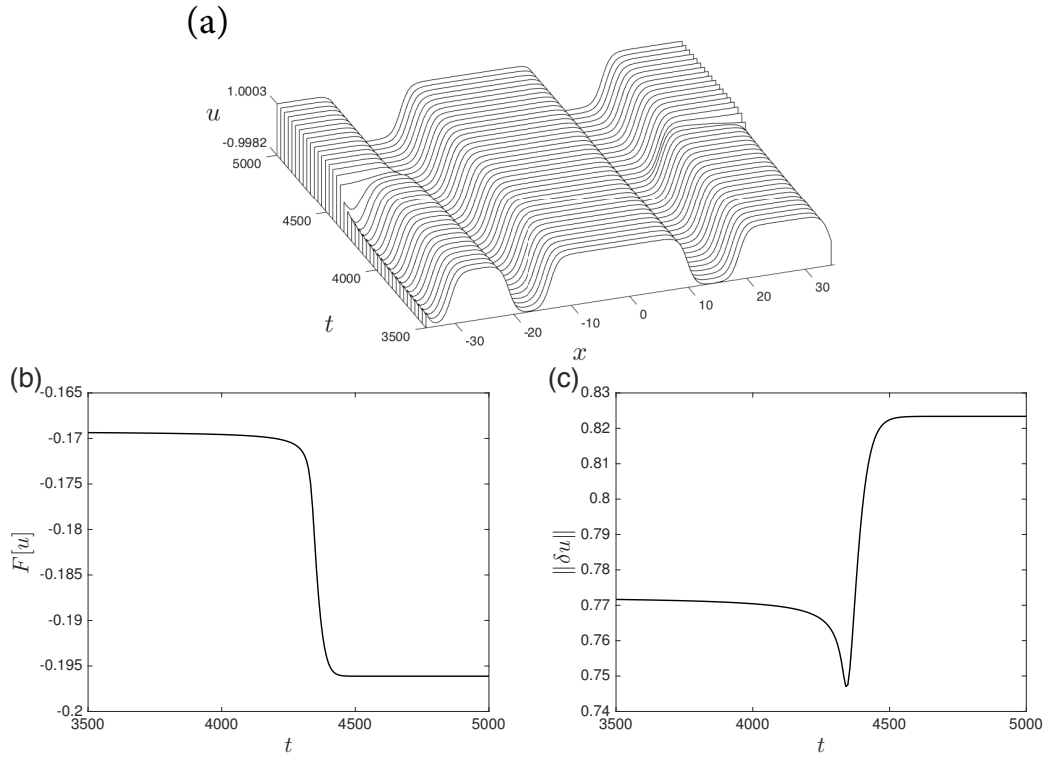

Figure 2.7: Numerical solution of the standard Cahn-Hilliard equation (2.11) on the periodic domain $[-35, 35]$ for $\bar{u} = 0.4$. Panel (a) shows the time evolution of the solution for $t \in [3500, 5000]$. Panel (b) shows the time evolution of the energy of the solution. Panel (c) shows the time evolution of the norm of the solution.

the norm increases and approaches a steady value. As a result, we obtain 4 droplets. We re-enumerate them by $1, \ldots, 4$. Droplets 1 and 3 are smaller than droplets 2 and 4.

In Fig. 2.6(a), we can observe that the coarsening process continues, namely, droplets 2 and 3 start to merge at about $t = 1700$. In panel (b), we can observe that the energy monotonically decreases again and attains an even smaller steady value. Panel (c) shows, that the norm of the solution also undergoes a relatively sharp change (non-monotonically this time) and attains a larger steady value.

Fig. 2.7 shows that the coarsening process further continues. Namely, in panel (a), we can see that the left and the right droplets start to merge (through the periodic boundaries) at about $t = 4300$. Panel (b) shows that the energy monotonically decreases again, and again attains a smaller steady value. Panel (c) shows, the norm of the solution also undergoes a relatively sharp non-monotonic change before attaining a larger steady value. As a result, we now have two droplets. We emphasise that the coarsening process does not stop, and eventually the two droplets should merge into one droplet. This last step, however, takes relatively long time, and we, therefore, do not show this merging.

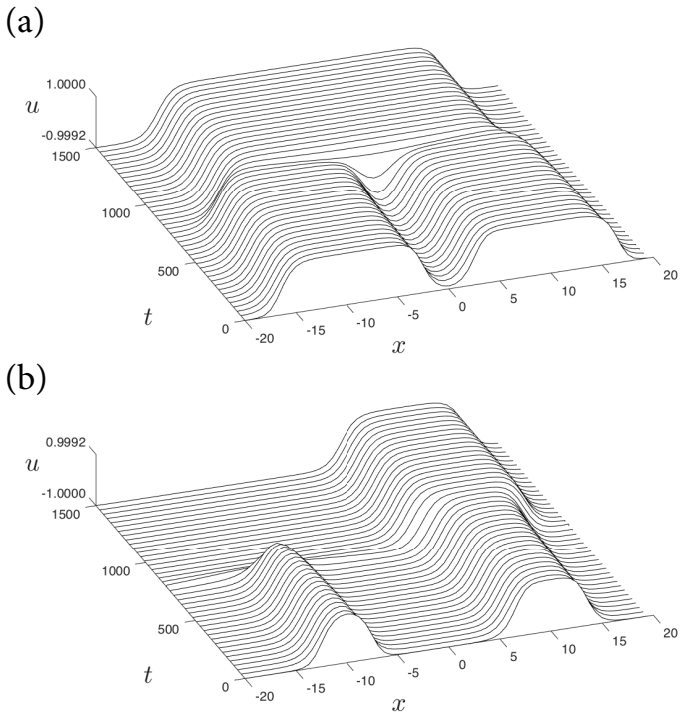

Figure 2.8: Numerical solution of the standard Cahn-Hilliard equation (2.11) on the periodic domain $[-20, 20]$ when (a) $\bar{u} = 0.4$ and (b) $\bar{u} = -0.4$ for $t \in [0, 1500]$. The initial conditions are two-droplet steady solutions superimposed with the most unstable eigenfunctions obtained in Section 5.4.1 (translational and volume modes for (a) and (b), respectively).

There are two main mechanisms of coarsening. One of these mechanisms is referred to as Ostwald ripening. In this mechanism, the centres of the clusters remain fixed in space while smaller clusters diffuse into larger clusters through the surrounding phase. This phenomenon was first described by Ostwald for the case of nucleation of crystals in liquids [84]. The theory to explain this process was first established by Lifshitz and Slyozov [74] and Wagner [116]. In this thesis, this mechanism will be referred to as coarsening due to the volume mode. In the other coarsening mechanism, the centres of the clusters are not fixed in space, and the coarsening happens due to the movement and joining of the clusters. This mechanism of coarsening will be referred to as coarsening due to the translational mode. References [13, 27, 78, 83, 91, 115, 122] provide more examples with modern explanations of the coarsening theory. In fact, both of these mechanisms play a role in the coarsening dynamics. However, one of the mechanisms maybe more important than the other, depending on the parameters of the system. We note that the relationship between these mechanisms for the case of coarsening of liquid droplets on surfaces has been analysed on both homogeneous and inhomogeneous surfaces, see Glasner and Witelski [41, 42], Pismen and Pomeau [88], Thiele [102] and Thiele et al. [104].

A detailed discussion of the coarsening mechanisms is given later in the Thesis, see Section 5.4.1. Here, we demonstrate the two coarsening mechanisms for the standard Cahn-Hilliard equation (2.11) in the time-dependant simulations presented in Fig. 2.8. The simulations have been performed again using the Fourier spectral method described in Section 2.5. The results are shown on the domain $[-L, L]$ with $L = 20$, and the initial conditions for the simulations are steady two-droplet solutions superimposed with $-0.1\cos(2\pi x/L) + 0.05\cos(\pi x/L)$. The time interval for both simulations is $[0, 1500]$. Panel (a) of the figure corresponds to $\bar{u} = 0.4$, and for this value of $\bar{u}$ the translational mode is apparently more unstable. We can observe that the two droplets move towards each other and eventually merge into one bigger droplet. Panel (b) of the figure corresponds to $\bar{u} = -0.4$, and for this value of $\bar{u}$ the volume mode is apparently more unstable. We can observe that in the time evolution, the size of one of the droplets decreases, while the size of the other one increases, i.e., the volume is transported from one of the droplets to the other one, and, eventually, we obtain one bigger droplet.

2.4 The convective Cahn-Hilliard equation

Our study is particularly focused on analysing how driving affects coarsening in two-droplet systems. As a model, we consider the following one-dimensional convective Cahn-Hilliard equation

$$u_t + Duu_x + (u - u^3 + u_{xx})_{xx} = 0. \tag{2.28}$$

Here, D is the driving force. This equation was derived, for example, by Golovin et al. [45, 46] as a model for a kinetically controlled growing crystal surface with a strongly anisotropic surface tension. In such a context, u is the surface slope and D is the growth driving force proportional to the difference between the bulk chemical potentials of the solid and fluid phases (see also Liu and Metiu [77] for modelling of growing crystal surfaces). Equation (2.28) was also obtained by Watson [118] as a small-slope approximation of the crystal-growth model obtained by Di Calro et al. [29] and Gurtin [51]. Related models have also been derived, for instance, in the context of epitaxial growth (see, for example, Šmilauer et al. [58]) and liquid droplets on inclined planes (see, for example, Thiele and Knobloch [105, 106], Thiele [102]). We note that coarsening dynamics for equation (2.28) has been studied in the limit $D \ll 1$ numerically by Emmott and Bray [36] and Golovin et al. [47] and analytically by Watson et al. [119], and scaling laws for the average separation between the successive

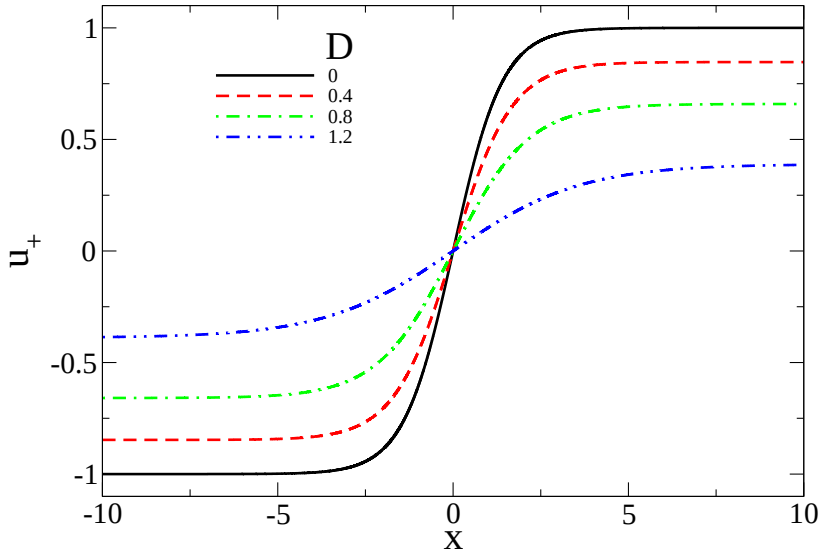

Figure 2.9: Exact kink solutions (2.32) of the convective Cahn-Hilliard equation (2.28) for different values of D, as is given in the legend.

phases as a function of time have been obtained. It has also been noticed by Zaks et al. [123] that driving can be used to stop coarsening for certain parameter values. One of our particular interests in the present thesis is to systematically investigate the effect of driving on coarsening for a wide range of parameter values and to construct detailed stability diagrams in the parameter planes. Note that due to the symmetry $(D, u) \to (-D, -u)$, it is sufficient to consider only non-negative values of D. Therefore, in this thesis, we will assume that $D \geq 0$.

The standard Cahn-Hilliard equation corresponds to the case $D = 0$. If the driving force grows there must be a transition from the coarsening dynamics to a chaotic spatio-temporal behavior, because if $D \to \infty$, then using the rescaling $u \to \tilde{u}/D$, equation (2.28) reduces to the well-known Kuramoto-Sivashinsky (KS) equation (see Golovin et al. [47]), that exhibits spatio-temporal chaos. Indeed, substituting $u = \tilde{u}/D$ in (2.28), we obtain

$$\frac{\tilde{u}_t}{D} + D\frac{\tilde{u}}{D}\frac{\tilde{u}_x}{D} + \left(\frac{\tilde{u}}{D} - \frac{\tilde{u}^3}{D^3} + \frac{\tilde{u}_{xx}}{D}\right)_{xx} = 0. \tag{2.29}$$

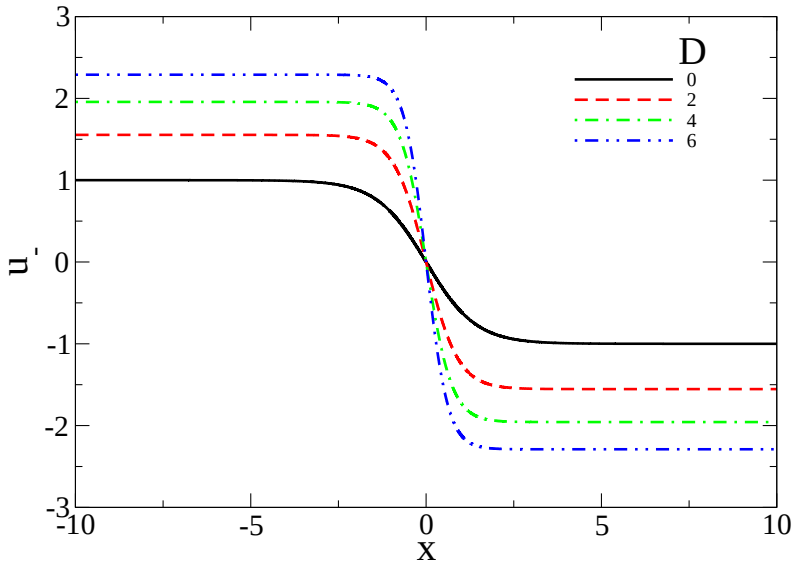

Figure 2.10: Exact anti-kink solutions (2.32) of the convective Cahn-Hilliard equation (2.28) for different values of D, as is given in the legend.

Multiplying by D, we get (after dropping tildes)

$$u_t + uu_x + \left(u - \frac{u^3}{D^2} + u_{xx}\right)_{xx} = 0. \tag{2.30}$$

Therefore, in the limit $D \to \infty$, we find

$$u_t + uu_x + (u + u_{xx})_{xx} = 0, \tag{2.31}$$

which is the Kuramoto-Sivashinsky (KS) equation, see Golovin et al. [47].

Equation (2.28) has exact kink and anti-kink solutions (see Golovin et al. [47]) given by

$$u_\pm(x) = \pm u_\pm^0 \tanh \frac{u_\pm^0}{\sqrt{2}} x, \qquad u_\pm^0 = \sqrt{1 \mp \frac{D}{\sqrt{2}}}, \tag{2.32}$$

for $\pm$ respectively. Examples of exact kink solutions $u_+(x)$ are shown in Fig. 2.9 for $D = 0$, 0.4, 0.8 and 1.2, as is indicated in the legend. Note that kink solutions exist only for $D < \sqrt{2}$. Examples of exact anti-kink solutions $u_-(x)$ are shown in Fig. 2.10 for $D = 0$, 2, 4 and 6, as is indicated in the legend.

2.4.1 Scalings for the convective Cahn-Hilliard equation

2.4.1.1 Scaling I

Let us consider the convective Cahn-Hilliard equation in the following general dimensional form:

$$\tilde{u}_{\tilde{t}} + \tilde{D}\tilde{u}\tilde{u}_{\tilde{x}} + \tilde{m}(\tilde{\kappa}\tilde{u}_{\tilde{x}\tilde{x}} + \tilde{a}\tilde{u} - \tilde{b}\tilde{u}^3)_{\tilde{x}\tilde{x}} = 0, \tag{2.33}$$

where $\tilde{t}$ and $\tilde{x}$ denote dimensional time and spatial variables, respectively, $\tilde{u}$ is a dimensional order parameter and $\tilde{a}$, $\tilde{b}$, $\tilde{m}$, $\tilde{\kappa}$ and $\tilde{D}$ denote constants with appropriate dimensions. Let us also assume that the equation is given on a domain of size $\tilde{d}$. We introduce non-dimensional variables by choosing a set of not-yet-specified scales τ, l and Γ for variables $\tilde{t}$, $\tilde{x}$ and $\tilde{u}$, respectively, and defining

$$t = \frac{\tilde{t}}{\tau}, \qquad x = \frac{\tilde{x}}{l}, \qquad u = \frac{\tilde{u}}{\Gamma}. \tag{2.34}$$

Substituting $\tilde{u} = \Gamma u$ in equation (2.33) and using that

$$\frac{\partial}{\partial \tilde{t}} = \frac{1}{\tau}\frac{\partial}{\partial t}, \qquad \frac{\partial}{\partial \tilde{x}} = \frac{1}{l}\frac{\partial}{\partial x}, \tag{2.35}$$

we obtain

$$u_t + \frac{\tilde{D}\Gamma\tau}{l}uu_x + \left(\frac{\tilde{m}\tilde{\kappa}\tau}{l^4}u_{xx} + \frac{\tilde{m}\tilde{a}\tau}{l^2}u - \frac{\tilde{m}\tilde{b}\tau\Gamma^2}{l^2}u^3\right)_{xx} = 0. \tag{2.36}$$

Next, we define the following dimensionless parameters:

$$D = \frac{\tilde{D}\Gamma\tau}{l}, \quad \kappa = \frac{\tilde{m}\tilde{\kappa}\tau}{l^4}, \quad a = \frac{\tilde{m}\tilde{a}\tau}{l^2}, \quad b = \frac{\tilde{m}\tilde{b}\tau\Gamma^2}{l^2}. \tag{2.37}$$

For the first non-dimensionalisation, we choose the scales so that $\kappa = a = b = 1$, i.e.,

$$\frac{\tilde{m}\tilde{\kappa}\tau}{l^4} = 1, \quad \frac{\tilde{m}\tilde{a}\tau}{l^2} = 1, \quad \frac{\tilde{m}\tilde{b}\tau\Gamma^2}{l^2} = 1. \tag{2.38}$$

It can be easily verified that these equations imply the following scales:

$$\tau = \frac{\tilde{\kappa}}{\tilde{m}\tilde{a}^2}, \quad l = \sqrt{\frac{\tilde{\kappa}}{\tilde{a}}}, \quad \Gamma = \sqrt{\frac{\tilde{a}}{\tilde{b}}}. \tag{2.39}$$

Substituting these scales into the definition of the dimensionless driving force, we obtain

$$D = \frac{\tilde{D}\sqrt{\tilde{\kappa}}}{\tilde{a}\tilde{m}\sqrt{\tilde{b}}}. \tag{2.40}$$

The dimensionless convective Cahn-Hilliard equation then takes the form

$$u_t + Duu_x + (u_{xx} + u - u^3)_{xx} = 0. \tag{2.41}$$

There is one dimensionless parameter appearing in the equation, which the driving-force parameter D. However, we note that there is one additional dimensionless parameter that does not explicitly appear in the equation. It is the dimensionless domain size,

$$d = \frac{\tilde{d}}{l} = \tilde{d}\sqrt{\frac{\tilde{a}}{\tilde{\kappa}}}. \tag{2.42}$$

Table 2.1 shows the dependence of the scales τ, l and Γ, the dimensionless driving force D and the dimensionless domain size d on the dimensional constants for Scaling I. It can be seen that the dimensionless driving force is directly proportional to $\tilde{D}$, and changing $\tilde{D}$ results only in the change of D and does not affect the scales τ, l and Γ. Note that parameter D can also be changed by changing any of the other dimensional parameters (except $\tilde{d}$), but this also results in the change of at least one of the scales.

	l	Γ	τ	D	d
$\tilde{a}$	✓	✓	✓	✓	✓
$\tilde{b}$	–	✓	–	✓	–
$\tilde{m}$	–	–	✓	✓	–
$\tilde{\kappa}$	✓	–	✓	✓	✓
$\tilde{D}$	–	–	–	✓	–
$\tilde{d}$	–	–	–	–	✓

Table 2.1: Dependence of the scales τ, l and Γ and the dimensionless driving force D and the dimensionless domain size d on the dimensional constants for Scaling I.

2.4.1.2 Scaling II

In this section, we discuss an alternative scaling. We now choose the length scale l so that the dimensionless domain size is 2π (for convenience), i.e, we choose

$$l = \frac{\tilde{d}}{2\pi}, \tag{2.43}$$

where $\tilde{d}$ is the dimensional domain size. Then, we define the following dimensionless parameters:

$$D = \frac{2\pi\tilde{D}\Gamma\tau}{\tilde{d}}, \quad \kappa = \frac{16\pi^4\tilde{m}\tilde{\kappa}\tau}{\tilde{d}^4}, \quad a = \frac{4\pi^2\tilde{m}\tilde{a}\tau}{\tilde{d}^2}, \quad b = \frac{4\pi^2\tilde{m}\tilde{b}\tau\Gamma^2}{\tilde{d}^2}. \tag{2.44}$$

Next, we choose the scales τ and Γ so that $\kappa = b = 1$, i.e.,

$$\frac{16\pi^4\tilde{m}\tilde{\kappa}\tau}{\tilde{d}^4} = 1, \qquad \frac{4\pi^2\tilde{m}\tilde{b}\tau\Gamma^2}{\tilde{d}^2} = 1. \tag{2.45}$$

It can be easily verified that these equations imply the following scales:

$$\tau = \frac{\tilde{d}^4}{16\pi^4\tilde{m}\tilde{\kappa}}, \qquad \Gamma = \frac{2\pi}{\tilde{d}}\sqrt{\frac{\tilde{\kappa}}{\tilde{b}}}. \tag{2.46}$$

Substituting these scales into the definition of the dimensionless driving force D and parameter a, we obtain

$$D = \frac{\tilde{D}\tilde{d}^2}{4\pi^2\tilde{m}\sqrt{\tilde{\kappa}\tilde{b}}}, \qquad a = \frac{\tilde{d}^2\tilde{a}}{4\pi^2\tilde{\kappa}}. \tag{2.47}$$

The dimensionless convective Cahn-Hilliard equation takes the form

$$u_t + Duu_x + (u_{xx} + au - u^3)_{xx} = 0. \tag{2.48}$$

The case of a positive a corresponds to spinodal decomposition or phase separation, whereas for the case of a negative a a homogeneous (mixed) state is linearly stable.

Table 2.2 shows the dependence of the scales τ, l and Γ and the dimensionless parameters D and a on the dimensional constants for Scaling II. It can be seen that the dimensionless driving force D is directly proportional to $\tilde{D}$, and changing $\tilde{D}$ results only in the change of D and does not affect the scales τ, l and Γ and the parameter a.

	l	Γ	τ	D	a
$\tilde{a}$	–	–	–	–	✓
$\tilde{b}$	–	✓	–	✓	–
$\tilde{m}$	–	–	✓	✓	–
$\tilde{\kappa}$	–	✓	✓	✓	✓
$\tilde{D}$	–	–	–	✓	–
$\tilde{d}$	✓	✓	✓	✓	✓

Table 2.2: Dependence of the scales τ, l and Γ and the dimensionless driving force D and dimensionless parameter a on the dimensional constants for Scaling II.

Also, the dimensionless parameter a is directly proportional to $\tilde{a}$, and changing $\tilde{a}$ results only in the change of a and does not affect the scales τ, l and Γ and the parameter D. Note that parameters D and a can also be changed by changing any of the other dimensional parameters, but this also results in the change of at least one of the scales.

2.5 Time-dependent solution by spectral methods

In our study, we are interested in analysing the behaviour of solutions of the convective Cahn-Hilliard equation for various values of parameters. One way to understand how the behaviour of the solutions changes as some of the parameters change is to perform time-dependent simulations. In this section, we discuss how to numerically find time-dependent solutions of the convective Cahn-Hilliard equation by a Fourier spectral method (see, e.g., Boyd [11] and Trefethen [112]) involving a Runge-Kutta integration in time, which is described, for example, in Gustafsson et al. [52].

We solve equation (2.11) on the domain $x \in [-L/2, L/2]$, with periodic boundary conditions. We can write equation (2.11) as

$$u_t + \frac{D}{2}(u^2)_x + u_{xx} - (u^3)_{xx} + u_{xxxx} = 0. \tag{2.49}$$

Next, our goal is to rewrite this equation in the Fourier space. To do this, we will take the Fourier transform of (2.49). After solving the equation in the Fourier space, we can obtain the solution in the real space by taking the inverse Fourier transform. The Fourier and the inverse Fourier transforms are defined by

$$\mathcal{F}[f](k) \equiv \hat{f}(k) = \int_{-\infty}^{\infty} f(x)e^{-ikx}dx, \tag{2.50}$$

$$\mathcal{F}^{-1}[\hat{f}](x) \equiv f(x) = \frac{1}{2\pi}\int_{-\infty}^{\infty} \hat{f}(k)e^{ikx}dk, \tag{2.51}$$

respectively. Taking the Fourier transform of (2.49), we obtain

$$\hat{u}_t + \frac{D}{2}(ik)\widehat{u^2} + (ik)^2\hat{u} - (ik)^2\widehat{u^3} + (ik)^4\hat{u} = 0, \tag{2.52}$$

and after rearrangement we obtain

$$\hat{u}_t + \frac{Dki}{2}\widehat{u^2} + k^2\widehat{u^3} + (k^4 - k^2)\hat{u} = 0. \tag{2.53}$$

Now, to remove stiffness, we multiply equation (2.53) by an integrating factor $e^{-s(k)t}$, where $s(k) = k^2 - k^4$,

$$e^{-s(k)t}\hat{u}_t + e^{-s(k)t}\left[\frac{Dki}{2}\widehat{u^2} + k^2\widehat{u^3}\right] - s(k)e^{-s(k)t}\hat{u} = 0. \tag{2.54}$$

We can write equation (2.54) as

$$(e^{-s(k)t}\hat{u})_t + e^{-s(k)t}\left[\frac{Dki}{2}\widehat{u^2} + k^2\widehat{u^3}\right] = 0. \tag{2.55}$$

We define

$$\hat{U} = e^{-s(k)t}\hat{u}. \tag{2.56}$$

Then,

$$\hat{u} = e^{s(k)t}\hat{U}. \tag{2.57}$$

Equation (2.54) takes the form

$$\hat{U}_t + e^{-s(k)t}\left[\frac{Dki}{2}\widehat{u^2} + k^2\widehat{u^3}\right] = 0. \tag{2.58}$$

We obtain that

$$u = \mathcal{F}^{-1}[e^{s(k)t}\hat{U}]. \tag{2.59}$$

Then

$$u^2 = (\mathcal{F}^{-1}[e^{s(k)t}\hat{U}])^2, \qquad u^3 = (\mathcal{F}^{-1}[e^{s(k)t}\hat{U}])^3. \tag{2.60}$$

Therefore, we obtain

$$\hat{U}_t + e^{-s(k)t}\left[\frac{Dki}{2}\mathcal{F}[(\mathcal{F}^{-1}[e^{s(k)t}\hat{U}])^2] + k^2\mathcal{F}[(\mathcal{F}^{-1}[e^{s(k)t}\hat{U}])^3]\right] = 0. \tag{2.61}$$

This equation can then be considered as a coupled system of ordinary differential equations for $\hat{U}(k)$ at a discrete set of values of the wave numbers. We can then solve this system of equations, for example, by the fourth-order Runge-Kutta method.

2.6 Numerical continuation and bifurcation analysis

If one is interested in analysing in detail the qualitative long-time behaviour of solutions of the convective Cahn-Hilliard equation for various parameter values, performing time-dependent simulations may be time-consuming and not very efficient. For such a purpose, performing numerical continuation and identifying regions for various attractors (e.g., equilibria, periodic orbits, homoclinic or heteroclinic orbits, invariant tori) in the parameter space (or parameter plane(s)) is more efficient and provides more detailed information on the long-time behaviour of the solutions. In this section, we briefly outline the main ideas of numerical continuation and bifurcation analysis. More detailed discussions can be found, for example, in Allgower et al. [2], Dhooge et al. [28], Dijkstra et al. [30], Doedel et al. [31], Krauskopf et al. [69], Kuznetsov [71], Thiele [102]. Note that there are several publicly available software packages for carrying numerical continuation and bifurcation analysis. In the present thesis, we use the packages Auto07p [31] and Matcont [28].

First, we note that the convective Cahn-Hilliard equation can be considered as an infinite-dimensional dynamical system on an appropriate function space, see, for example, Temam [101]. By appropriately discretising this partial differential equation, we can obtain a finite-dimensional dynamical system, i.e., the following system of first-order ordinary differential equations written in a vector form:

$$\frac{d\boldsymbol{u}}{dt} = \boldsymbol{f}(\boldsymbol{u}, \alpha), \tag{2.62}$$

where $\boldsymbol{u} \in \mathbb{R}^n$ represents the numerical solution of the partial differential equation (it can be, for example, a vector of function values at the given grid points for the case of a finite-difference discretisation, or a vector of Fourier coefficients for the case of a spectral representation). We also indicate here that the right-hand sides depend on a parameter α, and our aim is to analyse the dependence of the solutions on this parameter. For the case of the convective Cahn-Hilliard equation, we can choose α to be, for instance, the driving force, D, the domain size, L, or the mean value $\bar{u} = \int_0^L u\,dx$. We will use the notation $\boldsymbol{x} = (\boldsymbol{u}, \alpha) \in \mathbb{R}^{n+1}$.

First of all, we are interested in computing equilibrium solutions, i.e., solutions satisfying the condition

$$\frac{d\boldsymbol{u}}{dt} = 0 \qquad \Leftrightarrow \qquad \boldsymbol{f}(\boldsymbol{u}, \alpha) = 0. \tag{2.63}$$

We assume that for some parameter value α_0 we know one of the solutions $\boldsymbol{u}_0$, and that the Jacobian of $\boldsymbol{f}$ at $\boldsymbol{x}_0 = (\boldsymbol{u}_0, \alpha_0)$ is of full rank. A straight-forward method for computing the solution curve would be the *natural parameter continuation*, where parameter α is increased/decreased step by step using a sufficiently small step size $\Delta\alpha$ and Newton iterations to obtain solutions at the next steps with the initial guesses given by the solutions at the previous steps. The main disadvantage of the natural parameter continuation is that it fails at turning points (i.e., at saddle-node bifurcations). This can be fixed by utilising the *pseudo-arclength continuation method,* which is often used in practice. The method is based on choosing the arclength parameter s for parameterising the solution curve. The algorithm can then be implemented as a predictor-corrector method. Given the point $\boldsymbol{x}_i = (\boldsymbol{u}_i, \alpha_i)$ on the solution curve, a tangent prediction is used to obtain an initial guess $\tilde{\boldsymbol{x}}_{i+1}$ for $\boldsymbol{x}_{i+1}$, i.e.,

$$\tilde{\boldsymbol{x}}_{i+1} = \boldsymbol{x}_i + \Delta s\, \boldsymbol{v}_i, \tag{2.64}$$

where Δs is the chosen sufficiently small step size and $\boldsymbol{v}_i$ is a unit tangent vector to the solution curve at $\boldsymbol{x}_i$, i.e., a vector such that

$$\boldsymbol{f}_{\boldsymbol{x}}(\boldsymbol{x}_i)\boldsymbol{v}_i = 0, \qquad \|\boldsymbol{v}_i\|_2 = 1. \tag{2.65}$$

Here, $\boldsymbol{f}_{\boldsymbol{x}}(\boldsymbol{x}_i)$ denotes the Jacobian matrix of $\boldsymbol{f}$ at point $\boldsymbol{x}_i$. The correction step is to use Newton iterations to satisfy the following system of $n+1$ equations for $n+1$ unknowns:

$$\boldsymbol{f}(\boldsymbol{x}_{i+1}) = 0, \qquad g(\boldsymbol{x}_{i+1}) = 0, \tag{2.66}$$

where g is the following function:

$$g(\boldsymbol{x}) = \langle \boldsymbol{x} - \tilde{\boldsymbol{x}}_{i+1},\, \boldsymbol{v}_i \rangle. \tag{2.67}$$

Here, $\langle\, \cdot\,,\, \cdot\, \rangle$ denotes the usual dot product in $\mathbb{R}^{n+1}$. Solving system (2.66) means finding the point on the solution curve that belongs to the hyperplane that passes through $\tilde{\boldsymbol{x}}_{i+1}$ and that is orthogonal to $\boldsymbol{v}_i$.

The stability of a steady state solution $\boldsymbol{u}_i$ at $\alpha = \alpha_i$ can be assessed by analysing the eigenvalues of the Jacobian matrix $\boldsymbol{f}_{\boldsymbol{u}}(\boldsymbol{x}_i)$ of $\boldsymbol{f}$ with respect to $\boldsymbol{u}$. Indeed, by assuming that $\alpha = \alpha_i$ and substituting $\boldsymbol{u}(t) = \boldsymbol{u}_i + \epsilon\, \tilde{\boldsymbol{u}}(t)$ in (2.62), where $\epsilon \ll 1$, we obtain the

following linearised vector equation:

$$\frac{d\tilde{\boldsymbol{u}}}{dt} = \boldsymbol{f}_{\boldsymbol{u}}(\boldsymbol{x}_i)\tilde{\boldsymbol{u}}. \tag{2.68}$$

By considering solutions of the form $\tilde{\boldsymbol{u}} \propto \mathrm{e}^{\lambda t}\hat{\boldsymbol{u}}$, we obtain

$$\lambda\,\hat{\boldsymbol{u}} = \boldsymbol{f}_{\boldsymbol{u}}(\boldsymbol{x}_i)\hat{\boldsymbol{u}}, \tag{2.69}$$

i.e., the growth rate λ is an eigenvalue of the matrix $\boldsymbol{f}_{\boldsymbol{u}}(\boldsymbol{x}_i)$. Thus, if all the eigenvalues of $\boldsymbol{f}_{\boldsymbol{u}}(\boldsymbol{x}_i)$ have negative real parts, $\tilde{\boldsymbol{u}}$ will tend to zero as t increases, and the solution $\boldsymbol{u}_i$ is then linearly stable. On the other hand, if some of the eigenvalues have positive real parts, there will exist modes that grow in time, and $\boldsymbol{u}_i$ is then linearly unstable.

In addition to computing the solution curve and analysing the stability of equilibrium solutions, we are interested in detecting various bifurcation points (where the eigenvalues cross the imaginary axis) on the solution curve and computing side branches of, for example, steady-state and time-periodic solutions. Detection of bifurcation points can be implemented by monitoring additional test functions which change signs at the corresponding bifurcation points, e.g.,

$$\phi_1(\boldsymbol{x}) = \det\begin{pmatrix}\boldsymbol{f}_{\boldsymbol{x}}\\ \boldsymbol{v}^T\end{pmatrix}, \qquad \phi_2(\boldsymbol{x}) = v_{n+1} \tag{2.70}$$

can be used for detection of branch points and turning points (or saddle-nodes), respectively, where $\boldsymbol{v} \in \mathbb{R}^{n+1}$ is the tangent vector to the equilibrium solution curve. (See, for example, Dhooge et al. [28] for a test function for detection of Hopf bifurcations). Branch points (i.e., points at which there emerge side branches of equilibrium solutions) then correspond to $\phi_1 = 0$, whereas turning points (or saddle-node bifurcations) are detected by conditions $\phi_2 = 0$ and $\phi_1 \neq 0$. A proof that these conditions correctly determine the mentioned bifurcations is given, for example, in Kuznetsov [71]. After detecting a bifurcation point, we can either continue computing the primary branch of equilibrium solutions or switch to one of the solution curves emanating from this point, or we can add an extra parameter (if possible) and an extra algebraic condition to trace the location of this bifurcation in a parameter plane.

To conclude this section, we briefly discuss computation of time-periodic solutions (i.e., limit cycles) of (2.62). A time-periodic solution of (2.62) satisfies

$$\frac{d\boldsymbol{u}}{dt} = \boldsymbol{f}(\boldsymbol{u}, \alpha), \qquad \boldsymbol{u}(0) = \boldsymbol{u}(T), \tag{2.71}$$

where T is the time period. For convenience, we can introduce the rescaled time $\tau = t/T$ to obtain

$$\frac{d\boldsymbol{u}}{d\tau} = T\boldsymbol{f}(\boldsymbol{u}, \alpha), \qquad \boldsymbol{u}(0) = \boldsymbol{u}(1). \tag{2.72}$$

Note that the boundary-value problem (2.72) does not have a unique solution. Indeed, if $\boldsymbol{u}(\tau)$ is a solution, then $\boldsymbol{u}(\tau + \tau_0)$ is also a solution for any $\tau_0 \in (0, 1)$, due to periodicity. Thus, an extra phase condition is needed to break this non-uniqueness. There are different ways to implement this. One could use, for example, the following condition:

$$\langle \boldsymbol{u}(0) - \boldsymbol{v}(0), \dot{\boldsymbol{v}}(0) \rangle = 0, \tag{2.73}$$

where $\boldsymbol{v}$ is some reference time-periodic solution. This condition requires $\boldsymbol{u}$ to pass at $\tau = 0$ through a point that belongs to the hyperplane normal to the closed curve $\boldsymbol{v}(\tau)$ at $\tau = 0$. If a continuation of time-periodic solutions is performed in parameter α, $\boldsymbol{v}$ can be selected to be the solution computed at the previous step, i.e., $\boldsymbol{v}(\tau) = \boldsymbol{u}_i(\tau)$. We note that in practice the following more reliable integral phase condition is often used:

$$\int_0^1 \langle \boldsymbol{u}(\tau), \dot{\boldsymbol{u}}_i(\tau) \rangle \, d\tau = 0, \tag{2.74}$$

see, for example, Dhooge et al. [28] and Kuznetsov [71]. Thus, the complete boundary-value problem for computing a time-periodic solution $\boldsymbol{u}(\tau)$, given a reference solution $\boldsymbol{u}_i(\tau)$, is

$$\begin{cases} \dfrac{d\boldsymbol{u}}{d\tau} - T\boldsymbol{f}(\boldsymbol{u}, \alpha) = 0, \\ \boldsymbol{u}(0) - \boldsymbol{u}(1) = 0, \\ \int_0^1 \langle \boldsymbol{u}(\tau), \dot{\boldsymbol{u}}_i(\tau) \rangle \, d\tau = 0. \end{cases} \tag{2.75}$$

Next, this system can be discretised in a certain way. We can use, for example, finite differences for the time derivatives and the trapezoidal rule for the integral. If, for example, time interval $\tau \in [0, 1]$ is discretised into N subintervals and the unknowns $u^{j,k}$ representing the values of the j-components of $\boldsymbol{u}$ at $\tau = \tau_k = (k-1)/N$ are introduced, where $j = 1, \ldots, n$ and $k = 1, \ldots, N$, we find that system (2.75) can be represented as a system of $n\,N + 1$ algebraic equations for $n\,N$ unknowns $u^{j,k}$ and the time period T. Thus, time-periodic solutions of (2.71) correspond to fixed points of this algebraic system of $n\,N + 1$ equations for $n\,N + 1$ unknowns. Therefore, solution curves of time-periodic solutions can be found by, for example, performing the pseudo-arclength continuation discussed above for this algebraic system of equations.

Chapter 3

Linear stability of homogeneous solutions

3.1 Introduction

In this chapter, we analyse linear stability of homogeneous solutions of the standard and convective Cahn-Hilliard equations. We perform both the temporal (in Sections 3.2 and 3.3) and spatial (in Section 3.4) linear stability analysis. The temporal linear stability analysis allows to investigate the regions of the parameter values for which homogeneous solutions are stable or unstable to small-amplitude perturbations (i.e., when small-amplitude perturbations introduced on a homogeneous solution decay or grow in time). The temporal linear stability analysis also gives the phase velocity of small-amplitude sinusoidal perturbations. The spatial linear stability analysis, on the other hand, allows to investigate how a locally non-uniform solution, such as a single-interface solution (i.e., a kink or anti-kink solution) or a double-interface solution (such as a droplet or a cavity) approaches the uniform levels. The spatial linear stability analysis allows to investigate the rates at which the uniform levels are approached and also to obtain the period of the decaying oscillations that may be present on top of the uniform levels. The spatial linear stability analysis, in fact, reduces to the analysis of the stability of the fixed points of a finite-dimensional dynamical system. The locally non-uniform solutions then correspond to homoclinic, or heteroclinic orbits (or limit cycles passing in the vicinity of the fixed point(s)). A more detailed discussion of such locally non-uniform solutions and their investigation from the dynamical systems point of view is given in the final section of this chapter, Section 3.5.

3.2 Linear stability of homogeneous solutions

In this section, we analyse linear stability of homogeneous solutions of the convective Cahn-Hilliard equation (2.28). (Note that the linear stability of homogeneous solutions of the standard Cahn-Hilliard equation, when $D = 0$, was already discussed in Section 2.2.) To do this, we first linearise equation (2.28) by substituting $u = \bar{u} + \epsilon\tilde{u}$ in this equation, where $\bar{u}$ is a constant and $\epsilon \ll 1$, keep terms of size $O(\epsilon)$ and ignore higher-order terms. We obtain the equation

$$\tilde{u}_t = -D\bar{u}\tilde{u}_x - \tilde{u}_{xx} + 3\bar{u}^2\tilde{u}_{xx} - \tilde{u}_{xxxx}. \tag{3.1}$$

Next, we assume the ansatz $\tilde{u} = \exp(ikx + \beta t)$ and obtain

$$\tilde{u}_t = \beta e^{ikx+\beta t}, \quad \tilde{u}_x = ike^{ikx+\beta t}, \quad \tilde{u}_{xx} = -k^2 e^{ikx+\beta t}, \quad \tilde{u}_{xxxx} = k^4 e^{ikx+\beta t}. \tag{3.2}$$

Substituting expressions (3.2) into (3.1), we find the dispersion relation

$$\beta(k) = -iD\bar{u}k + k^2 - 3\bar{u}^2k^2 - k^4. \tag{3.3}$$

Assuming that k is real, the real part of $\beta(k)$ gives the growth rate, $w(k)$, of a wave with the wavenumber k. So we obtain

$$w(k) = [(1 - 3\bar{u}^2) - k^2]k^2. \tag{3.4}$$

Now we solve equation $w(k_c) = 0$ to find the cutoff wavenumber k_c:

$$k_c^2(1 - 3\bar{u}^2 - k_c^2) = 0. \tag{3.5}$$

We are interested only in positive solutions, and we find that the only positive solution of equation (3.5) is

$$k_c = \sqrt{1 - 3\bar{u}^2}. \tag{3.6}$$

This solution exists only when $1 - 3\bar{u}^2 > 0$, i.e., when $-\sqrt{1/3} < \bar{u} < \sqrt{1/3}$. In this case, there is a band of unstable wavenumbers, $k \in (0,\, k_c)$, see Fig. 3.1 showing the dimensionless growth rate $w(k)$ as a function of k for $\bar{u} = 0$ by a thick solid line. Otherwise, if $1 - 3\bar{u}^2 < 0$, i.e., when $\bar{u} > \sqrt{1/3}$ or $\bar{u} < -\sqrt{1/3}$, we find that $w(k) < 0$ for all $k > 0$, see Fig. 3.1 showing the growth rate $w(k)$ as a function of k for $u_0 = 0.6$

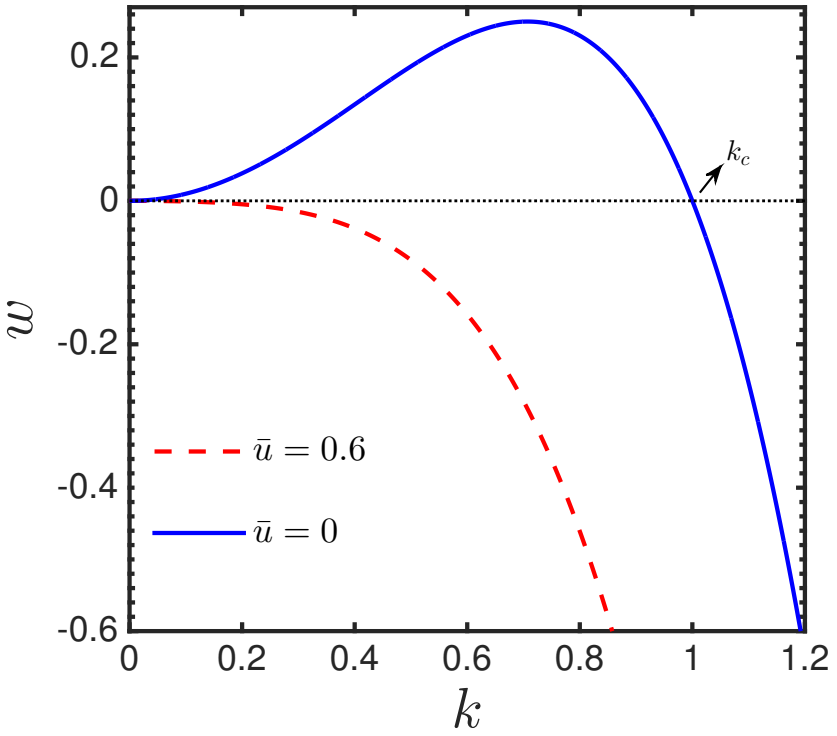

Figure 3.1: The dependence of dimensionless growth rate of perturbations, $w(k)$, on the dimensionless wavenumber k. The solid line corresponds to $\bar{u} = 0$. For this value of $\bar{u}$, there is a band of unstable wavenumbers, $k \in (0,\ k_c)$, where $k_c = 1$. The dashed line corresponds to $\bar{u} = 0.6$. For this value of $\bar{u}$, $w(k) < 0$ for all $k > 0$. The thin horizontal dotted line shows the line $w = 0$ in the (k, w)-plane.

by a thick dotted line. This corresponds to the linearly stable case. The thin dotted line in Fig. 3.1 shows the line $w = 0$ in the (k, w)-plane.

3.3 Linear stability of homogeneous solutions in a co-moving frame

In this section, we analyse linear stability of homogeneous solutions of the convective Cahn-Hilliard equation (2.28) in a frame moving at a constant velocity v in the x-direction, i.e., we introduce a new variable $\tilde{x} = x - vt$, and denote $\hat{u}(\tilde{x}, t) = u(x, t)$. Then equation (2.28) takes the form

$$\hat{u}_t - v\hat{u}_{\tilde{x}} + D\hat{u}\hat{u}_{\tilde{x}} + (\hat{u} - \hat{u}^3 + \hat{u}_{\tilde{x}\tilde{x}})_{\tilde{x}\tilde{x}} = 0. \tag{3.7}$$

For simplicity, we drop the hats and the tildes, i.e., we consider the equation in the form

$$u_t - vu_x + Duu_x + (u - u^3 + u_{xx})_{xx} = 0. \tag{3.8}$$

Next, we linearise equation (3.8) by substituting $u = \bar{u} + \epsilon\tilde{u}$ into this equation, where $\bar{u}$ is a constant and $\epsilon \ll 1$. Keeping terms of size $O(\epsilon)$ and ignore higher-order terms, we obtain the equation

$$\tilde{u}_t = v\tilde{u}_x - D\bar{u}\tilde{u}_x - \tilde{u}_{xx} + 3\bar{u}^2\tilde{u}_{xx} - \tilde{u}_{xxxx}. \tag{3.9}$$

Next, we assume the ansatz $\tilde{u} = \exp(ikx + \beta t)$ and obtain

$$\beta(k) = ivk - D\bar{u}ik + k^2 - 3\bar{u}^2k^2 - k^4. \tag{3.10}$$

We obtain

$$w(k) = \mathrm{Re}\,\beta = k^2 - 3\bar{u}^2k^2 - k^4, \qquad \mathrm{Im}\,\beta = vk - D\bar{u}k, \tag{3.11}$$

where $\mathrm{Re}\,\beta$ and $\mathrm{Im}\,\beta$ denote the real and imaginary part of β, respectively. When the imaginary part of β is zero, the wave does not move in the corresponding frame. The condition $\mathrm{Im}\,\beta = 0$ implies

$$vk - D\bar{u}k = 0 \qquad \Rightarrow \qquad v = D\bar{u}. \tag{3.12}$$

So small-amplitude sinusoidal waves do not move in a frame propagating at velocity $v = D\bar{u}$, or, equivalently, the velocity of small-amplitude sinusoidal waves is $v = D\bar{u}$. The real part of β gives the growth rate of the amplitude of small-amplitude sinusoidal waves, and this was discussed in the previous section.

3.4 Linear stability of homogeneous solutions in space

In this section, we analyse linear stability in space of homogeneous solutions of the convective Cahn-Hilliard equation in a co-moving frame (3.8). One way to do this, is to first linearise equation (3.8) by substituting $u = \bar{u} + \epsilon\tilde{u}$ in this equation. Keeping terms of size $O(\epsilon)$ and ignoring higher-order terms, we obtain the equation

$$\tilde{u}_t - v\tilde{u}_x + D\bar{u}\tilde{u}_x + \tilde{u}_{xx} - 3\bar{u}^2\tilde{u}_{xx} + \tilde{u}_{xxxx} = 0. \tag{3.13}$$

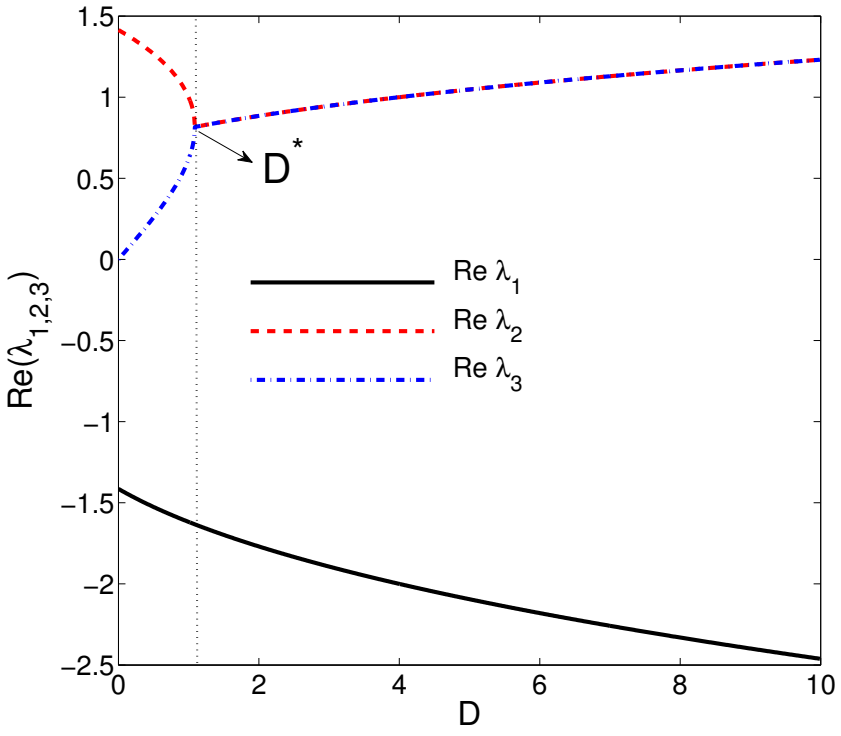

Figure 3.2: Shown is the dependence on D of the real parts of the eigenvalues λ_1, λ_2 and λ_3 obtained from the spatial linear stability analysis for $\bar{u} = 1$ and $v = 0$ by solid, dashed and dotted lines, respectively.

Next, we assume the ansatz $\tilde{u} = \exp(\lambda x)$. Then we obtain

$$\tilde{u}_t = 0, \quad \tilde{u}_x = \lambda e^{\lambda x}, \quad \tilde{u}_{xx} = \lambda^2 e^{\lambda x}, \quad \tilde{u}_{xxxx} = \lambda^4 e^{\lambda x}. \tag{3.14}$$

Substituting expressions (3.14) into (3.13), we find the following characteristic equation for the eigenvalues λ

$$\lambda^4 + (1 - 3\bar{u}^2)\lambda^2 - (v - D\bar{u})\lambda = 0. \tag{3.15}$$

One solution of this equation is $\lambda_0 = 0$, and we have three more solutions, $\lambda_{1,2,3}$, that satisfy the cubic equation

$$\lambda^3 + (1 - 3\bar{u}^2)\lambda - (v - D\bar{u}) = 0. \tag{3.16}$$

Fig. 3.2 shows the dependence on D of the real parts of $\lambda_{1,2,3}$ and Fig. 3.3 shows the dependence on D of the imaginary parts of $\lambda_{1,2,3}$, for the case when $v = 0$ and $\bar{u} = 1$.

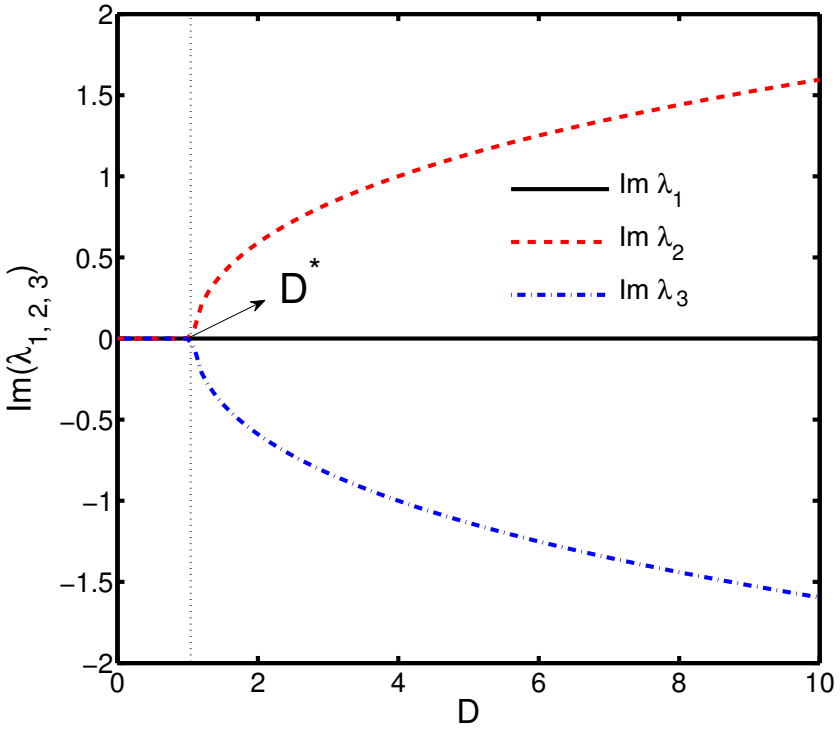

Figure 3.3: Shown is the dependence on D of the imaginary parts of the eigenvalues λ_1, λ_2 and λ_3 obtained from the spatial linear stability analysis for $\bar{u} = \pm 1$ and $v = 0$ by solid, dashed and dotted lines, respectively.

Fig. 3.4 shows the dependence on D of the real parts of $\lambda_{1,2,3}$ for the case when $v = 0$ and $\bar{u} = -1$. Note that the real parts of $\lambda_{1,2,3}$ for $\bar{u} = -1$ are obtained from the real parts of $\lambda_{1,2,3}$ for $\bar{u} = 1$ by reflection with respect to the horizontal axis. The imaginary parts are also obtained by the reflection with respect to the abscissa, but since one root is real and the remaining two are either real or complex conjugate, we obtain that the dependence of the imaginary parts of $\lambda_{1,2,3}$ for $v = 0$ and $\bar{u} = -1$ is the same as for $v = 0$ and $\bar{u} = 1$ and is, therefore, shown in Fig. 3.3.

To prove this symmetry, it can be seen by a direct substitution that if λ is a solution of equation (3.16), then $-\lambda$ is a solution of the same equation with $\bar{u}$ replaced by $-\bar{u}$ (when $v = 0$). In fact, the equation remains unchanged under the transformation

$$\bar{u} \to -\bar{u}, \qquad \lambda \to -\lambda. \tag{3.17}$$

This explains the symmetry of the roots discussed above.

We can see in Fig. 3.2 that for $\bar{u} = 1$ there is always one root that is real and negative. The other two roots have positive real parts. These two roots are real when D is

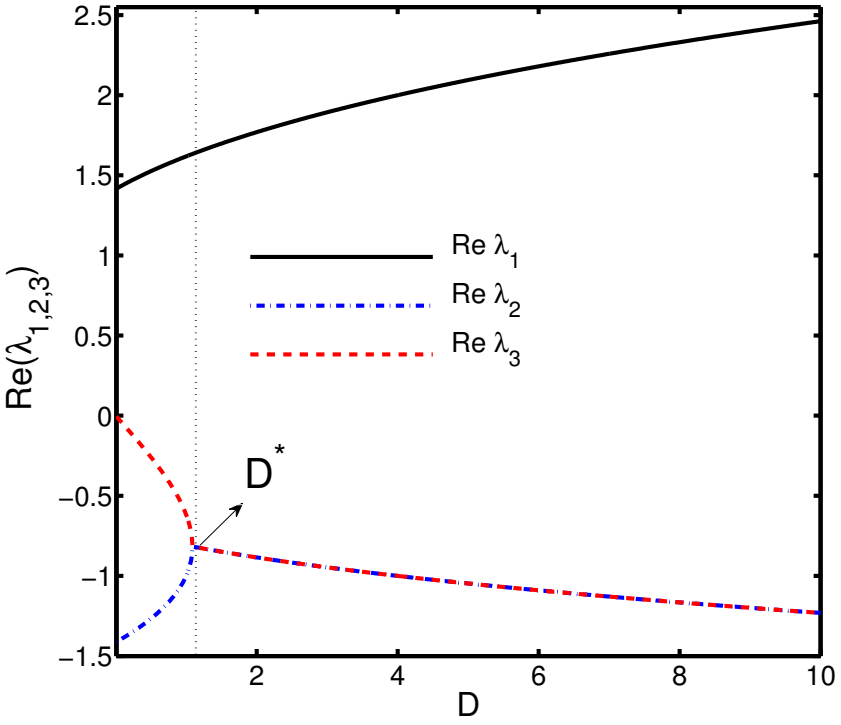

Figure 3.4: Shown is the dependence on D of the real parts of the eigenvalues λ_1, λ_2 and λ_3 obtained from spatial linear stability analysis for $\bar{u} = -1$ and $v = 0$ by solid, dashed and dotted lines, respectively.

smaller than a certain value D^* = 1.0887 and become complex conjugate with non-zero imaginary parts when D is larger than this value.

To calculate the value of D^*, in Fig. 3.2, we note that all three eigenvalues are real for small D, and another form of equation (3.16) is

$$(\lambda - \lambda_1)(\lambda - \lambda_2)(\lambda - \lambda_3) = 0. \tag{3.18}$$

Now at the value of D where two eigenvalues coincide (let us call it D^*) we can set $\lambda_2 = \lambda_3$, i.e.

$$(\lambda - \lambda_1)(\lambda - \lambda_2)^2 = 0. \tag{3.19}$$

Then

$$\lambda^3 - (\lambda_1 + 2\lambda_2)\lambda^2 + (\lambda_2^2 + 2\lambda_1\lambda_2)\lambda - \lambda_1\lambda_2^2 = 0. \tag{3.20}$$

Now we compare (3.20) and (3.16) to obtain

$$\lambda_1 + 2\lambda_2 = 0 \qquad \Rightarrow \qquad \lambda_1 = -2\lambda_2, \tag{3.21}$$

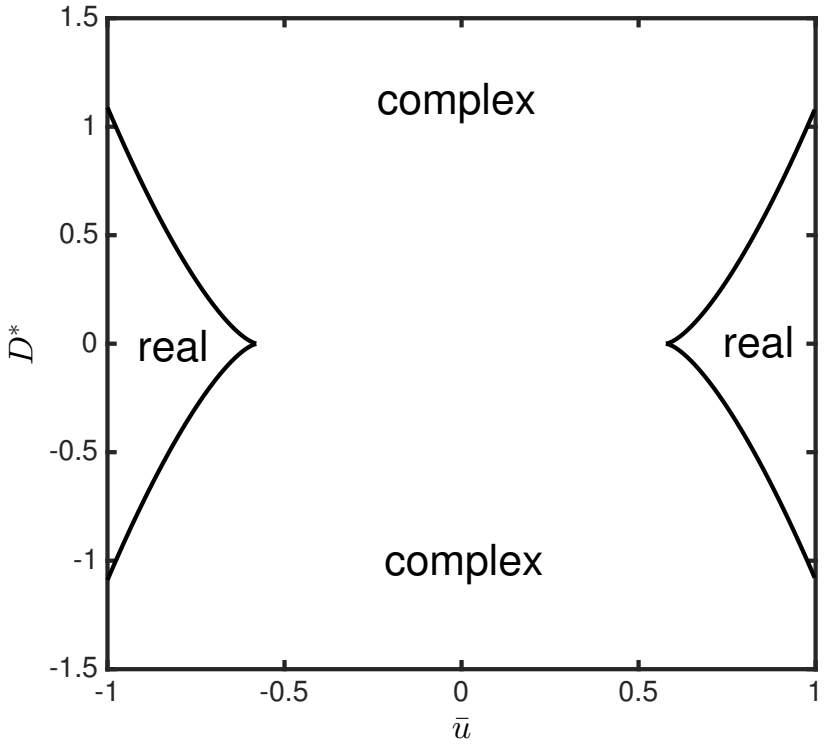

Figure 3.5: Shown is the dependence of D^* on $\bar{u}$ given by equation (3.27) when $-1 < \bar{u} < \frac{-1}{\sqrt{3}}$, $\frac{1}{\sqrt{3}} < \bar{u} < 1$ and $v = 0$.

and

$$\lambda_2^2 + 2\lambda_1\lambda_2 = 1 - 3\bar{u}^2, \tag{3.22}$$

and

$$\lambda_1\lambda_2^2 = v - D^*\bar{u}. \tag{3.23}$$

From equation (3.22), after substituting $\lambda_1 = -2\lambda_2$, we obtain

$$\lambda_2^2 - 4\lambda_2^2 = 1 - 3\bar{u}^2. \tag{3.24}$$

Then

$$\lambda_2 = \pm\sqrt{\frac{3\bar{u}^2 - 1}{3}}. \tag{3.25}$$

From equation (3.23) (after substituting $\lambda_1 = -2\lambda_2$), we get

$$D^* = \frac{2\lambda_2^3 + v}{\bar{u}}. \tag{3.26}$$

Next, we substitute equation (3.25) into equation (3.26), and obtain the following general formula forD^*:

$$D^* = \frac{\pm 2\left(\frac{3\bar{u}^2-1}{3}\right)^{3/2} + v}{\bar{u}}. \tag{3.27}$$

In particular, for $v = 0$ and $\bar{u} = \pm 1$, we obtain $D^* = \pm 2^{5/2}/3^{3/2} \approx 1.0887$.

Fig. 3.5 shows the dependence of D^* on the $\bar{u}$ given by equation (3.27) when $-1 < u_0 < -1/\sqrt{3}$, $1/\sqrt{3} < u_0 < 1$ and $v = 0$. The regions indicated by "real" show the regions where all the roots are real and the region indicated by"complex" shows the region where one root is real and there is a pair of complex conjugate roots.

We note equation (3.16) in addition to the symmetry $(\lambda, D) \to (-\lambda, D)$ has the symmetry $(\bar{u}, D) \to (-\bar{u}, -D)$.

We note that the value D^* can also be obtained by requiring that the so-called discriminant of equation (3.16) vanishes. For a general cubic equation

$$\lambda^3 + a_1\lambda^2 + a_2\lambda + a_3 = 0, \tag{3.28}$$

the discriminant is given by

$$\Delta = Q^3 + R^2, \tag{3.29}$$

where

$$Q = \frac{3a_2 - a_1^2}{9}, \quad R = \frac{9a_1a_2 - 27a_3 - 2a_1^3}{54} \tag{3.30}$$

(see, for example, [98]). For equation (3.16), $a_1 = 0$, $a_2 = 1 - 3\bar{u}^2$ and $a_3 = D\bar{u} - v$. Therefore,

$$Q = \frac{1 - 3\bar{u}^2}{3}, \quad R = \frac{v - D\bar{u}}{2}. \tag{3.31}$$

The discriminant becomes

$$\Delta = \left(\frac{1 - 3\bar{u}^2}{3}\right)^3 + \left(\frac{v - D\bar{u}}{2}\right)^2. \tag{3.32}$$

By solving equation $\Delta = 0$ for the driving force, we obtain the same formula as (3.27).

Finally, we note that the linear stability of homogeneous solutions in space can be performed in a slightly different way. For this, we consider a steady version of equation (3.8):

$$-vu_{0x} + Du_0u_{0x} + (u_0 - u_0^3 + u_{0xx})_{xx} = 0, \tag{3.33}$$

and integrate it once to obtain the equation

$$-vu_0 + \frac{D}{2}u_0^2 + (u_0 - u_0^3 + u_{0xx})_x = C_0, \tag{3.34}$$

where C_0 is a constant of integration. Next, we rewrite equation (3.34) as a three-dimensional dynamical system by introducing the functions $y_1 = u_0$, $y_2 = u_{0x}$ and $y_3 = u_{0xx}$:

$$y_1' = y_2, \tag{3.35}$$
$$y_2' = y_3, \tag{3.36}$$
$$y_3' = C_0 + vy_1 - \frac{D}{2}y_1^2 - y_2 + 3y_1^2 y_2. \tag{3.37}$$

A uniform solution $\bar{u}$ corresponds to the fixed point $(\bar{u}, 0, 0)$ of this system with

$$C_0 = -v\bar{u} + \frac{D}{2}\bar{u}^2. \tag{3.38}$$

The stability of the fixed point is obtained by computing the eigenvalues of the Jacobian:

$$J = \begin{pmatrix} 0 & 1 & 0 \\ 0 & 0 & 1 \\ v - D\bar{u} & 3\bar{u}^2 - 1 & 0 \end{pmatrix}. \tag{3.39}$$

The eigenvalues satisfy the equation

$$\det(\lambda I - J) = \begin{vmatrix} \lambda & -1 & 0 \\ 0 & \lambda & -1 \\ D\bar{u} - v & 1 - 3\bar{u}^2 & \lambda \end{vmatrix} = \lambda^3 + (1 - 3\bar{u}^2)\lambda - (v - D\bar{u}) = 0, \tag{3.40}$$

which is exactly the same as equation (3.16).

3.5 Single- and double-interface solutions

In this section, we discuss single- and double-interface solutions of the standard and convective Cahn-Hilliard equations. A single-interface solution is a solution that approaches two different constants as $x \to \pm\infty$. Let us denote these constants by $\bar{u}_a$ and $\bar{u}_b$ for $x \to \mp\infty$, respectively. If $\bar{u}_a < \bar{u}_b$ we obtain a so-called kink solution. If

$\bar{u}_a > \bar{u}_b$, we obtain an anti-kink (or front) solution. A double-interface solution, is a solution that approaches the same constant (say $\bar{u}_b$) as $x \to \pm\infty$, but has a region where it approaches a different constant (say $\bar{u}_a$). If $\bar{u}_a < \bar{u}_b$, we obtain a cavity solution, otherwise, we obtain a solution in the form of a droplet. We note that our discussion of single- and double-interface solutions partly follows the discussions of Emmott and Bray [36], Golovin et al. [47], Korzec et al. [68], Zaks et al. [123].

3.5.1 The case of the standard Cahn-Hilliard equation

For the standard Cahn-Hilliard equation, when $D = 0$, the dynamical system (3.35)–(3.37) takes the form

$$y_1' = y_2, \tag{3.41}$$
$$y_2' = y_3, \tag{3.42}$$
$$y_3' = C_0 + vy_1 - y_2 + 3y_1^2 y_2. \tag{3.43}$$

If $v \neq 0$, we find that there exists only one fixed point for this system, $(-C_0/v, 0, 0)$. Therefore, for the existence of single- and double-interface solutions, we must have $v = 0$, which also implies that $C_0 = 0$. Then, equation (3.34) can be integrated one more time, giving

$$u_0 - u_0^3 + u_{0xx} = C_1, \tag{3.44}$$

where C_1 is a constant. Thus, we obtain the following two-dimensional dynamical system:

$$y_1' = y_2, \tag{3.45}$$
$$y_2' = C_1 - y_1 + y_1^3. \tag{3.46}$$

It can be easily seen that this system is Hamiltonian with the Hamiltonian given by

$$\mathcal{H}(y_1, y_2) = C_1 y_1 - \frac{y_1^2}{2} + \frac{y_1^4}{4} - \frac{y_2^2}{2}. \tag{3.47}$$

Assuming that there exists a single-interface solution that connects uniform solutions $\bar{u}_a$ and $\bar{u}_b$, we obtain that the dynamical system (3.45), (3.46) has the fixed points

$$(\bar{u}_a, 0), \qquad (\bar{u}_b, 0), \tag{3.48}$$

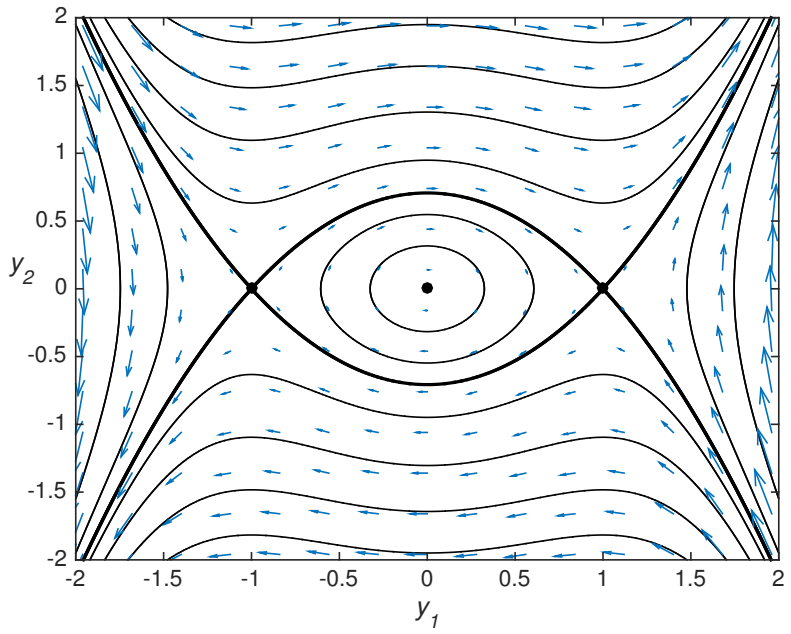

Figure 3.6: Phase portrait for the dynamical system (3.45), (3.46) when $C_1 = 0$. The solid dots indicate the fixed points.

for which

$$\bar{u}_a - \bar{u}_a^3 = \bar{u}_b - \bar{u}_b^3 = C_1, \tag{3.49}$$

and also

$$\mathcal{H}(\bar{u}_a, 0) = \mathcal{H}(\bar{u}_b, 0), \tag{3.50}$$

i.e.,

$$C_1\bar{u}_a - \frac{\bar{u}_a^2}{2} + \frac{\bar{u}_a^4}{4} = C_1\bar{u}_b - \frac{\bar{u}_b^2}{2} + \frac{\bar{u}_b^4}{4}, \tag{3.51}$$

which can be written as

$$\frac{\bar{u}_a^2/2 - \bar{u}_a^4/4 - \bar{u}_b^2/2 + \bar{u}_b^4/4}{u_a - u_b} = C_1. \tag{3.52}$$

Note that equations (3.49) and (3.52) can be written as

$$f'(\bar{u}_a) = f'(\bar{u}_b) = -C_1, \tag{3.53}$$

and

$$\frac{f(\bar{u}_a) - f(\bar{u}_b)}{\bar{u}_a - \bar{u}_b} = -C_1, \tag{3.54}$$

respectively, where $f(u)$ is the local free energy that for the standard Cahn-Hilliard equation is given by

$$f(u) = -\frac{u^2}{2} + \frac{u^4}{4}. \tag{3.55}$$

Note also that equations (3.53) and (3.54) are exactly the equations determining points on the binodal line. It can be easily verified that for the standard Cahn-Hilliard equation the only solution of these equations for which $\bar{u}_a \neq \bar{u}_b$ are

$$\bar{u}_a = \pm 1, \qquad \bar{u}_b = \mp 1, \tag{3.56}$$

and then $C_1 = 0$. Let us choose $\bar{u}_a = 1$ and $\bar{u}_b = -1$. Hence, when $C_1 = 0$, we expect that there exist heteroclinic orbits for the dynamical system (3.45), (3.46) that connect the fixed points $(1, 0)$ and $(-1, 0)$, and, indeed, these orbits are given by the equations:

$$y_2 = \pm\sqrt{\frac{1}{2} + \frac{y_1^4}{2} - y_1^2}. \tag{3.57}$$

The positive sign corresponds to the orbit connecting $(-1, 0)$ with $(1, 0)$, which, in turn, corresponds to a kink solution of the Cahn-Hilliard equation. The negative sign corresponds to the orbit connecting $(1, 0)$ with $(-1, 0)$, which, in turn, corresponds to an anti-kink solution. These two heteroclinic orbits form a heteroclinic loop for the fixed points $(-1, 0)$ and $(1, 0)$. This is confirmed by the phase portrait for the dynamical system (3.45), (3.46) shown in Fig. 3.6 for the case when $C_1 = 0$. In fact, equations (3.57) become ordinary differential equations for $u_0(x)$ (when y_1 and y_2 are replaced with u_0 and u_{0x}, respectively), and it can be easily verified that the solutions are

$$u_0(x) = \pm \tanh\left(\frac{x}{\sqrt{2}}\right), \tag{3.58}$$

which for the case of the positive sign is consistent with (2.32).

We also note that there are infinitely many closed trajectories that pass near the two fixed points. These trajectories correspond to periodically extended droplet solutions. The closer the trajectory passes near the fixed points, the longer the period of the droplet is.

If $C_1 \neq 0$, this heteroclinic loop breaks down, and if $|C_1| < 2/\sqrt{27}$, we instead obtain a homoclinic orbit for one of the two fixed points, which correspond to localised pulse or anti-pulse (hollow) solutions (if $|C_1| > 2/\sqrt{27}$, the dynamical system has just one fixed

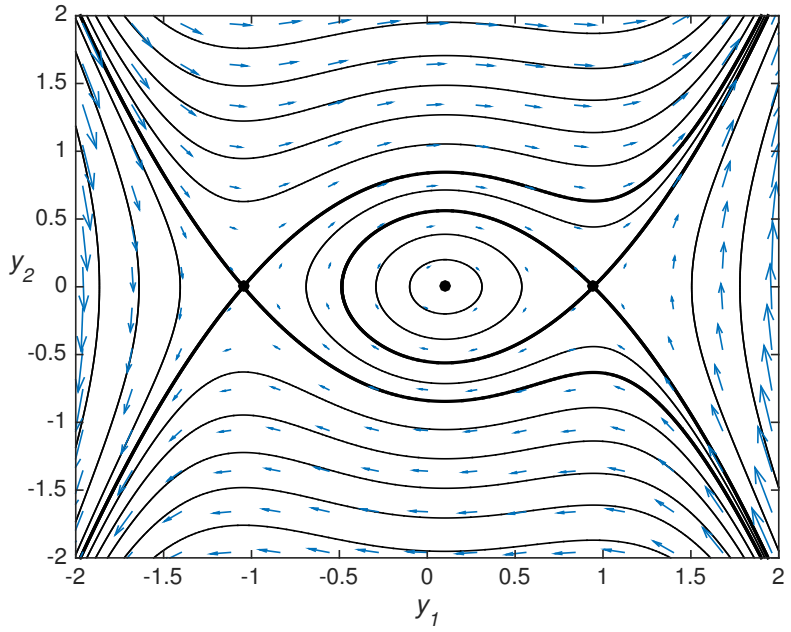

Figure 3.7: Phase portrait for the dynamical system (3.45), (3.46) when $C_1 = 0.1$. The solid dots indicate the fixed points.

point for which there are no homoclinic orbits). An example of the phase portrait for the dynamical system (3.45), (3.46) when $C_1 \neq 0$ is shown in Fig. 3.7 for the case when $C_1 = 0.1$. As for $C_1 = 0$, there are infinitely many closed trajectories that pass near the fixed point. These trajectories correspond to periodically extended pulse or anti-pulse (hollow) solutions. The closer the trajectory passes near the fixed points, the longer the period of the pulse or anti-pulse is. We also note that if C_1 is sufficiently close to zero, then the closed trajectory also spends a sufficient amount of "time" near the second fixed point, i.e., the periodically extended pulse or anti-pulse solutions have the shape of a droplet whose width is smaller or larger, respectively, than the width of the cavity. The numerical results for droplet and single-interface solutions for the standard Cahn-Hilliard equation are discussed in Section 4.3.

3.5.2 The case of the convective Cahn-Hilliard equation

For the convective Cahn-Hilliard equation, when $D \neq 0$, we consider the three-dimensional dynamical system (3.35)–(3.37). The fixed points of this dynamical system satisfy $y_2 = y_3 = 0$ and

$$\frac{D}{2} y_1^2 - v y_1 - C_0 = 0. \tag{3.59}$$

Assuming that there exists a single-interface solution that connects uniform solutions $\bar{u}_a$ and $\bar{u}_b$ (let $\bar{u}_a > \bar{u}_b$), we obtain that

$$v = \frac{D}{2}(\bar{u}_a + \bar{u}_b), \qquad C_0 = -\frac{D}{2}\bar{u}_a\bar{u}_b. \tag{3.60}$$

A single-interface solution then corresponds to a heteroclinic orbit connecting the fixed point $(\bar{u}_b, 0, 0)$ to the fixed point $(\bar{u}_a, 0, 0)$ (a kink solutions) or vice versa (an anti-kink solution). Heteroclinic orbits are trajectories that connect the two fixed points along the unstable manifold of the first one and the stable manifold of the second one. We will denote the stable and unstable manifolds of $(\bar{u}_{a,b}, 0, 0)$ by $W_{s,u}(\bar{u}_{a,b})$, where the subscripts s and u correspond to stable and unstable manifolds, respectively.

Using the spatial linear stability analysis presented in Section 3.4, we find that the eigenvalues for the fixed point $(\bar{u}_a, 0, 0)$ satisfy

$$\lambda^3 + (1 - 3\bar{u}_a^2)\lambda + \frac{D}{2}(\bar{u}_a - \bar{u}_b) = 0, \tag{3.61}$$

and the eigenvalues for the fixed point $(\bar{u}_b, 0, 0)$ satisfy

$$\lambda^3 + (1 - 3\bar{u}_b^2)\lambda - \frac{D}{2}(\bar{u}_a - \bar{u}_b) = 0. \tag{3.62}$$

Since the coefficients of λ^2 are zero in these equations, we obtain that either one of the roots is positive and real and the other two have negative real parts (and are either real or complex conjugate), or one of the roots is negative and real and the other two have positive real parts (and are either real or complex conjugate). So, in theory, the following cases are possible:

1. $\dim(W_u(\bar{u}_a)) = 2, \dim(W_s(\bar{u}_a)) = 1, \dim(W_u(\bar{u}_b)) = 1, \dim(W_s(\bar{u}_b)) = 2,$
2. $\dim(W_u(\bar{u}_a)) = 2, \dim(W_s(\bar{u}_a)) = 1, \dim(W_u(\bar{u}_b)) = 2, \dim(W_s(\bar{u}_b)) = 1,$
3. $\dim(W_u(\bar{u}_a)) = 1, \dim(W_s(\bar{u}_a)) = 2, \dim(W_u(\bar{u}_b)) = 1, \dim(W_s(\bar{u}_b)) = 2,$
4. $\dim(W_u(\bar{u}_a)) = 1, \dim(W_s(\bar{u}_a)) = 2, \dim(W_u(\bar{u}_b)) = 2, \dim(W_s(\bar{u}_b)) = 1,$

where $W_{s,u}$ are used to indicate stable/unstable manifolds of the respective points.

Let us assume that a heteroclinic orbit connects $(\bar{u}_b, 0, 0)$ to $(\bar{u}_a, 0, 0)$ (i.e., we have a kink solution). Then, in Case 4 we expect that there will exist heteroclinic orbits for any sufficiently small changes of $\bar{u}_a$ and $\bar{u}_b$ (two-dimensional surfaces generically intersect

along a one-dimensional curve). In Cases 2 and 3, we expect that there will be a curve in the $(\bar{u}_a, \bar{u}_b)$-plane for which such a heteroclinic orbit exists. In Case 1, we expect that such an orbit exists only for a discrete set of values in the $(\bar{u}_a, \bar{u}_b)$-plane.

Similarly, assuming that a hetoroclinic orbit connects $(\bar{u}_a, 0, 0)$ to $(\bar{u}_b, 0, 0)$ (i.e., we have an anti-kink solution), we obtain the following options: In Case 1, we expect that there will exist heteroclinic orbits for any sufficiently small changes of $\bar{u}_a$ and $\bar{u}_b$. In Cases 2 and 3, we expect that there will be a curve in the $(\bar{u}_a, \bar{u}_b)$-plane for which such a heteroclinic orbit exists. In Case 4, we expect that such an orbit exists only for a discrete set of values in the $(\bar{u}_a, \bar{u}_b)$-plane.

In fact, from Section 2.4, we know an exact kink solution of the convective Cahn-Hilliard equation that is given by

$$u_0(x) = \bar{u}_a \tanh\left(\frac{\bar{u}_a}{\sqrt{2}}x\right), \tag{3.63}$$

where $\bar{u}_a = \sqrt{1 - D/\sqrt{2}}$, and for which $v = 0$. For this solution, $\bar{u}_b = -\sqrt{1 - D/\sqrt{2}}$.

Figs. 3.8 and 3.9 show the dependence on D of the real and imaginary parts, respectively, of the eigenvalues for $\bar{u}_a$. It can be seen that one eigenvalue, λ_1, is real and negative for all $D \in (0, \sqrt{2})$. The other two eigenvalues, λ_2 and λ_3, have positive real parts and are real for $D \in (0, \hat{D})$ and are complex conjugate for $D \in (\hat{D}, \sqrt{2})$, where $\hat{D} \approx 0.47$. Note that as $D \to \sqrt{2}$, $\bar{u}_a \to 0$, and $\lambda_1 \to 0$, $\lambda_{2,3} \to \pm i$. The exact value of $\hat{D}$ satisfies the equation $\Delta = 0$, where Δ is the discriminant given by equation (3.32). For $\bar{u} = \bar{u}_a = \sqrt{1 - D/\sqrt{2}}$, the equation for $\hat{D}$ becomes

$$\hat{D}^3 - 3\sqrt{2}\hat{D}^2 + \frac{16}{3}\hat{D} - \frac{32\sqrt{2}}{27} = 0. \tag{3.64}$$

It can be checked that the roots of this polynomial are $\sqrt{2}/3$ (of multiplicity 1) and $4\sqrt{2}/3$ (of multiplicity 2). Since $\hat{D}$ must be less than $\sqrt{2}$, we conclude that

$$\hat{D} = \frac{\sqrt{2}}{3}. \tag{3.65}$$

The eigenvalues for $\bar{u}_b$ are $-\lambda_{1,2,3}$ (due to the symmetry of the characteristic equation that was discussed above). Therefore, for $\bar{u}_b$, one eigenvalue is real and positive and the other two eigenvalues have negative real parts and are real for $D \in (0, \hat{D})$ and are complex conjugate for $D \in (\hat{D}, \sqrt{2})$. We conclude that $\dim(W_u(\bar{u}_a)) = 2$,

$\dim(W_s(\bar{u}_a)) = 1$, $\dim(W_u(\bar{u}_b)) = 1$, $\dim(W_s(\bar{u}_b)) = 2$, which corresponds to Case 1 discussed above. Therefore, there exists a unique kink solution for each value of D in the interval $(0, \sqrt{2})$ and for the point $(\bar{u}_a, \bar{u}_b)$ in some neighbourhood of the point $\left([1 - D/\sqrt{2}]^{1/2}, -[1 - D/\sqrt{2}]^{1/2}\right)$. This solution is given by equation (3.63). However, we expect that there exist anti-kink solutions for any sufficiently small changes of $\bar{u}_a$ and $\bar{u}_b$. We also note that although kink solutions (3.63) exist for $D \in [0, \sqrt{2})$ (we consider only the case when D is non-negative, as the case of a negative D can be recovered from the case of a positive D by symmetry considerations), the flat parts of such solutions become linearly unstable (in the sense of temporal linear stability analysis) when $D > \check{D} = 2\sqrt{2}/3$. We therefore do not expect to observe such kink solutions in time-dependent simulations when $D > \check{D}$.

We note that the real parts of the eigenvalues determine the rates at which the fixed points are approached, whereas the imaginary parts are responsible for the oscillatory behaviour. Let us consider, for example, Case 1, and assume that there exists an anti-kink solution, i.e., a heteroclinic orbit connecting $(\bar{u}_a, 0, 0)$ to $(\bar{u}_b, 0, 0)$. Let us additionally assume that the eigenvalues for $(\bar{u}_a, 0, 0)$ are $\lambda_1^a < 0$, and $\lambda_{2,3}^a = \gamma^a \pm i\delta^a$, where γ^a and δ^a are positive. Let us also assume that the eigenvalues for $(\bar{u}_b, 0, 0)$ are $\lambda_1^b > 0$, and $\lambda_{2,3}^b = -\gamma^b \pm i\delta^b$, where γ^b and δ^b are positive. Then, the anti-kink solution u_0 will approach $\bar{u}_a$ and $\bar{u}_b$ as $x \to -\infty$ and $x \to \infty$, respectively, in an oscillatory manner with the amplitude of the oscillations decaying as $\exp(\gamma^a x)$ and $\exp(-\gamma^b x)$, respectively, and the periods of the oscillations given by $2\pi/\delta^a$ and $2\pi/\delta^b$, respectively.

The double-interface (and, in fact, many-interface) solutions can be analysed, for example, by using the Shilnikov-type approach, see, for example, Glendinning and Sparrow [43], Guckenheimer and Holmes [50], Knobloch and Wagenknecht [66], Kuznetsov [71], Tseluiko et al. [114]. Indeed, let us consider Case 1, and let us assume that for $\bar{u}_a = \bar{u}_a^*$ and $\bar{u}_b = \bar{u}_b^*$ there exists a heteroclinic chain connecting $\boldsymbol{u}_a = (\bar{u}_a^*, 0, 0)$ to $\boldsymbol{u}_b = (\bar{u}_b^*, 0, 0)$ and $\boldsymbol{u}_b = (\bar{u}_b^*, 0, 0)$ to $\boldsymbol{u}_a = (\bar{u}_a^*, 0, 0)$. A schematic representation of such a chain is given in Figure 3.10. Then, for example, for the fixed value $\bar{u}_a^*$, we expect that there will exist an infinite but countable number of the values of $\bar{u}_b = \bar{u}_{b,k}$, $k \in \mathbb{N}$, in the neighbourhood of $\bar{u}_b^*$ for which there exist homoclinic orbits for the fixed points $(\bar{u}_{b,k}, 0, 0)$ that pass near $(\bar{u}_a^*, 0, 0)$. Such orbits then correspond to droplet solutions, and such droplet solutions differ by their lengths (the difference in the lengths of two droplet solutions is approximately proportional to $2\pi/\delta^a$). We note that if the droplet solution is sufficiently narrow, then it can be characterised rather as a pulse solution

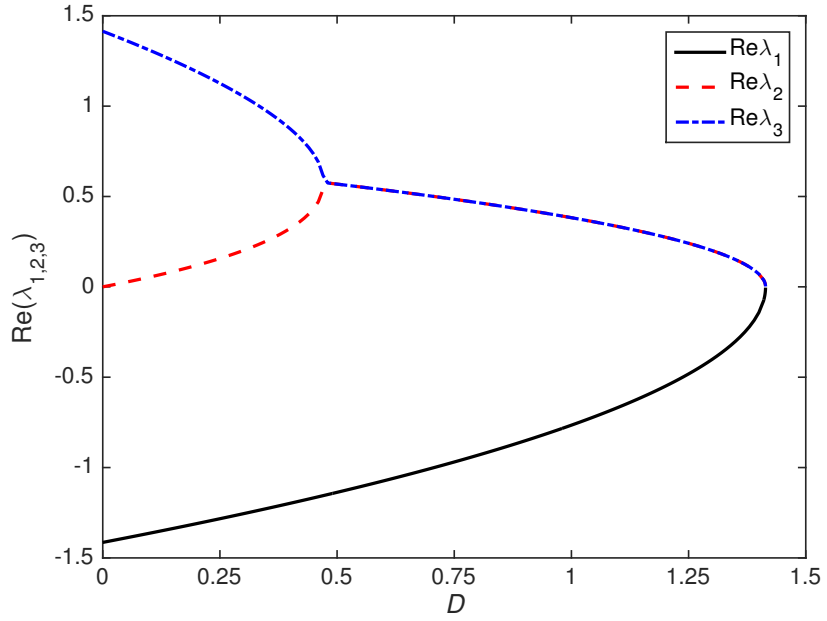

Figure 3.8: Shown is the dependence on D of the real parts of the eigenvalues λ_1, λ_2 and λ_3 obtained from the spatial linear stability analysis for $\bar{u} = \sqrt{1 - D/\sqrt{2}}$ and $v = 0$ by solid, dashed and dotted lines, respectively.

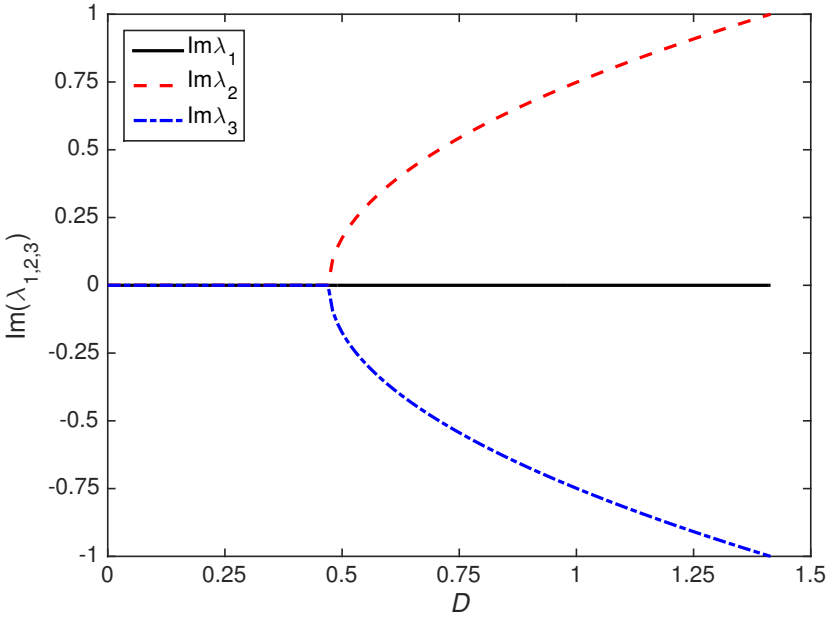

Figure 3.9: Shown is the dependence on D of the imaginary parts of the eigenvalues λ_1, λ_2 and λ_3 obtained from the spatial linear stability analysis for $\bar{u} = \pm\sqrt{1 - D/\sqrt{2}}$ and $v = 0$ by solid, dashed and dotted lines, respectively.

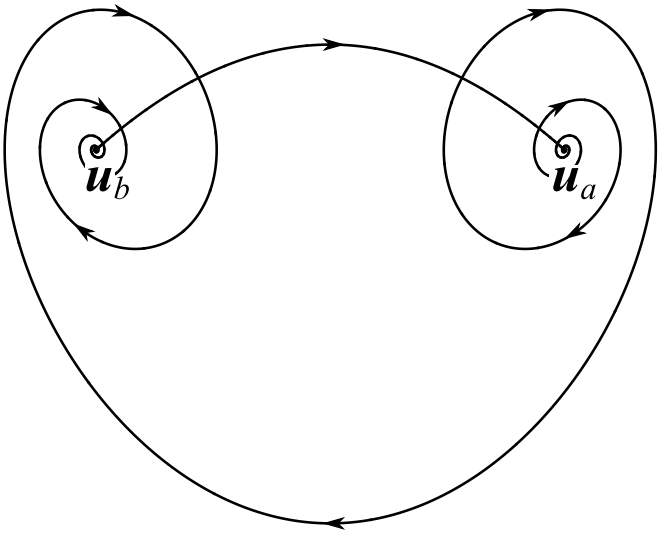

Figure 3.10: A schematic representation of a heteroclinic chain connecting $\boldsymbol{u}_a = (\bar{u}_a^*, 0, 0)$ to $\boldsymbol{u}_b = (\bar{u}_b^*, 0, 0)$ and $\boldsymbol{u}_b = (\bar{u}_b^*, 0, 0)$ to $\boldsymbol{u}_a = (\bar{u}_a^*, 0, 0)$ for Case 1, when $\dim(W_u(\bar{u}_a)) = 2$, $\dim(W_s(\bar{u}_a)) = 1$, $\dim(W_u(\bar{u}_b)) = 1$, $\dim(W_s(\bar{u}_b)) = 2$.

than a droplet. Then, assuming that $\gamma^b < \lambda_1^b$, Shilnikov's theory implies the existence of an infinite but countable number of subsidiary homoclinic orbits in the vicinity of the primary orbit (i.e., when $\bar{u}_b$ is near $\bar{u}_{b,k}$) that pass near $(\bar{u}_a^*, 0, 0)$ several times before achieving homoclinicity. Such subsidiary homoclinic orbits correspond to multi-droplet (or multi-pulse) solutions. In addition, Shilnikov's theory implies the existence of an infinite number of limit cycles in the vicinity of the primary homoclinic orbits. Such limit cycles correspond to periodic arrays of droplets (or pulses). In a similar way, we can analyse cavity solutions (and negative-pulse solutions which correspond to narrow cavities), and can obtain finite or periodic arrays of cavity (or negative-pulse) solutions (we note that, of course, periodic arrays of cavity solutions are equivalent to periodic arrays of droplet solutions).

The numerical computation of droplet and single-interface solutions for the convective Cahn-Hilliard equation is discussed in Chapter 4. However, here we present some time-dependent simulations (obtained by using the spectral method described in Section 2.5) confirming differences in the solutions that we expect to see for $D \in (0, \hat{D})$, $D \in (\hat{D}, \check{D})$, $D \in (\check{D}, \sqrt{2})$, $D > \sqrt{2}$. Figs. 3.11, 3.12, 3.13 and 3.14 show the results of numerical simulations of the convective Cahn-Hilliard equation (2.28) on the periodic domain $[-40, 40]$ for $D = \sqrt{2}/6$, $\sqrt{2}/2$, $5\sqrt{2}/6$ and 1.5, respectively. The equation was solved by the spectral method explained in Section 2.5. We have used 512 Fourier

modes and the time step was chosen to be 7.8125×10^{-4}. The initial condition for the simulations was chosen to be

$$u(x,0) = -\sqrt{1 - D/\sqrt{2}}\tanh[10\sin(\pi x/L)] \tag{3.66}$$

for $D = \sqrt{2}/6, \sqrt{2}/2, 5\sqrt{2}/6$ and

$$u(x,0) = -0.1\tanh[10\sin(\pi x/L)] \tag{3.67}$$

for $D = 1.5$.

Panels (a) of the figures show the time evolution of the solution for t changing from 0 to 1000. Panels (b) show the initial (dashed line) and the final (solid line) solutions profiles. Panels (c) show the time evolutions of the norms of the solutions.

As expected, for $D = \sqrt{2}/6$ the solution evolves into a droplet solution and there appears a ridge on top of the right-hand side of the droplet followed by a depression in the cavity, and it can be seen that both change monotonically. The norm of the solution increases monotonically in time and approaches a constant value meaning that the solution evolves into a steady-state droplet solution.

For $D = \sqrt{2}/2$ the solution also evolves into a droplet solution with a ridge on top of the right-hand side of the droplet followed by a depression in the cavity. However, in agreement with the theory, now the ridge and the depression are non-monotonic, but actually decay exponentially as x decreases/increases, respectively. For the case of the ridge, this is confirmed by in the inset of Fig. 3.12 showing the dependence of $\log|u(x,1000) - (1 - D/\sqrt{2})^{1/2}|$ on x for negative values of x. The norm of the solution first monotonically increases, but then decreases monotonically and approaches a constant value meaning that the solution again evolves into a steady-state droplet solution.

For $D = 5\sqrt{2}/6$ the theory predicts that the droplet solutions should be unstable if the domain size is large enough. Indeed, in Fig. 3.12 we can observe that the solution first tends to evolve into a droplet solution, but then this solution becomes unstable and beaks up into smaller, pulse-like structures. The norm, after an initial transient period approaches a constant value at around $t = 200$ corresponding to a droplet solution. However, later there appear oscillations of an amplitude that grows in time, and for $t > 600$ the solution completely diverges away from the droplet shape and the norm, after

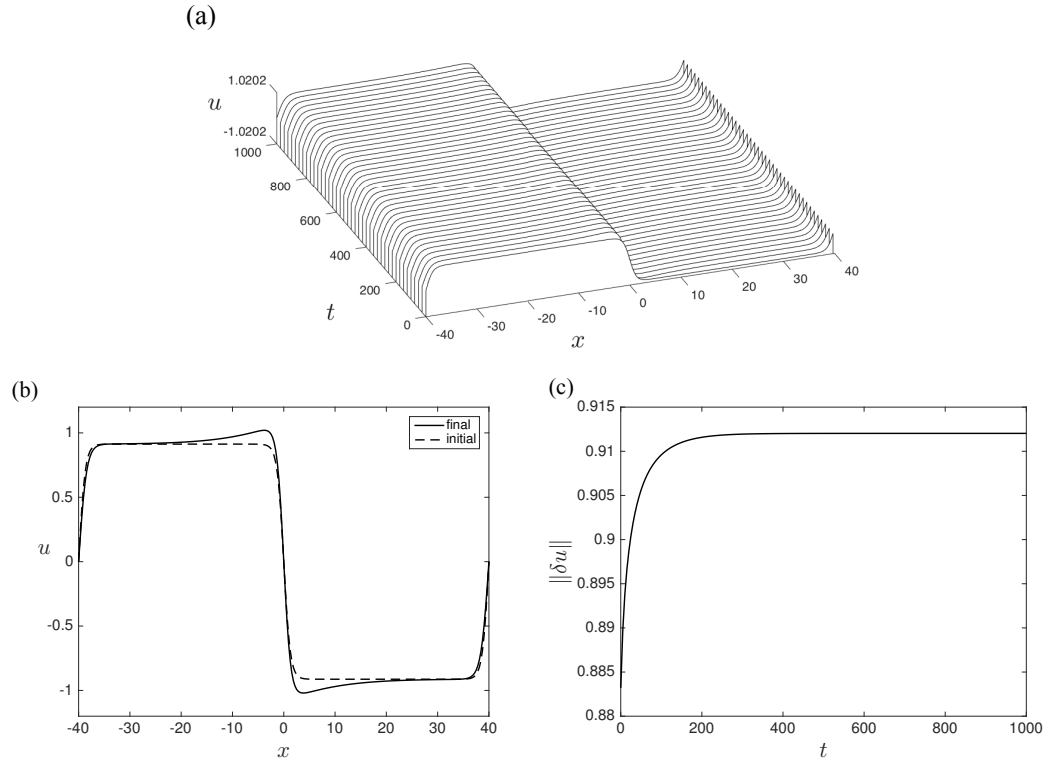

Figure 3.11: Numerical solution of the convective Cahn-Hilliard equation (2.28) on the periodic domain $[-40, 40]$ for $D = \sqrt{2}/6$. Panel (a) shows the time evolution of the solution for $t \in [0, 1000]$. Panel (b) shows the initial (dashed line) and the final (solid line) solution profiles at $t = 0$ and $t = 1000$, respectively. Panel (c) shows the time evolution of the norm of the solution.

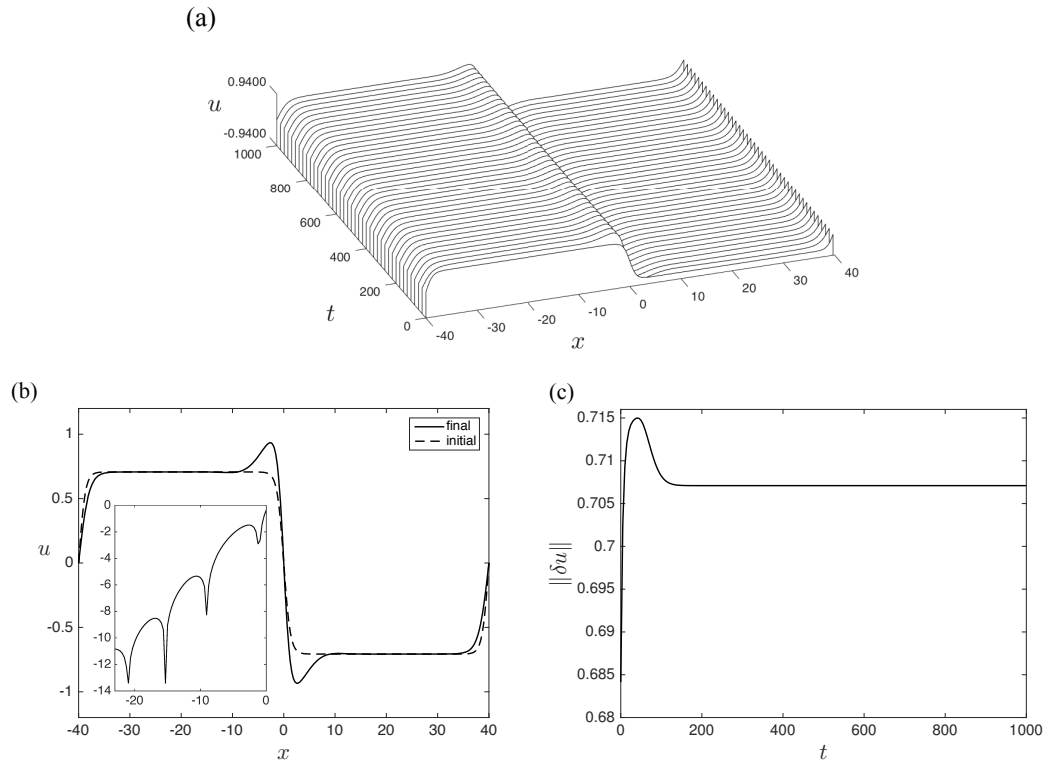

Figure 3.12: Numerical solution of the convective Cahn-Hilliard equation (2.28) on the periodic domain $[-40, 40]$ for $D = \sqrt{2}/2$. Panel (a) shows the time evolution of the solution for $t \in [0, 1000]$. Panel (b) shows the initial (dashed line) and the final (solid line) solution profiles at $t = 0$ and $t = 1000$, respectively. The inset shows the $\log|u(x, 1000) - (1 - D/\sqrt{2})^{1/2}|$ for negative values of x, and confirms the presence of oscillations. Panel (c) shows the time evolution of the norm of the solution.

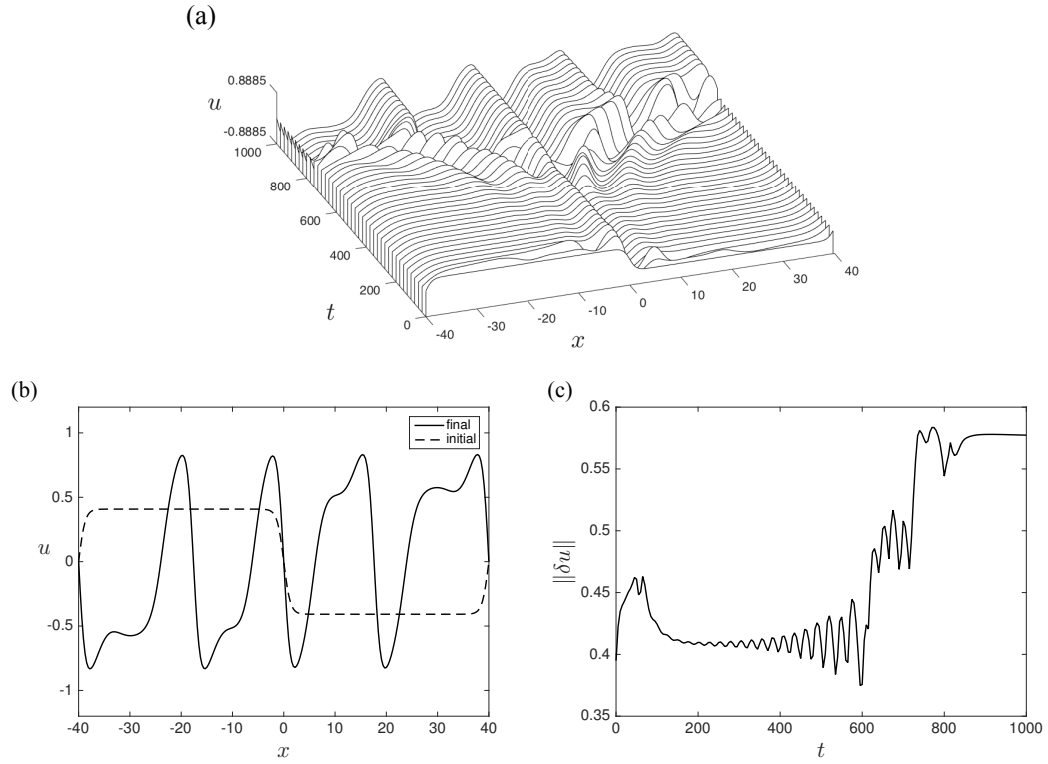

Figure 3.13: Numerical solution of the convective Cahn-Hilliard equation (2.28) on the periodic domain $[-40, 40]$ for $D = 5\sqrt{2}/6$. Panel (a) shows the time evolution of the solution for $t \in [0, 1000]$. Panel (b) shows the initial (dashed line) and the final (solid line) solution profiles at $t = 0$ and $t = 1000$, respectively. Panel (c) shows the time evolution of the norm of the solution.

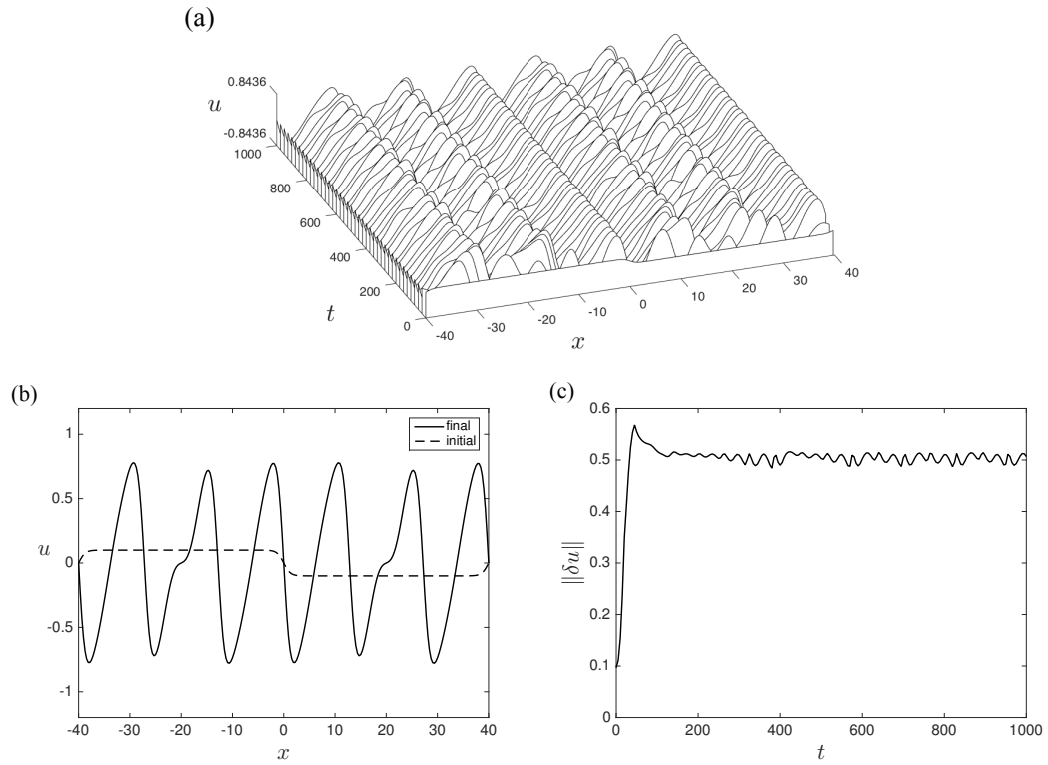

Figure 3.14: Numerical solution of the convective Cahn-Hilliard equation (2.28) on the periodic domain $[-40, 40]$ for $D = 1.5$. Panel (a) shows the time evolution of the solution for $t \in [0, 1000]$. Panel (b) shows the initial (dashed line) and the final (solid line) solution profiles at $t = 0$ and $t = 1000$, respectively. Panel (c) shows the time evolution of the norm of the solution.

a number of oscillations approaches a different constant corresponding to the solution consisting of the superposition of the smaller structures.

Finally, for $D = 1.5$, we observe that the solution does not evolve into a droplet shape (even intermediately) but directly evolves into a superposition of smaller pulse-like structures. The norm first grows rapidly until approaching a saturation value, and then oscillates around this value in a manner indicating that the solution probably approaches a quasi-periodic or chaotic attractor.

To conclude this section, we note that without the derivatives of second and higher orders, the convective Cahn-Hilliard equation reduces to the following scalar conservation law:

$$\partial_t u + \partial_x[\chi(u)] = 0, \tag{3.68}$$

where the flux is $\chi(u) = D\,u^2/2$ and is a uniformly convex function of u for positive D (since $\chi''(u) = D > 0$). Note that this is precisely the inviscid Burgers equation, see, for example, Evans [38]. It is well known that the inviscid Burgers' equation can develop discontinuities for certain initial conditions, i.e., it admits shock-wave solutions. For classical (compressive) shocks, the entropy condition must be satisfied (see, e.g., Evans [38], Lax [72]):

$$\chi'(u_l) > \sigma > \chi'(u_r), \tag{3.69}$$

where σ is the speed of the shock wave and u_l and u_r are the solution values just before the shock and right after the shock. This condition tells that the speed of the characteristics behind the shock must be greater than the speed of the shock and the speed of the characteristics in front of the shock must be smaller that the speed of the shock. This basically implies that the characteristics from the left and the characteristics from the right must hit the curve in the (t, x)-plane along which the solution is discontinuous. On the contrary, if the speed of the characteristics for smaller values of x is less than the speed of the characteristics for larger values of x, we can obtain rarefaction waves.

For classical compressive shocks, the additional Rankine-Hugoniot condition gives the speed σ of the shock:

$$\sigma = \frac{\chi(u_l) - \chi(u_r)}{u_l - u_r}. \tag{3.70}$$

Note that for a uniformly convex flux the entropy condition is equivalent to the inequality

$$u_l > u_r. \tag{3.71}$$

If an initial condition is discontinuous and such that $u_l < u_r$, then we obtain rarefaction waves.

Adding certain terms to the inviscid Burgers' equation can be considered as a regularisation of the equation. In particular, by adding the term $\epsilon^2 u_{xx}$ to the right-hand side of (3.68), we obtain the viscous Burgers' equation which was proposed by Burgers as a model for analysing turbulent flows, see Burgers [15]. It arises in numerous other applications, such as gas dynamics, water waves, traffic flow (see, e.g., Johnson [60] Whitham [120]). For a wide class of initial conditions, solutions to the viscous Burgers' equation are single-valued and continuous (i.e., do not develop shocks), contrary to the behaviour of the solutions to the inviscid Burgers' equation. Remarkably, the nonlinear viscous Burger's equation can be transformed into the linear heat equation by the so-called Cole-Hopf transformation, see Cole [22] and Hopf [56], and, therefore, solutions to the viscous Burger's equation can be written in terms of the solutions to the heat equation. Introduction of the viscous term smoothes out sharp shock solution. Nevertheless, for sufficiently small ϵ, the solutions can have rapid transitions and are well approximated by shock solutions of the inviscid Burgers' equation (if the shock strength, $(u_l - u_r)/u_r$ does not tend to zero). A closed-form travelling anti-kink solution of the viscous Burgers' equation is known as the Taylor shock profile, see, e.g., [60], and it propagates with the shock velocity and has the width that tends to zero as $\epsilon \to 0$.

The convective Cahn-Hilliard equation can also be considered as a regularisation of the inviscid Burgers' equation. (We note that for a systematic investigation of such a regularisation, it would be appropriate to introduce parameters multiplying the additional terms and consider the limit when these parameters become small so that the balance between energy production and energy dissipation is maintained.) Then kink and anti-kink solutions can be classified as "smoothed shocks". Note that the first equation in (3.60) giving the speed of a kink or anti-kink solutions is in agreement with the Rankine-Hugoniot condition (3.70) giving the speed of the shock wave. Note also that for the discussed anti-kink solutions, the speed of the characteristics behind the "smoothed shock" is larger than the speed of the characteristics in front of the "smoothed shock". So anti-kink solutions presumably correspond to classical compressive shock solutions. This is, however, not the case for kink solutions. Namely, for kink solutions we obtain that the speed of the characteristics behind the "smoothed shock" is smaller than the speed of the characteristics in front of the "smoothed shock". So kink solutions presumably correspond to undercompressive shocks. Undercompressive shocks have been

introduced by Shearer et al. [96] in the study of a 2×2 system of conservation laws with application to oil recovery, see Schaeffer and Shearer [93]. Since then they have been extensively studied, for example, for conservation laws with non-convex fluxes (see, e.g., Hayes et al. [53], Schulze and Shearer[94]) and in particular for thin-film-type equations (see, e.g., Bertozzi et al. [7], Münch [80] Bertozzi and Shearer [9], Bertozzi et al. [8], Golovin et al. [48], Segin et al. [95]). Undercompressive shocks have also been observed experimentally, for example, in thin liquid films driven by thermally induced surface tension gradient acting against gravity, see Bertozzi et al. [6], Sur et al. [100].

Chapter 4

Numerical computation of single- and double-interface solutions

4.1 Introduction

In this chapter, we compute various bifurcation diagrams for single- and double-interface solutions both for the standard (when $D = 0$) and the convective (when $D \neq 0$) Cahn-Hilliard equation. For the computations, we use a numerical continuation procedure implemented in the continuation and bifurcation software Auto07p [31]. The details of the computational procedure are explained in Section 4.2. The case of the standard Cahn-Hilliard equation is analysed in Section 4.3. We start the computations from neutrally stable small-amplitude sinusoidal waves, and perform first continuations in the domain-size parameter L. This leads to double-interface (droplet) solutions. As expected, we find that the computed solutions are always stationary when $D = 0$, and, depending on the mean thickness parameter $\bar{u}$, we obtain various types of bifurcation diagrams. In Section 4.4, we perform continuations both in the driving force parameter, D, and the domain size parameter, L, and analyse how the bifurcation diagrams change depending on the driving force. Finally, single-interface solutions (kinks and anti-kinks) are computed in Section 4.4.3.

4.2 Numerical procedures

4.2.1 Computation of double-interface solutions

In this section, we explain the computational procedure of double-interface solutions (i.e., droplets) of the convective Cahn-Hilliard equation (2.28). First, we write this equation in the form

$$u_t = -\left[\frac{Du^2}{2} + (u - u^3 + u_{xx})_x\right]_x. \tag{4.1}$$

This equation, written in the frame moving at velocity v (i.e., after the tranformation $x \to x - vt$), becomes

$$u_t - vu_x = -\left[\frac{Du^2}{2} + (u - u^3 + u_{xx})_x\right]_x. \tag{4.2}$$

A stationary (when $v = 0$) or travelling (when $v \neq 0$) solution is then a steady solution of this equation, i.e., a solution of

$$-vu_0' = -\left[\frac{Du_0^2}{2} + (u_0 - u_0^3 + u_0'')'\right]', \tag{4.3}$$

where now u_0 is a function of x only and primes denote differentiation with respect to x.

Next, we integrate equation (4.3) to obtain

$$0 = -\left[\frac{Du_0^2}{2} + (u_0 - u_0^3 + u_0'')'\right] + vu_0 + C_0, \tag{4.4}$$

where C_0 is the constant of integration that corresponds to the flux in the co-moving frame.

To solve equation (4.4) numerically, we use the continuation and bifurcation software Auto07p [31]. First we write (4.4) as a system of first-order autonomous ordinary differential equation on the domain [0, 1]. To do this, we introduce the variables $y_1 = u_0 - \bar{u}$, $y_2 = u_0'$ and $y_3 = u_0''$. Here $\bar{u}$ denotes the mean thickness. We obtain from equation

(4.3) the following three-dimensional dynamical system:

$$\dot{y}_1 = Ly_2, \tag{4.5}$$

$$\dot{y}_2 = Ly_3, \tag{4.6}$$

$$\dot{y}_3 = L[C_0 + v(y_1 + \bar{u}) - D(y_1 + \bar{u})^2/2 - y_2 + 3(y_1 + \bar{u})^2 y_2], \tag{4.7}$$

where L is the physical domain size, and dots denote derivatives with respect to the variable $\alpha \equiv x/L$. We note that in Auto07p the dimension of the system is described by the variable $NDIM$, so we set $NDIM = 3$. The system of the equations is specified in the user-supplied subroutine $FUNC$. The advantage of the used form is that the fields $y_1(\alpha)$, $y_2(\alpha)$ and $y_3(\alpha)$ correspond to the correctly scaled physical fields $u_0(L\alpha)$, $u_0'(L\alpha)$ and $u_0''(L\alpha)$. To compute periodic droplet solutions, we use periodic boundary conditions for y_1, y_2 and y_3, i.e.,

$$y_1(0) = y_1(1), \tag{4.8}$$

$$y_2(0) = y_2(1), \tag{4.9}$$

$$y_3(0) = y_3(1), \tag{4.10}$$

We note that in Auto07p, the number of the boundary conditions is described by the variable NBC, so we set $NBC = 3$. The boundary conditions are specified in the user-supplied subroutine $BCND$. In addition, we use two integral conditions, namely, one pinning condition breaking the translational invariance of the equation, and the condition for the mean thickness:

$$\int_0^1 y_1 d\alpha = 0. \tag{4.11}$$

In Auto07p, the integral conditions are specified in the user-supplied subroutine $ICND$, and the parameter representing the number of the integral conditions is $NINT$. So, we set $NINT = 2$. We note that the number of the so-called free parameters (i.e., the parameters that are allowed to vary for the well-posedness of the continuations) is given by the formula:

$$NBC + NINT - NDIM + 1. \tag{4.12}$$

For our problem we find that the number of the free parameters is 3. So, if we choose one of the parameters as the principal one, e.g., the domain size or the driving force, two more parameters must adapt. As the additional parameters, we have the flux C_0 and the velocity v.

4.2.2 Computation of single-interface solutions

In this section, we explain the computational procedure of single-interface solutions (i.e., kinks and anti-kinks) of the convective Cahn-Hilliard equation (2.28). Let us assume that the two homogeneous levels are $\bar{u}_a$ and $\bar{u}_b$, and let us assume that $\bar{u}_a > \bar{u}_b$. These are two additional parameters that are introduced in the problem. For the computation of the kink solutions, we impose the following conditions:

$$y_1(0) = \bar{u}_b, \tag{4.13}$$

$$y_1(1) = \bar{u}_a, \tag{4.14}$$

whereas for the computation of the anti-kink solutions, we impose the following conditions:

$$y_1(0) = \bar{u}_a, \tag{4.15}$$

$$y_1(1) = \bar{u}_b. \tag{4.16}$$

We are primarily interested in the computation of the kink and anti-kink solutions that bifurcate from the analytical $\tanh$ solutions for $D = 0$. According to the results of the previous Chapter, we expect that for such solutions $\dim(W_u(\bar{u}_a)) = 2$, $\dim(W_s(\bar{u}_a)) = 1$, $\dim(W_u(\bar{u}_b)) = 1$, $\dim(W_s(\bar{u}_b)) = 2$, for at least some range of positive D values. Thus, an anti-kink solution corresponds the intersection of the two-dimensional manifolds $\dim(W_u(\bar{u}_a))$ and $\dim(W_s(\bar{u}_b))$, and is, therefore, expected to exist for any sufficiently small changes of $\bar{u}_a$ and $\bar{u}_b$ for a given value of D. Therefore, as for the case of double-interface solutions, for anti-kink solutions we need three free parameters (e.g., when D is the primary continuation parameter, just two other parameters should be adapted, e.g., C_0 and v, and the remaining two parameters can be kept fixed). We achieve this by imposing the following boundary conditions (in addition to conditions (4.15) and (4.16)):

$$y_2(0) = 0, \tag{4.17}$$

$$y_2(1) = 0, \tag{4.18}$$

and the following integral condition:

$$\int_0^1 y_1 d\alpha = \frac{\bar{u}_a + \bar{u}_b}{2}. \tag{4.19}$$

This condition plays the role of a pinning condition and places the interface between the two phases approximately in the middle of the domain.

Next, a kink solution corresponds to the intersection of the one-dimensional manifolds $\dim(W_u(\bar{u}_b))$ and $\dim(W_s(\bar{u}_a))$ and is, therefore, expected to exist for a discrete set of values of $\bar{u}_a$ and $\bar{u}_b$ for a given value of D. Thus, we expect that in a continuation with a primary parameter, e.g., D, not only the flux C_0 and the velocity v must be adapted, but also $\bar{u}_a$ and $\bar{u}_b$, i.e., we should have five free parameters. We achieve this by imposing the following boundary conditions (in addition to conditions (4.13) and (4.14)):

$$y_2(0) = 0, \tag{4.20}$$
$$y_2(1) = 0, \tag{4.21}$$
$$y_3(0) = 0, \tag{4.22}$$
$$y_3(1) = 0, \tag{4.23}$$

and the integral condition (4.19). We can start the continuation procedure for kink and anti-kink solutions from, e.g., the truncated analytically know $\tanh$ profiles at $D = 0$. Note that for anti-kink solutions we can also start from a half of a small-amplitude cosine wave of a cutoff wavelength, which is consistent with the boundary conditions that we impose for anti-kink solutions.

4.3 The case of the standard Cahn-Hilliard equation

4.3.1 Double-interface solutions of the standard Cahn-Hilliard equation for $\bar{u} = 0$

In this section, we compute solutions to the standard Cahn-Hilliard equation, when $D = 0$, for the case when the average value of the solution is zero, i.e., $\bar{u} = (1/L)\int_0^L u_0\,dx = 0$. The solutions are characterised by the norm $\|\delta u_0\| = \sqrt{(1/L)\int_0^L u_0^2\,dx}$, the velocity v and the flux C_0. We use the domain size as the control parameter. To initiate the continuation procedure, a starting solution must be used (in Auto07p, it should be specified in the user-supplied subroutine $STPNT$), and we choose a small amplitude sinusoidal wave of a cutoff wavelength L_c, that is obtained from the linear stability

analysis discussed in Section 3.2, i.e.,

$$L_c = \frac{2\pi}{k_c}, \quad \text{where} \quad k_c = \sqrt{1 - 3\bar{u}^2}. \tag{4.24}$$

For the case when $\bar{u} = 0$, we find $L_c = 2\pi$. By choosing this value of L_c, we can obtain solutions that have the shape of one droplet (i.e., double-interface solutions). If we choose instead the solutions of the same period but given on the domain size that is an n multiple of L_c, then we will obtain n-droplet solutions. In this Chapter, we only consider the case when $n = 1$. The case when $n = 2$ will be considered in the next Chapter.

Figs. 4.1 and 4.2 show the results of the calculations, where the first figure shows the bifurcation diagrams and the second figure shows solution profiles for some values of the domain size L. In Fig. 4.1(a), the dependence of the norm $\|\delta u_0\|$ on the domain size, L, is shown. The branch of spatially non-uniform solutions bifurcates supercritically from the homogeneous branch at $L = L_c$. We can see that the norm increases monotonically and tends to 1 as L increases. In Fig. 4.2, we can observe that the solution profile approaches a droplet shape as L increases, with the minimum value equal to -1 and the maximum value equal to 1. (The profiles are shown for $L = 2\pi \approx 6.28, 7, 10, 20, 50, 400$, see the legend for the corresponding lines). To analyse the large L behaviour we present in Fig. 4.1(b) the same data as in Fig. 4.1(a), but in a different form. Namely, we give the dependence of $1 - \|\delta u_0\|$ on the domain size L on a log-log scale. The slope of the line for large L is equal to -1. This is confirmed by the straight (red) dashed line which has the slope -1 on a log-log scale. Therefore, we conclude that $1 - \|\delta u_0\|$ goes to zero as L^{-1} when L increases.

The facts that for large L the solution has the form of a droplet that changes from -1 to 1 and that $1 - \|\delta u_0\| \propto L^{-1}$ for large L can be explained by the analysis presented in Section 3.5, and also by the following argument. Let us assume that $\bar{u}$ is fixed and is not necessarily zero and that the solution has the form of a droplet that changes between two values $\bar{u}_a$ and $\bar{u}_b$, where $\bar{u}_a > \bar{u}_b$. The solution profile in the transition regions from $\bar{u}_a$ to $\bar{u}_b$ and from $\bar{u}_b$ to $\bar{u}_a$ does not change much when L becomes sufficiently large. So, effectively, just the sizes of the regions where $u_0 \approx \bar{u}_a$ and where $u_0 \approx \bar{u}_b$ increase as L increases, and the sizes of the transition regions between the two values become smaller relative to the domain size, so effectively we can ignore these regions (i.e., consider the sharp interface limit). Let us assume that L_a is the width of the droplet. Since the

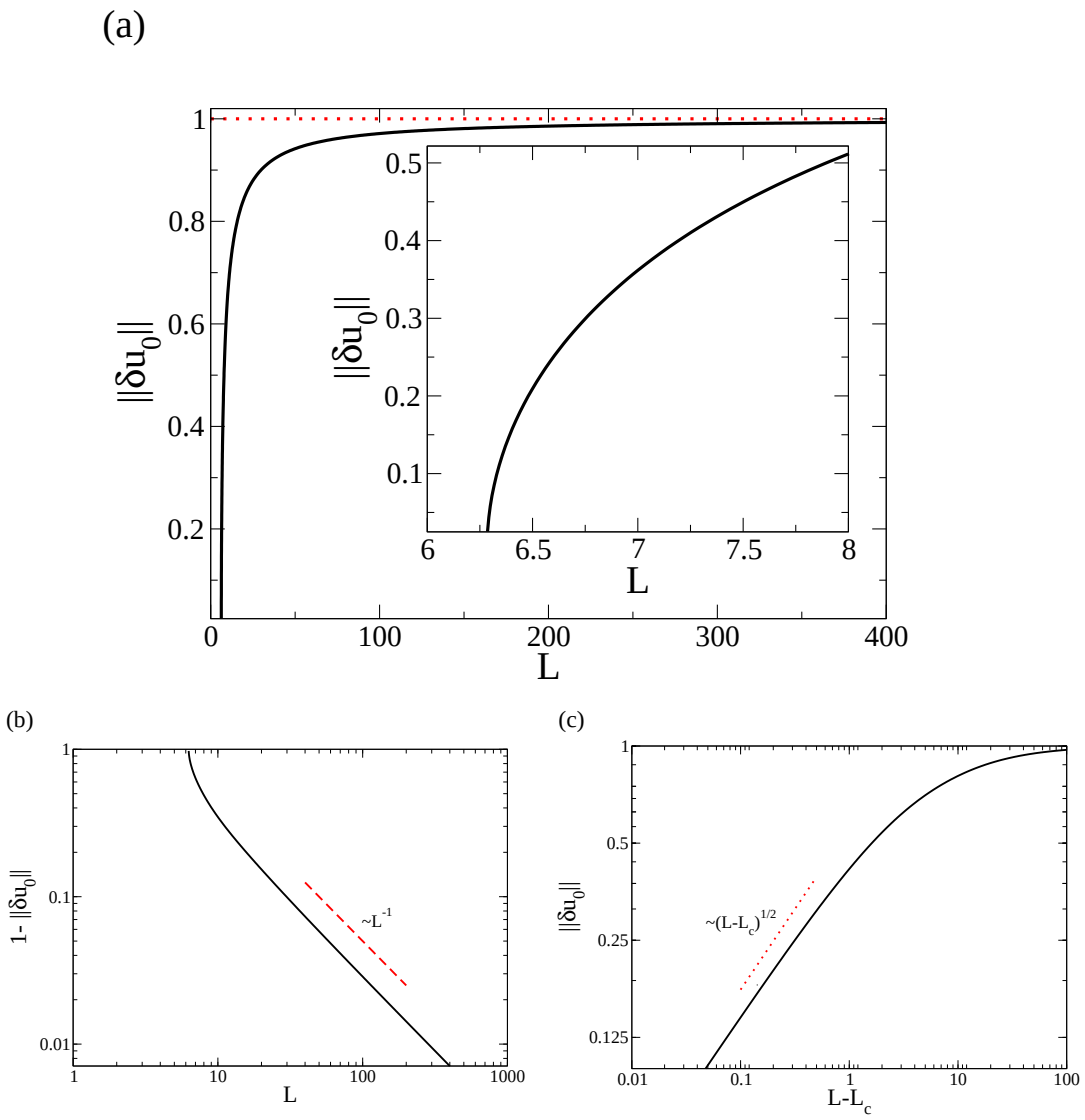

Figure 4.1: (a) The bifurcation diagram of the one-droplet ($n = 1$) steady solutions of the standard Cahn-Hilliard equation (2.28), when $D = 0$, for the case when $\bar{u} = 0$, showing the dependence of the norm $\|\delta u_0\|$ on the domain size L. The dotted line corresponds to the value $\sqrt{1-\bar{u}^2} = 1$ towards which the norm converges as L increases, according to (4.35). The inset gives a zoom at small values of L. Panel (b) shows the dependence of $1 - \|\delta u_0\|$ on L on a log-log scale. The red dashed line has the slope -1 on a log-log scale and confirms that $1 - \|\delta u_0\| \propto L^{-1}$ as L increases. Panel (c) shows the dependence of $\|\delta u_0\|$ on $L - L_c$, where $L_c = 2\pi$, on a log-log scale. The red dotted line has the slope $1/2$ on a log-log scale and confirms that $\|\delta u_0\| \propto (L - L_c)^{1/2}$ as $L \to L_c$.

droplet u_0 is a steady solution, according to (2.16), we have

$$\left.\frac{\delta F[u]}{\delta u}\right|_{u=u_0} = C_1, \tag{4.25}$$

or, equivalently,

$$f'(u_0) - u_{0xx} = C_1, \tag{4.26}$$

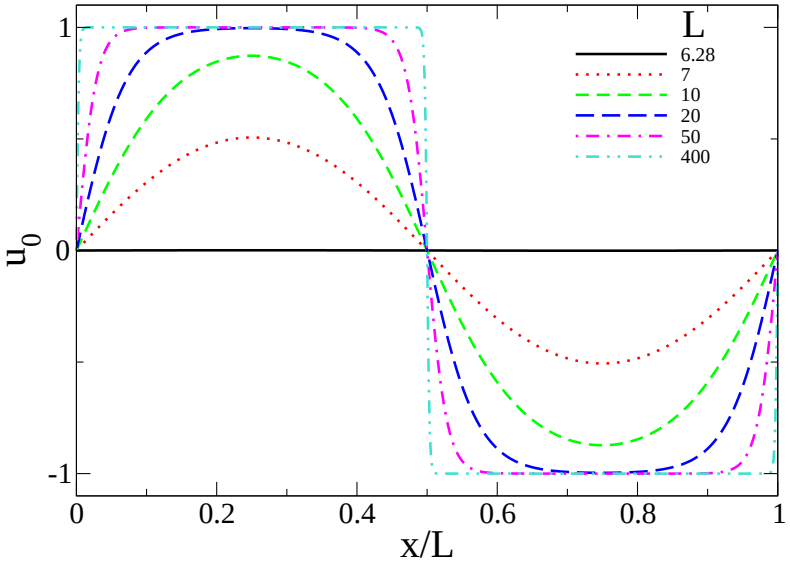

Figure 4.2: One-droplet ($n = 1$) steady solution profiles $u_0(x)$ of the standard Cahn-Hilliard equation (i.e., equation (2.28) with $D = 0$) for $\bar{u} = 0$ for different values of the domain size L, as is given in the legend.

where C_1 is a constant. In the sharp interface limit, this implies

$$f'(\bar{u}_a) = f'(\bar{u}_b) = C_1. \tag{4.27}$$

On multiplying (4.26) by u_{0x} and integrating, we also find

$$f(u_0) - \frac{1}{2}u_{0x}^2 = C_1 u_0 + C_2, \tag{4.28}$$

where C_2 is another constant. In the sharp interface limit, this condition implies

$$f(\bar{u}_a) - C_1\bar{u}_a = f(\bar{u}_b) - C_1\bar{u}_b, \tag{4.29}$$

or, equivalently,

$$\frac{f(\bar{u}_a) - f(\bar{u}_b)}{\bar{u}_a - \bar{u}_b} = C_1. \tag{4.30}$$

Note that conditions (4.27) and (4.30) are exactly the conditions determining points on the binodal line. It can be easily verified that for the standard Cahn-Hilliard equation the only solution of these equations for which $\bar{u}_a > \bar{u}_b$ is

$$\bar{u}_a = 1, \qquad \bar{u}_b = -1. \tag{4.31}$$

This explains why the droplet profiles change from -1 to 1 when the domain size is

sufficiently large. Additionally, in the sharp interface limit, the following condition must be satisfied (which ensures that the mean of the solution is $\bar{u}$):

$$l_a \bar{u}_a + (1 - l_a)\bar{u}_b = \bar{u}, \tag{4.32}$$

where $l_a = L_a/L$ is the relative width of the droplet. This implies

$$l_a = \frac{\bar{u} - \bar{u}_b}{\bar{u}_a - \bar{u}_b}. \tag{4.33}$$

Using that for the standard Cahn-Hilliard equation $\bar{u}_{a,b} = \pm 1$, we find

$$l_a = \frac{1 + \bar{u}}{2}. \tag{4.34}$$

Now we can estimate the norm $\|\delta u_0\|$ in the limit $L \to \infty$:

$$\begin{aligned} \|\delta u_0\| \;&\to\; \sqrt{l_a(\bar{u}_a - \bar{u})^2 + (1 - l_a)(\bar{u}_b - \bar{u})^2} \\ &= \sqrt{\frac{1 + \bar{u}}{2}(1 - \bar{u})^2 + \frac{1 - \bar{u}}{2}(1 + \bar{u})^2} = \sqrt{1 - \bar{u}^2}. \end{aligned} \tag{4.35}$$

For example, for $\bar{u} = 0$, we find that $\|\delta u_0\| \to 1$, which is consistent with the results presented in Fig. 4.1(a). Moreover, we can show that $\sqrt{1 - \bar{u}^2} - \|\delta u_0\| \to 0$ as L^{-1} when L increases. Indeed, if L is sufficiently large, the solution profile approaches a shape of a droplet so that u_0 changes from 1 to -1. The solution profile in the transition regions from 1 to -1 and from -1 to 1 does not change much and tends to a certain limiting profile when L increases. Let $(a_1, L_a - a_2)$ and $(L_a + a_3, L - a_4)$ be the regions where $u_0 \approx \pm 1$, respectively. Then

$$\begin{aligned} \int_0^L (u_0 - \bar{u})^2 dx \;\approx\; & (L_a - a_1 - a_2)(1 - \bar{u})^2 + (L - L_a - a_3 - a_4)(1 + \bar{u})^2 \\ & + \int_0^{a_1} (u_0 - \bar{u})^2 dx + \int_{L_a - a_2}^{L_a + a_3} (u_0 - \bar{u})^2 dx \\ & + \int_{L - a_4}^{L} (u_0 - \bar{u})^2 dx. \end{aligned} \tag{4.36}$$

Denoting

$$\begin{aligned} A \;=\; & (a_1 + a_2)(1 - \bar{u})^2 + (a_3 + a_4)(1 + \bar{u})^2 \\ & - \int_0^{a_1} (u_0 - \bar{u})^2 dx - \int_{L_a - a_2}^{L_a + a_3} (u_0 - \bar{u})^2 dx - \int_{L - a_4}^{L} (u_0 - \bar{u})^2 dx \end{aligned} \tag{4.37}$$

and using the fact that A tends to a certain limit as L increases, we obtain

$$\begin{aligned}\int_0^L (u_0-\bar{u})^2 dx &\approx L_a(1-\bar{u})^2+(L-L_a)(1+\bar{u})^2-A \\ &= L\frac{1+\bar{u}}{2}(1-\bar{u})^2+L\frac{1-\bar{u}}{2}(1+\bar{u})^2-A \\ &= L(1-\bar{u}^2)-A. \end{aligned} \tag{4.38}$$

Thus,

$$\|\delta u_0\| \approx \sqrt{\frac{L(1-\bar{u}^2)-A}{L}} = \sqrt{1-\bar{u}^2}-\frac{A}{2(1-\bar{u}^2)}L^{-1}+O(L^{-2}), \tag{4.39}$$

i.e., indeed,

$$\sqrt{1-\bar{u}^2}-\|\delta u_0\| \approx \frac{A}{2(1-\bar{u}^2)}L^{-1}+O(L^{-2}) \propto L^{-1}, \tag{4.40}$$

for $L \to \infty$. For example, for $\bar{u}=0$, we find $1-\|\delta u_0\| \propto L^{-1}$, which is consistent with the results presented in Fig. 4.1(b).

In Fig. 4.1(c), we again plot the same data but present it differently, namely, we plot the dependence of $\|\delta u_0\|$ on the difference of the domain size and the cutoff domain size, $L-L_c$, on a log-log scale, and we focus on the region where L is close to L_c. The slope of line is equal to $1/2$ as $L \to L_c$. This is confirmed by the straight (red) dotted line which has the slope $1/2$ on a log-log scale. Therefore, the norm $\|\delta u_0\|$ goes to zero when $(L-L_c)^{1/2}$ as $L \to L_c$. This fact can be explained by the weakly nonlinear analysis presented in Section 4.5.1, which implies that for L close to L_c, the amplitude of the small-amplitude sinusoidal wave scales as $(L-L_c)^{1/2}$, and, therefore, indeed $\|\delta u_0\|$ scales as $(L-L_c)^{1/2}$ when $L \to L_c$.

We also note that in all our calculations the velocity v and the flux C_0 turn out to be equal to zeros for all the values of L (up to numerical noise), as expected for the standard Cahn-Hilliard equation. Therefore, we do not present the corresponding figures.

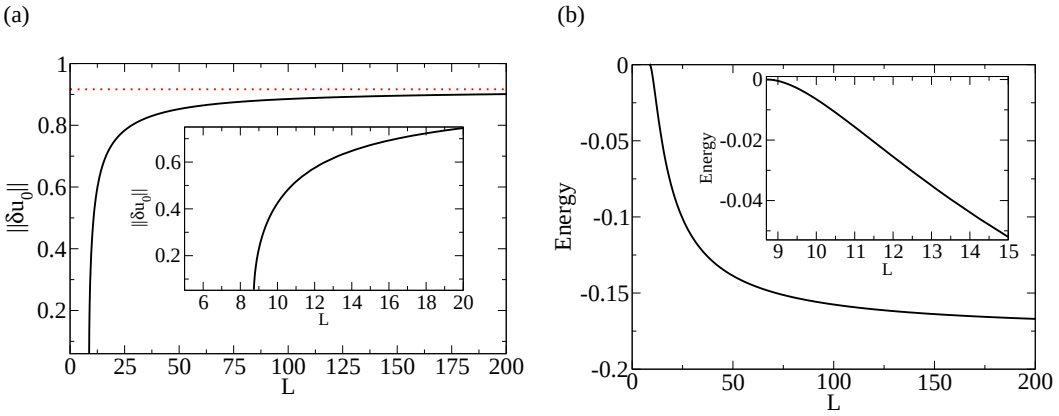

Figure 4.3: (a) The bifurcation diagram of the one-droplet ($n = 1$) steady solutions of the standard Cahn-Hilliard equation (2.28), when $D = 0$, for the case when $\bar{u} = 0.4$, showing the dependence of the norm $\|\delta u_0\|$ on the domain size L. The dotted line corresponds to the value $\sqrt{1-\bar{u}^2} \approx 0.9165$ towards which the norm converges as L increases, according to (4.35). The inset gives a zoom at small values of L. Panel (b) shows in addition the dependence of the energy defined by (2.7) on the domain size L. The inset gives a zoom at small values of L.

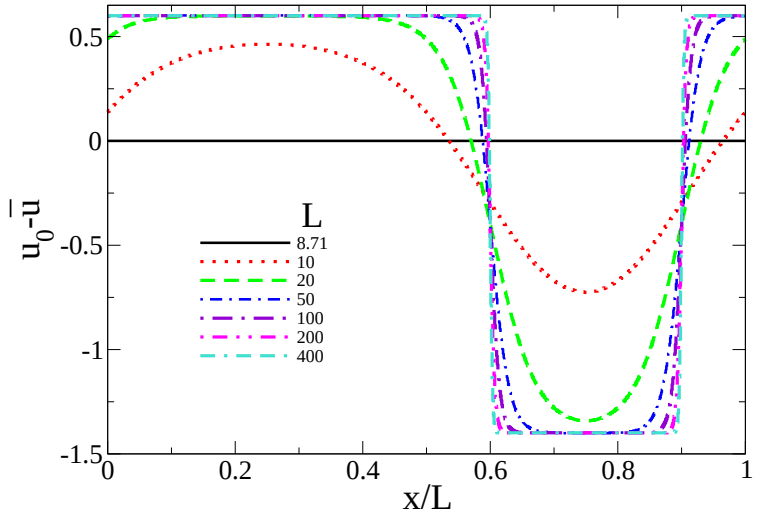

Figure 4.4: One-droplet ($n = 1$) steady solution profiles $u_0(x)$ of the standard Cahn-Hilliard equation (i.e., equation (2.28) with $D = 0$) for $\bar{u} = 0.4$ for different values of the domain size L, as is given in the legend.

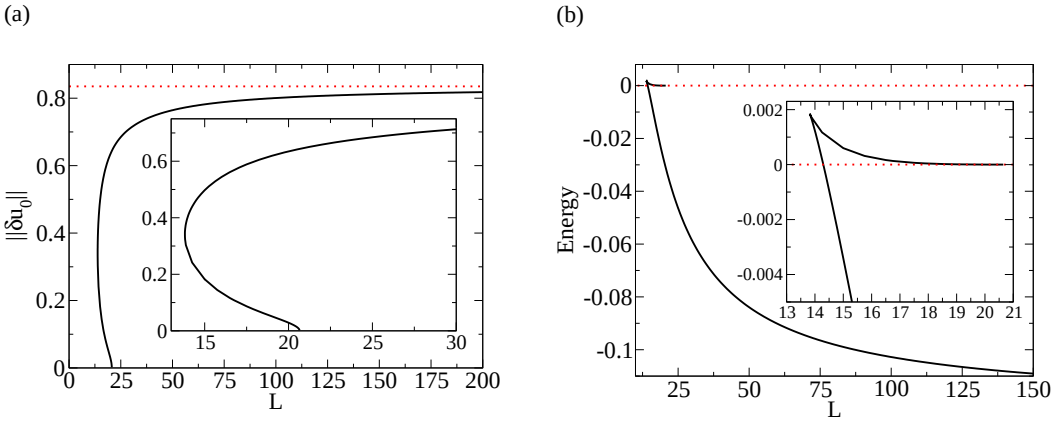

Figure 4.5: (a) The bifurcation diagram of the one-droplet ($n = 1$) steady solutions of the standard Cahn-Hilliard equation (2.28), when $D = 0$, for the case when $\bar{u} = 0.55$, showing the dependence of the norm $\|\delta u_0\|$ on the domain size L. The dotted line corresponds to the value $\sqrt{1-\bar{u}^2} \approx 0.8352$ towards which the norm converges as L increases, according to (4.35). The inset gives a zoom at small values of L. Panel (b) shows in addition the dependence of the energy defined by (2.7) on the domain size L. The inset gives a zoom at small values of$L$.

4.3.2 Double-interface solutions of the standard Cahn-Hilliard equation for $\bar{u} = 0.4, 0.55$ and 0.6

In this section, we continue to analyse droplet solutions of the standard Cahn-Hilliard equation (2.28), when $D = 0$, but now we consider the cases when the average value of the solution is $\bar{u} = 0.4,\ 0.55$ and 0.6, and characterise the solutions both by their norms $\|\delta u_0\|$ and their free energies $F(u_0)$ (defined by (2.7)). Note that for $|\bar{u}| < 1/\sqrt{3}$, the flat solution $u_0 = \bar{u}$ becomes unstable when $L > L_c = 2\pi/k_c$, where $k_c = \sqrt{1-3\bar{u}^2}$. We compute L_c at $\bar{u} = 0.4$ and 0.55 we find that $L_c = 8.7$ and 20.66, respectively. Whereas for $\bar{u} = 0.6$ the flat solution is linearly stable for any domain size.

The results showing the dependence of the norm $\|\delta u_0\|$ on the domain size L for $\bar{u} = 0.4$ are given in Fig. 4.3(a) and the results showing the dependence of the energy $F(u_0)$ on L are given in Fig. 4.3(b). In Fig. 4.3(a), we can see that the primary bifurcation at $L_c = 8.7$ is supercritical for this value of $\bar{u}$. Also, the dotted line corresponds to the value $\sqrt{1-\bar{u}^2} \approx 0.9165$, and we can see that the norm approaches this value as L increases, in agreement with (4.35). We can also observe that the energy of the non-uniform solution monotonically decreases as L increases and is smaller than the energy of the flat solution. Fig. 4.5(a) shows the dependence of the norm $\|\delta u_0\|$ on the domain size L for $\bar{u} = 0.55$ and Fig. 4.5(b) shows the dependence of the energy $F(u_0)$ on L for this value of $\bar{u}$. For this value of $\bar{u}$, we can see that the primary bifurcation at $L_c = 20.66$

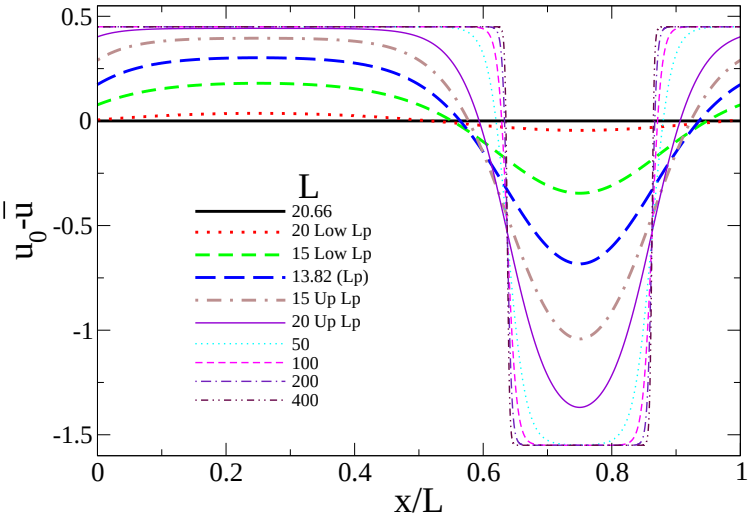

Figure 4.6: One-droplet ($n = 1$) steady solution profiles $u_0(x)$ of the standard Cahn-Hilliard equation (i.e., equation (2.28) with $D = 0$) for $\bar{u} = 0.55$ for different values of the domain size L, as is given in the legend.

is subcritical. The branch of non-uniform solutions initially follows to decreasing values of the domain size L and is unstable up to the saddle-node bifurcation at $L = L_s \approx 13.818$. After this point the branch turns back and becomes stable. Also, the dotted line corresponds to the value $\sqrt{1-\bar{u}^2} \approx 0.8352$, and we can see that the norm approaches this value as L increases, in agreement with (4.35). We conclude that the nature of the bifurcation switches from supercritical to subcritical at some value of $\bar{u} \in (0.4,\, 0.55)$. The exact value of $\bar{u}$ at which this changeover happens can be obtained by the weakly nonlinear analysis given in Section 4.5.1. It turns out that this value is $\bar{u}^* = 1/\sqrt{5} \approx 0.45$. Note that for $\bar{u} = 0.55$ the energy of the non-uniform solution first increases monotonically, up to the saddle-node bifurcation, and then decreases monotonically. It remains positive up to a certain value of the domain size, $L_m \approx 14.30$ between L_s and L_c, and then becomes negative. The point $L = L_m$ is the so-called Maxwell point. At this point, both linearly stable solutions, i.e. the uniform solution and the nonuniform solution with the larger value of the norm, have the same value of the energy. For $L \in (L_s,\, L_m)$, the uniform solution has lower free energy, whereas for $L > L_m$, the non-uniform solution has lower free energy.

As mentioned above, since $\bar{u} = 0.6 > 1/\sqrt{3}$, the flat solution $u = \bar{u}$ is linearly stable for any L, i.e., there is no primary bifurcation on the uniform solution. To produce

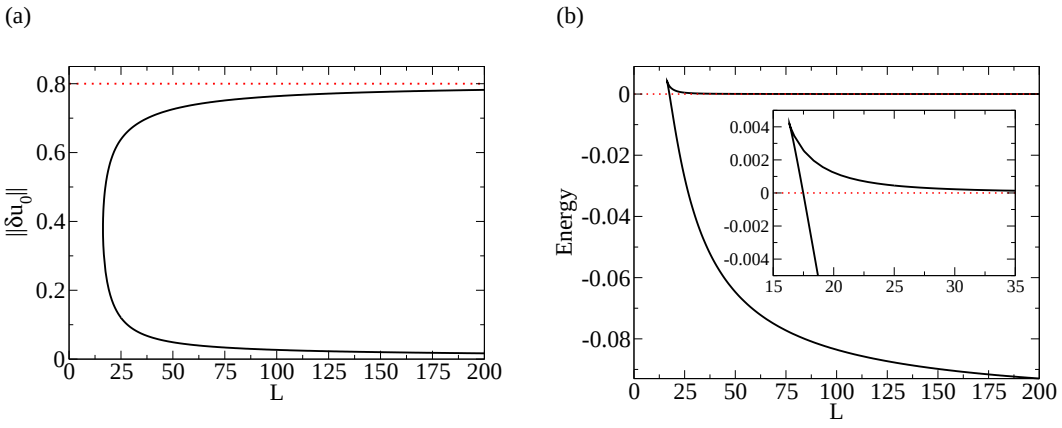

Figure 4.7: (a) The bifurcation diagram of the one-droplet ($n = 1$) steady solutions of the standard Cahn-Hilliard equation (2.28), when $D = 0$, for the case when $\bar{u} = 0.6$, showing the dependence of the norm $\|\delta u_0\|$ on the domain size L. The dotted line corresponds to the value $\sqrt{1-\bar{u}^2} = 0.8$ towards which the norm converges as L increases, according to (4.35). Panel (b) shows in addition the dependence of the energy defined by (2.7) on the domain size L. The inset gives a zoom at small values of$L$.

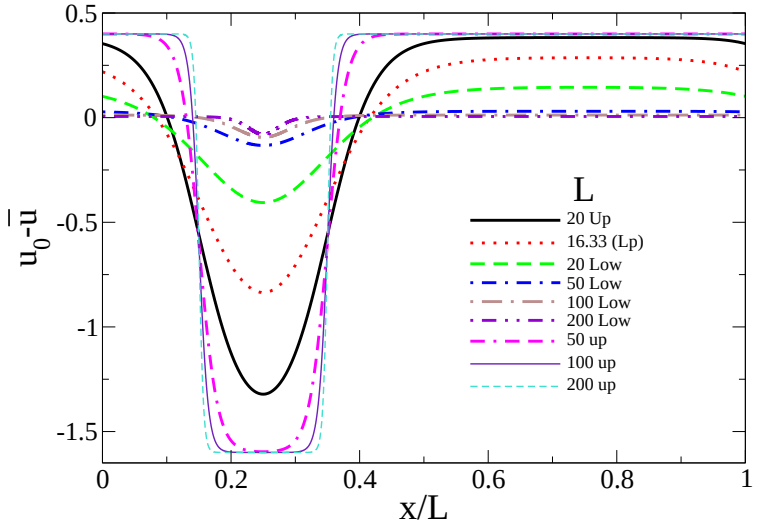

Figure 4.8: One-droplet ($n = 1$) steady solution profiles $u_0(x)$ of the standard Cahn-Hilliard equation (i.e., equation (2.28) with $D = 0$) for $\bar{u} = 0.60$ for different values of the domain size L, as is given in the legend.

the branch of non-uniform solutions, we can first compute the branch of non-uniform solutions for $\bar{u} = 0$, and then select a solution on this branch at a sufficiently large value of L (e.g., at $L = 100$). We can then keep L fixed and perform a continuation in $\bar{u}$, until we reach the value $\bar{u} = 0.6$. This produces the non-uniform solution for $\bar{u} = 0.6$ at $L = 100$. After that, we can again keep $\bar{u}$ fixed and perform a continuation in L, going in both directions, which produces the whole branch of non-uniform solutions. The results are shown in Fig. 4.7. Panel (a) of Fig. 4.7 shows the dependence of the norm

$\|\delta u_0\|$ on the domain size. We can observe that the branch of non-uniform solutions has a turning point at $L = L'_s \approx 16.327$. For each $L > L'_s$, there are two non-uniform solutions, one is unstable and is of smaller norm while the other one is stable and is of larger norm. The dotted line corresponds to the value $\sqrt{1-\bar{u}^2} \approx 0.8$, and we can see that the norm of the stable solution approaches this value as L increases, in agreement with (4.35). The energy of the linearly unstable non-uniform solution monotonically decreases from some positive value to zero as L changes from L'_s to ∞ (see panel b of Fig. 4.7). Whereas the energy of the linearly stable non-uniform solution decreases monotonically from a positive value to negative values crossing zero at the Maxwell point, $L'_m \approx 17.466$. In other words, we obtain metastability for $L > L'_s$: We have two linearly stable solutions (a uniform one and a non-uniform one of large norm) that are "separated" by a linearly unstable non-uniform solution of smaller norm. Moreover, for $L \in (L'_s, L'_m)$, the uniform solution has lower energy than the linearly stable non-uniform solution and vice versa for $L > L'_m$.

4.4 The case of the convective Cahn-Hilliard equation

4.4.1 Double-interface solutions of the convective Cahn-Hilliard equation for $\bar{u} = 0$

In this section we consider how the introduction of the driving force affects the solutions of the Cahn-Hilliard equation, namely, we consider equation (2.28) with $D \neq 0$. We mainly consider the domain size $L = 50$ and use the driving force D as the control parameter.

We first consider the case of zero mean concentration, $\bar{u} = 0$. Fig. 4.9(a) shows the dependence of the norm $\|\delta u_0\|$ on the driving force D for $L = 50$. We can see that the norm monotonically decreases as D increases. The inset shows a zoom at smaller values of D, and we can observe that there is a relatively sharp change of the behaviour at a value of D between 1 and 1.5 – for D smaller than this value the graph is concave down, whereas for larger values of D the graph is concave up. This actually can be associated with the fact that for $D > \sqrt{2}$, there fails to exist a kink solution connecting two values $\bar{u}_b$ and $\bar{u}_a$ when $x \to \pm\infty$, as was discussed in Chapter 3 (here $\bar{u}_b < \bar{u}_a$). Therefore, for $D > \sqrt{2}$, the limit cycles that correspond to periodic solutions are not

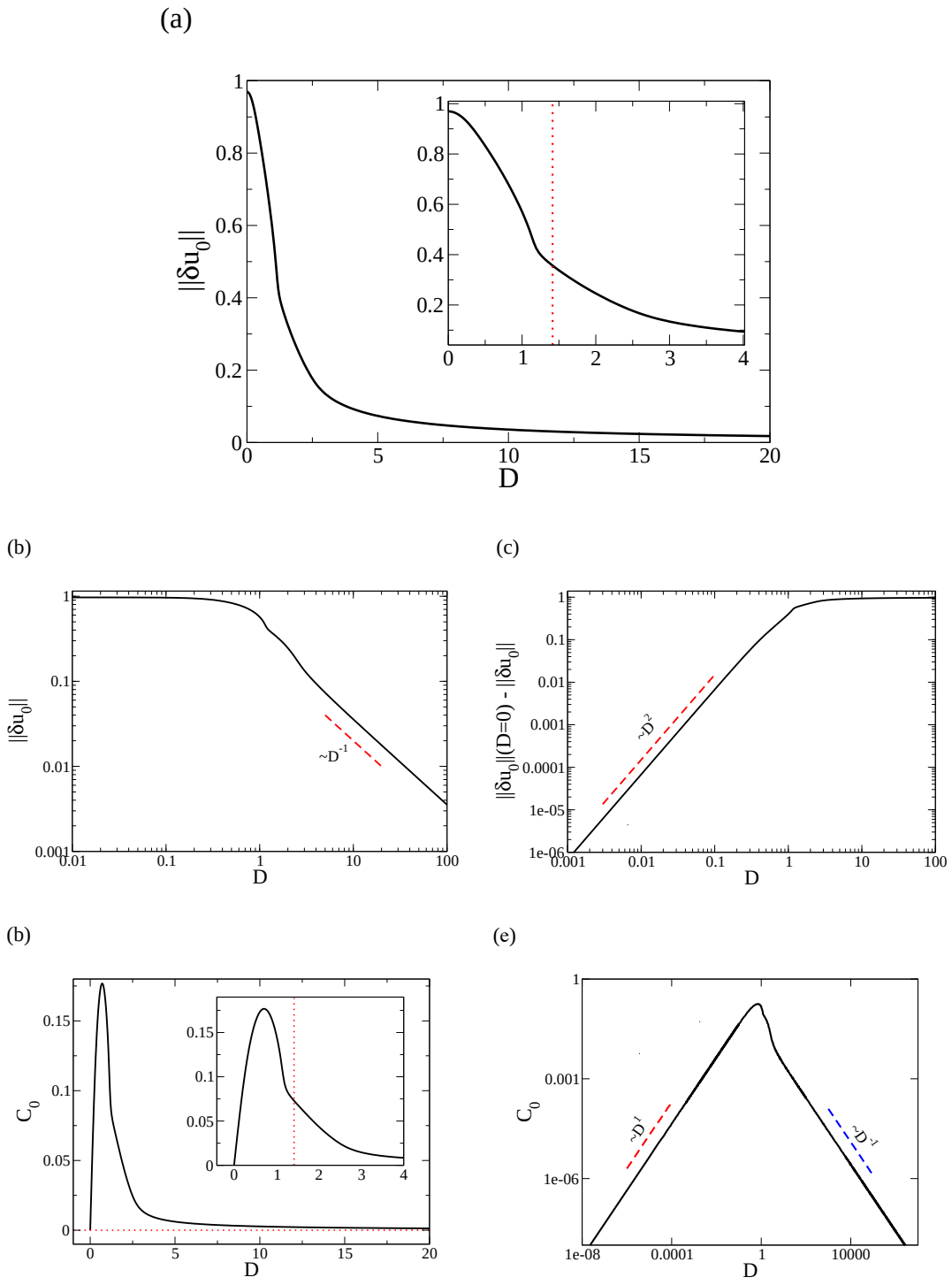

Figure 4.9: (a) The bifurcation diagram of the one-droplet ($n = 1$) solutions of the convective Cahn-Hilliard equation (2.28) when $\bar{u} = 0$ and $L = 50$ showing the dependence of the norm $\|\delta u_0\|$ on the driving force D. The inset gives a zoom at smaller values of D. The red dotted line corresponds to $D = \sqrt{2}$. Panel (b) shows the same result but on a log-log scale. The red dashed line has the slope -1 on a log-log scale and confirms that $\|\delta u_0\| \propto D^{-1}$ as D increases. Panel (c) shows the dependence of $\|\delta u_0\|_{D=0} - \|\delta u_0\|$ on D on a log-log scale. The red dashed line has the slope 2 on a log-log scale and confirms that $\|\delta u_0\|_{D=0} - \|\delta u_0\| \propto D^2$ as D approaches zero. Panel (d) shows the dependence of the flux C_0 on the driving force D. The inset gives a zoom at smaller values of D. Panel (e) shows the same data as in panel (d) but on a log-log scale. The red dashed and the blue dashed lines have the slopes 1 and -1, respectively, on a log-log scale, which confirms that $C_0 \propto D$ as $D \to 0$ and $C_0 \propto D^{-1}$ as $D \to \infty$.

actually limit cycles that exist in the vicinity of a heteroclinic loop connecting $(\bar{u}_b, 0, 0)$ to $(\bar{u}_a, 0, 0)$ and $(\bar{u}_a, 0, 0)$ to $(\bar{u}_b, 0, 0)$ (as is the case for $D < \sqrt{2}$), but correspond to a different type of solutions. To better understand the behaviour for larger and smaller values of D, we additionally present panels (b) and (c). Panel (b) of Fig. 4.9 shows the dependence of $\|\delta u_0\|$ on the driving force D on a log-log scale. The red dashed line in this panel has the slope -1 on a log-log scale, which indicates that the norm $\|\delta u_0\|$ approaches zero as D^{-1} as D increases. This is consistent with the fact that u_0 scales as D^{-1} as D increases, as was shown before. Panel (c) of Fig. 4.9 shows the dependence of $\|\delta u_0\|_{D=0} - \|\delta u_0\|$ on the driving force D on a log-log scale. The red dashed line in this panel has the slope 2 on a log-log scale, which indicates that $\|\delta u_0\|_{D=0} - \|\delta u_0\| \propto D^2$ as $D \to 0$. We note that the velocity v of the computed solutions turns out to be zero (up to a numerical noise), and, therefore, we do not show the corresponding diagram here. This means that for the zero mean concentration the travelling-wave solutions are in fact steady-state solutions. However, we know that in the limit $D \to \infty$, we approach the Kuramoto-Sivashinsky equation, which has a chaotic stable attractor on a sufficiently large domain, see Collet et al. [23, 24], Goodman [49], Hyman et al. [57], Jolly et al. [61], Il'yashenko [59], Kevrekidis et al. [63], Otto [85], Papageorgiou and Smyrlis [86], Smyrlis and Papageorgiou [97]. We therefore do not expect the computed travelling waves to be stable for sufficiently large values of D. Panel (d) of Fig. 4.9 shows the dependence of the flux C_0 on D. It can be observed that the flux starts from zero at $D = 0$, then increases monotonically before achieving a maximum value at $D \approx 0.7$. After that, it decreases monotonically to zero and has a sharp change at $D \approx 1.2$, after which the graph becomes concave up. Panel (c) of Fig. 4.9 shows the same dependence of the flux C_0 on D but presents it on a log-log scale. The red dashed and the blue dashed lines in this panel have the slopes 1 and -1, respectively. These lines reveal that the flux goes to zero as D when $D \to 0$, and it goes to zero as D^{-1} when $D \to \infty$.

A confirmation that the qualitative change in the behaviour happens in the vicinity of $D = \sqrt{2}$ is given in Fig. 4.10 that shows the same bifurcation diagram as in Fig. 4.9(a) but for $L = 200$. We can observe that now the transition to a different type of solutions becomes sharper. To additionally verify that for $D > \sqrt{2}$, we obtain a different type of solutions, we performed continuation over L for several fixed values of D. The results are given in Fig. 4.11. Panel (a) of this figure corresponds to $D = 0.8$, and it can be observed that the primary bifurcation is supercritical and the norm $\|\delta u_0\|$ approaches a constant value for increasing values of L, in agreement with the fact that

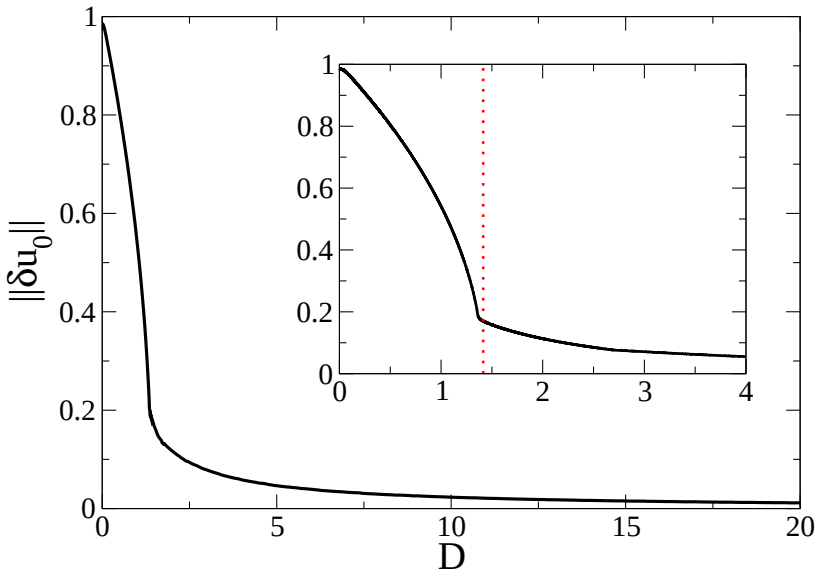

Figure 4.10: The bifurcation diagram of the one-droplet ($n = 1$) solutions of the convective Cahn-Hilliard equation (2.28) when $\bar{u} = 0$ and $L = 200$ showing the dependence of the norm $\|\delta u_0\|$ on the driving force D. The inset gives a zoom at smaller values of D. The red dotted line corresponds to $D = \sqrt{2}$.

for $D < \sqrt{2}$ there should exist heteroclinic loops connecting $(\bar{u}_b, 0, 0)$ to $(\bar{u}_a, 0, 0)$ and $(\bar{u}_a, 0, 0)$ to $(\bar{u}_b, 0, 0)$ and corresponding to one-droplet solutions. Interestingly, there exists another branch of solutions shown by a solid red curve. As D increases, these two branches approach each other and reconnect at some value of D between $D = 0.825$ (see Fig. 4.11(b)) and $D = 0.83$ (see Fig. 4.11(c)). We also note that there apparently exist further branches of solutions and several more reconnection events happen, as we can see a qualitative change in the shapes between panels (b) and (c). However, here we do not investigate this further. In fact, Zaks et al. [123] have already noticed and discussed this in their work. In Fig. 4.11(d) that corresponds to $D = 1.5$, we can observe that the branch that extends to large values of L does not approach a constant value anymore. Instead, we observe that the norm $\|\delta u_0\|$ is a monotonically decreasing function of L. This is in agreement with the fact that for $D > \sqrt{2}$ the solutions do not anymore correspond to limit cycles in the vicinity of a heteroclinic loop. Instead, we obtain a different type of solutions – one-hollow solutions (or one-hole solutions or negative solitary waves, see, for example, the terminology in Chang and Demekhin [21]) with oscillations on the left side of the hollow, as shown in Fig. 4.12 for $D = 1.5$

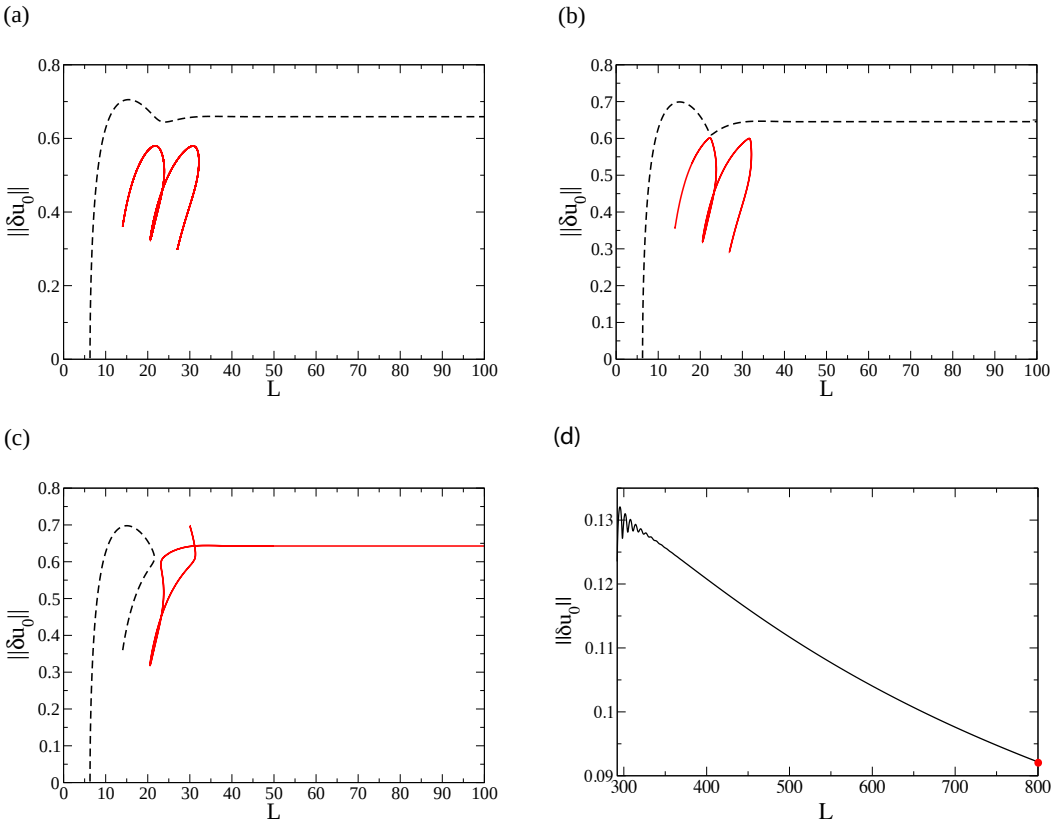

Figure 4.11: (a) The bifurcation diagrams of solutions of the convective Cahn-Hilliard equation (2.28) when $\bar{u} = 0$ and (a) $D = 0.8$, (b) $D = 0.825$, (c) $D = 0.83$ and (d) $D = 1.5$, showing the dependence of the norm $\|\delta u_0\|$ on the domain size L. The red circle corresponds to the solution shown in Fig. 4.12.

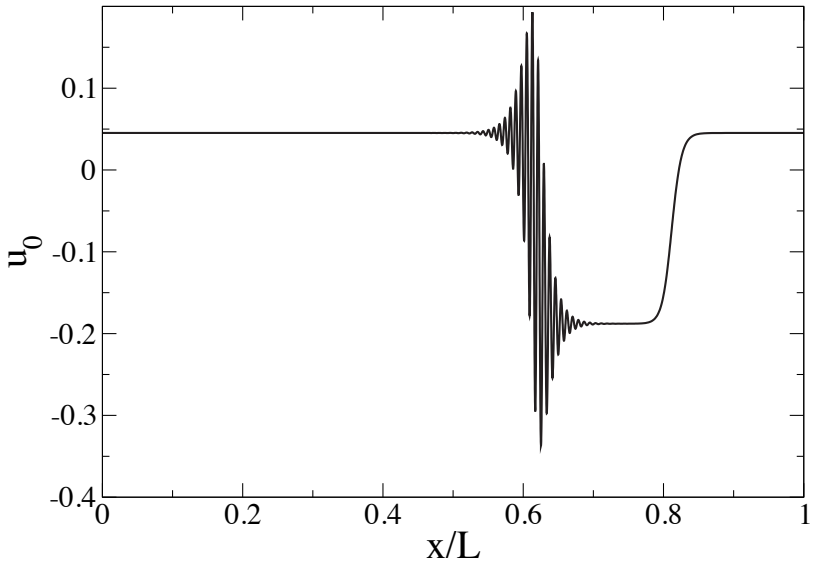

Figure 4.12: The solution profile of the convective Cahn-Hilliard equation (2.28) when $\bar{u} = 0$, $L = 800$ and $D = 1.5$.

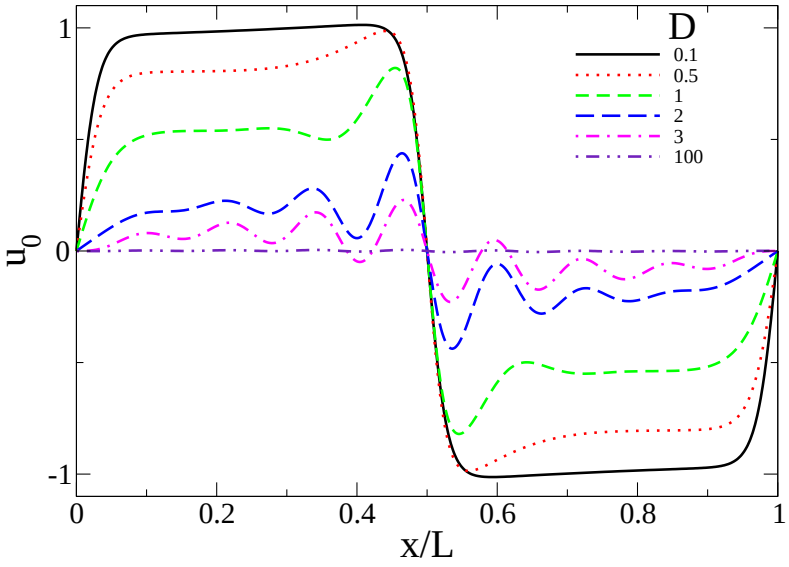

Figure 4.13: One-droplet ($n = 1$) solution profiles $u_0(x)$ of the convective Cahn-Hilliard equation (2.28) when $\bar{u} = 0$ and $L = 50$ and $v = 0$ for different values of the driving force D, as is given in the legend.

and $L = 800$. As L increases, the width of the hollow remains approximately constant, resulting in the fact that the norm $\|\delta u_0\|$ monotonically decreases.

Fig. 4.13 shows travelling-wave solution profiles $u_0(x)$ when $\bar{u} = 0$ and $L = 50$ for different values of the driving force, $D = 0.1, 0.5, 1, 2, 3$ and 100. For smaller values of D, the solution profile has a droplet shape (as was the case for $D = 0$). As D increases, we can see that the amplitude of $u_0(x)$ decreases and the droplet shape is deformed. First, there appears a ridge on top of the right-hand side of the droplet followed by a depression in the cavity. As D is increased, the ridge and the depression become more pronounced and there appear more visible oscillations. The appearance of such oscillations can be understood by the linear stability analysis of the homogeneous solutions in space given in Chapter 3, see Section 3.5.2 in particular. In that Chapter, it was shown that the droplet amplitude should scale approximately as $\sqrt{1 - D/\sqrt{2}}$ for $D < \sqrt{2}$, (since only for $D < \sqrt{2}$ we find that there exist kink solutions, which should give the left side of the droplet, and these solutions are given by the tanh formula). We also found there that when $D > \sqrt{2}/3$, the spatial linear stability analysis of the homogeneous solution $u_0 \equiv \sqrt{1 - D/\sqrt{2}}$ results in a pair of complex conjugate eigenvalues, $\lambda = \lambda_R \pm i\lambda_I$ with positive real part λ_R. The period of these oscillations is $2\pi/\lambda_I$. The oscillations decay exponentially at the rate $e^{\lambda_R x}$ as $x \to -\infty$. Similarly, the spatial

linear stability analysis of the homogeneous solution $u_0 \equiv -\sqrt{1 - D/\sqrt{2}}$ results in a pair of complex conjugate eigenvalues, $\lambda = -\lambda_R \pm i\lambda_I$, i.e., for $u_0 \equiv -1$ the period of the oscillations is the same as for $u_0 \equiv \sqrt{1 - D/\sqrt{2}}$, but these oscillations decay exponentially as $x \to \infty$ (not as $x \to -\infty$). For $D > \sqrt{2}$, we do not expect to see true droplet solutions, and, indeed, we see that the solutions presented in Fig. 4.13 for $D > \sqrt{2}$ do not have the form of a droplet.

4.4.2 Double-interface solutions of the convective Cahn-Hilliard equation for $\bar{u} = 0.4, 0.55$ and 0.6

In this section, we continue to analyse droplet solutions of the convective Cahn-Hilliard equation (2.28) with $D \neq 0$. As before, we will use both D and L as the control paramters, and we consider three different mean concentrations, $\bar{u} = 0.4$, 0.55 and 0.6, as we did for the standard Cahn-Hilliard equation. We remind that the flat solution $u = \bar{u}$ is linearly unstable when $L > L_c = 2\pi/k_c$, $k_c = \sqrt{1 - 3\bar{u}^2}$, and for $|\bar{u}| > 1/\sqrt{3}$ the flat solution $u = \bar{u}$ is linearly stable for any value of L. We find that for $\bar{u} = 0.4$ and 0.55, $L_c = 8.7$ and 20.66, respectively, and for $\bar{u} = 0.6$, the flat solution is linearly stable for any value of L. Moreover, we found in Section 4.3.2 that for $D = 0$ the primary bifurcation changes from supercritical to subcritical at $\bar{u} = \bar{u}^* = 1/\sqrt{5}$. This value should change as D changes. This is indeed the case, as will be seen in our numerical results presented below, and the exact value at which this changeover happens can be found by the weakly nonlinear analysis presented in Section 4.5.1

First, let us consider the case $\bar{u} = 0.4$, where the primary bifurcation is supercritical for $D = 0$ (when L is used as the control parameter). Fig. 4.14(a) shows the dependence of the norm $\|\delta u_0\|$ on the driving force D for different values of the domain size L as is indicated in the legend. We can see that for all the considered values of L, the norm $\|\delta u_0\|$ is a monotonically decreasing function of the driving force D. Moreover, at a fixed small value of D, the norm $\|\delta u_0\|$ monotonically increases as the domain size L increases, whereas for a fixed large value of D, $\|\delta u_0\|$ monotonically decreased as L increases. Fig. 4.14(b) shows the same results as in Fig. 4.14(a) but on a log-log scale. The red dotted line in this figure has the slope -1 on a log-log scale, which confirms that the norm tends to zero as D^{-1} as $D \to \infty$. The corresponding dependence of the wave velocity v on the driving force D is shown in Fig. 4.14(c). The dotted line (best

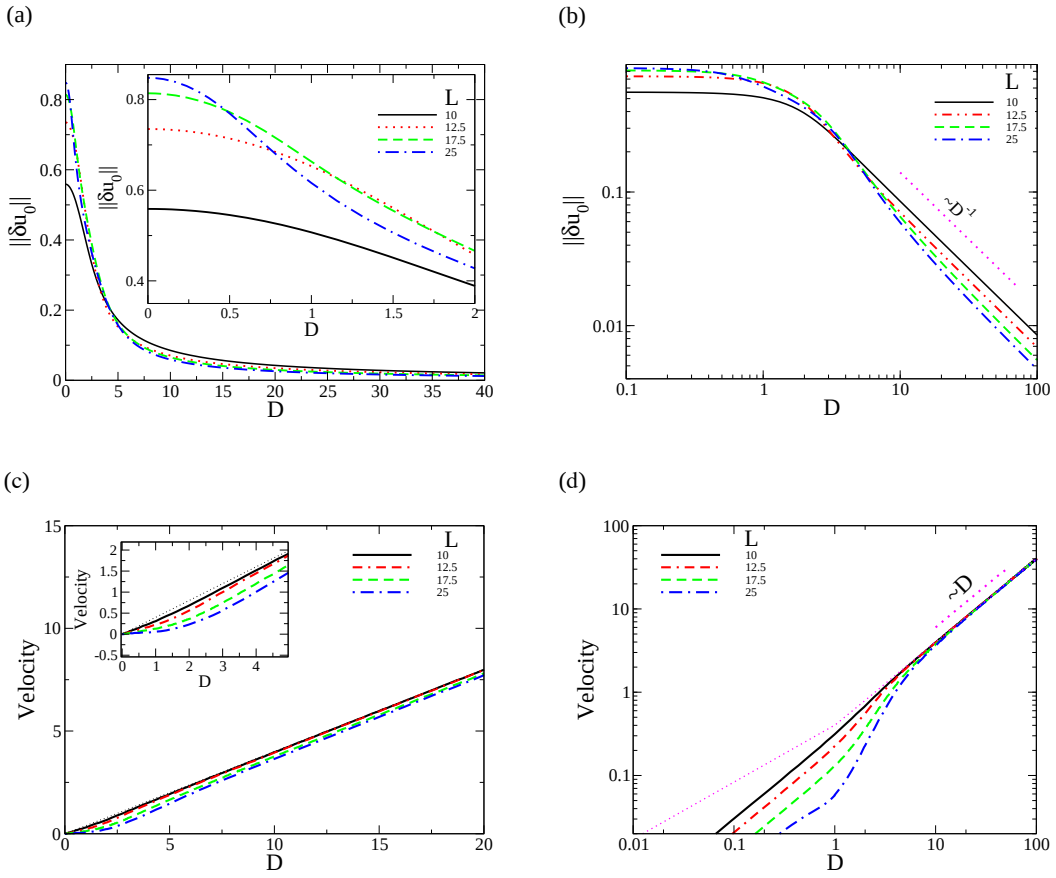

Figure 4.14: (a) The bifurcation diagram of the one-droplet ($n = 1$) solutions of the convective Cahn-Hilliard equation (2.28) for the case $\bar{u} = 0.4$ for various values of the domain size L, as is indicated in the legend. (a,b) Shown is the dependence of the norm $\|\delta u_0\|$ on the driving force D. The inset in panel (a) gives a zoom at smaller values of D. Panel (b) shows the same results as in panel (a) but on a log-log scale. The red dotted line has the slope -1 on a log-log scale and confirms that $\|\delta u_0\| \propto D^{-1}$ as $D \to \infty$ for all the values of L. (c,d) Shown is the dependence of wave velocity v on the driving force D. The inset in panel (c) gives a zoom at smaller values of D. The dotted line is the phase velocity $v = 0.4D$ as obtained from linear stability analysis. Panel (d) shows the same results as in panel (c) but on a log-log scale. The red dotted line has the slope 1 on a log-log scale and confirms that $v\| \propto D$ as $D \to \infty$ for all the values of L.

visible in the inset of Fig. 4.14(c)) is the phase velocity $v = 0.4D$ as obtained from linear stability analysis (see Section 3.2). It can be seen that this phase velocity line forms an upper bound for the other curves. We can see that the velocity is positive for all L for $\bar{u} = 0.4$ when $D > 0$. Fig. 4.14(d) shows the same results as in Fig. 4.14(c) but on a log-log scale. The red dotted line in this figure has the slope 1 on a log-log scale, and it confirms that we find $v \propto D$ for large driving force D. We know that when $\bar{u} = 0$ the velocity was equal to zero for all values of D. However, when the mean concentration $\bar{u}$ is positive, the velocity v is positive for positive values of D.

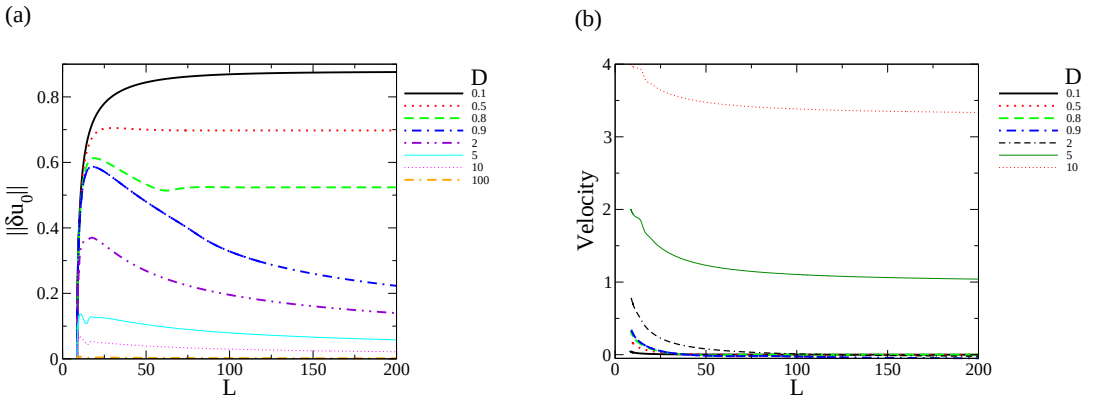

Figure 4.15: Panels (a) and (b) show the bifurcation diagrams of the one-droplet ($n = 1$) solutions of the convective Cahn-Hilliard equation (2.28) for the case $\bar{u} = 0.4$ for various values of the driving force D, as is indicated in the legend. Panel (a) shows the dependence of the norm $\|\delta u_0\|$ on the domain size L, and panel (b) shows the dependence of the wave velocity on the domain size L.

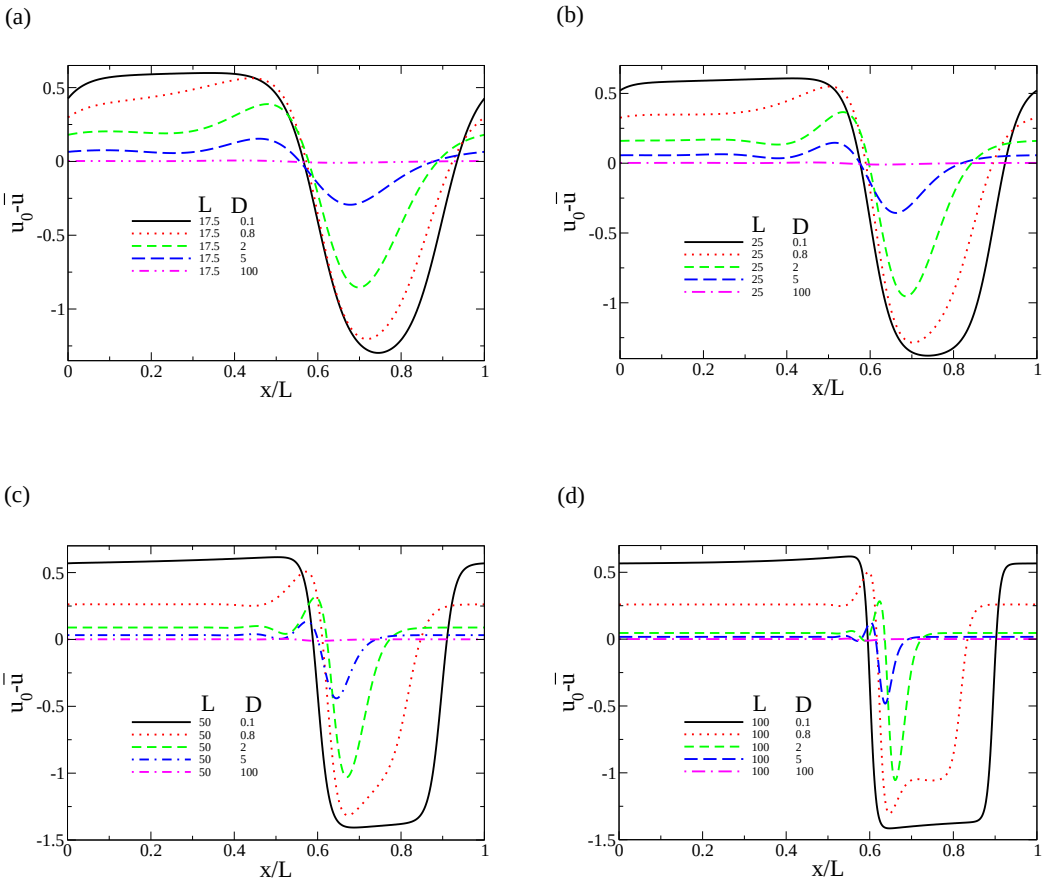

Figure 4.16: One-droplet ($n = 1$) solution profiles $u_0(x)$ of the convective Cahn-Hilliard equation (2.28) when $\bar{u} = 0.4$ and (a) $L = 17.5$, (b) $L = 25$, (c) $L = 50$, (d) $L = 100$ for different values of the driving force D, as is given in the legends.

In Fig. 4.15(a), the dependence of the norm $\|\delta u_0\|$ on the domain size, L, is shown when $\bar{u} = 0.4$ for various values of the driving force, as is indicated in the legend. We can observe that all the branches of spatially non-uniform solutions bifurcate supercritically from the homogeneous branch at $L = L_c$. This is consistent with the weakly nonlinear analysis presented in Section 4.5.1, where it is found that for $\bar{u} < 1/\sqrt{5} \approx 0.45$, the primary bifurcation is supercritical for any value of the driving force. We can also observe that for small values of D, the norm increases monotonically and tends to a constant as L increases. As D increases, the norm becomes a non-monotonic function of L but still tends to a constant as L increases (see, for example, the line for $D = 0.8$). For even larger values of D this behaviour seems to change – the norm first monotonically increases, then it may be characterised by a few oscillations, and after that it monotonically decreases. In Fig. 4.15(b), the dependence of the wave velocity on the domain size L is shown for various values of the driving force, as is indicated in the legend. We can see that in all the cases, the velocity is positive and is a monotonically decreasing function of the domain size. Fig. 4.16 shows solution profiles $u_0(x)$ when $\bar{u} = 0.4$ and (a) $L = 17.5$, (b) $L = 25$, (c) $L = 50$, (d) $L = 100$ for various values of D, as is indicated in the legend. As for the case of $\bar{u} = 0$, we can see that for smaller values of D, the solution profile has a droplet shape. As D increases, the solution becomes flatter and the droplet shape is deformed, namely, there appears a ridge on top of the right-hand side of the droplet. Also, for larger values of L, the ridge is followed by a cavity in the depression. For larger values of D, the ridge first becomes more pronounced and then decreases in the amplitude and there appear additional visible oscillations of amplitude that decays upstream. As for the case $\bar{u} = 0$, the appearance of such oscillations can be understood by the spatial linear stability analysis given in Section 3.4. Also, it can be observed that for any value of D, the width of the droplet increases as D increases and the cavity narrows down. In fact, as discussed in Chapter 3, true droplet solutions exist only for $D < \sqrt{2}$, since only for these values of D there exist kink solutions, which give the left side of the droplet. Strictly speaking, the solution profiles for $D > \sqrt{2}$ should be classified rather as anti-pulse (hollow) solutions than droplet solutions.

Next, we consider the case $\bar{u} = 0.55$, where the primary bifurcation is subcritical for $D = 0$ (when L is used as the control parameter). Fig. 4.17(a) shows the dependence of the norm $\|\delta u_0\|$ on the driving force D for different values of the domain size L, as is given in the legend. We note that for $L < L_c$ the branches start at $D = 0$, then have saddle-node bifurcations at some positive values of D, and then return to $D = 0$. As L increases, the saddle-node bifurcation shifts to the left. For $L = L_c$, the branch starts

at $D = 0$, then has one saddle-node bifurcation at a positive value of D. However, it does not go back to $D = 0$. Instead, the branch terminates at the horizontal axis, where $\|\delta u_0\| = 0$, at some positive value of the driving force, $D = D_c \approx 1.3$. For $L > L_c$, the branches start at $D = 0$, but are characterised by two saddle-node bifurcations. After the second saddle-node bifurcation, the branch continues to infinity. For sufficiently large L, both saddle-node bifurcations annihilate each other, as will be discussed in more detail later. In fact, the value D_c is precisely the value at which the primary bifurcation changes from subcritical to supercritical when the domain size L is used as the control parameter, and it can be found exactly by the weakly nonlinear analysis presented in Section 4.5.1 and is given by the formula

$$D_c = \pm\sqrt{-540\bar{u}^4 + 288\bar{u}^2 - 36}, \tag{4.41}$$

which for $\bar{u} = 0.55$ gives $D_c \approx \pm 1.3064$.

Fig. 4.17(b) shows the dependence of the wave velocity v on the driving force D when $\bar{u} = 0.55$ for different values of the domain size L, as is given in the legend. The velocity is positive for all positive values of D. Also, we can see in Fig. 4.17(b) that for $L < L_c$ the branches start at $D = 0$, monotonically increase with D, then have one saddle-node bifurcations at some positive values of D, then return to $D = 0$. For $L = L_c$, the branch starts at $D = 0$, then has one saddle-node bifurcation at a positive value of D. However, it does not return to $D = 0$ as all the curves for $L < L_c$ do. Instead, it ends in a special bifurcation at $D = D_c \approx 1.3$. Note that this bifurcation is not visible in a linear stability analysis but has to be described with weakly nonlinear methods. The branch terminates at $v = 0.55D_c$ (phase velocity). For $L > L_c$, the branches start at $D = 0$, however, they are characterised by two saddle-node bifurcations. After the second saddle-node bifurcation, the branches continue to infinity approaching the line $v = 0.55D$ at large values of D.

In Fig. 4.18(a), the dependence of the norm $\|\delta u_0\|$ on the domain size L is shown for $\bar{u} = 0.55$ and for various values of the driving force D, as is indicated in the legend. We can observe that the primary bifurcation is subcritical for $D \lesssim 1.3$ while it is supercritical for $D \gtrsim 1.3$. This is consistent with the weakly nonlinear analysis presented in Section 4.5.1. When $D \lesssim 1.3$, there is only one saddle-node bifurcation. On the other hand, when $D \gtrsim 1.3$, there are two saddle-node bifurcation – the branch bifurcates supercritically from the uniform solution, then turns back at the first saddle-node

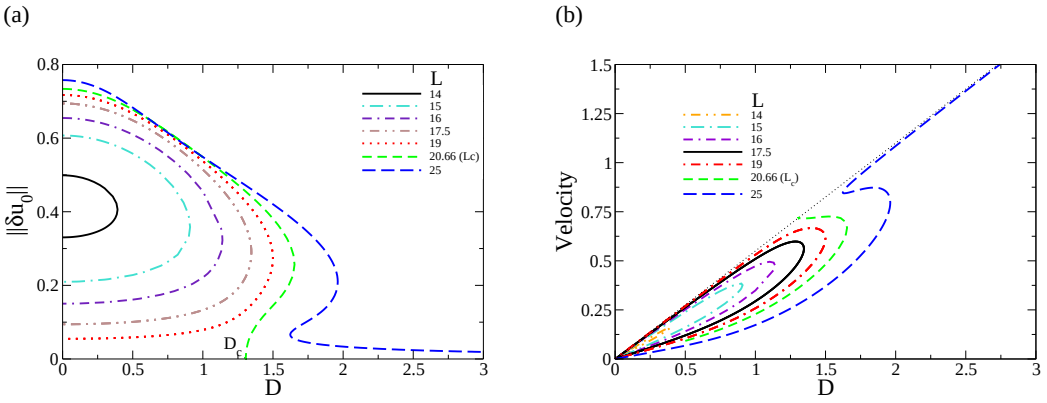

Figure 4.17: Panels (a) and (b) show the bifurcation diagrams of the one-droplet ($n = 1$) solutions of the convective Cahn-Hilliard equation (2.28) for the case $\bar{u} = 0.55$ for various values of the domain size L, as is indicated in the legend. Panel (a) shows the dependence of the norm $\|\delta u_0\|$ on the driving force D, and panel (b) shows the dependence of the wave velocity on the driving force D.

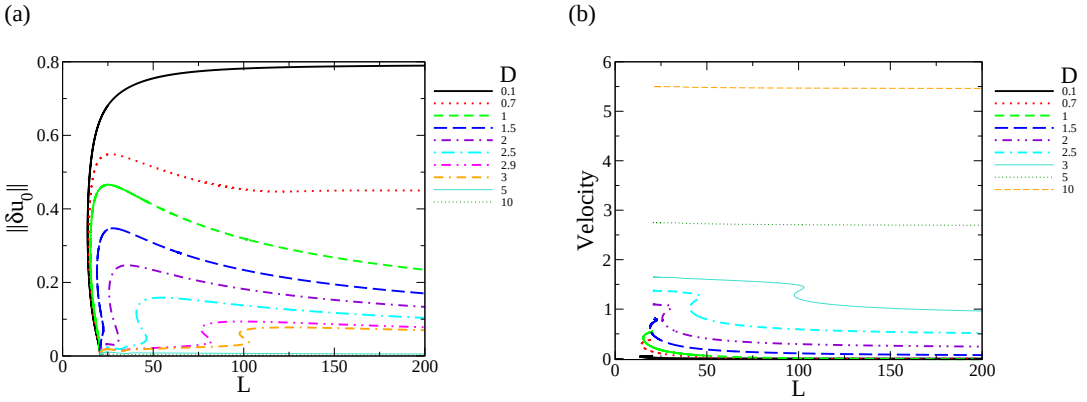

Figure 4.18: Panels (a) and (b) show the bifurcation diagrams of the one-droplet ($n = 1$) solutions of the convective Cahn-Hilliard equation (2.28) for the case $\bar{u} = 0.55$ for various values of the driving force D, as is indicated in the legend. Panel (a) shows the dependence of the norm $\|\delta u_0\|$ on the domain size L, and panel (b) shows the dependence of the wave velocity on the domain size L.

bifurcation, and then turns again at the second saddle-node bifurcation and continues off to infinity. This is consistent with the results presented in Fig. 4.17(a), which show that for moderately large values of L that are greater than L_c there exist three different solutions for a certain range of the driving force D. For all D, at large L the norms $\|\delta u_0\|$ approach constant values. Fig. 4.18(b) shows the corresponding dependence of the wave velocity on the domain size L for various values of the driving force D. We can see that the velocity is positive for all D. Also, we can see that when the driving force D increases the velocity increases. In addition, we observe that for all D, at large L the velocity approaches a constant value.

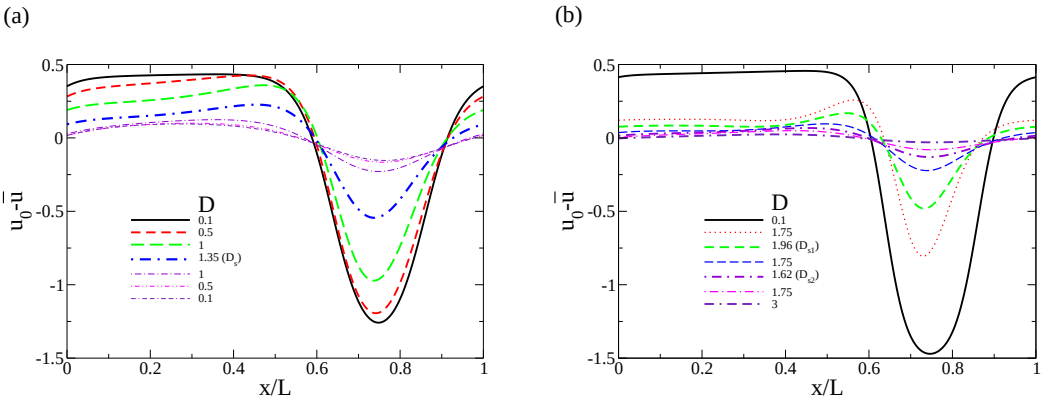

Figure 4.19: One-droplet ($n = 1$) solution profiles $u_0(x)$ of the convective Cahn-Hilliard equation (2.28) when $\bar{u} = 0.55$ and (a) $L = 17.5$ and (b) $L = 25$ for different values of the driving force D, as is given in the legends.

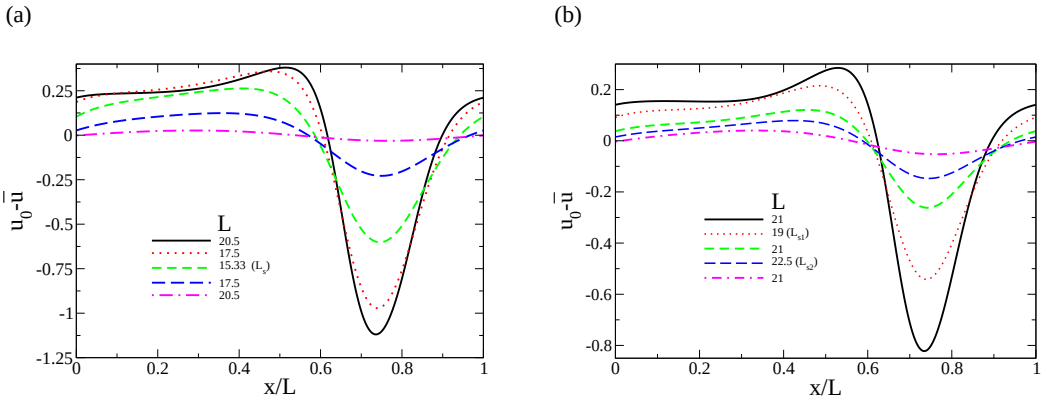

Figure 4.20: One-droplet ($n = 1$) solution profiles $u_0(x)$ of the convective Cahn-Hilliard equation (2.28) when $\bar{u} = 0.55$ and (a) $D = 1$ and (b) $D = 1.5$ for different values of the domain size L, as is given in the legends.

Fig. 4.19 shows solution profiles $u_0(x)$ when $\bar{u} = 0.55$ and (a) $L = 17.5$ and (b) $L = 25$ for various values of D, as is indicated in the legend. In Fig. 4.19(a), we can see two different solutions at the same values of D before the saddle-node bifurcation that occurs at $D_s \approx 1.35$. For $D = 0.1$, 0.5 and 1, the solutions with larger amplitudes belong to the upper part of the branch shown in panel (a) of Fig. 4.17 and are stable, whereas solutions with smaller amplitudes belong to the lower part of this branch and are unstable. In Fig. 4.19(b), we can see three different solutions at the same values of D between the two saddle-node bifurcations that occur at $D_{s1} \approx 1.96$ and $D_{s2} \approx 1.62$. For $D = 1.75$ the solutions with larger and the smaller amplitudes belong to the upper and the lower parts of the branch shown in panel (b) of Fig. 4.17 and are stable, whereas the solution with the intermediate value of the amplitude belongs to the middle part of the branch and is unstable. As D increases further, we can see that the solution becomes flatter, and the ridge that was pronounced for smaller values of D decreases in

amplitude. We also remind here that the solution profiles that we observe for $D > \sqrt{2}$ and sufficiently large L should be classified as rather anti-pulse (hollow) solutions than droplet solutions.

Fig. 4.20 shows the travelling-wave solution profiles $u_0(x)$ when $\bar{u} = 0.55$ and (a) $D = 1$ and (b) $D = 1.5$. In Fig. 4.20(a), we can see two different solutions at the same values of L between the cutoff value $L_c \approx 20.66$ and the the saddle-node bifurcation that occurs at $L_s \approx 15.3$. For $L = 17.5$ and 20.5, the solutions with larger amplitudes belong to the upper part of the branch shown in panel (a) of Fig. 4.18 and are stable, whereas solutions with smaller amplitudes belong to the lower part of this branch and are unstable. In Fig. 4.20(b), we can see three different solutions at the same value of $L = 21$ between the two saddle-node bifurcations that occur at $L_{s1} \approx 19.00$ and $L_{s2} \approx 22.5$. The solutions with larger and the smaller amplitudes belong to the upper and the lower parts of the branch shown in panel (b) of Fig. 4.18 and are stable, whereas the solution with the intermediate value of the amplitude belongs to the middle part of the branch and is unstable.

Finally, we consider the case $\bar{u} = 0.6$, where there is no primary bifurcation and the uniform solution is stable (when L is used as the control parameter). Fig. 4.21(a) shows the dependence of the norm $\|\delta u_0\|$ on the driving force D for different values of the domain size L as is indicated in the legend. We can see that for all the considered values of L, the branches start at $D = 0$, then have one saddle-node bifurcation at some positive values of D, and then the branches return to $D = 0$. The corresponding dependence of the wave velocity v on the driving force D is shown in Fig. 4.21(b). The inset shows a zoom at smaller values of D. The dotted line is the phase velocity $v = 0.6D$ as obtained from linear stability analysis (see Section 3.2). It can be seen that this phase velocity line forms an upper bound for the other curves. We can see that the velocity is positive for all L for $\bar{u} = 0.6$ when $D > 0$. For all the considered values of L, the branches start at $D = 0$ where $v = 0$, then have one saddle-node bifurcation at some positive value of D, and then the branches returns to $D = 0$ where $v = 0$.

In Fig. 4.22(a), the dependence of the norm $\|\delta u_0\|$ on the domain size L is shown for $\bar{u} = 0.6$ and for various values of the driving force D, as is indicated in the legend. There are no primary bifurcations for all the values of D, and we always find a saddle-node bifurcation. We can see that for smaller values of D, the upper parts of the branches monotonically increase as L increases, whereas for larger value of D, the upper parts of

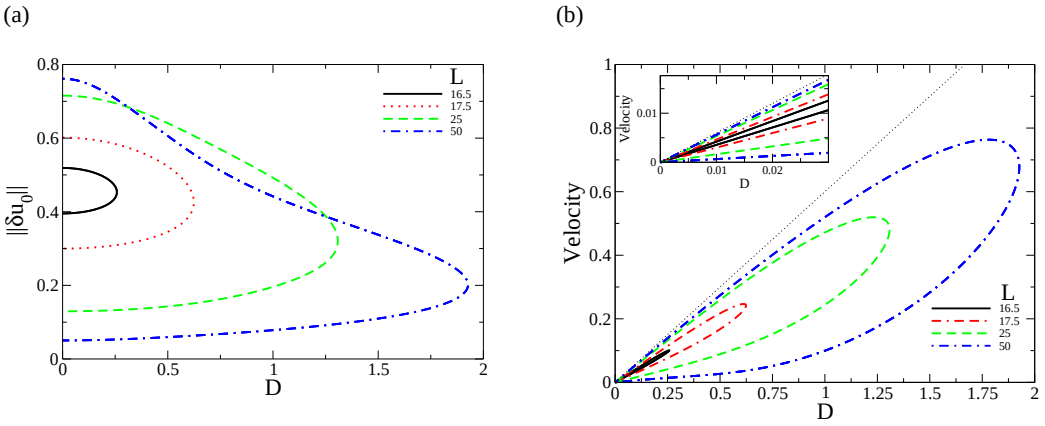

Figure 4.21: Panels (a) and (b) show the bifurcation diagrams of the one-droplet ($n = 1$) solutions of the convective Cahn-Hilliard equation (2.28) for the case $\bar{u} = 0.6$ for various values of the domain size L, as is indicated in the legend. Panel (a) shows the dependence of the norm $\|\delta u_0\|$ on the driving force D, and panel (b) shows the dependence of the wave velocity on the driving force D.The dotted line is $v = 0.6D$. The inset gives a zoom at smaller values of D.

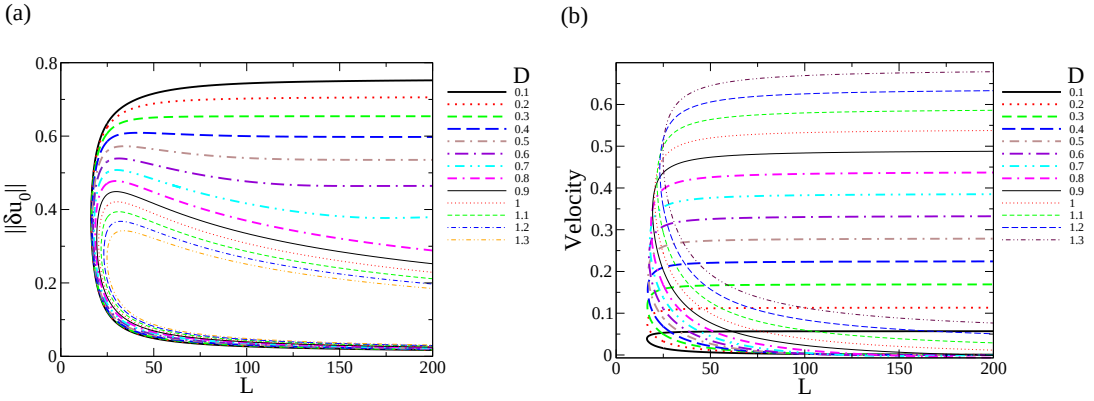

Figure 4.22: Panels (a) and (b) show the bifurcation diagrams of the one-droplet ($n = 1$) solutions of the convective Cahn-Hilliard equation (2.28) for the case $\bar{u} = 0.6$ for various values of the driving force D, as is indicated in the legend. Panel (a) shows the dependence of the norm $\|\delta u_0\|$ on the domain size L, and panel (b) shows the dependence of the wave velocity on the domain size L.

the branches first monotonically increase and then monotonically decrease. Fig. 4.22(b) shows the corresponding dependence of the wave velocity on the driving force D. The velocity is positive for all the values of D. As expected, all the branches have saddle-nodes. The upper parts of the branches monotonically increase as L increases, whereas the lower parts of the branches monotonically decrease as L increases.

Fig. 4.23(a) shows solution profiles $u_0(x)$ when $\bar{u} = 0.6$ and $L = 25$ for various values of D, as is indicated in the legend. In this case, we have two different solutions at same value of D before the saddle-node bifurcation that occurs at $D_s \approx 1.31$. In particular, for $D = 0.1$, 0.5 and 1 the solutions with larger amplitudes belong to the upper part of the branch for $L = 25$ shown in the panel (a) of Fig. 4.21 (these solutions are stable),

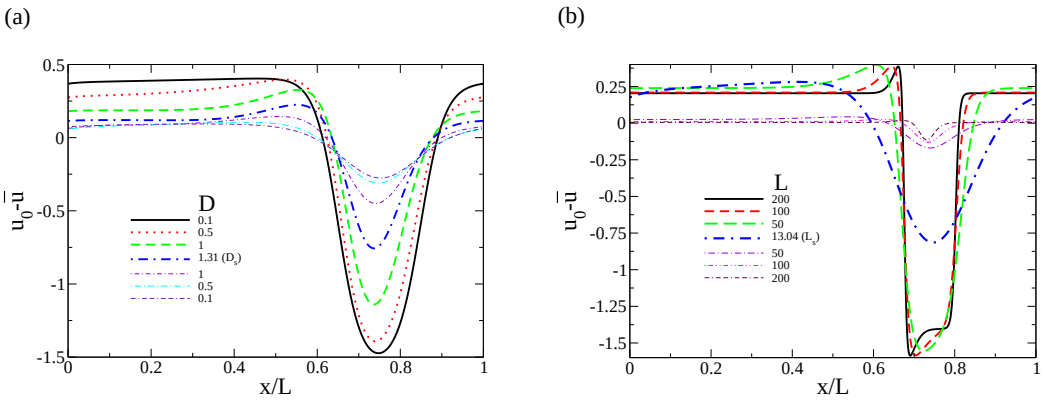

Figure 4.23: One-droplet ($n = 1$) solution profiles $u_0(x)$ of the convective Cahn-Hilliard equation (2.28) when $\bar{u} = 0.6$ and (a) $L = 25$ and for various values of the driving force D, as is given in the legend, and (b) $D = 0.5$ and for different values of the domain size L, as is given in the legend.

whereas solutions with smaller amplitudes belong to the lower part of this branch (these solutions are unstable).

Fig. 4.23(b) shows solution profiles $u_0(x)$ when $\bar{u} = 0.6$ and $D = 0.5$ for various values of L, as is indicated in the legend. In this case, we have two different solutions at same value of L after the value of saddle-node bifurcation, $L_s \approx 13.04$. For $L = 50$, 100 and 200 the solutions with larger amplitudes belong to the upper part of the branch for $D = 0.5$ shown in panel (a) of Fig. 4.22 (these solutions are stable), whereas the solutions with smaller amplitudes belong to the lower part of this branch (these solutions are unstable). We can see that the solutions of the upper part of the branch have droplet shapes and for larger values of L are characterised by a ridge on top of the right-hand side of the droplet that is followed by a depression in the cavity, whereas the solutions of the lower part of the branch become flatter as L increases.

From panel (a) of Fig. 4.17, it is difficult to infer where exactly the saddle-nodes appear. To understand this process better, we follow in Fig. 4.24(a) the loci of saddle-node bifurcations of Fig. 4.17 (i.e., for $\bar{u} = 0.55$) in the (D, L)-plane. The horizontal dotted line indicates the cutoff period $L_c = 2\pi/k_c$ for the linear stability of uniform solution $\bar{u} = 0.55$. We see that for $L < L_c$ there is only one saddle-node bifurcation. On the other hand, for $L > L_c$, there are two saddle-node bifurcations. For sufficiently large L, the two saddle-node bifurcations annihilate each other. Fig. 4.24(b) shows the loci of saddle-node bifurcations for $\bar{u} = 0.6$ in the (D, L) plane. We see that for all the values of $L \geq L_{sn}$ where L_{sn} is the locus of the saddle-node bifurcation at $D = 0$ (cf.

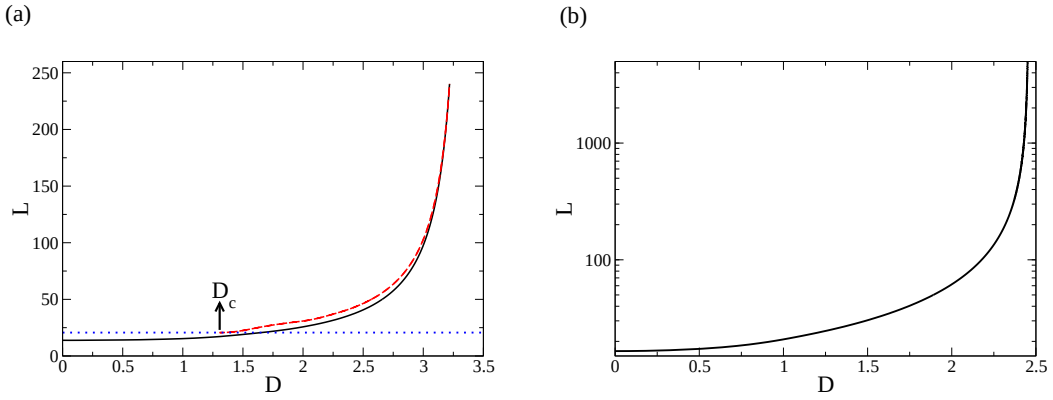

Figure 4.24: The loci of saddle-node bifurcations on the one-droplet ($n = 1$) solution branches in the (D, L)-plane at (a) $\bar{u} = 0.55$ and (b) $\bar{u} = 0.6$. The horizontal dotted line in panel (a) indicates the cutoff period $L_c = 2\pi/k_c$ for the linear stability of the uniform solution $\bar{u} = 0.55$.

Fig. 4.7), there is one saddle-node bifurcation. For $\bar{u} = 0.4$ there are no saddle-node bifurcations, so we cannot plot the loci of saddle-node bifurcation.

4.4.3 Single-interface solutions of the convective Cahn-Hilliard equation

In Chapter 3, see in particular Section 3.5.1, it was discussed that for the standard Cahn-Hilliard equations there exist single interface solutions given by the $\tanh$ profiles, namely,

$$u_0(x) = \pm \tanh\left(\frac{x}{\sqrt{2}}\right). \tag{4.42}$$

In this Section, we are interested in analysing how the introduction of the driving force affects these solutions. We will be interested in analysing both kink and anti-kink solutions, which correspond to the positive/negative signs in (4.42).

4.4.3.1 Kink solutions

For kink solutions, we in fact know an analytical formula given in Section 2.4, namely, such solutions are given by

$$u_0(x) = \bar{u}_a \tanh\left(\frac{\bar{u}_a}{\sqrt{2}}x\right), \tag{4.43}$$

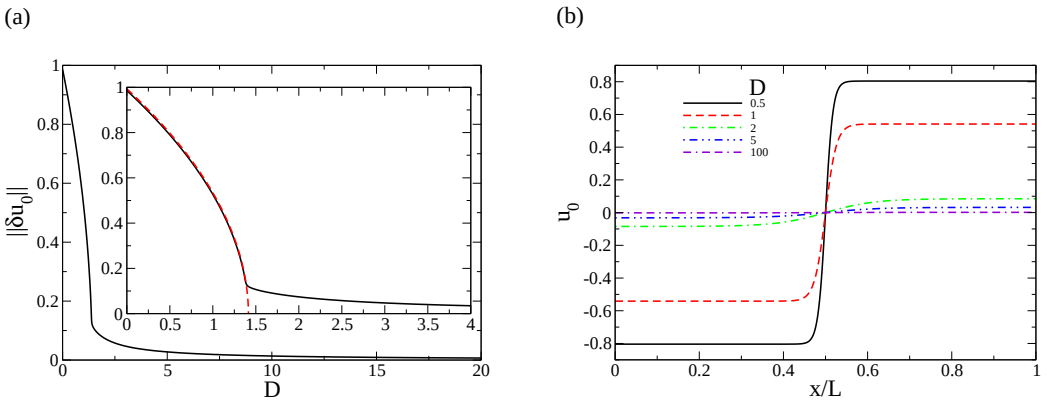

Figure 4.25: (a) The bifurcation diagram of the kink solutions of the convective Cahn-Hilliard equation (2.28) when $L = 100$ showing the dependence of the norm $\|\delta u_0\|$ on the driving force D. The inset gives a zoom at smaller values of D. The red dashed line in the inset shows the dependence of the norm of the exact analytical solution (4.43) on D. (b) Kink solution profiles $u_0(x)$ of the convective Cahn-Hilliard equation (2.28) when $L = 200$ for different values of the driving force D, as is given in the legend.

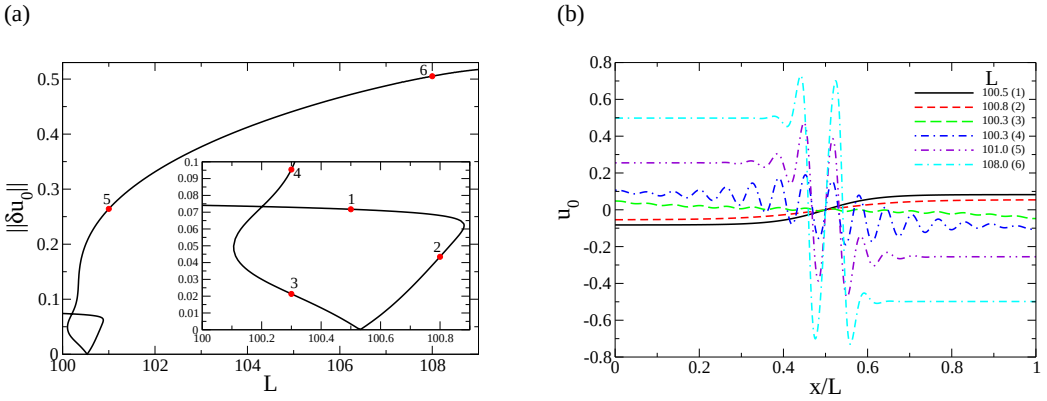

Figure 4.26: (a) The bifurcation diagram of the kink/anti-kink solutions of the convective Cahn-Hilliard equation (2.28) when $D = 2$ showing the dependence of the norm $\|\delta u_0\|$ on the domain size L. (b) The solution profiles $u_0(x)$ of the convective Cahn-Hilliard equation (2.28) for $D = 2$ for different values of the domain size L, as is given in the legend, corresponding to points 1–5 in panel (a).

where $\bar{u}_a = \sqrt{1 - D/\sqrt{2}}$, and for which $v = 0$. Moreover, the linear stability analysis presented in Chapter 3 implies that for each value of $D \in [0, \sqrt{2})$ there exist a unique kink solution in some neighbourhood of the solution (4.43). These observations are supported by our numerical results. We use the numerical procedure described in Section 4.2.2. The results of our numerical calculations are shown in Fig. 4.25. The calculations are performed on the domain of size $L = 100$, and the truncated analytical solution (4.42) is used as the starting solution. Fig. 4.25(a) shows the dependence of the norm $\|\delta u_0\|$ on the driving force D. We can see that the norm decays monotonically as D increases and has a sharp change in the behaviour at $D \approx \sqrt{2}$. Notice that the true analytical solution (4.43) exists only for $D \in [0, \sqrt{2})$, and the norm of this solution on the domain of size L is shown by the red dashed line and is given by the formula

$$\sqrt{\bar{u}_a^2 - \frac{\sqrt{2}\,\bar{u}_a}{L} \tanh\left(\frac{\bar{u}_a L}{\sqrt{2}}\right)}. \tag{4.44}$$

(Of course, it converges to $\bar{u}_a = \sqrt{1 - D/\sqrt{2}}$ as $L \to \infty$.) We can notice that the branch corresponding to the numerical solutions is very close to the branch corresponding to the analytical solutions, but does not terminate at $D = \sqrt{2}$ but instead is connected to a branch of a solutions of a different type. This is due to the finite size of the domain. The larger the domain size is, the closer to each other the branches are. Note also the similarity of the numerically computed branch presented in this figure to the branches presented in Figs. 4.9(a) and 4.10. Fig. 4.25(b) shows selected solutions at different values of D, and is given in the legend.

A confirmation that the numerically computed solutions for $D > \sqrt{2}$ do not correspond to kink solutions is given in Fig. 4.26. In this figure, we take the solution computed in Fig. 4.25 corresponding to $D = 2$ and perform a continuation starting from it in the domain size L. Fig. 4.25(a) shows the branch of the computed solutions and the inset shows the zoom onto the region of the values of L close to 100. It can be seen that the branch of the solutions first monotonically decreases and has a saddle node at $L \approx 100.85$ after which it continues to monotonically decrease until the point $L \approx 100.53$ where $\|\delta u_0\| \approx 0$. We note that the linear stability analysis discussed in Chapter 3 predicts that for $\bar{u} = 0$ there is a bifurcation of the uniform solution solution at $L = 2\pi$, and a periodic solution emerges. We note that 100.53 turns out to be a value that is close to an integer multiple of the period of this periodic solution, namely $100.53 \approx 32\pi$. This means that when the domain size equals to 32π, the uniform solution has a bifurcation, and a periodic solution of the period approximately equal to 2π emerges

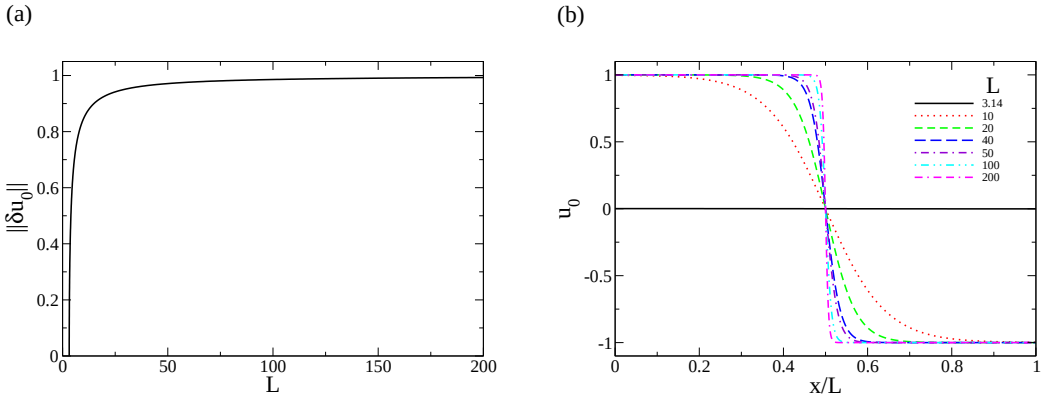

Figure 4.27: (a) The bifurcation diagram of the anti-kink solutions of the standard Cahn-Hilliard equation (2.28), when $D = 0$, for $C_0 = 0$ and $v = 0$, showing the dependence of the norm $\|\delta u_0\|$ on the domain size L. (b) Anti-kink solution profiles $u_0(x)$ of the standard Cahn-Hilliard equation (2.28), when $D = 0$, for different values of the domain size L, as is given in the legend.

(so there are 16 waves in the domain of size 32π). We note, however, that for the computation of kink solutions, we do not impose periodic boundary conditions, but use conditions prescribing the solution values at the left and right end points and requiring that u_0' and u_0'' vanish at the end points. Presumably, for these conditions there still exists a solution that is close to the 2π-periodic solution. It turns out that our numerical continuation code is able to pass onto a branch of such solutions, and this happens at $L \approx 32\pi$. After this point, the branch monotonically increases, reaches a saddle node at $L \approx 100.1$ and continues to monotonically increase. The enumerated red dots from 1 to 6 in Fig. 4.26(a) correspond to $L = 100.5, 100.8, 100.3, 100.3, 101, 108$, respectively, and the corresponding solution profiles are shown in Fig. 4.26(b). It can be seen that up to the point where the branch starts to monotonically increase the solutions resemble kink solutions but have a widening front and a decreasing amplitude. After this point, the nature of the solutions changes and the value at the left end-point of the interval becomes larger than the value at the right end point. Additionally, we observe that right after this point, the solutions are characterised by oscillations, and, to be precise, we observe 16 local maxima or minima, which is in agreement with our earlier observation. For larger values of L, the solutions converge to an anti-kink solution with an additional oscillation in-between.

4.4.3.2 Anti-kink solutions

To compute anti-kink solutions, it is possible to start from a half of a small-amplitude cosine wave of the cutoff wavelength, as is explained in Section 4.2.2. Fig. 4.27 shows the results of such a calculation for $D = 0$ (although this value of D corresponds to the standard Cahn-Hilliard equation, we use this value of D to start our discussion of numerically computed anti-kink solutions). The domain size is used as the control parameter and the left-end and the right-end values $\bar{u}_a$ and $\bar{u}_b$, respectively, are adapted in the calculation. The velocity v and the flux C_0 are fixed at zero. Fig. 4.27(a) shows the bifurcation diagram for the norm $\|\delta u_0\|$ of the solution, which, as expected, is a monotonically increasing function of L, and resembles the bifurcation diagram given in Fig. 4.1. The solution profiles for the different values of L shown in Fig. 4.27(b) converge to the $\tanh$ profile (4.42), as expected, with $\bar{u}_a \approx 1$ and $\bar{u}_b \approx -1$.

Then, we select a solution for $L = 200$ and perform a continuation in the driving force D, keeping $\bar{u}_a$ and $\bar{u}_b$ fixed and using the velocity v and the flux C_0 as the additional continuation parameters. The results are shown in Fig. 4.28. Panel (a) of this figure shows the dependence of the norm $\|\delta u_0\|$ on the driving force D. We can see that it is a monotonically increasing function of D that approaches a constant value. We note that the velocity v turns out to be zero in this calculation (up to a numerical noise), and we do not show such a graph here. Fig. 4.28(b) shows two solution profiles for $D = 0.8$ (black solid line) and $D = 5$ (red dashed line). We note that the linear stability theory presented in Section 3.4 implies that for $D < 2^{5/2}/3^{3/2} \approx 1.0887$ all the eigenvalues for both $\bar{u}_a = 1$ and $\bar{u}_b = -1$ are real. Therefore, the solution should approach the constants $\bar{u}_a$ and $\bar{u}_b$ exponentially and monotonically as $e^{\lambda_a x}$ and $e^{\lambda_b x}$, for $x \to \mp\infty$, respectively, where λ_a is the smallest of the positive eigenvalues of $\bar{u}_a$ and $\lambda_b = -\lambda_a$ is the smallest in absolute value of the negative eigenvalues of $\bar{u}_b$. A confirmation of this is given in Fig. 4.29(a) showing $|u_0(x) - \bar{u}_a|$ over x/L on a log-log scale for $D = 0.8$. It turns out that for this value of D the smallest of the positive eigenvalues of $\bar{u}_a$ is 0.4437, and the red dashed line in Fig. 4.29(a) corresponds to $Ae^{0.4437\,x}$ (for a suitable value of A). We can observe a perfect agreement between the slopes of the computed solution and the theoretical prediction. For $D > 2^{5/2}/3^{3/2}$, the solution should approach the constants $\bar{u}_a$ and $\bar{u}_b$ in an oscillatory manner with the amplitude of oscillations decaying exponentially. More precisely the solutions should behave as $e^{(\mathrm{Re}\,\lambda_a)x}\cos(\mathrm{Im}\,\lambda_a x + \phi_a)$ when $x \to -\infty$, where λ_a is one of the two complex conjugate eigenvalues for $\bar{u}_a$ with a positive real

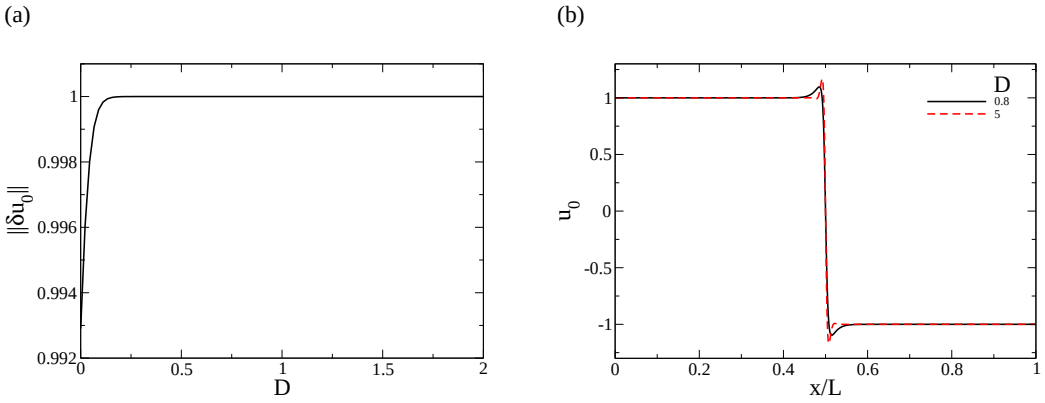

Figure 4.28: (a) The bifurcation diagram of the anti-kink solutions of the convective Cahn-Hilliard equation (2.28) when $L = 200$ for $\bar{u}_a = 1$ and $\bar{u}_b = -1$ showing the dependence of the norm $\|\delta u_0\|$ on the driving force D. (b) Anti-kink solution profiles $u_0(x)$ of the convective Cahn-Hilliard equation (2.28) when $L = 200$, $\bar{u}_a = 1$ and $\bar{u}_b = -1$ for $D = 0.8$ (black solid line) and $D = 5$ (red dashed line).

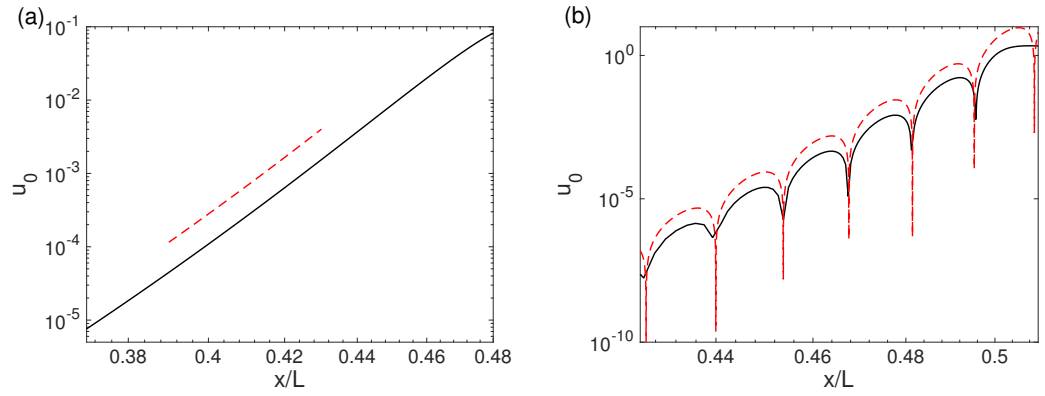

Figure 4.29: (a) Shown is $|u_0(x) - \bar{u}_a|$ on a log-log scale, where $u_0(x)$ is the anti-kink solution of the convective Cahn-Hilliard equation (2.28) for $L = 200$ and $D = 0.8$ (Fig. 4.28(b), black solid line). The red dashed line shows $Ae^{\lambda_a x}$ (for a suitable value of A), where $\lambda_a \approx 0.4437$ is the theoretically predicted eigenvalue. (b) Shown is $|u_0(x) - \bar{u}_a|$ on a log-log scale, where $u_0(x)$ is the anti-kink solution of the convective Cahn-Hilliard equation (2.28) for $L = 200$ and $D = 5$ (Fig. 4.28(b), red dashed line). The red dashed line shows $Ae^{(\mathrm{Re}\,\lambda_a)x}|\cos((\mathrm{Im}\lambda_a)x + \phi_a)|$ (for suitable values of A and ϕ_a), where $\lambda_a \approx 1.0473 + 1.1359\,i$ is the theoretically predicted eigenvalue.

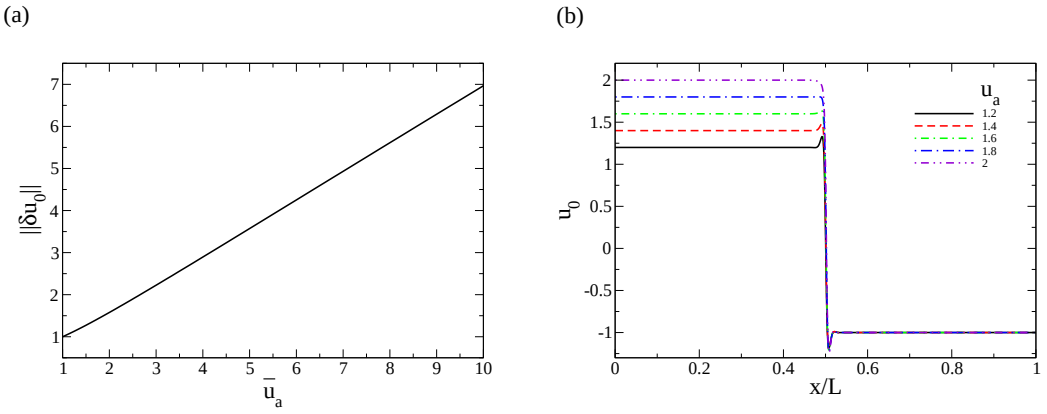

Figure 4.30: (a) The bifurcation diagram of the anti-kink solutions of the convective Cahn-Hilliard equation (2.28) when $L = 200$, $D = 5$ and $\bar{u}_b = -1$ showing the dependence of the norm $\|\delta u_0\|$ on $\bar{u}_a$. (b) Anti-kink solution profiles $u_0(x)$ of the convective Cahn-Hilliard equation (2.28) when $L = 200$, $D = 5$ and $\bar{u}_b = -1$ for different values of $\bar{u}_a$, as is given in the legend.

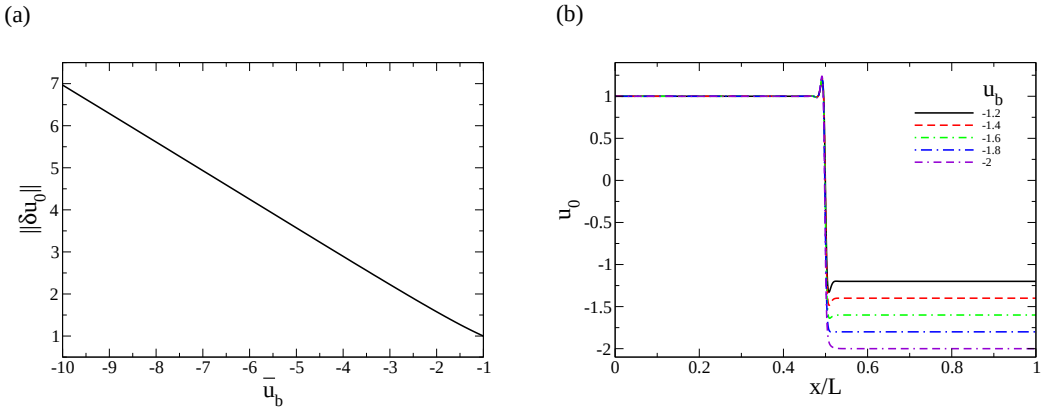

Figure 4.31: (a) The bifurcation diagram of the anti-kink solutions of the convective Cahn-Hilliard equation (2.28) when $L = 200$, $D = 5$ and $\bar{u}_a = 1$ showing the dependence of the norm $\|\delta u_0\|$ on $\bar{u}_b$. (b) Anti-kink solution profiles $u_0(x)$ of the convective Cahn-Hilliard equation (2.28) when $L = 200$, $D = 5$ and $\bar{u}_a = 1$ for different values of $\bar{u}_b$, as is given in the legend.

part and ϕ_a is an appropriate phase shift, and as $e^{(\mathrm{Re}\,\lambda_b)x}\cos(\mathrm{Im}\,\lambda_b x + \phi_b)$ when $x \to \infty$, where $\lambda_b = -\lambda_a$ is one of the two complex conjugate eigenvalues for $\bar{u}_b$ with a negative real part and ϕ_b is an appropriate phase shift. A confirmation of this is given in Fig. 4.29(b) showing $|u_0(x) - \bar{u}_a|$ over x/L on a log-log scale for $D = 5$. It turns out that for this value of D the complex conjugate eigenvalues of $\bar{u}_a$ are $1.0473 \pm 1.1359\,i$, and red dashed line in Fig. 4.29(b) corresponds to $Ae^{1.0473\,x}|\cos(1.1359\,x + \phi_a)|$ (for suitable values of A and ϕ_a). We can observe a perfect agreement between both the rate of the decay and the periods of the oscillations of computed solution and the theoretical prediction.

Finally, we remind that, unlike for kink solutions, for anti-kink solutions there is a freedom in changing the values of $\bar{u}_a$ and $\bar{u}_b$. A confirmation of this is given in Figs. 4.30 and 4.31. Fig. 4.30 corresponds to a continuation in $\bar{u}_a$ with $\bar{u}_b$ being fixed at -1 when $L = 200$ and $D = 5$. Panel (a) of this figure shows the dependence of the norm $\|\delta u_0\|$ on $\bar{u}_a$, and panel (b) shows several anti-kink solution profiles for different value of $\bar{u}_a$, as is given in the legend. Fig. 4.31 corresponds to a continuation in $\bar{u}_b$ with $\bar{u}_a$ being fixed at 1 when $L = 200$ and $D = 5$. Panel (a) of this figure shows the dependence of the norm $\|\delta u_0\|$ on $\bar{u}_a$, and panel (b) shows several anti-kink solution profiles for different value of $\bar{u}_b$, as is given in the legend.

4.5 Weakly nonlinear analysis

4.5.1 Weakly nonlinear analysis for the general convective Cahn-Hilliard-type equation with scaling 1

The aim of this section is to analyse the primary bifurcation for the convective Cahn-Hilliard equation when the domain size is used as the control parameter and all the other parameters are fixed. In particular, we wish to derive an amplitude equation for the first linearly unstable mode in the vicinity of the bifurcation point. In order to obtain such an equation, we perform a weakly non-linear analysis. To extend our analysis, we consider the general convective Cahn-Hilliard-type equation that in the frame moving at constant velocity v in the x-direction has the form

$$u_t = vu_x - D[\chi(u)]_x + \left[Q(u)\left(\frac{\delta F(u)}{\delta u}\right)_x\right]_x, \tag{4.45}$$

where $D\chi(u)$ is the driving force term with D being the driving force strength (for the standard Cahn-Hilliard equation is $\chi(u) = u^2/2$), $Q(u)$ is the mobility (that will be assumed to be non-negative for any u) and $F[u]$ is the free energy functional given by

$$F[u] = \int \varphi(u, u_x)dx, \tag{4.46}$$

with $\varphi(u, u_x)$ denoting the free energy density and given by

$$\varphi(u, u_x) = f(u) + \frac{1}{2}u_x^2. \tag{4.47}$$

Here $f(u)$ is the local free energy that for the standard Cahn-Hilliard equation is

$$f(u) = \frac{1}{4}u^4 - \frac{1}{2}u^2. \tag{4.48}$$

Note that

$$\frac{\delta F[u]}{\delta u} = f'(u) - u_{xx}, \tag{4.49}$$

which for the standard Cahn-Hilliard equation becomes

$$\frac{\delta F[u]}{\delta u} = u^3 - u^2 - u_{xx}. \tag{4.50}$$

Next, let us consider a uniform solution $\bar{u}$ and add a small perturbation to it, i.e., we write $u(x,t) = \bar{u} + w(x,t)$ and substitute it into equation (4.45). Then we obtain the following equation for $w(x,t)$:

$$w_t = vw_x - D\chi'(\bar{u} + w)w_x + [Q(\bar{u} + w)(f'(\bar{u} + w) - w_{xx})_x]_x. \tag{4.51}$$

Assuming that $w = \epsilon\tilde{w}$, where $|\epsilon| \ll 1$, we obtain the following linearised equation:

$$\tilde{w}_t = v\tilde{w}_x - D\chi'(\bar{u})\tilde{w}_x + [Q(\bar{u})(f'(\bar{u}) - \tilde{w}_{xx})_x]_x. \tag{4.52}$$

By substituting $\tilde{w} = e^{\beta t + ikx}$ in equation (4.52), we obtain the following dispersion relation:

$$\beta = ivk - iD\chi'(\bar{u})k - Q(\bar{u})f''(\bar{u})k^2 - Q(\bar{u})k^4. \tag{4.53}$$

The real and imaginary parts of this dispersion relation are

$$\mathrm{Re}(\beta) = -Q(\bar{u})f''(\bar{u})k^2 - Q(\bar{u})k^4, \tag{4.54}$$

$$\mathrm{Im}(\beta) = vk - D\chi'(\bar{u})k. \tag{4.55}$$

The condition $\mathrm{Im}(\beta) = 0$ gives $v = D\chi'(\bar{u})$, which is the velocity of the moving frame in which small-amplitude sinusoidal solutions are stationary. The condition $\mathrm{Re}(\beta) = 0$ determines the cutoff wavenumber, or, equivalently, the cutoff domain size corresponding to the primary bifurcation. Indeed, assuming that $Q(\bar{u}) \neq 0$ and $f''(\bar{u}) < 0$, we find that the cutoff wavenumber is $k_c = \sqrt{-f''(\bar{u})}$ (i.e., the cutoff domain size is $L_c = 2\pi/k_c$), namely, the following holds:

- if $k > k_c$ (or $L < L_c$), then $\beta < 0$ and the corresponding mode is linearly stable,
- if $k < k_c$ (or $L > L_c$), then $\beta > 0$ and the corresponding mode is linearly unstable.

Substituting $v = D\chi'(\bar{u})$ in equation (4.51), we obtain

$$\begin{aligned} w_t &= D\chi'(\bar{u})w_x - D\chi'(\bar{u}+w)w_x + [Q(\bar{u}+w)(f'(\bar{u}+w) - w_{xx})_x]_x. \\ &= D\chi'(\bar{u})w_x - D\chi'(\bar{u}+w)w_x - Q'(\bar{u}+w)w_x w_{xxx} \\ &\quad -Q(\bar{u}+w)w_{xxxx} + Q'(\bar{u}+w)f''(\bar{u}+w)w_x^2 \\ &\quad +Q(\bar{u}+w)f'''(\bar{u}+w)w_x^2 + Q(\bar{u}+w)f''(\bar{u}+w)w_{xx}. \end{aligned} \tag{4.56}$$

We consider equation (4.56) on the domain $x \in [0, L]$. For convenience, we introduce the variable ξ so that $x = (L/2\pi)\xi$ and we also rescale time $t = (L/2\pi)\tau$ (i.e., $\xi = (2\pi/L)x$ and $\tau = (2\pi/L)t$). Then the domain size is fixed, $\xi \in [0, 2\pi]$, and we obtain the following equation

$$\begin{aligned} w_\tau &= D\chi'(\bar{u})w_\xi - D\chi'(\bar{u}+w)w_\xi - \nu^3 Q'(\bar{u}+w)w_\xi w_{\xi\xi} \\ &\quad -\nu^3 Q(\bar{u}+w)w_{\xi\xi\xi\xi} + \nu Q'(\bar{u}+w)f''(\bar{u}+w)w_\xi^2 \\ &\quad +\nu Q(\bar{u}+w)f'''(\bar{u}+w)w_\xi^2 + \nu Q(\bar{u}+w)f''(\bar{u}+w)w_{\xi\xi}, \end{aligned} \tag{4.57}$$

where $\nu = 2\pi/L$. Now instead of varying the domain size, we vary the parameter ν. The value of the parameter ν that corresponds to the primary bifurcation is $\nu_c = 2\pi/L_c = k_c = \sqrt{-f''(\bar{u})}$ (we consider a value of $\bar{u}$ for which $f''(\bar{u}) < 0$). Assuming that $w \propto e^{s\tau + in\xi}$ for $n = 0, \pm 1, \pm 2, \ldots$, we obtain the following dispersion relation

$$s(n) = -\nu^3 Q(\bar{u})n^4 - \nu Q(\bar{u})f''(\bar{u})n^2. \tag{4.58}$$

Let us assume that $\nu = \nu_c - \epsilon^2$, where ϵ is a small parameter, i.e., we are just beyond the cutoff value where the uniform solution $u = \bar{u}$ becomes linearly unstable. Then we

find that for $n = \pm 2, \pm 3, \ldots, s(n) < 0$ (if ϵ is sufficiently small), whereas for $n = 1$ we obtain

$$s(1) = -2f''(\bar{u})Q(\bar{u})\epsilon^2 + O(\epsilon^4), \tag{4.59}$$

which is positive for sufficiently small ϵ. Thus, we find that the growth rate of the unstable mode is $O(\epsilon^2)$, which suggests that it is appropriate to rescale the time as $\tau = T/\epsilon^2$. Next, we use a regular asymptotic expansion for w:

$$w = \epsilon w_1 + \epsilon^2 w_2 + \epsilon^3 w_3 + \cdots, \tag{4.60}$$

where $w_k = w_k(\xi, T)$, $k = 1, 2, \ldots$.

Substituting expansion (4.60) in (4.57) and using Taylor series expansions of χ', Q, Q', f'' and f''' at $\bar{u}$, we obtain at order $O(\epsilon)$:

$$Q(\bar{u})\nu_c^3(w_{1\xi\xi\xi\xi} + w_{1\xi\xi}) = 0, \tag{4.61}$$

that simplifies to

$$w_{1\xi\xi} + w_{1\xi\xi\xi\xi} = 0. \tag{4.62}$$

The general solution of equation (4.62) is

$$w_1 = c_0 + c_1\xi + A_1 e^{i\xi} + A_1^* e^{-i\xi}, \tag{4.63}$$

where c_0 and c_1 are real functions of T, A_1 is a complex-valued function of T and A_1^* denotes the complex conjugate of A_1. Since w_1 has to be a periodic function of ξ, then in fact

$$c_1 = 0. \tag{4.64}$$

Also, we have

$$\int_0^{2\pi} w_1 \, d\xi = 0, \tag{4.65}$$

which implies that

$$c_0 = 0. \tag{4.66}$$

Therefore,

$$w_1 = A_1 e^{i\xi} + A_1^* e^{-i\xi}, \tag{4.67}$$

where $A_1 = A_1(T)$ is the amplitude of the unstable mode $e^{i\xi}$.

At order $O(\epsilon^2)$, we obtain:

$$\begin{aligned} Q(\bar{u})\nu_c^3(w_{2\xi\xi\xi\xi} + w_{2\xi\xi}) &= [-2\nu_c Q(\bar{u})f'''(u_0) - iD\chi''(\bar{u})]A_1^2 e^{2i\xi} \\ &+ [-2\nu_c Q(\bar{u})f'''(\bar{u}) + iD\chi''(\bar{u})]A_1^{*2} e^{-2i\xi}, \end{aligned} \tag{4.68}$$

which after division by $Q(\bar{u})\nu_c^3$ becomes

$$\begin{aligned} w_{2\xi\xi\xi\xi} + w_{2\xi\xi} &= \left[-\frac{2f'''(\bar{u})}{\nu_c^2} - \frac{iD\chi''(\bar{u})}{Q(u_0)\nu_c^3}\right] A_1^2 e^{2i\xi} \\ &+ \left[-\frac{2f'''(\bar{u})}{\nu_c^2} + \frac{iD\chi''(\bar{u})}{Q(\bar{u})\nu_c^3}\right] A_1^{*2} e^{-2i\xi}. \end{aligned} \tag{4.69}$$

The general solution of equation (4.69) is

$$w_2 = w_{2h} + w_{2p}, \tag{4.70}$$

where w_{2h} is a solution of the homogeneous equation, i.e., the solution of

$$w_{2h\xi\xi} + w_{2h\xi\xi\xi\xi} = 0, \tag{4.71}$$

which is given by

$$w_{2h} = A_2 e^{i\xi} + A_2^* e^{-i\xi}, \tag{4.72}$$

and w_{2p} is a particular solution of equation (4.69). We look for a particular solution in the form

$$w_{2p} = Be^{2i\xi} + B^* e^{-2i\xi}. \tag{4.73}$$

Substituting this ansatz in the left-hand side of (4.69), we find

$$w_{2p\xi\xi} + w_{2p\xi\xi\xi\xi} = 12Be^{2i\xi} + 12B^* e^{-2i\xi}. \tag{4.74}$$

By comparing the right-hand sides of equations (4.74) and (4.69), we obtain

$$B = \left[-\frac{f'''(\bar{u})}{6\nu_c^2} - \frac{iD\chi''(\bar{u})}{12Q(\bar{u})\nu_c^3}\right] A_1^2, \tag{4.75}$$

so, the particular solution is

$$w_{2p} = \left[-\frac{f'''(\bar{u})}{6\nu_c^2} - \frac{iD\chi''(\bar{u})}{12Q(\bar{u})\nu_c^3}\right] A_1^2 e^{2i\xi} + \left[-\frac{f'''(\bar{u})}{6\nu_c^2} + \frac{iD\chi''(\bar{u})}{12Q(\bar{u})\nu_c^3}\right] A_1^{*2} e^{-2i\xi}, \tag{4.76}$$

Adding w_{2h} and w_{2p} together, we obtain

$$w_2 = w_{2h} + w_{2p} = A_2 e^{i\xi} + A_2^* e^{-i\xi} + \left[-\frac{f'''(\bar{u})}{6\nu_c^2} - \frac{iD\chi''(\bar{u})}{12Q(\bar{u})\nu_c^3} \right] A_1^2 e^{2i\xi} + \left[-\frac{f'''(\bar{u})}{6\nu_c^2} + \frac{iD\chi''(\bar{u})}{12Q(\bar{u})\nu_c^3} \right] A_1^{*2} e^{-2i\xi} \quad (4.77)$$

At order $O(\epsilon^3)$, we find:

$$\begin{aligned} Q(\bar{u})\nu_c^3(w_{3\xi\xi\xi\xi} + w_{3\xi\xi}) \;=\; & \Bigg[A_{1T} - 2\nu_c^2 Q(\bar{u}) A_1 + \Bigg(\frac{1}{2}\nu_c Q(\bar{u}) f''''(\bar{u}) - \frac{1}{6}\frac{Q(\bar{u})(f'''(\bar{u}))^2}{\nu_c} \\ & + \frac{1}{12}\frac{D^2(\chi''(\bar{u}))^2}{\nu_c^3 Q(\bar{u})} + \frac{1}{2}iD\chi'''(\bar{u}) - \frac{1}{4}i\frac{D\chi''(\bar{u})f'''(\bar{u})}{\nu_c^2} \\ & - \frac{1}{2}i\frac{D\chi''(\bar{u})Q'(\bar{u})}{Q(\bar{u})} \Bigg) A_1^2 A_1^* \Bigg] e^{i\xi} + \text{c.c.} + \ldots, \end{aligned} \quad (4.78)$$

where c.c. denotes the complex conjugate of the first term. Also, on the right-hand, there are terms proportional to $e^{\pm 2i\xi}$ and $e^{\pm 3i\xi}$, which are lengthy and, therefore, are not shown.

We note that $e^{i\xi}$ and $e^{-i\xi}$ span the null space of the linear operator on the left-hand side of this equation (when this operator is considered on the space of periodic functions of zero mean). Then, the Fredholm alternative solvability condition requires that the right-hand side of this equation should be orthogonal to $e^{i\xi}$ and $e^{-i\xi}$ (with respect to the usual inner product in the L^2-space of complex-valued functions). This implies that the coefficient of $e^{i\xi}$ (or, equivalently, of $e^{-i\xi}$) should vanish. We, therefore, obtain the following amplitude (or Stuart-Landau) equation:

$$\begin{aligned} \frac{dA_1}{dT} = 2\nu_c^2 Q(\bar{u}) A_1 - \Bigg(& \frac{1}{2}\nu_c Q(\bar{u}) f''''(\bar{u}) - \frac{1}{6}\frac{Q(\bar{u})(f'''(\bar{u}))^2}{\nu_c} + \frac{1}{12}\frac{D^2(\chi''(\bar{u}))^2}{\nu_c^3 Q(\bar{u})} \\ & + \frac{1}{2}iD\chi'''(\bar{u}) - \frac{1}{4}i\frac{D\chi''(\bar{u})f'''(\bar{u})}{\nu_c^2} - \frac{1}{2}i\frac{D\chi''(\bar{u})Q'(\bar{u})}{Q(\bar{u})} \Bigg) A_1^2 A_1^*. \end{aligned} \quad (4.79)$$

For brevity, let us denote the term in the round brackets in the latter equation by $h = h(\bar{u}, D)$. Then, we have

$$\frac{dA_1}{dT} = 2\nu_c^2 Q(\bar{u}) A_1 - h|A_1|^2 A_1. \quad (4.80)$$

and also

$$\frac{dA_1^*}{dT} = 2\nu_c^2 Q(\bar{u}) A_1^* - h^*|A_1|^2 A_1^*. \quad (4.81)$$

Multiplying (4.80) by A_1^* and adding (4.81) multiplied by A_1, we find

$$\begin{aligned} A_1^*\frac{dA_1}{dT} + A_1\frac{dA_1^*}{dT} &= A_1^*[2\nu_c^2 Q(\bar{u})A_1 - h|A_1|^2 A_1] \\ &+ A_1[2\nu_c^2 Q(\bar{u})A_1^* - h^*|A_1|^2 A_1^*] \\ &= 4\nu_c^2 Q(\bar{u})|A_1|^2 - 2\,\mathrm{Re}(h)|A_1|^4. \end{aligned} \tag{4.82}$$

Since $A_1^*(dA_1/dT) + A_1(dA_1^*/dT) = d(A_1A_1^*)/dT = d(|A_1|^2)/dT$, we obtain

$$\frac{d(|A_1|^2)}{dT} = \left(4\nu_c^2 Q(\bar{u}) - 2\,\mathrm{Re}(h)|A_1|^2\right)|A_1|^2, \tag{4.83}$$

or, equivalently,

$$\frac{d(|A_1|)}{dT} = \left(2\nu_c^2 Q(\bar{u}) - \mathrm{Re}(h)|A_1|^2\right)|A_1|. \tag{4.84}$$

When $\mathrm{Re}(h) < 0$, this ODE for $|A_1|$ has only one fixed point, namely, $|A_1| = 0$. Therefore, for $\mathrm{Re}(h) < 0$ there do not exist small-amplitude sinusoidal solutions beyond the primary bifurcation point. This means that the primary bifurcation is subcritical in this case. On the other hand, when $\mathrm{Re}(h) > 0$, ODE (4.84) for $|A_1|$ has two fixed points, namely, an unstable fixed point $|A_1| = 0$ and a stable fixed point $|A_1| = (2\nu_c^2 Q(\bar{u})/\mathrm{Re}(h))^{1/2}$. Therefore, for $\mathrm{Re}(h) > 0$ there exists a small-amplitude sinusoidal solutions beyond the primary bifurcation point whose amplitude is given by

$$|A_1| = \sqrt{\frac{2\nu_c^2 Q(\bar{u})}{\mathrm{Re}(h)}}. \tag{4.85}$$

This means that the primary bifurcation is supercritical when $\mathrm{Re}(h) > 0$. Therefore, we find that the change from supercritical to subcritical bifurcation happens when

$$\mathrm{Re}(h) = 0, \tag{4.86}$$

which for given $\bar{u}$ determines the driving force D_c at which the change in the primary bifurcation happens:

$$D_c = \pm\sqrt{\frac{2\nu_c^2 Q^2(\bar{u})(f'''(\bar{u}))^2}{(\chi''(\bar{u}))^2} - \frac{6\nu_c^4 Q^2(\bar{u})f''''(\bar{u})}{(\chi''(\bar{u}))^2}}. \tag{4.87}$$

We see that the primary bifurcation can change its nature as D varies only when the expression under the square root is positive, which implies the following condition:

$$(f'''(\bar{u}))^2 > 3\nu_c^2 f''''(\bar{u}) \equiv -3f''(\bar{u})f''''(\bar{u}). \tag{4.88}$$

(We remind that for the existence of the primary bifurcation the condition $f''(\bar{u}) < 0$ must also be satisfied.)

Let us now analyse the small-amplitude sinusoidal solution in more detail. Substituting (4.85) in (4.80), we obtain

$$\frac{dA_1}{dT} = -\frac{2\nu_c^2 Q(\bar{u})\mathrm{Im}(h)}{\mathrm{Re}(h)} iA_1. \tag{4.89}$$

This together with (4.85) implies that A_1 for the small-amplitude sinusoidal solution is given by

$$A_1 = \sqrt{\frac{2\nu_c^2 Q(\bar{u})}{\mathrm{Re}(h)}} \exp\left[-i\left(\frac{2\nu_c^2 Q(\bar{u})\mathrm{Im}(h)}{\mathrm{Re}(h)} T + \varphi_0\right)\right], \tag{4.90}$$

where φ_0 is a constant. Thus, we find that

$$\begin{aligned} w &= \epsilon A_1 e^{i\xi} + \text{c.c.} + O(\epsilon^2) \\ &= \epsilon\sqrt{\frac{2\nu_c^2 Q(\bar{u})}{\mathrm{Re}(h)}} \exp\left[i\left(\xi - \frac{2\nu_c^2 Q(\bar{u})\mathrm{Im}(h)}{\mathrm{Re}(h)} T\right) - i\varphi_0\right] + \text{c.c.} + O(\epsilon^2). \end{aligned} \tag{4.91}$$

Using that $\xi = (2\pi/L)x$ and $T = \epsilon^2\tau = \epsilon^2(2\pi/L)t$, we find the following expression for w in the original variables x and t:

$$w = \epsilon\sqrt{\frac{2\nu_c^2 Q(\bar{u})}{\mathrm{Re}(h)}} \exp\left[\frac{2\pi i}{L}\left(x - \epsilon^2 \frac{2\nu_c^2 Q(\bar{u})\mathrm{Im}(h)}{\mathrm{Re}(h)} t\right) - i\varphi_0\right] + \text{c.c.} + O(\epsilon^2). \tag{4.92}$$

Thus, the speed of the small-amplitude sinusoidal wave in the frame moving at velocity $D\chi'(\bar{u})$ is

$$c = \epsilon^2 \frac{2\nu_c^2 Q(\bar{u})\mathrm{Im}(h)}{\mathrm{Re}(h)}. \tag{4.93}$$

Since $\epsilon = \sqrt{\nu_c - \nu} = \sqrt{2\pi(L_c^{-1} - L^{-1})} \propto \sqrt{L - L_c}$ (when L is near L_c), we obtain that the wave amplitude scales as $\sqrt{L - L_c}$ and the wave speed in the frame moving at velocity $D\chi'(\bar{u})$ scales as $L - L_c$.

For the standard convective Cahn-Hilliard equation with scaling 1, equation (2.28), we have

$$Q(\bar{u}) \equiv 1, \quad h = 3\nu_c - 6\frac{\bar{u}^2}{\nu_c} + \frac{D^2}{12\nu_c^3} - \frac{3iD\bar{u}}{2\nu_c^2}, \tag{4.94}$$

where $\nu_c = \sqrt{1 - 3\bar{u}^2}$. Therefore, the amplitude equation takes the form

$$\frac{dA_1}{dT} = 2\nu_c^2 A_1 - \left(3\nu_c - 6\frac{\bar{u}^2}{\nu_c} + \frac{D^2}{12\nu_c^3} - \frac{3iD\bar{u}}{2\nu_c^2}\right) A_1^2 A_1^*, \tag{4.95}$$

and the condition for the change from supercritical to subcritical primary bifurcation becomes

$$\mathrm{Re}(h) = 3\nu_c - 6\frac{\bar{u}^2}{\nu_c} + \frac{D^2}{12\nu_c^3} = 0, \tag{4.96}$$

which for given $\bar{u}$ determines the values D_c of the driving force at which the change in the nature of the primary bifurcation happens:

$$D_c = \pm\sqrt{-540\bar{u}^4 + 288\bar{u}^2 - 36}. \tag{4.97}$$

For example, for $\bar{u} = 0.55$, we find

$$D_c \approx \pm 1.3064, \tag{4.98}$$

which is consistent with the numerical results presented in Section 4.4.2. Also, note that the expression under the square root in (4.97) is positive only when $1/\sqrt{5} < |\bar{u}| < 1/\sqrt{3}$, i.e., the driving force can switch the bifurcation from supercritical to subcritical only when $1/\sqrt{5} < |\bar{u}| < 1/\sqrt{3}$. If $|\bar{u}| < 1/\sqrt{5}$, the primary bifurcation will be supercritical for any value of the driving force. We also remind that if $|\bar{u}| > 1/\sqrt{3}$, there is no primary bifurcation and the uniform solution is linearly stable for any value of the driving force. The graph showing the dependence of $|D_c|$ on $|\bar{u}|$ is shown in Fig. 4.32. For the parameter values in the region below this graph, the primary bifurcation is subcritical. It can be easily found that the graph achieves its maximum point at $|\bar{u}| = 2/\sqrt{15}$, and the maximum value is $|D_c^{\max}| = 2\sqrt{3/5} \approx 1.55$. Note that for a fixed non-zero value of the driving force so that $|D| < |D_c^{\max}|$, there are two values of $|\bar{u}|$ where the primary bifurcation first changes from supercritical to subcritical (at the smaller value of $|\bar{u}|$) and then back from subcritical to supercritical (at the larger value of $|\bar{u}|$). Note that as $D \to 0$, the smaller and the larger values of $|u|$ at which the nature of the primary bifurcation changes tend to $1/\sqrt{5}$ and $1/\sqrt{3}$, respectively. Since the value $1/\sqrt{3}$ corresponds to the point where the primary bifurcation disappears, we conclude that for the standard Cahn-Hilliard equation, when $D = 0$, there is only one value of $|u|$ were the nature of the bifurcation changes, namely, $1/\sqrt{5} \approx 0.45$. This is consistent with the numerical results presented in Section 4.3.2.

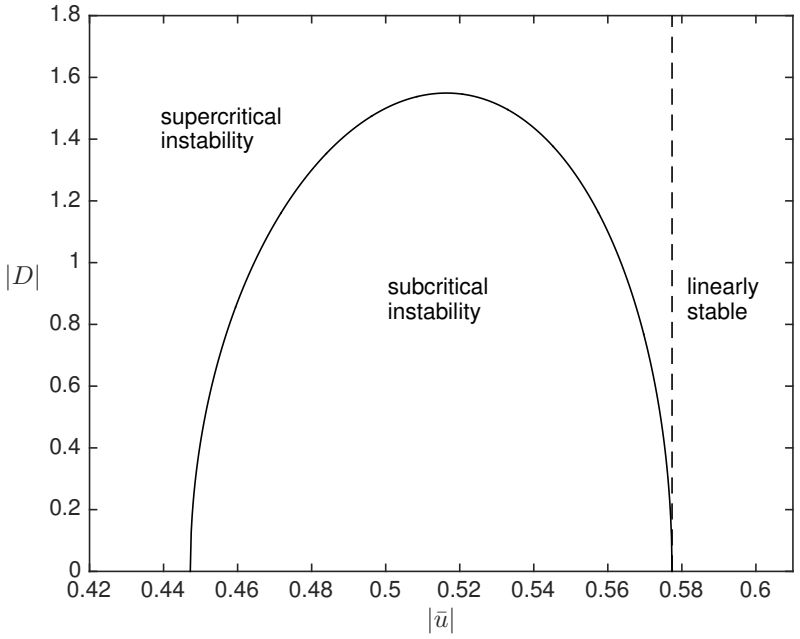

Figure 4.32: The solid line shows dependence of D_c (the magnitude of the driving force at which the primary bifurcation changes from subcritical to supercritical) on the magnitude of the mean concentration for the standard convective Cahn-Hilliard equation with scaling 1, equation (2.28). The region to the right of the vertical dashed line is the region where the homogeneous solution is linearly stable. For the region below/above the solid line, the primary bifurcation is subcritical/supercritical.

4.5.2 Weakly nonlinear analysis for the general convective Cahn-Hilliard-type equation with scaling 2

In this section, we again analyse the primary bifurcation for the general convective Cahn-Hilliard-type equation, but in the alternative scaling 2. The equation has the same form as equation (4.45), but now it is given on the domain $x \in [0, 2\pi]$, and we assume that φ additionally depends on a parameter a in the following way:

$$\varphi(u, u_x, a) = f(u, a) + \frac{1}{2}u_x^2. \tag{4.99}$$

By adding a small perturbation to a uniform solution $\bar{u}$, i.e. $u(x,t) = \bar{u} + w(x,t)$, we obtain the following equation for $w(x,t)$:

$$w_t = vw_x - D\chi'(\bar{u}+w)w_x + [Q(\bar{u}+w)(f_u(\bar{u}+w,a) - w_{xx})_x]_x. \tag{4.100}$$

It can be easily found that the dispersion relation for this equation has the form

$$\beta(k) = ivk - iD\chi'(\bar{u})k - Q(\bar{u})f_{uu}(\bar{u},a)k^2 - Q(\bar{u})k^4, \tag{4.101}$$

from which we find that the velocity of the small-amplitude sinusoidal waves is

$$v = D\chi'(\bar{u}) \tag{4.102}$$

and the primary bifurcation point a_c is a solution of the equation

$$f_{uu}(\bar{u}, a_c) = -1. \tag{4.103}$$

Substituting $v = D\chi'(\bar{u})$ in equation (4.100), we obtain

$$\begin{aligned} w_t = D\chi'(\bar{u})w_x - D\chi'(\bar{u}+w)w_x - Q'(\bar{u}+w)w_x w_{xxx} - Q(\bar{u}+w)w_{xxxx} \\ +Q'(\bar{u}+w)f_{uu}(\bar{u}+w,a)w_x^2 + Q(\bar{u}+w)f_{uuu}(\bar{u}+w,a)w_x^2 \\ +Q(\bar{u}+w)f_{uu}(\bar{u}+w,a)w_{xx}. \end{aligned} \tag{4.104}$$

Next, we assume that $f_{uu}(\bar{u}, a)$ is a monotonically decreasing function of a in the neighbourhood of $a = a_c$, and we write $a = a_c - \epsilon^2$. We additionally rescale $t = T/\epsilon^2$ and use the asymptotic expansion:

$$w = \epsilon w_1 + \epsilon^2 w_2 + \epsilon^3 w_3 + \cdots, \tag{4.105}$$

where $w_k = w_k(x, T)$, $k = 1, 2, \ldots$. Proceeding in the same way as in the previous section, we find that the solution of the equation at order $O(\epsilon)$ is

$$w_1 = A_1 e^{ix} + A_1^* e^{-ix}, \tag{4.106}$$

where $A_1 = A_1(T)$ where A_1 is the amplitude of the unstable mode e^{ix}. The solution at order $O(\epsilon^2)$ is

$$\begin{aligned} w_2 \;=\; & A_2 e^{ix} + A_2^* e^{-ix} + \left[-\frac{f_{uuu}(\bar{u}, a_c)}{6} - \frac{iD\chi''(\bar{u})}{12Q(\bar{u})} \right] A_1^2 e^{2ix} \\ & + \left[-\frac{f_{uuu}(\bar{u}, a_c)}{6} + \frac{iD\chi''(\bar{u})}{12Q(\bar{u})} \right] A_1^{*2} e^{-2ix}. \end{aligned} \tag{4.107}$$

Finally, the solvability condition at order $O(\epsilon^3)$ results in the following amplitude equation for A_1:

$$\frac{dA_1}{dT} = f_{uuu}(\bar{u},a_c)Q(\bar{u})A_1 - \left(\frac{1}{2}Q(\bar{u})f_{uuuu}(\bar{u},a_c) - \frac{1}{6}Q(\bar{u})f_{uuu}^2(\bar{u},a_c) + \frac{1}{12}\frac{D^2(\chi''(\bar{u}))^2}{Q(\bar{u})} + \frac{1}{2}iD\chi'''(\bar{u}) - \frac{1}{4}iD\chi''(\bar{u})f_{uuu}(\bar{u},a_c) - \frac{1}{2}i\frac{D\chi''(\bar{u})Q'(\bar{u})}{Q(\bar{u})}\right)A_1^2A_1^*. \quad (4.108)$$

Denoting the term in the round brackets by $h = h(\bar{u}, D)$, we can rewrite this equation as

$$\frac{dA_1}{dT} = f_{uuu}(\bar{u},a_c)Q(\bar{u})A_1 - h|A_1|^2A_1. \quad (4.109)$$

Then, in the same way as in the previous section, we can find that

$$\frac{d(|A_1|)}{dT} = (f_{uuu}(\bar{u},a_c)Q(\bar{u}) - \mathrm{Re}(h)|A_1|^2)|A_1|. \quad (4.110)$$

Assuming that $f_{uuu}(\bar{u},a_c) > 0$ and $Q(\bar{u}) > 0$, we find that if $\mathrm{Re}(h) < 0$, the only fixed point of this ODE is $|A_1| = 0$, i.e., the primary bifurcation is subcritical, and if $\mathrm{Re}(h) > 0$, there is another fixed point of this ODE,

$$|A_1| = \sqrt{\frac{f_{uuu}(\bar{u},a_c)Q(\bar{u})}{\mathrm{Re}(h)}}, \quad (4.111)$$

and the primary bifurcation is supercritical.

As in the previous section, for the supercritical case, we can find that the sinusoidal travelling-wave solution is given by

$$A_1 = \sqrt{\frac{f_{uuu}(\bar{u},a_c)Q(\bar{u})}{\mathrm{Re}(h)}}\exp\left[-i\left(\frac{f_{uuu}(\bar{u},a_c)\mathrm{Im}(h)}{\mathrm{Re}(h)}T + \varphi_0\right)\right], \quad (4.112)$$

and, therefore, the solution of (4.100) is given by

$$\begin{aligned} w &= \epsilon A_1 e^{ix} + \text{c.c.} + O(\epsilon^2) \\ &= \epsilon\sqrt{\frac{f_{uuu}(\bar{u},a_c)Q(\bar{u})}{\mathrm{Re}(h)}}\exp\left[i\left(x - \epsilon^2\frac{f_{uuu}(\bar{u},a_c)Q(\bar{u})\mathrm{Im}(h)}{\mathrm{Re}(h)}t\right) - i\varphi_0\right] \\ &\qquad + \text{c.c.} + O(\epsilon^2). \end{aligned} \quad (4.113)$$

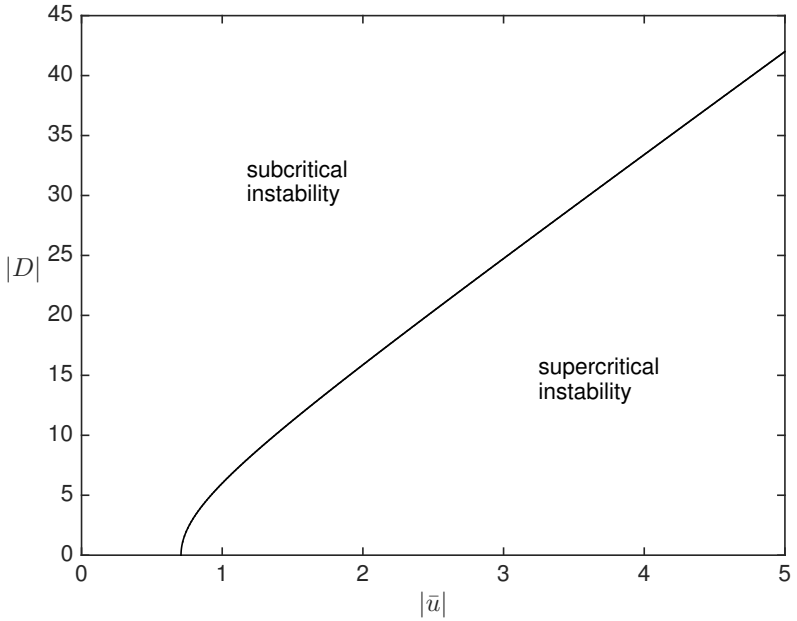

Figure 4.33: The solid line shows dependence of D_c (the magnitude of the driving force at which the primary bifurcation changes from subcritical to supercritical) on the magnitude of the mean concentration for the standard convective Cahn-Hilliard equation with scaling 2, equation (2.48). For the region above/below the solid line, the primary bifurcation is subcritical/supercritical.

Thus, the speed of the small-amplitude sinusoidal wave is given by

$$c = \epsilon^2 \frac{f_{uuu}(\bar{u}, a_c) Q(\bar{u}) \mathrm{Im}(h)}{\mathrm{Re}(h)} = (a - a_c) \frac{f_{uuu}(\bar{u}, a_c) Q(\bar{u}) \mathrm{Im}(h)}{\mathrm{Re}(h)} \tag{4.114}$$

For the standard convective Cahn-Hilliard equation with scaling 2, equation (2.48), we have

$$Q(u) \equiv 1, \quad \chi(u) = \frac{u^2}{2}, \quad f(u, a) = \frac{1}{4}u^4 - \frac{a}{2}u^2. \tag{4.115}$$

Then the condition for the primary bifurcation (4.103) implies:

$$a_c = 1 + 3\bar{u}^2. \tag{4.116}$$

Then we find that

$$h = 3 - 6\bar{u}^2 + \frac{D^2}{12} - \frac{3iD\bar{u}}{2}, \tag{4.117}$$

and the condition for the switch from the supercritical to subcritical bifurcation becomes:

$$\mathrm{Re}(h) = 3 - 6\bar{u}^2 + \frac{D^2}{12} = 0, \tag{4.118}$$

which determines the value D_c of the driving force at which the change in the nature of the primary bifurcation occurs:

$$|D_c| = \sqrt{72\bar{u}^2 - 36}. \tag{4.119}$$

The graph showing the dependence of $|D_c|$ on $|\bar{u}|$ is given if Fig. 4.33. For the parameter values to the left of this graph, the primary bifurcation is subcritical, whereas to the right of this graph, the primary bifurcation is supercritical. In particular, for the standard Cahn-Hilliard equation, when $D = 0$, we obtain that the bifurcation is subcritical when $|\bar{u}| < 1/\sqrt{2}$ and supercritical otherwise.

Finally, we note that weakly nonlinear analyses similar to the one presented here have been conducted in the literature for a number of systems, for example, for modelling the dynamics of self-oscillating fields (see Kuramoto [70]), for rupture of free films (see Erneux and Davis [37] and also Thiele et al. [111], where a diffuse interface model coupled to hydrodynamics was used and the transition between subcritical and supercritical bifurcations was determined as a border between nucleation- and instability-dominated dewetting), for liquid films on inclined heated plates (see Thiele and Knobloch [106], Thiele et al. [109]), in the study of sliding drops (see Thiele et al. [110], where a bifurcation similar to that shown in Fig. 4.17(a) at $D = D_c$ was also obtained; it is also worth mentioning that Thiele et al. [110] showed that the convective Cahn-Hilliard equation can be derived from a thin-film equation in a certain limit).

Chapter 5

Linear stability of inhomogeneous solutions

5.1 Introduction

In this chapter, we study in detail the linear stability properties of the various possible spatially periodic traveling solutions of the convective Cahn-Hilliard equation. The formulation of the linear stability problem for inhomogeneous solutions is done in Section 5.2. The linear stability properties are studied by implementing the continuation of both inhomogeneous solutions and their eigenvalues in the driving force D, utilising the continuation and bifurcation software Auto07p [31]. The details of the computational procedure are explained in Section 5.3. We note that we actually implement three different numerical procedures, one for $D = 0$ (which allows for one additional integration of the equation for stationary solutions), see Section 5.3.1, one for $D \neq 0$ allowing for the computation of real eigenvalues, see Section 5.3.2.1, and one more for $D \neq 0$ allowing for the computation of complex eigenvalues, see Section 5.3.2.2. In addition, to obtain a more complete picture, we construct branches of time-periodic solutions. The numerical procedure for the computation of the branches of time-periodic solutions is explained in Section 5.3.2.3. In Section 5.4, we present results for the linear stability of two-droplet solutions and of the solutions of the side branches bifurcating from the 2-mode primary branches (i.e., of broken-symmetry solutions). Moreover, we identify the coarsening modes of the two-droplet solutions (i.e., translational and volume modes). All this information is used to construct detailed stability diagrams in the (D, L)- and $(D, \bar{u})$-planes.

5.2 Linear stability problem for stationary and travelling periodic solutions on finite and infinite domains

In this section, we formulate the linear stability problem for stationary (when the speed is zero) and travelling (when the speed is non-zero) solutions of the convective Cahn-Hilliard equation (2.28) with respect to small random perturbations in the finite and infinite domains. Equation (2.28), written in the frame moving at velocity v is (see also Section 4.2.1, equation (4.2))

$$u_t - vu_x = -\left[\frac{Du^2}{2} + (u - u^3 + u_{xx})_x\right]_x. \tag{5.1}$$

As explained in Section 4.2.1, a stationary (when $v = 0$) or travelling (when $v \neq 0$) solution $u_0(x)$ is a steady solution of this equation, i.e., a solution of

$$-vu_0' = -\left[\frac{Du_0^2}{2} + (u_0 - u_0^3 + u_0'')'\right]'. \tag{5.2}$$

We assume that $u_0(x)$ is a periodic function of period L.

To analyse the linear stability of the solution $u_0(x)$, we need to linearise the convective Cahn-Hilliard equation (5.1) about this solution. To do this, we write

$$u = u_0(x) + u_1(x,t), \tag{5.3}$$

where $u_1(x,t)$ is a small perturbation to the solution $u_0(x)$. If u_1 grows (in some appropriate norm, e.g., in the L^2- or L^∞-norm) as t increases, then $u_0(x)$ is unstable, otherwise $u_0(x)$ is stable.

We substitute (5.3) in (5.1) and obtain the following linearised equation for u_1, ignoring the terms of order $o(|u_1|)$:

$$u_{1t} = \left[vu_1 - Du_0u_1 - ([1 - 3u_0^2]u_1 + u_{1xx})_x\right]_x, \tag{5.4}$$

or, equivalently,

$$\begin{aligned} u_{1t} = (-Du_0' + 6u_0'^2 + 6u_0u_0'')u_1 + (v - Du_0 + 12u_0u_0')u_{1x} \\ +(3u_0^2 - 1)u_{1xx} - u_{1xxxx}. \end{aligned} \tag{5.5}$$

This is a fourth-order linear differential equation which can be written as

$$u_{1t} = \mathcal{L}[u_1], \tag{5.6}$$

where $\mathcal{L}$ is a linear differential operator with non-constant coefficients (see, e.g., Egorov and Shubin [34], Evans [38], Gustafsson et al. [52]) given by

$$\begin{aligned} \mathcal{L}[f] &= [(v - Du_0)f - ([1 - 3u_0^2]f + f_{xx})_x]_x \\ &= (-Du_0' + 6u_0'^2 + 6u_0u_0'')f + (v - Du_0 + 12u_0u_0')f_x \\ &\quad +(3u_0^2 - 1)f_{xx} - f_{xxxx}. \end{aligned} \tag{5.7}$$

To analyse the linear stability, we write $u_1 = e^{st}\eta(x)$ and substitute it in equation (5.6). The left-hand side becomes

$$u_{1t} = se^{st}\eta(x), \tag{5.8}$$

while the right-hand side becomes

$$\mathcal{L}[u_1] = \mathcal{L}[e^{st}\eta(x)] = e^{st}\mathcal{L}[\eta(x)]. \tag{5.9}$$

As a result, we obtain

$$s\,\eta(x) = \mathcal{L}[\eta(x)], \tag{5.10}$$

which is an eigenvalue problem for the operator $\mathcal{L}$. So, s should belong to the spectrum of $\mathcal{L}$, denoted by $\sigma(\mathcal{L})$. If part of the spectrum has positive real part then $|\tilde{u}|$ grows as t increases, i.e. the solution $u_0(x)$ is (spectrally) unstable. On the other hand, if all the spectrum has negative real part then $|\tilde{u}| \to 0$ as t increases, i.e. the solution $u_0(x)$ is (spectrally) stable, see, e.g., Sandstede [92]. See Fig. 5.1 for a schematic representation of these two cases.

If a linear differential operator $\mathcal{L}$ is defined on a finite periodic domain, L_c, (which in our case should be an integer multiple of L, i.e. $L_c = nL$ for some $n \in \mathbb{N}$), then the spectrum of such an operator typically consists of the point spectrum, i.e., of isolated eigenvalues of finite multiplicities. Numerically, the spectrum can be computed by adopting a Fourier spectral method (see, for example, Boyd [11] and Trefethen [112]), where functions are represented by truncated Fourier series, e.g., $\eta(x) = \sum_{k=-N}^{N} \hat{\eta}_k e^{ikx}$. Then, the eigenvalue problem (5.10) can be converted into a matrix eigenvalue problem

$$\hat{s}\,\hat{\boldsymbol{\eta}} = \widehat{\boldsymbol{\mathcal{L}}}\,\hat{\boldsymbol{\eta}}, \tag{5.11}$$

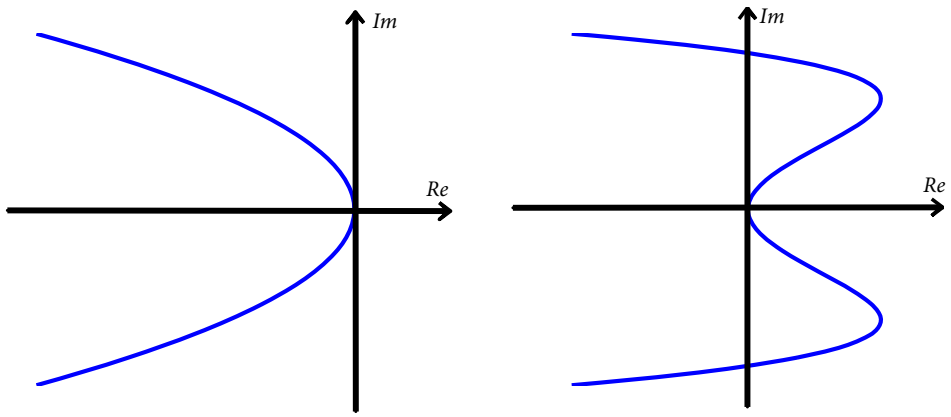

Figure 5.1: Two possible spectra of operator $\mathcal{L}$ shown as a solid (blue) curve in the complex plane. The left figure corresponds to the linearly stable case, the right figure corresponds to the linearly unstable case.

where $\hat{\boldsymbol{\eta}}$ is a vector consisting of the Fourier coefficients of $\eta(x)$, $\widehat{\boldsymbol{\mathcal{L}}}$ is a matrix representation of the operator $\mathcal{L}$, and $\hat{s}$ is an eigenvalue of this matrix, which is a numerical approximation of an eigenvalue of the operator $\mathcal{L}$. Any spurious eigenvalues are eliminated and the accuracy of the computed spectrum is verified by recomputing the spectrum for the increasing values of N.

On an infinite domain, the point spectrum of the operator $\mathcal{L}$ is empty and thus it consists only of the essential spectrum (see, for example, Sandstede [92]). To analyse the essential spectrum of the operator $\mathcal{L}$ on an infinite domain, we write

$$\eta(x) = e^{ikx} g(x), \tag{5.12}$$

where $k \in [-\pi/L, \pi/L]$ is the so-called Bloch wavenumber (see, for example, Mielke [79], Tseluiko et al. [113]), and $g(x)$ is a periodic function of the same period as $u_0(x)$. We then find

$$s\, e^{ikx} g(x) = \mathcal{L}[e^{ikx} g(x)]. \tag{5.13}$$

After multiplying by e^{-ikx}, we obtain

$$s\, g(x) = e^{-ikx} \mathcal{L}[e^{ikx} g(x)]. \tag{5.14}$$

In equation (5.14), let us denote the right-hand side by $\mathcal{L}_k[g(x)]$. So

$$\mathcal{L}_k[g(x)] = e^{-ikx} \mathcal{L}[e^{ikx} g(x)]. \tag{5.15}$$

For the operator $\mathcal{L}$ given by equation (5.7), we obtain

$$\begin{aligned}\mathcal{L}_k[g] &= (-Du_0' + 6u_0'^2 + 6u_0u_0'')g + (v - Du_0 + 12u_0u_0')e^{-ikx}(e^{ikx}g)_x \\ &\quad +(3u_0^2 - 1)e^{-ikx}(e^{ikx}g)_{xx} - e^{-ikx}(e^{ikx}g)_{xxxx}. \quad (5.16)\end{aligned}$$

Taking into account the fact that

$$e^{-ikx}\partial_x^n(e^{ikx}f(x)) = (\partial_x + ik)^n f(x), \quad (5.17)$$

for $n \in \mathbb{N}$ (which can be easily proved by induction), equation (5.16) takes the form

$$\begin{aligned}\mathcal{L}_k[g] &= (-Du_0' + 6u_0'^2 + 6u_0u_0'')g + (v - Du_0 + 12u_0u_0')(\partial_x + ik)g \\ &\quad +(3u_0^2 - 1)(\partial_x + ik)^2 g - (\partial_x + ik)^4 g. \quad (5.18)\end{aligned}$$

By the Floquet-Bloch theory, the spectrum of the operator $\mathcal{L}$ is given by the union of the spectra of all the operators $\mathcal{L}_k$, i.e.,

$$\sigma(\mathcal{L}) = \bigcup_{k\in[\frac{-\pi}{L},\frac{\pi}{L}]} \sigma(\mathcal{L}_k), \quad (5.19)$$

where $\sigma(\mathcal{L}_k)$ is the spectrum of $\mathcal{L}_k$. Numerically, the spectrum is approximated by discretising the interval $[-\pi/L, \pi/L]$ into a sufficiently large number of points k_j, $j = 1, 2, \ldots, M+1$, (for example, we can choose $k_j = -\pi/L + 2\pi(j-1)/(ML)$), and computing the spectra for each of the operators $\mathcal{L}_{k_j}$, $j = 1, 2, \ldots, M+1$ by the Fourier spectral method discussed above (since each of the operators $\mathcal{L}_{k_j}$ is defined on a finite periodic domain of length L). By increasing M and N (i.e., the number of the Fourier modes), the numerically computed spectrum will converge to $\sigma(\mathcal{L})$. Numerical codes for computation of the spectra along the lines discussed above are implemented in Matlab.

5.3 Numerical investigation of linear stability of stationary and travelling periodic solutions on finite domains by continuation techniques

5.3.1 The case of the standard Cahn-Hilliard equation

In this section, we explain the numerical continuation procedure for computation of stationary periodic solutions of the standard Cahn-Hilliard equation (2.11) along with their eigenvalues, which allows to investigate the stability of such solutions. A steady solution u_0 of the standard Cahn-Hilliard equation satisfies

$$0 = -(u_0 - u_0^3 + u_0'')''. \tag{5.20}$$

Integrating this equation twice with respect to x, we find

$$0 = -(u_0 - u_0^3 + u_0'') + C_1 x + C_0, \tag{5.21}$$

where C_1 and C_0 are the constants of integration. Due to periodicity of u_0, we find that C_1 must be zero, i.e., we obtain

$$0 = -(u_0 - u_0^3 + u_0'') + C_0. \tag{5.22}$$

To investigate the stability of u_0, we also need to linearise the equation and solve the resulting eigenvalue problem given by eqution (5.5) with $D = 0$, i.e.,

$$u_{1t} = (6u_0'^2 + 6u_0u_0'')u_1 + 12u_0u_0'u_{1x} + (3u_0^2 - 1)u_{1xx} - u_{1xxxx}. \tag{5.23}$$

By substituting $u_1 = e^{st}\eta(x)$ in equation (5.23), we obtain

$$s\,\eta = (6u_0'^2 + 6u_0u_0'')\eta + 12u_0u_0'\eta' + (3u_0^2 - 1)\eta'' - \eta'''', \tag{5.24}$$

where as before s is the growth rate and $\eta(x)$ is the eigenfunction.

We solve the second-order equation (5.22) for a steady solution u_0 along with the fourth-order equation (5.24) for the eigenfunction $\eta(x)$ and the growth rate s by continuation techniques using Auto07p [31]. We first write the two equations as a system of six first-order autonomous ordinary differential equations on the interval [0, 1]. So we introduce

the variables $y_1 = u_0 - \bar{u}$, $y_2 = u_0'$ and obtain from equation (5.22) the following two-dimensional dynamical system:

$$\dot{y}_1 = Ly_2, \tag{5.25}$$
$$\dot{y}_2 = L[(y_1 + \bar{u})^3 - (y_1 + \bar{u}) + C_0], \tag{5.26}$$

where L is the physical domain size, and dots denote derivatives with respect to $\alpha \equiv x/L$. We note that the fields $y_1(\alpha)$ and $y_2(\alpha)$ correspond to the correctly scaled physical fields $u_0(L\alpha) - \bar{u}$, $u_0'(L\alpha)$.

Further we introduce $y_3 = \eta$, $y_4 = \eta'$, $y_5 = \eta''$, $y_6 = \eta'''$ and rewrite equation (5.24) as a four-dimensional dynamical system,

$$\dot{y}_3 = Ly_4, \tag{5.27}$$
$$\dot{y}_4 = Ly_5, \tag{5.28}$$
$$\dot{y}_5 = Ly_6, \tag{5.29}$$
$$\dot{y}_6 = L\big[- sy_3 + (6y_2^2 + 6[y_1 + \bar{u}][(y_1 + \bar{u})^3 - (y_1 + \bar{u}) + C_0])y_3 + 12(y_1 + \bar{u})y_2y_4 + (3[y_1 + \bar{u}]^2 - 1)y_5\big]. \tag{5.30}$$

Thus, the dimension of the system described by the variable $NDIM$ in a Auto07p is 6. The system of the equations is specified in the user-supplied subroutine $FUNC$. We use periodic boundary conditions for all the variables y_i meaning that the number of the boundary conditions that is described by the variable NBC is 6. The boundary conditions are specified in the user-supplied subroutine $BCND$ and take form

$$y_i(0) = y_i(1), \quad i = 1, \ldots, 6. \tag{5.31}$$

We also introduce an integral condition for mass conservation of the steady solution,

$$\int_0^1 y_1 d\alpha = 0, \tag{5.32}$$

an integral condition fixing the norm of the eigenfunction,

$$\int_0^1 y_3^2 d\alpha = c, \tag{5.33}$$

where c is a fixed positive constant, and computational pinning to break the translational symmetry. So the number of the integral conditions that is described by the variable

$NINT$ is 3.

We remind that the number of the free parameters (i.e., the parameters that are allowed to vary for the well-posedness of the continuations) is given by the formula

$$NBC + NINT - NDIM + 1, \tag{5.34}$$

which for our problem turns out to be 4. So, if we choose one of the parameters as the principal one, for example, the domain size, L, or the average value of the solution, $\bar{u}$, then three more parameters must adapt in the continuation. We have only two other parameters that can adapt, namely, the eigenvalue, s, and the parameter C_0. Hence, one more parameter is missing. This complication comes from the fact that equation (5.22) corresponds to a Hamiltonian dynamical system. To break this, we introduce an additional so-called unfolding parameter ϵ, and rewrite system (5.25), (5.26) as

$$\dot{y}_1 = Ly_2 - \epsilon[(y_1 + \bar{u})^3 - (y_1 + \bar{u}) + C_0], \tag{5.35}$$

$$\dot{y}_2 = L[(y_1 + \bar{u})^3 - (y_1 + \bar{u}) + C_0]. \tag{5.36}$$

A continuous family of periodic solutions to this system exists only for $\epsilon = 0$, and the solutions then are the same as those of (5.25), (5.26). Therefore, parameter ϵ can be used as an additional parameter in the continuation, and it will stay at approximately zero value during continuation runs. This technique is used, for example, in the Auto07p tutorial 'r3b' [31], Aronson et al. [5] for a conservative system and is explained in more detail, for example, in Doedel et al. [32], Muñoz-Almaraz et al. [81, 82]. This techniques has also been used in Auto tutorials by Thiele et al. [107, 108].

5.3.2 The case of the convective Cahn-Hilliard equation

5.3.2.1 Real eigenvalue problem for the convective Cahn-Hilliard equation

In this section, we explain the numerical continuation procedure for computation of stationary and travelling periodic solutions of the convective Cahn-Hilliard equation (2.28) along with their eigenvalues, and we will first discuss the real eigenvalues. Integrating equation (5.2) for stationary and travelling solutions once, we obtain

$$0 = -\left[\frac{Du_0^2}{2} - (u_0 - u_0^3 + u_0'')'\right] + vu_0 - C_0, \tag{5.37}$$

where C_0 corresponds to the flux in the co-moving frame. Our goal is to solve this equation along with the eigenvalue problem (5.10), which can be written as

$$s\,\eta = (-Du_0' + 6u_0'^2 + 6u_0u_0'')\eta + (v - Du_0 + 12u_0u_0')\eta' + (3u_0^2 - 1)\eta'' - \eta'''', \quad (5.38)$$

where as before s is the growth rate and $\eta(x)$ is the eigenfunction. Here, we will assume that s is real.

To use Auto07p, we first write these equations as an autonomous system of seven first-order ordinary differential equations on the interval $[0, 1]$. So we introduce the variables $y_1 = u_0 - \bar{u}$, $y_2 = u_0'$, $y_3 = u_0''$ and obtain from equation (5.37) the following three-dimensional dynamical system:

$$\dot{y}_1 = Ly_2, \quad (5.39)$$
$$\dot{y}_2 = Ly_3, \quad (5.40)$$
$$\dot{y}_3 = L[C_0 + v(y_1 + \bar{u}) - D(y_1 + \bar{u})^2/2 - y_2 + 3(y_1 + \bar{u})^2 y_2], \quad (5.41)$$

where L is the physical domain size, and dots denote derivatives with respect to $\alpha \equiv x/L$. Note that, the fields $y_1(\alpha)$, $y_2(\alpha)$ and $y_3(\alpha)$ correspond to the correctly scaled physical fields $u_0(L\alpha) - \bar{u}$, $u_0'(L\alpha)$ and $u_0''(L\alpha)$.

Further, we introduce the variables $y_4 = \eta$, $y_5 = \eta'$, $y_6 = \eta''$, $y_7 = \eta'''$ and rewrite equation (5.38) as a fourth-order dynamical system:

$$\begin{aligned}
\dot{y}_4 &= Ly_5 && (5.42)\\
\dot{y}_5 &= Ly_6 && (5.43)\\
\dot{y}_6 &= Ly_7 && (5.44)\\
\dot{y}_7 &= L\big[-sy_4 + (-Dy_2 + 6y_2^2 + 6[y_1 + \bar{u}]y_3)y_4 \\
&\qquad +(v - D[y_1 + \bar{u}] + 12[y_1 + \bar{u}]y_2)y_5 + (3[y_1 + \bar{u}]^2 - 1)y_6\big]. && (5.45)
\end{aligned}$$

Thus, in total we have $NDIM = 7$ equations. We use periodic boundary conditions for all the variables y_i:

$$y_i(0) = y_i(1), \quad i = 1, \ldots, 7, \quad (5.46)$$

so that $NBC = 7$, and an integral condition for mass conservation of u_0,

$$\int_0^1 y_1 d\alpha = 0, \tag{5.47}$$

an integral condition fixing the norm of the eigenfunction,

$$\int_0^1 y_4^2 d\alpha = c, \tag{5.48}$$

where c is a positive constant, and computational pinning to break the translational symmetry, so that $NINT = 3$.

The number of the free parameters is

$$NBC + NINT - NDIM + 1 = 4. \tag{5.49}$$

Thus, when choosing, for example, the driving force, D, as the principal continuation parameter, we additionally choose the eigenvalue, s, the flux, C_0, and the velocity, v, as the parameters that must adapt during the continuation.

5.3.2.2 Complex eigenvalue problem for the convective Cahn-Hilliard equation

In this section, we will discuss how to compute complex eigenvalues of the convective Cahn-Hilliard equation by continuation techniques. Let us assume that an eigenvalue s in (5.38) is a complex number. We write

$$s = s_R + i s_I, \tag{5.50}$$

where $s_R = \mathrm{Re}(s)$ and $s_I = \mathrm{Im}(s)$. The eigenfunction η then also has real and imaginary parts, η_R and η_I, respectively, i.e.,

$$\eta = \eta_R + i\eta_I. \tag{5.51}$$

Multiplying (5.50) by (5.51), we obtain

$$s\,\eta = \underbrace{(s_R\eta_R - s_I\eta_I)}_{\mathrm{Re}(s\,\eta)} + i\,\underbrace{(s_R\eta_I + s_I\eta_R)}_{\mathrm{Im}(s\,\eta)}. \tag{5.52}$$

Then, we can easily find that the real part of equation (5.38) is

$$\begin{aligned} s_R\eta_R - s_I\eta_I &= (-Du_0' + 6u_0'^2 + 6u_0u_0'')\eta_R + (v - Du_0 + 12u_0u_0')\eta_R' \\ &\quad +(3u_0^2 - 1)\eta_R'' - \eta_R'''', \end{aligned} \tag{5.53}$$

and the imaginary part of equation (5.38) is

$$\begin{aligned} s_R\eta_I + s_I\eta_R &= (-Du_0' + 6u_0'^2 + 6u_0u_0'')\eta_I + (v - Du_0 + 12u_0u_0')\eta_I' \\ &\quad +(3u_0^2 - 1)\eta_I'' - \eta_I''''. \end{aligned} \tag{5.54}$$

Now, we have a third-order ordinary differential equation (5.37) for u_0 that we have to solve together with the fourth-order equations (5.53) and (5.54) for η_R and η_I.

To use Auto07p, we rewrite these equations as an autonomous system of eleven first-order ordinary differential equations on the interval $[0, 1]$. So we introduce the variables $y_1 = u_0 - \bar{u}$, $y_2 = u_0'$, $y_3 = u_0''$ and obtain from equation (5.37) the same three-dimensional dynamical system as in the previous section, i.e., equations (5.39)–(5.41).

Further we introduce the variables $y_4 = \eta_R$, $y_5 = \eta_R'$, $y_6 = \eta_R''$, $y_7 = \eta_R'''$ and $y_8 = \eta_I$, $y_9 = \eta_{I'}$, $y_{10} = \eta_I''$, $y_{11} = \eta_I'''$, and rewrite equations (5.53) and (5.54) as

$$\dot{y}_4 = Ly_5 \tag{5.55}$$

$$\dot{y}_5 = Ly_6 \tag{5.56}$$

$$\dot{y}_6 = Ly_7 \tag{5.57}$$

$$\begin{aligned} \dot{y}_7 &= L\big[- s_Ry_4 + s_Iy_8 + (-Dy_2 + 6y_2^2 + 6[y_1 + \bar{u}]y_3)y_4 \\ &\quad +(v - D[y_1 + \bar{u}] + 12[y_1 + \bar{u}]y_2)y_5 + (3[y_1 + \bar{u}]^2 - 1)y_6\big], \end{aligned} \tag{5.58}$$

$$\dot{y}_8 = Ly_9 \tag{5.59}$$

$$\dot{y}_9 = Ly_{10} \tag{5.60}$$

$$\dot{y}_{10} = Ly_{11} \tag{5.61}$$

$$\begin{aligned} \dot{y}_{11} &= L\big[- s_Ry_8 - s_Iy_4 + (-Dy_2 + 6y_2^2 + 6[y_1 + \bar{u}]y_3)y_8 \\ &\quad +(v - D[y_1 + \bar{u}] + 12[y_1 + \bar{u}]y_2)y_9 + (3[y_1 + \bar{u}]^2 - 1)y_{10}\big]. \end{aligned} \tag{5.62}$$

Thus, in total we have $NDIM = 11$ equations. As before, we use periodic boundary conditions for all the varialbes y_i:

$$y_i(0) = y_i(1), \quad i = 1, \ldots, 11. \tag{5.63}$$

Therefore, the number of boundary conditions is $NBC = 11$. We also use an integral condition for mass conservation of u_0,

$$\int_0^1 y_1 d\alpha = 0, \tag{5.64}$$

computational pinning to break the translational symmetry of u_0, and an integral condition fixing the norm of the eigenfunction,

$$\int_0^1 (y_4^2 + y_8^2) d\alpha = c. \tag{5.65}$$

We note that an eigenfunction with a given norm multiplied by $e^{i\varphi}$ is again an eigenfunction with the same norm. To break this invariance, we need to impose one more condition. Numerically, this can be implemented by imposing computational pinning for y_8. As a result, the number of integral conditions is $NINT = 4$.

The number of the free parameters is

$$NBC + NINT - NDIM + 1 = 5. \tag{5.66}$$

Thus, when choosing, for example, the driving force, D, as the principal continuation parameter, we additionally choose the real and the imaginary parts of the eigenvalue, s_R and s_I, repsectively, the flux, C_0, and the velocity, v, as the parameters that must adapt during the continuation. We also note that for initial guesses for complex eigenvalues, we often use the Matlab numerical procedure described in Section 5.2.

5.3.2.3 Numerical computation of branches of time-periodic solutions

In this section, we discuss how continuation techniques can be used to compute, in addition to branches of stationary and travelling periodic solutions, branches of time-periodic solutions of the convective Cahn-Hilliard equations, see also Lin et al. [75] for a more generalised discussion, and also Bordyugov and Engel [10], Köpf and Thiele [67], Lin et al. [76], Pototsky et al. [90, 91] for the discussion of similar computational

approaches. (We note here that time-periodic solutions do not exist for the standard Cahn-Hilliard equation, since for such a solution the energy $F[u]$ would also be periodic in time, which is not possible as it is a Lyapunov functional and should be decaying in time.) Introducing a generalised moving coordinate $x \to x - a(t)$ in equation (2.28), we obtain

$$u_t = \dot{a}u_x - Duu_x - (u - u^3 + u_{xx})_{xx} = 0, \tag{5.67}$$

where the dot denotes differentiation with respect to time. We assume here that the speed of the moving frame, $\dot{a}$, is not necessarily a constant, but can vary in time. This will allow us to compute not only stationary and travelling periodic solutions but also time-periodic solutions. We consider this equation on a periodic domain of length L.

As usual, we impose the condition fixing the mean value of the solution over the spatial period,

$$\frac{1}{L}\int_0^L u\,dx = \bar{u}. \tag{5.68}$$

To break the translational symmetry due to periodic boundary conditions, we also impose the following integral constraint:

$$\int_0^L u\sin(nqx)\,dx = 0, \tag{5.69}$$

where $q = 2\pi/L$ and n is an integer.

Next, we represent u as a truncated Fourier series,

$$u(x,t) = \hat{u}_0(t) + \sum_{k=1}^{N}[\hat{u}_{2k-1}(t)\cos(kqx) + \hat{u}_{2k}(t)\sin(kqx)], \tag{5.70}$$

where $\hat{u}_i$'s are the Fourier coefficients of u and N is a sufficiently large integer. Note that

$$\hat{u}_0 = \bar{u}, \qquad \hat{u}_{2n} = 0, \tag{5.71}$$

due to conditions (5.68) and (5.69), respectively. Substituting (5.70) in (5.67), we obtain the following dynamical system for the Fourier coefficients:

$$\frac{d\hat{u}_i}{dt} = \mathcal{N}_i(\hat{u}_0, \ldots, \hat{u}_{2N}), \quad i = 1, \ldots, 2n-1, 2n+1, \ldots, 2N, \tag{5.72}$$

where $\mathcal{N}_i$'s are nonlinear functions of all the Fourier coefficients. Note that in our numerical implementation, given the Fourier coefficients $\hat{u}_0, \ldots, \hat{u}_{2N}$, we use the inverse fast Fourier transform to obtain a numerical approximation of u and to compute

the right-hand side of (5.67). After that, we can apply the fast Fourier transform to the right-hand side of (5.67) to obtain $\mathcal{N}_i(\hat{u}_0, \ldots, \hat{u}_{2N}), i = 1, \ldots, 2n-1, 2n+1, \ldots, 2N$.

Multiplying equation (5.67) by $\sin(nqx)$ and integrating over the domain, we find that the speed, $\dot{a}$, should satisfy

$$\dot{a} = \frac{\int_0^L \left[Duu_x + (u - u^3 + u_{xx})_{xx}\right] \sin(nqx)\, dx}{\int_0^L u_x \sin(nqx)\, dx}. \tag{5.73}$$

Stationary and travelling periodic solutions of (2.28) correspond to steady-state solutions of (5.72), where the speed is given by (5.73) and is a constant. By using Auto07p [31] together with FFTW3 package [1, 39] and performing a continuation with respect to the domain size, L, or the driving force D, or the mean value of the solution, $\bar{u}$, we can obtain branches of stationary and travelling periodic solutions, which are identical to the branches computed by the methods discussed in the previous sections. In addition to branch points that may appear on the solution branches and that correspond to bifurcations to side branches, our formulation allows for the detection of Hopf-bifurcation points where time-periodic solutions bifurcate. By starting from these bifurcation points and switching branches, we can compute such secondary branches of time-periodic solutions, see, for example, Auto tutorial 'abc' [31] for the computation of time-periodic solutions from Hopf bifurcations. Note that for time-periodic solutions the wave speed is not a constant anymore, but is a time-periodic function and is fully determined by the solution through formula (5.73). Having computed a time-periodic solutions, we can obtain the speed, $\dot{a}$, and then we can transform the solution back to the original frame of reference.

5.4 Linear stability and coarsening of two double-interface (droplet) solutions

In Chapter 4, we discussed numerical computation of single- and double-interface solutions of the standard ($D = 0$) and convective ($D \neq 0$) Cahn-Hilliard equations. However, as discussed in Section 2.3, for the standard Cahn-Hilliard equation, it is known that the dynamics, after the initial stage of evolution from a homogeneous state towards a superposition of large-amplitude structures of a typical length scale that is mainly determined by the initial perturbation and the length scale of the most unstable

mode, evolves towards large-amplitude structures of larger length scales, i.e., coarsening takes place. This is due to the fact that the structures of the smaller length scale are unstable to perturbations of larger length scales, the so-called coarsening modes (see, e.g., [102]). Thus, the coarsening process can happen in several stages, namely, the structures that are obtained after the initial stage of evolution coarsen to structures of larger spatial length scales, which in turn coarsen to structures of even larger spatial length scales, and so on, until a stable structure of the system size is obtained. This process was demonstrated in time-dependent simulations from a random initial condition in Section 2.3. In the following Sections, we analyse in detail the coarsening of two-droplet solutions of the standard and convective Cahn-Hilliard equations by performing the linear stability study of such solutions.

5.4.1 The case of the standard Cahn-Hilliard equation

First, we note that branches of two-droplet solutions (when $n = 2$) for the standard Cahn-Hilliard equation can be obtained from the $n = 1$ branches (that were discussed in Chapter 4) by multiplying the solution period for the latter branches by $n = 2$. Our calculations show, that there are no side branches for the standard Cahn-Hilliard equation, and, therefore, there is actually no need in recomputing the primary branches. We only need to analyse the stability of two-droplet solutions. First, we note that zero is always an eigenvalue of the linearised problem with the eigenfunction given by $u_0'(x)$, and it is associated with the translational invariance of the equation. The emergence of the various coarsening mechanisms can then be explained by the following consideration (see also Thiele et al. [102, 104]). Each of the two-droplet solutions can be considered as a superposition of four fronts (two kink and two anti-kink solutions). Each of these solutions, when considered individually, has a zero eigenvalue with the eigenfunction given by the derivative of the solution (due to the translational invariance). When the fronts are superimposed, the corresponding eigenfunctions are also superimposed (with small corrections). For a single droplet, the superimposed eigenfunctions result in two qualitatively different cases: either both fronts are shifted in the same direction (which results in the overall translation of the droplet) or the fronts are shifted in the opposite directions (which results in the decrease or increase of the volume of the droplet). Schematic representations are shown in Figs. 5.2(a) and (b). For a pair of droplets on a periodic domain, only the three (up to the positive or negative sign) possible combinations corresponding to the overall mass conservation should be considered. One of

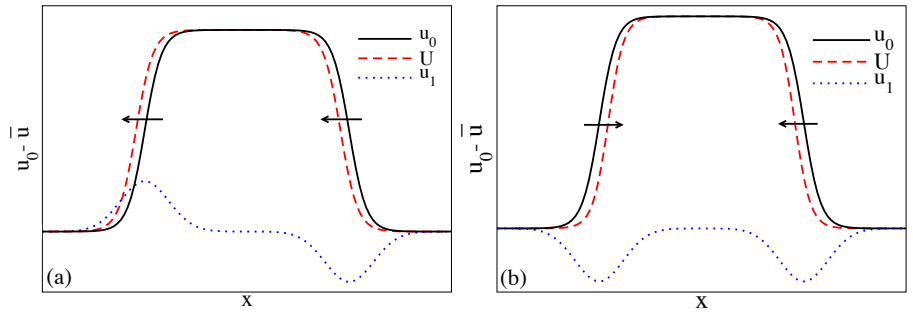

Figure 5.2: Shown are symmetry modes for one-droplet solutions. Panel (a) represents the translational mode and panel (b) represent the volume mode. The solid lines correspond to the solutions $u_0(x)$. The dotted lines correspond to the eigenfunctions $u_1(x)$. The dashed lines correspond to the solution $u_0(x)$ superimposed with eigenfunction $u_1(x)$ multiplied by a small coefficient ϵ, i.e., $U(x) = u_0(x) + \epsilon u_1(x)$. The arrows indicate the directions where the fronts of the droplets shift after the eigenfunctions are added.

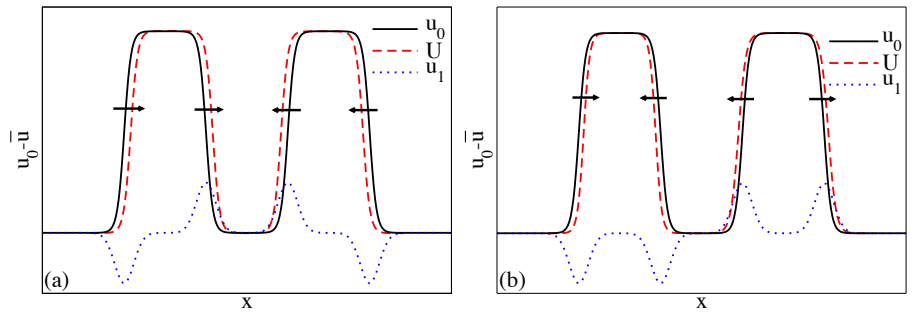

Figure 5.3: Shown are symmetry modes for two-droplet solutions. Panel (a) represents the translational mode and panel (b) represent the volume mode. The solid lines correspond to the solutions $u_0(x)$. The dotted lines correspond to the eigenfunctions $u_1(x)$. The dashed lines correspond to the solution $u_0(x)$ superimposed with eigenfunction $u_1(x)$ multiplied by a small coefficient ϵ, i.e., $U(x) = u_0(x) + \epsilon u_1(x)$. The arrows indicate the directions where the fronts of the droplets shift after the eigenfunctions are added.

these combinations will result in the overall translation of both droplets in the same direction, and it must correspond to the zero eigenvalue. The other two will correspond to two coarsening modes, namely, the translational and volume modes, see schematic representations in Figs. 5.3(a) and (b). The arrows in these figures indicate the directions in which the fronts are shifted when the eigenfunctions are added. As can be seen in these figures, for the translational mode the droplets move towards each other, and for the volume mode the volume of one of the droplets decreases while the volume of the other one increases. The eigenvalues for these modes correspond to the perturbed zero eigenvalue. The larger the separation distances between the fronts are the closer to zero these eigenvalues should be. It is also interesting to note that the translational/volume

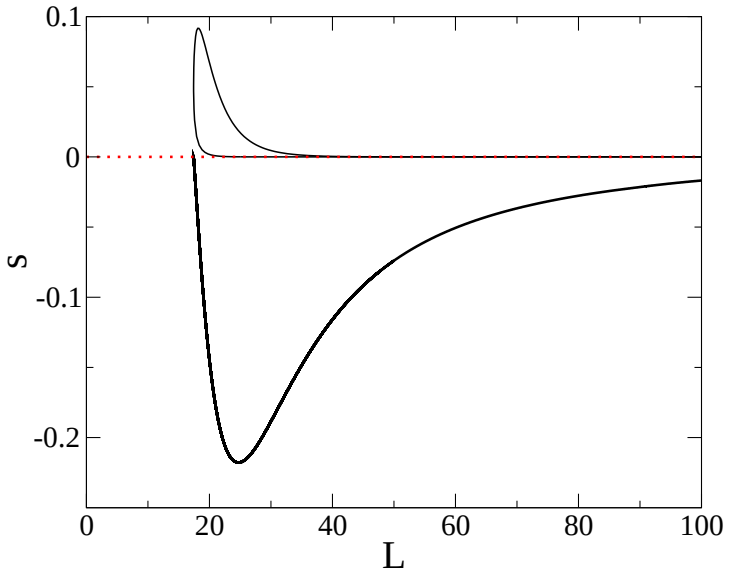

Figure 5.4: The dependence on the domain size L of the dominant eigenvalues s of two-droplet solutions of the standard Cahn-Hilliard equation (2.28), when $D = 0$, for the case when $\bar{u} = 0.4$. The thin solid lines correspond to two positive eigenvalues, and the thick solid line shows the dominant negative eigenvalue.

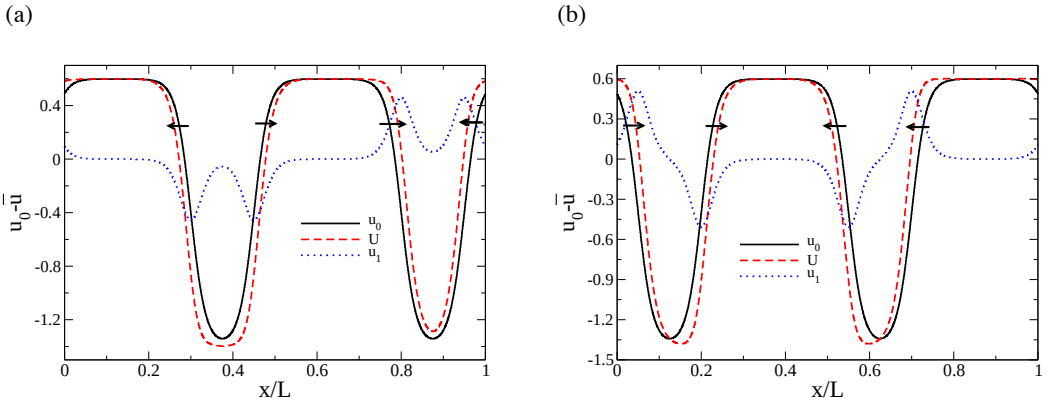

Figure 5.5: Shown are symmetry modes for two-droplet solutions of the standard Cahn-Hilliard equation (2.28), when $D = 0$, for the case when $\bar{u} = 0.4$ and $L = 40$. Panel (a) corresponds to the dominant coarsening mode (which turns out to be the translational mode) and panel (b) corresponds to the other coarsening mode (which turns out to be the volume mode). The solid lines correspond to the solutions $u_0(x)$. The dotted lines correspond to the eigenfunctions $u_1(x)$. The dashed lines correspond to the solution $u_0(x)$ superimposed with eigenfunction $u_1(x)$ multiplied by a small coefficient ϵ, i.e., $U(x) = u_0(x) + \epsilon u_1(x)$. The arrows indicate the directions where the fronts of the droplets shift after the eigenfunctions are added.

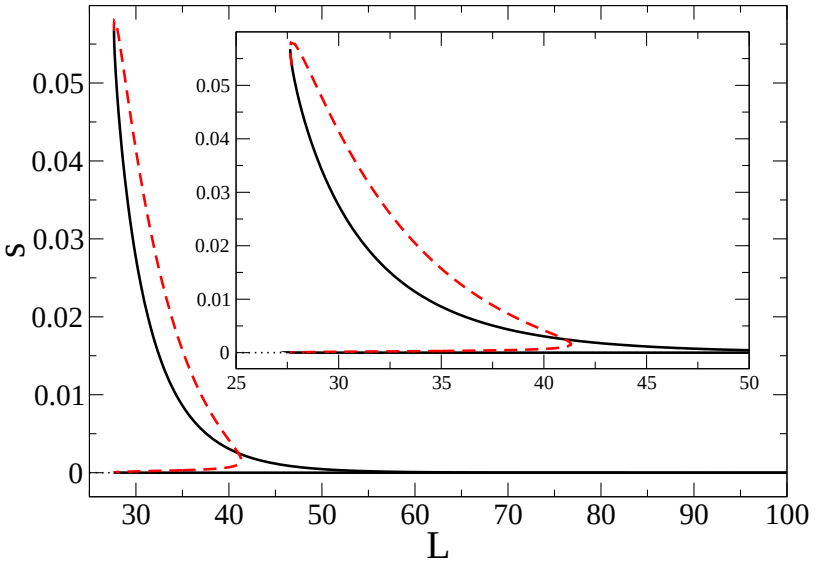

Figure 5.6: The dependence on the domain size L of the positive eigenvalues s corresponding to coarsening modes of two-droplet solutions of the standard Cahn-Hilliard equation (2.28), when $D = 0$, for the case when $\bar{u} = 0.55$. The black solid lines correspond to the upper branch of solutions, and the red dashed lines correspond to the lower branch of solutions that bifurcates subcritically from the homogenous solution.

mode for a two-droplet solution turns out to be the volume/translational mode for the corresponding two holes.

The calculations confirm that for a two-droplet solution there are additionally two positive eigenvalues close to zero. The dependence of the positive eigenvalues (thin solid line) and the first negative eigenvalue (thick solid line) on the domain size is shown in Fig. 5.4 for $\bar{u} = 0.4$. We can see that the two eigenvalues annihilate in a saddle-node bifurcation at the linear stability threshold for the homogeneous solution. The eigenfunctions u_1 corresponding to the largest and the smallest positive eigenvalues are shown in Figs. 5.5(a) and (b), respectively, by blue dotted lines for $L = 40$. The black solid lines in these figures show the two-droplet solutions, u_0, and the red dashed lines show the two-droplet solutions superimposed with the eigenfunctions, $U = u_0 + \epsilon u_1$ for sufficiently small ϵ. We can observe that the perturbed profiles again look like two-droplet solutions. However, the fronts of the solutions are shifted. The arrows indicate in which direction the fronts are shifted. In Fig. 5.5(a), we can observe that for each of the droplets both fronts are shifted in the same direction. This results in one droplet moving to the left and the other one moving to the right, i.e., we obtain coarsening by

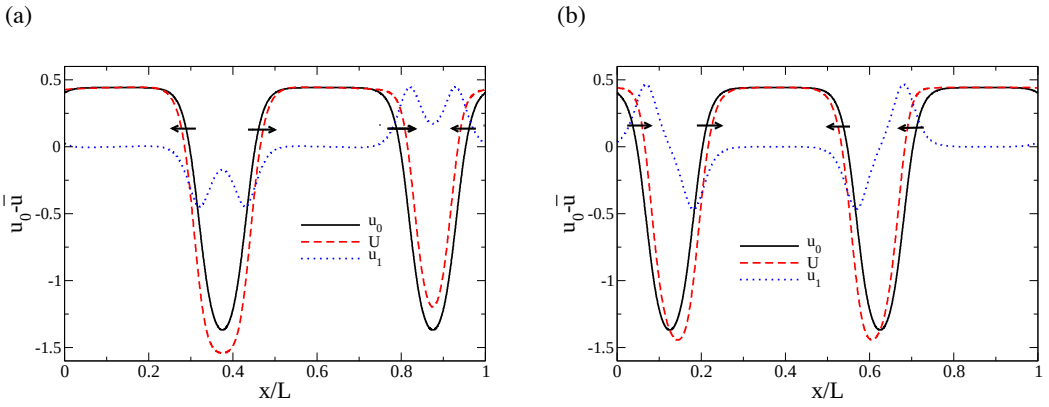

Figure 5.7: Shown are symmetry modes for the upper branch of two-droplet solutions of the standard Cahn-Hilliard equation (2.28), when $D = 0$, for the case when $\bar{u} = 0.55$ and $L = 40$. Panel (a) corresponds to the dominant coarsening mode (which turns out to be the translational mode) and panel (b) corresponds to the other coarsening mode (which turns out to be the volume mode). The solid lines correspond to the solutions $u_0(x)$. The dotted lines correspond to the eigenfunctions $u_1(x)$. The dashed lines correspond to the solution $u_0(x)$ superimposed with eigenfunction $u_1(x)$ multiplied by a small coefficient ϵ, i.e., $U(x) = u_0(x) + \epsilon u_1(x)$. The arrows indicate the directions where the fronts of the droplets shift after the eigenfunctions are added.

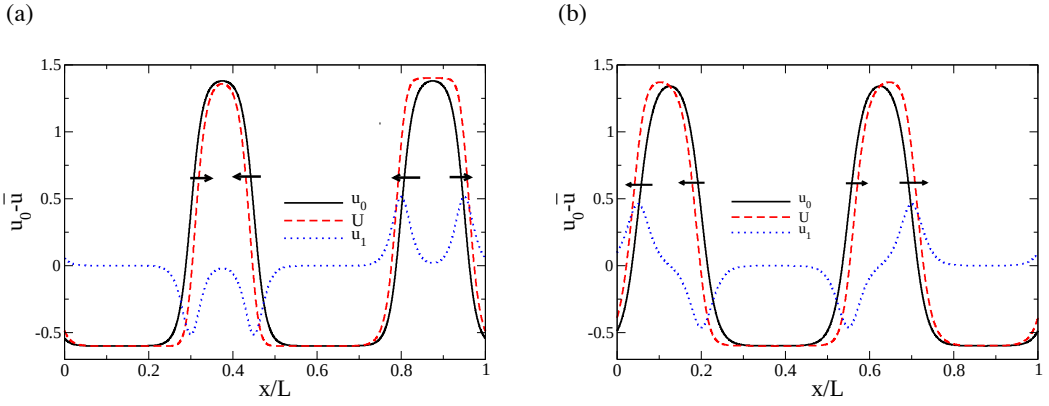

Figure 5.8: Shown are symmetry modes for two-droplet solutions of the standard Cahn-Hilliard equation (2.28), when $D = 0$, for the case when $\bar{u} = -0.4$ and $L = 40$. Panel (a) corresponds to the dominant coarsening mode (which turns out to be the volume mode) and panel (b) corresponds to the other coarsening mode (which turns out to be the translational mode). The solid lines correspond to the solutions $u_0(x)$. The dotted lines correspond to the eigenfunctions $u_1(x)$. The dashed lines correspond to the solution $u_0(x)$ superimposed with eigenfunction $u_1(x)$ multiplied by a small coefficient ϵ, i.e., $U(x) = u_0(x) + \epsilon u_1(x)$. The arrows indicate the directions where the fronts of the droplets shift after the eigenfunctions are added.

translation and the corresponding eigenfunction is the translational mode. In Fig. 5.5(b), we can observe that for each of the droplets both fronts are shifted in the opposite directions. This results in the fact that the volume of one of the droplet is decreasing and the volume of the other one increasing, i.e., we obtain coarsening by the volume transfer from one of the droplets to the other one and the corresponding eigenfunction is the volume mode. For $\bar{u} = 0.4$, we see that the dominant mode (corresponding to the largest positive eigenvalue) is the translational one. The coarsening due to the translational mode is demonstrated in time-dependent simulations for $\bar{u} = 0.4$ in Fig. 2.8(a) in Section 2.3.

The results for $\bar{u} = 0.55$ are additionally shown in Figs. 5.6 and 5.7. Note that for this value of $\bar{u}$ the primary bifurcation is subcritical and there exists a range of L values for which there exist two solutions, see Fig. 4.5. The solutions of smaller norm (lower brach) are linearly unstable even for $n = 1$. The solutions of larger norm (upper branch) are linearly stable for $n = 1$ but become unstable to coarsening modes for $n = 2$. Fig. 5.6 shows the dependence of the positive eigenvalues corresponding to coarsening modes, where the black solid lines correspond to the upper branch of solutions and the red dashed lines correspond to the lower branch of solutions. The eigenfunctions u_1 corresponding to the largest and the smallest positive eigenvalues for the upper branch of solutions are shown in Figs. 5.7(a) and (b), respectively, by blue dotted lines along with the solution profiles (black solid lines) and the perturbed solutions profiles (red dashed lines) for $L = 40$. As for $\bar{u} = 0.55$, we can observe that the dominant coarsening mode is translational and the other mode is the volume mode.

Next, let us point out that if u_0 is a steady solution of the standard Cahn-Hilliard equation for a particular value of $\bar{u}$, then $-u_0$ is again a steady solution of the standard Cahn-Hilliard equation for the mean value equal to $-\bar{u}$. More interestingly, from equation 5.7, it can be noticed that the linearised operator does not change. Thus, the eigenvalues and the eigenfunctions will be exactly the same as for the mean value equal to $\bar{u}$. Therefore, for example for $\bar{u} = -0.4$, the eigenvalues are also given by Fig. 5.4. We again obtain two coarsening modes (which are exactly the same as for $\bar{u} = 0.4$). However, when the steady solutions are superimposed with the eigenfunctions, as shown in Fig. 5.8, we can observe that the roles of the coarsening modes are interchanged, namely, the dominant mode is now the volume mode and the other mode is now translational. The coarsening due to the volume mode is demonstrated in time-dependent simulations for $\bar{u} = -0.4$ in Fig. 2.8(b) in Section 2.3.

5.4.2 The case of the convective Cahn-Hilliard equation

In this section, we study in detail how the introduction of the driving force affects two-droplet solutions of the Cahn-Hilliard equation, namely, we consider two-droplet solutions of equation (2.28) with $D \neq 0$. We compute both primary branches and side branches of symmetry-broken solutions along with branches of time-periodic solutions, and we discuss linear stability of primary and side branches and construct linear stability diagrams in the (D, L)- and $(D, \bar{u})$-planes.

5.4.2.1 Symmetry breaking

First, we compute by continuation branches of two-droplet solutions in dependence of the driving force D for several fixed values of the domain size, L, and fixed values of $\bar{u}$. Note that branches of two-droplet solutions (when $n = 2$) can in fact be obtained from the $n = 1$ branches (that were discussed in Chapter 4) by multiplying the solution period for the latter branches by $n = 2$. We call the resulting solution branches 2-mode primary branches. Solutions on such branches have discrete internal translational symmetry. Solution branches bifurcating from these primary branches in secondary bifurcations will be called secondary solution branches. Notice that the secondary bifurcations should break the discrete symmetry of solutions (otherwise, if side branches with a discrete internal translational symmetry existed, they would also appear in the calculations presented in Chapter 4). Thus, secondary bifurcations result in a larger spatial period and, hence, if stable, are associated with coarsening of the pattern. However, we emphasise here that at least for $D < \sqrt{2}$ (as discussed in Chapter 3) for a two-droplet solution given on a domain of certain length there exists a one-droplet solution of the period equal to that domain length, and true coarsening would correspond to evolution towards such a droplet solution. For completeness of the bifurcation diagrams, we also include branches of such one-droplet (i.e., 1-mode) solutions.

Figs. 5.9–5.23 show the results of the calculations for several values of L and for $\bar{u} = 0.4$ and 0.55. In the bifurcation diagrams, we use black solid lines to show the 2-mode primary branches (that are identical to the $n = 1$ primary branches, only the domain sizes L have twice the values of those for $n = 1$ branches). The secondary branches are shown by dashed lines, and the dotted lines show the time-periodic branches. The bifurcation points to secondary branches are indicated by red circles, the

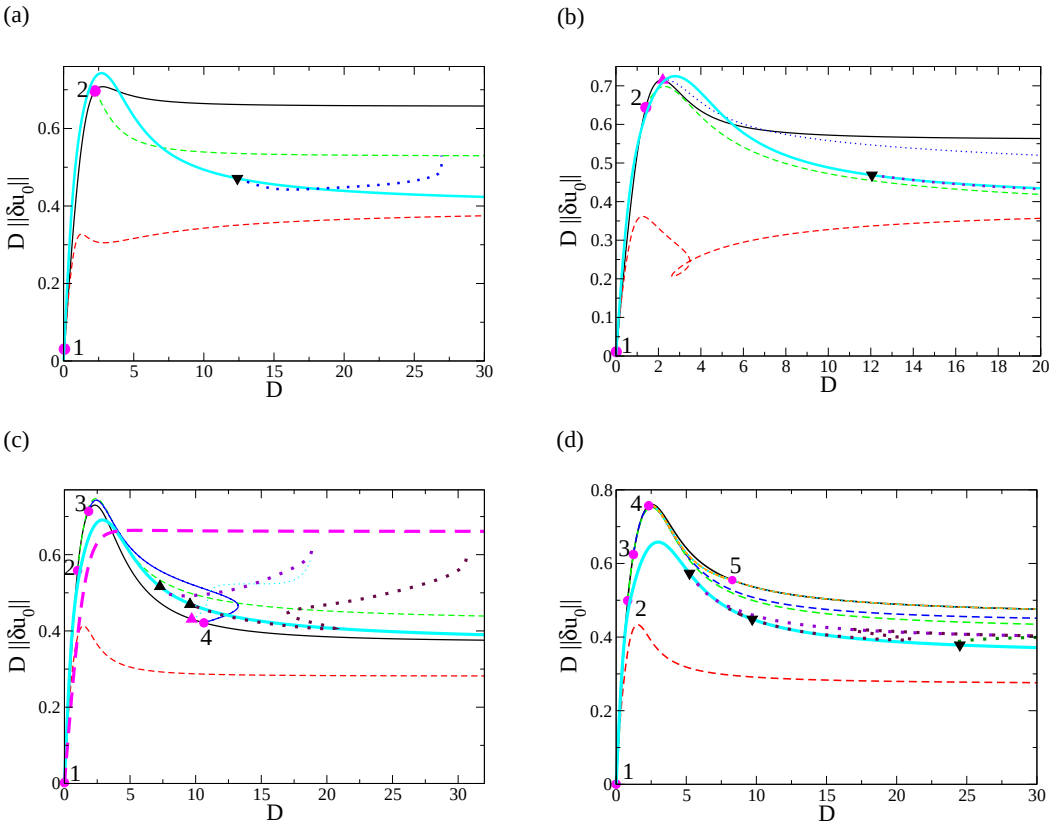

Figure 5.9: The bifurcation diagrams of the one- and two-droplet ($n = 1$ and $n = 2$) solutions of the convective Cahn-Hilliard equation (2.28) for the case $\bar{u} = 0.4$ with (a) $L = 22$, (b) $L = 25$, (c) $L = 30$ and (d) $L = 35$. Shown is the dependence of the norm $\|\delta u_0\|$ (multiplied by D for presentational purposes) on the driving force D. The (blue) thick solid lines show the 1-mode branches, the thin solid lines show the 2-mode primary branches, the dashed lines show the secondary branches, the thick dotted lines show the time-periodic branches bifurcating from the 1-mode branches and the thin dotted lines show the time-periodic branches bifurcating from the 2-mode primary branches. The red circles indicate pitchfork bifurcations to side branches on the 2-mode primary branches, the black triangles indicate Hopf bifurcations to time-periodic solutions from the 1-mode branches and the red triangles indicate Hopf bifurcations to time-periodic solutions from the 2-mode primary branches. In panel (c), we also show a 3-mode branch of solutions by a thick dashed line to which the branches of time-periodic solutions bifurcating from the 1-mode branch apparently tend.

red solid squares indicate saddle-node bifurcations, and the red solid triangles indicate Hopf bifurcations to time-periodic branches. In addition, (blue) thick solid lines show the branches of one-droplet solutions of the period equal to the domain length L. The black solid squares indicate saddle-node bifurcations on these 1-mode branches and the black solid triangles indicate Hopf bifurcations to time-periodic branches on the 1-mode branches. The thick dotted lines show such branches of time-periodic solutions.

Figs. 5.9(a)–(d) show bifurcation diagrams for $\bar{u} = 0.4$ and $L = 22$, 25, 30 and 35, respectively. We can see that the primary branches do not have saddle nodes and continue

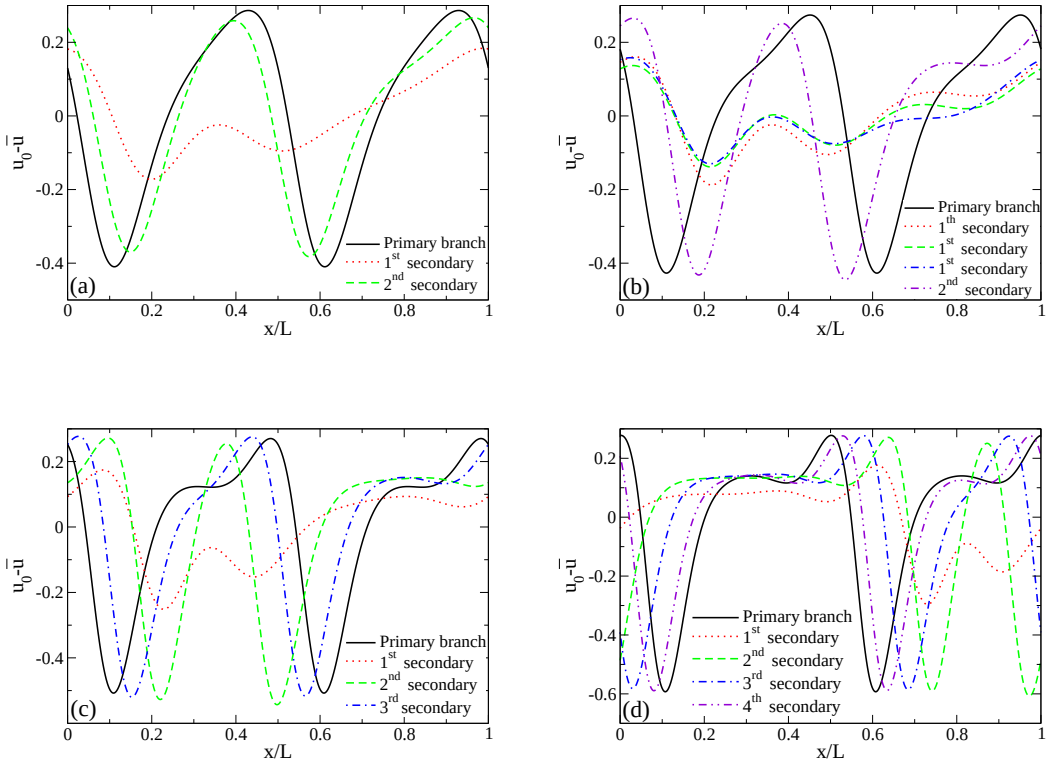

Figure 5.10: Solution profiles from the 2-mode primary and secondary branches for $\bar{u} = 0.4$ when $D = 3$ and (a) $L = 22$, (b) $L = 25$, (c) $L = 30$ and (d) $L = 35$, see Figs. 5.9(a)-(d). The different solutions are explained in the legends. Note that in panel (b) there are three different solutions from the first secondary branch at $D = 3$ shown by the dotted, dashed and dot-dashed lines. These solutions are shown in the order of decreasing norm $\|\delta u\|$, i.e. the dotted line corresponds to the solution with the largest norm and the dot-dashed line corresponds to the solution with the smallest norm.

towards infinite D, in agreement with the results presented in Chapter 4. We can also observe in Figs. 5.9(a) and (b) that for $L = 22$ and 25 there are two bifurcation points on the 2-mode primary branch, and the secondary branches that start at these bifurcation points do not reconnect to the primary branch but also continue towards infinite D. Figs. 5.9(b) and (c) have one Hopf bifurcation each on the 2-mode primary branches, and the time-periodic branches starting at these bifurcation points extend large values of D. Figs. 5.9(c) and (d) show that for $L = 30$ and 35 there are four and five bifurcation points on the 2-mode primary branches, respectively. Some of the secondary branches that start at these points reach large values of D and may continue to infinity, whereas secondary branches starting at other bifurcation points reconnect to the primary branch. In particular, the secondary branches starting at bifurcation points 1 and 2 in Fig. 5.9(c) and the secondary branches starting at bifurcation points 1, 2 and 3 in Fig. 5.9(d) go off to infinity, while bifurcation points 3 and 4 in Fig. 5.9(c) and bifurcation points 4 and 5 in Fig. 5.9(d) are connected to each other by secondary branches. As regards the

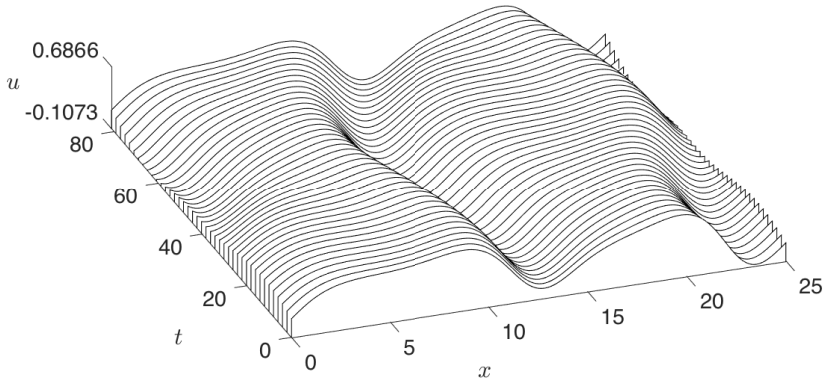

Figure 5.11: Time evolution over one period of time of the time-periodic solution for $\bar{u} = 0.4$, $L = 25$ when $D = 3$ (see Fig. 5.10(b)).

1-mode branches (blue thick solid line), we find that in panes (a) and (b), there exist one Hopf bifurcation on each of the branches. The time-periodic branch emanating at the Hopf bifurcation in panel (a) terminates on the secondary branch (apparently in a homoclinic bifurcation) emanating from the second bifurcation point on the 2-mode primary branch. The time-periodic branch emanating at the Hopf bifurcation in panel (b) extends to large values of D. In panel (c), we can see that there are two Hopf bifurcation points on the 1-mode branch. Our numerical results indicate that these branches possibly terminate on the 3-mode branch (show by the thick dashed line in the inset) in homoclinic bifurcation, although should mention that we had numerical difficulties in continuing these branches beyond certain points and we not able to approach the 3-mode branch sufficiently closely. In panel (d), we observe that there are three Hopf bifurcation points on the 1-mode branch, and the time-periodic branches starting at these bifurcation points extend to large values of D.

Figs. 5.10(a)–(d) show selected solution profiles for $\bar{u} = 0.4$ when $D = 3$ for $L = 22$, 25, 30 and 35, respectively (see the corresponding panels of Fig. 5.9). We exclude the solution profiles for the 1-mode branches. Note that at $L = 25$, there are three different solutions on the first secondary branch that correspond to $D = 3$. These solutions are shown by the dotted, dashed and dot-dashed lines and are ordered in the decreasing norm $\|\delta u_0\|$, i.e., the dotted line corresponds to the solution with the largest norm and the dot-dashed line corresponds to the solution with the smallest norm. In general, we

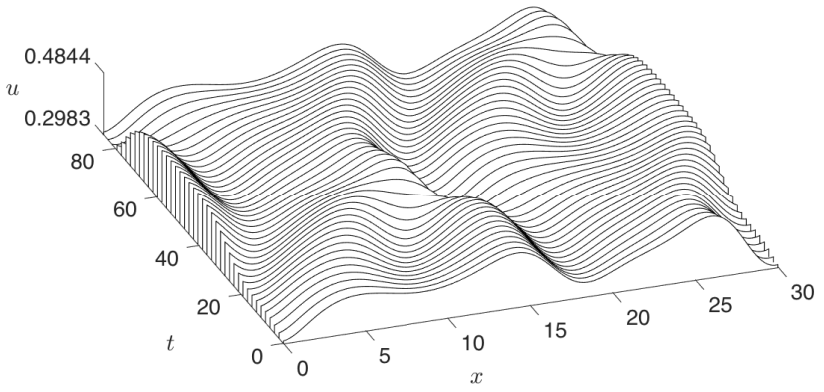

Figure 5.12: Time evolution over one period of time of the time-periodic solution for $\bar{u} = 0.4$, $L = 30$ when $D = 12$ (see Fig. 5.10(c)).

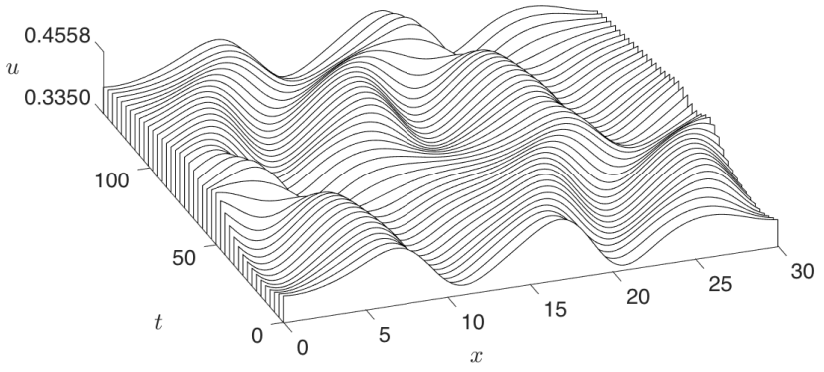

Figure 5.13: Time evolution over one period of time of the time-periodic solution for $\bar{u} = 0.4$, $L = 30$ when $D = 17$ (see Fig. 5.10(c)).

can observe that the solutions of the secondary branches that are located closer to the primary branch have profiles that are closer to the profiles of the solutions of the primary branch.

Time evolution over one period of time of several time-periodic solutions from the time-periodic branches bifurcating from the 2-mode primary branches presented in Figs. 5.10(b) and (c) are shown in Figs. 5.11–5.13. In particular, Fig. 5.11 shows the time-periodic solution corresponding to Fig. 5.10(b) for $\bar{u} = 0.4$, $L = 25$ when $D = 3$. We can see that the solution looks like a superposition of two droplets (a smaller one and a bigger one) periodically exchanging mass. Figs. 5.12 and 5.13 shows the time periodic solutions corresponding to Fig. 5.10(c) for $\bar{u} = 0.4$, $L = 30$ when $D = 12$ and 17, respectively. We can see that for the smaller value of D, the solution again looks like a superposition of two droplets periodically exchanging mass. However, now the larger droplet starts to resemble a superposition of two smaller ones. For the larger value of D, the solution now looks rather like a superposition of three smaller droplets continuously exchanging mass.

Figs. 5.14(a) and (b) show bifurcation diagrams for $\bar{u} = 0.55$ and $L = 35$ and 50, respectively. For the larger value of L the 2-mode primary branch has a pair of saddle nodes, while for the smaller value of L it has only one saddle node. We can observe in Fig. 5.14(a) that for $L = 35$ there are four bifurcation points and one saddle-node bifurcation on the 2-mode primary branch. The secondary branches that start at these bifurcation points reconnect to the 2-mode primary branch. Also, we denote the upper and the lower parts of the primary branch by letters (a) and (b), respectively. We can observe that points 1 and 2 on the upper part are connected to points 4 and 3, respectively on the lower part. As regards the 1-mode branch (blue thick solid line), we find two saddle-nodes, but there are no other bifurcation points. Fig. 5.14(b) shows that for $L = 50$ there are five bifurcation points and two saddle-node bifurcations on the 2-mode primary branch. Some of the secondary branches that start at these points reach large values of D and may continue to infinity, whereas secondary branches starting at other bifurcation points reconnect to the primary branch. We call the upper part of the primary branch (up to the first saddle node) part (a), the part connecting the two saddle nodes part (b), and the lower part (starting from the second saddle node) part (c). We find

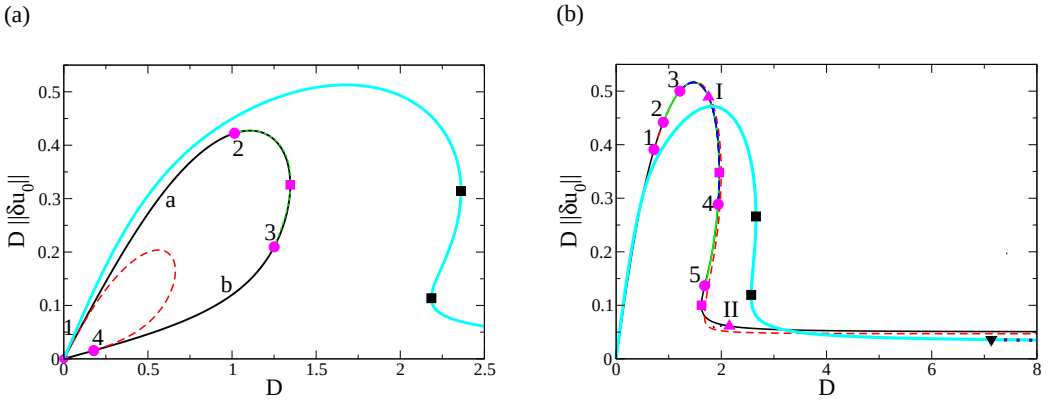

Figure 5.14: The bifurcation diagrams of the one- and two-droplet ($n = 1$ and $n = 2$) solutions of the convective Cahn-Hilliard equation (2.28) for the case $\bar{u} = 0.55$ with (a) $L = 35$ and (b) $L = 50$. Shown is the dependence of the norm $\|\delta u_0\|$ (multiplied by D for presentational purposes) on the driving force D. The (blue) thick solid lines show the 1-mode branches, the thin solid lines show the 2-mode primary branches, the dashed lines show the secondary branches, the thick dotted lines show the time-periodic branches bifurcating from the 1-mode branches, and the thin dotted lines show the time-periodic branches bifurcating from the 2-mode branchs. The red circles indicate pitchfork bifurcations to side branches on the 2-mode primary branches, the black squares indicate the saddle-node bifurcations on the 1-mode branches, the red squares indicate the saddle-node bifurcations on the 2-mode primary branches, the black triangles indicate Hopf bifurcations to branches of time-periodic solutions bifurcating from the 1-mode branches, the red triangles indicate Hopf bifurcations to branches of time-periodic solutions bifurcating from the 2-mode primary branches. In panel (a), the upper and lower parts of the primary branch are denoted by letters a and b, respectively.

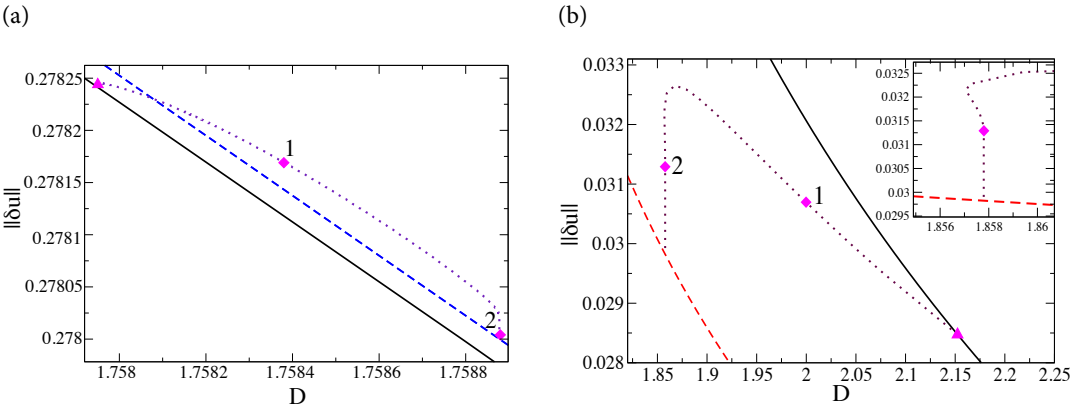

Figure 5.15: Zooms of the time-periodic branches shown in Fig. 5.14(b) and starting from point I and II (panels (a) and (b), respectively). The red triangles indicate Hopf bifurcations. The red diamonds 1 and 2 in panel (a) correspond to time-periodic solutions shown in Figs. 5.20 and 5.21, respectively. The red diamonds 1 and 2 in panel (b) correspond to time-periodic solutions shown in Figs. 5.22 and 5.23, respectively. The inset in panel (b) shows the zoom of the time-periodic branch near the homoclinic bifurcation and shows a snaking behaviour of the branch.

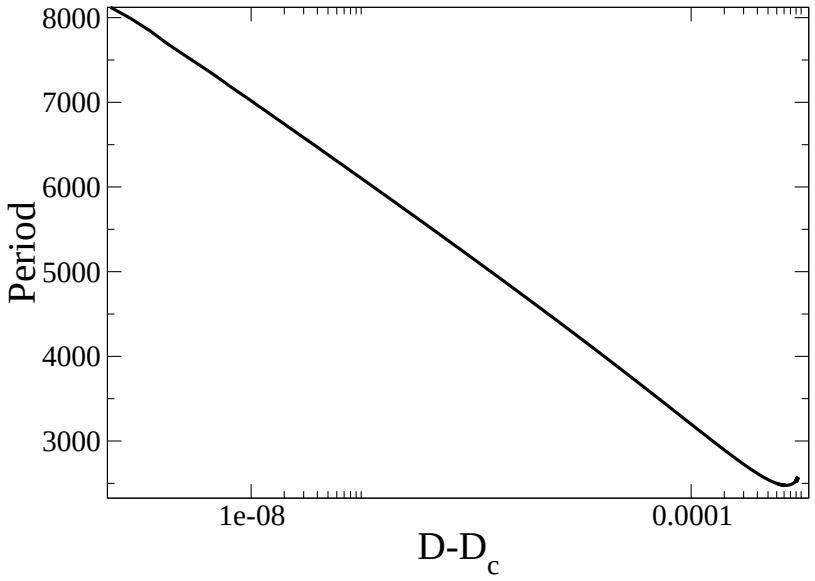

Figure 5.16: A plot of the period over $D - D_c$ of the solution on the time-periodic branch originating from point II in Fig. 5.14(b) and also shown in Fig. 5.15(b) on a semi-log scale. Here D_c is the value of the driving force, D, corresponding to the homoclinic bifurcation.

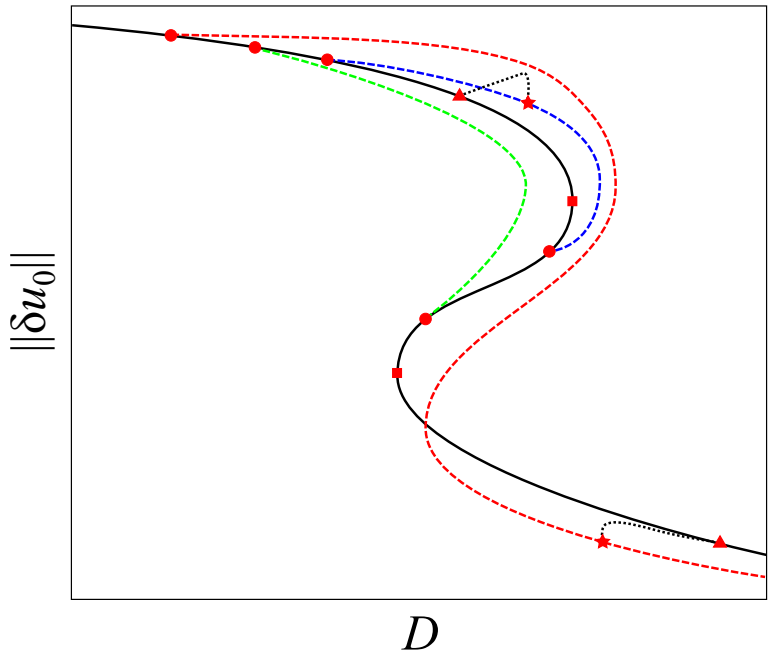

Figure 5.17: Schematic representation of the branches in Fig. 5.14(b) (excluding the 1-mode branch and the branch of time-periodic solutions emanating from the 1-mode branch). The line styles are the same as in Fig. 5.14(b). As in Fig. 5.14(b), the red circles show the bifurcation points to side branches, red triangles show Hopf bifurcation points to branches of time-periodic solutions, red squares on the primary branch indicate saddle-nodes and, additionally, red stars indicate homoclinic bifurcations. Note that only the homoclinic bifurcations on the secondary branches are shown and the other bifurcation points on the secondary branches are not given in this schematic figure.

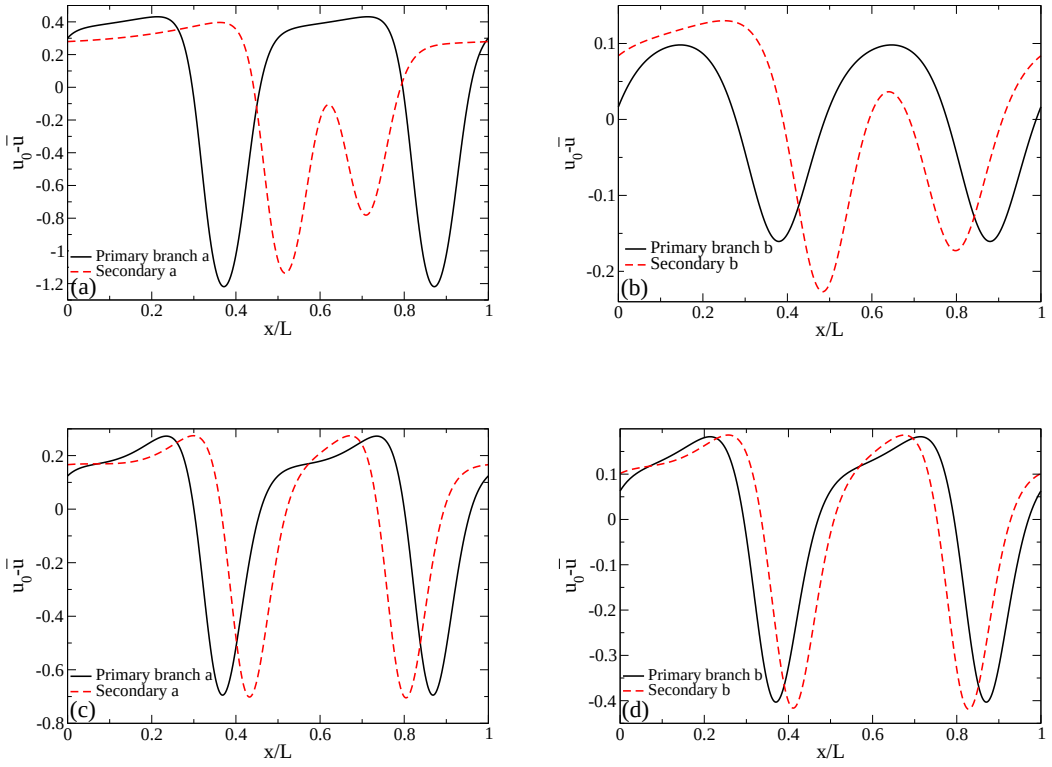

Figure 5.18: Solution profiles from the 2-mode primary (black solid lines) and secondary (red dashed lines) branches for $\bar{u} = 0.55$ and $L = 35$ at $D = 0.4$ and 1.3 (top and bottom panels, respectively). The left and right panels correspond to the upper and lower parts of the branches, respectively.

that the secondary branch starting at bifurcation point 1 on part (a) continues to infinity, while bifurcation point 2 on part (a) is connected to point 5 on part (b), and bifurcation point 3 on part (a) is connected to point 4 on part (b). For $L = 50$, we additionally find that there are two Hopf bifurcations on the 2-mode primary branch, denoted by symbols I and II. It is interesting to note that these bifurcation points are not connected to each other by a time-periodic branch, and the time-periodic branches that emerge from these points do not extend to large values of D. Instead, these time-periodic branches are connected to side branches (the dashed blue and red branches, respectively). This is confirmed in Figs. 5.15(a) and (b) for the time-periodic branches starting at points I and II, respectively. Moreover, the inset in Fig. 5.15(b) indicates a possible exponential snaking behaviour of the time-periodic branch – one saddle-node is clearly visible, and one more can be obtained by another zoom; however, to clearly determine if there is a snaking behaviour, higher accuracy of calculations is need, and this is left as a topic for future investigation. Interestingly, the approach to the side branches is through homoclinic bifurcations. This is confirmed for the branch starting at point II in Fig. 5.16

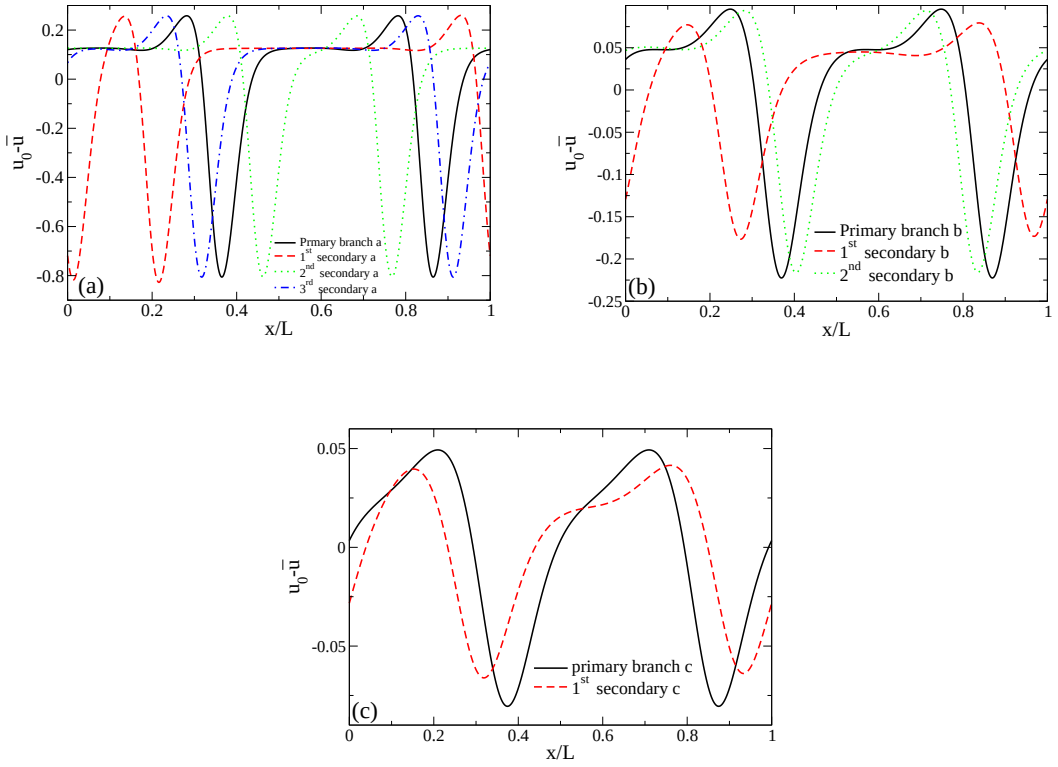

Figure 5.19: Solution profiles from the 2-mode primary and secondary branches for $\bar{u} = 0.55$ and $L = 50$ at $D = 1.75$ and 1.3 (top and bottom panels, respectively), see Fig. 5.14(b). Panel (a) corresponds to the solution of part (a) of the primary branch (black solid line) and the solutions of the parts of the side branches passing in the vicinity of part (a) and originating from points 1, 2 and 3 (red dashed, green dotted and blue dot-dashed lines, respectively). Panel (b) corresponds to the solution of part (b) of the primary branch (black solid line) and the solutions of the parts of the side branches passing in the vicinity of part (b) and originating from points 1 and 2 (red dashed and green dotted lines, respectively). Panel (c) corresponds to the solution of part (c) of the primary branch (black solid line) and the solution of the part of the side branche passing in the vicinity of part (c) and originating from points 1 (red dashed line).

showing the dependence of the time-period of the solution over $D - D_c$, where D_c is an estimated value of D at which the side branch is reached. This dependence is shown on a semi-log scale and it indicates that the period scales as $|\log(D - D_c)|$, indicating that the bifurcation is homoclinic, see Strogatz [99]. We conjecture that the time-periodic branch starting at point I results from a Takens-Bogdanov-type codimension-2 bifurcation at the pitchfork bifurcation point 3 (we note that for the usual Takens-Bogdanov bifurcation the time-periodic branch emerges from a saddle-node bifurcation, not from a pitchfork bifurcation, see, for example, Kuznetsov [71]). Similarly, the time-periodic branch starting at point II results from such a codimension-2 bifurcation, but at pitchfork bifurcation that has been moved to larger values of D (or to infinity). For better understanding of the various branches of solutions presented in Fig. 5.14(b), a schematic

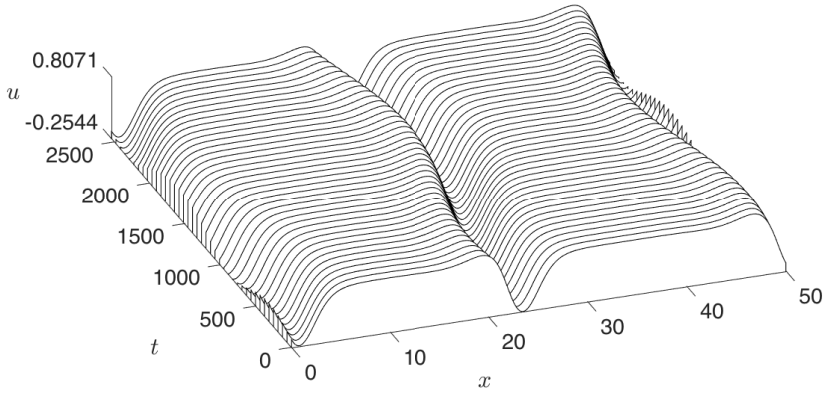

Figure 5.20: Time evolution over one period of time of the time-periodic solution for $\bar{u} = 0.55$ and $L = 50$ corresponding to point 1 shown in Fig. 5.15(a).

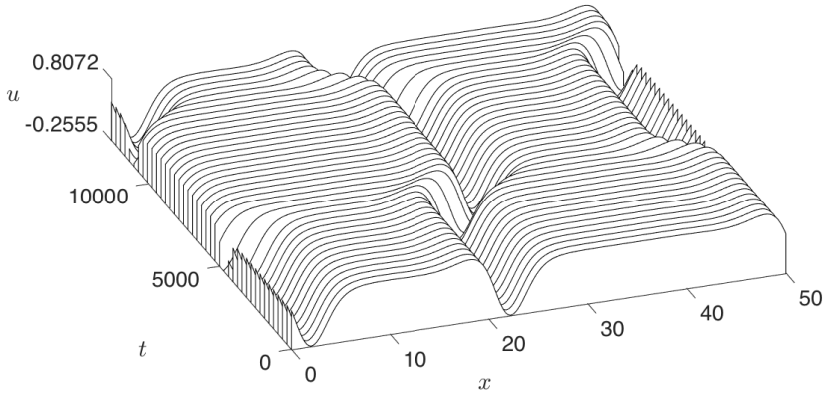

Figure 5.21: Time evolution over one period of time of the time-periodic solution for $\bar{u} = 0.55$ and $L = 50$ corresponding to point 2 shown in Fig. 5.15(a).

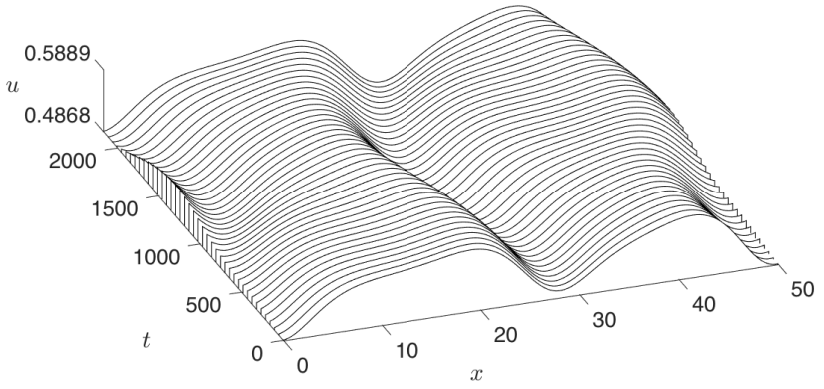

Figure 5.22: Time evolution over one period of time of the time-periodic solution for $\bar{u} = 0.55$ and $L = 50$ corresponding to point 1 shown in Fig. 5.15(b).

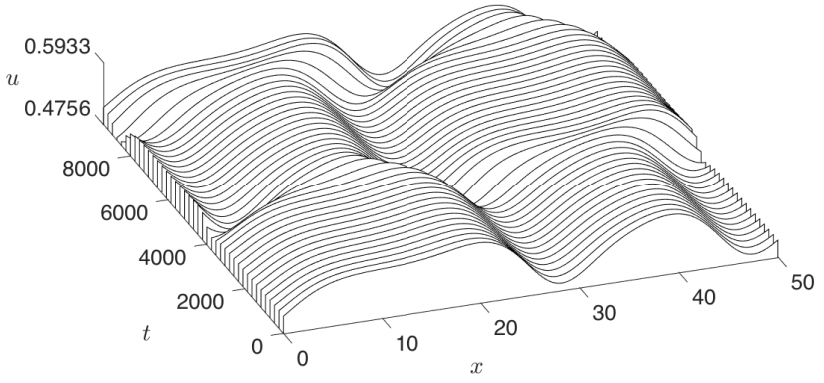

Figure 5.23: Time evolution over one period of time of the time-periodic solution for $\bar{u} = 0.55$ and $L = 50$ corresponding to point 2 shown in Fig. 5.15(b).

representation of these various branches is shown in Fig. 5.17 (excluding the 1-mode branch and the time periodic branch bifurcating from this branch). In Fig. 5.14(b), we additionally observe that the 1-mode branch (blue thick solid line) has two saddle-node bifurcations and one Hopf bifurcation. The branch of time-periodic solutions starting at this bifurcation point is connected to the first side branch (red dashed line) at a homoclinic bifurcation. (see the inset) at $D \approx 31.15$.

Figs. 5.18(a)–(d) show solution profiles for $\bar{u} = 0.55$ and $L = 35$ for $D = 0.4$ and $D = 1.3$ (top and bottom panels, respectively), see Fig. 5.14(a). (We exclude the solution profiles for the 1-mode branches.) Note that for this value of L, each of the branches has upper and lower parts. The solution profiles that correspond to the upper parts of the branches are show in the left panels of Fig. 5.18, whereas the solutions that correspond to the lower parts of the branches are shown in the right panels of Fig. 5.18.

Figs. 5.19(a)–(c) show the solution profiles for $\bar{u} = 0.55$, $L = 50$ and $D = 1.75$ (see Fig. 5.14(b)). (We exclude the solution profiles for the 1-mode branches.) Panel (a) corresponds to the profiles of part (a) of the primary branch (black solid line) and the side branches starting at points 1, 2 and 3 in Fig. 5.14(b) and passing in the vicinity of part (a) of the primary branch (red dashed, green dotted and blue dot-dashed lines, respectively). Panel (b) corresponds to the profiles of part (b) of the primary branch (black solid line) and the side branches starting at points 1 and 2 and passing in the vicinity of part (b) of the primary branch (red dashed and green dotted lines, respectively). Finally, panel (c) corresponds to the profiles of part (c) of the primary branch (black solid line) and the side branch starting at point 1 and passing in the vicinity of part (c) of the primary branch (red dashed line). In general, we can observe that the solutions of the secondary branches that are located closer to the primary branch have profiles that are closer to the profile of the solution of the primary branch.

Figs. 5.20–5.23 show the time evolution of over one period of time of several time-periodic solutions from the time-periodic branches bifurcating from the 2-mode primary branches presented in Fig. 5.14(b) and also in Figs. 5.15(a) and (b) for $\bar{u} = 0.55$, and $L = 50$. Figs. 5.20 and 5.21 correspond to points 1 and 2, respectively, shown by red diamonds in Fig. 5.15(a). We can see in Fig. 5.20 that the solution looks like a superposition of two droplets (a smaller one and a larger one) periodically exchanging mass. In Fig. 5.21, we can see that as the homoclinic bifurcation is approached, the solution still looks like a superposition of a smaller and a larger droplet. However, now the mass-exchange events happen over relatively short time intervals and for most of the time the solution looks like a quasi-steady superposition of two droplets. Similar observations

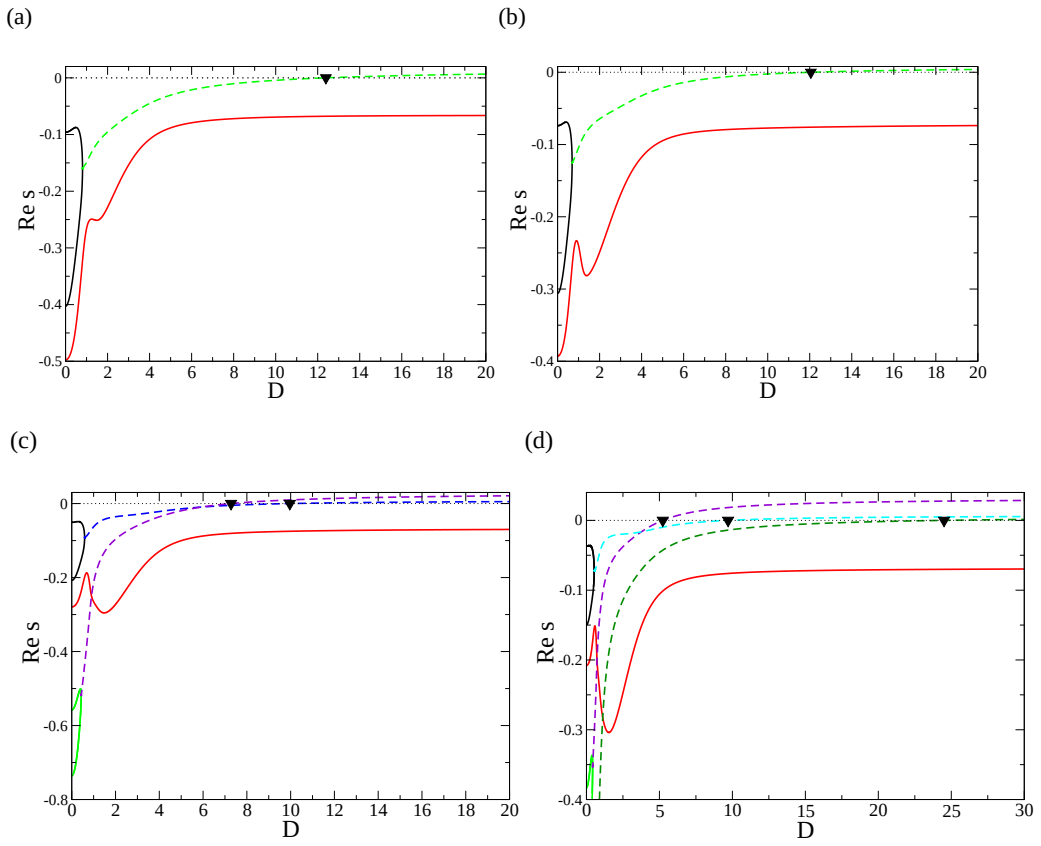

Figure 5.24: The dependence of the real parts of the dominant eigenvalues s on the driving force D along the 1-mode primary branch when $L = 22, 25, 30$ and 35 (panels (a), (b), (c) and (d), respectively) at $\bar{u} = 0.4$ (Fig. 5.9). The solid lines correspond to the eigenvalues with zero imaginary part. The dashed lines correspond to the eigenvalues with non-zero imaginary part. The black triangles indicate Hopf bifurcations to branches of time-periodic solutions.

hold for the solutions presented in Figs. 5.22 and 5.23 that correspond to points 1 and 2, respectively, shown by red diamonds in Fig. 5.15(b). Strictly speaking, we can see that after each mass-exchange event the order of the smaller and the larger droplets swaps, so it would be more precise to state that the time-periodic branch approaches two stationary solutions at the same time, i.e., a 'heteroclinic' bifurcation is approached. We note, however, that due to periodic boundary conditions we can identify any solutions that can be obtained from each other by a translation, and since the two statinonary solutions that are approached by the time-periodic branch are obtained from each other by such a translation, we can still justify the use of the term 'homoclinic' bifurcation.

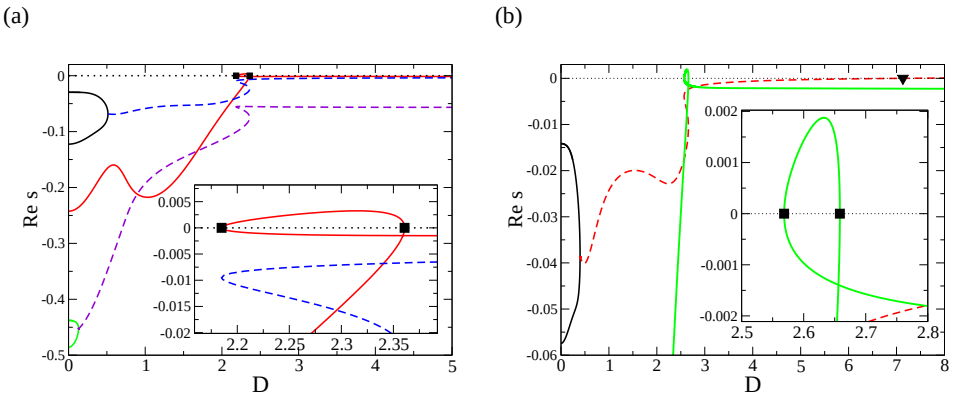

Figure 5.25: The dependence of the real parts of the dominant eigenvalues s on the driving force D along the 1-mode primary branch when $L = 35$ and 50 (panels (a) and (b), respectively) at $\bar{u} = 0.55$ (Fig. 5.14). The solid lines correspond to the eigenvalues with zero imaginary part. The dashed lines correspond to the eigenvalues with non-zero imaginary part. The black squares indicate the saddle-node bifurcations and the black triangles indicate Hopf bifurcations to branches of time-periodic solutions.

5.4.2.2 Linear stability of 1-mode branches

Figs. 5.24 and 5.25 show the real parts of the dominant eigenvalues along the 1-mode primary branches presented in Figs. 5.9 and 5.14, respectively. The solid lines correspond to the real eigenvalues. The dashed lines correspond to the eigenvalues with non-zero imaginary parts. The black solid triangles correspond to the Hopf bifurcations to time-periodic solutions.

Figs. 5.24(a)–(d) correspond to $L = 22$, 25, 30 and 35, respectively, at $\bar{u} = 0.4$ (see Figs. 5.9 (a), (b), (c) and (d), respectively). In Figs. 5.24(a) and (b), we see that for $L = 22$ and 25 there is one Hopf bifurcation and there are stable intervals for 1-mode solutions for $D \lesssim 12.39$ and $D \lesssim 12.05$, respectively. In Fig. 5.24(c), we can see that for $L = 30$ there are two Hopf bifurcations, and there is a stable interval for 1-mode solutions for $D \lesssim 7.28$. In Fig. 5.24(d), we can see that for $L = 35$ there are three Hopf bifurcations, and there is a stable interval for 1-mode solutions for $D \lesssim 5.23$.

Figs. 5.25(a) and (b) correspond to $L = 35$ and 50, respectively, at $\bar{u} = 0.55$ (see Figs. 5.14 (a) and (b), respectively). In Fig. 5.25(a), we see that for $L = 35$ there are two saddle-node bifurcations and there are no Hopf bifurcations. Also, part of the branch is unstable for D between 2.18 and 2.36, but there are stable solutions for all the values of D. In Fig. 5.25(b), we can see that for $L = 50$ there are two saddle-node bifurcations (at $D \approx 2.57$ and $D \approx 2.67$) and there is one Hopf bifurcation at $D \approx 7.13$, so that there are stable 1-mode solutions for $D \lesssim 7.13$. We generally observe that sufficiently

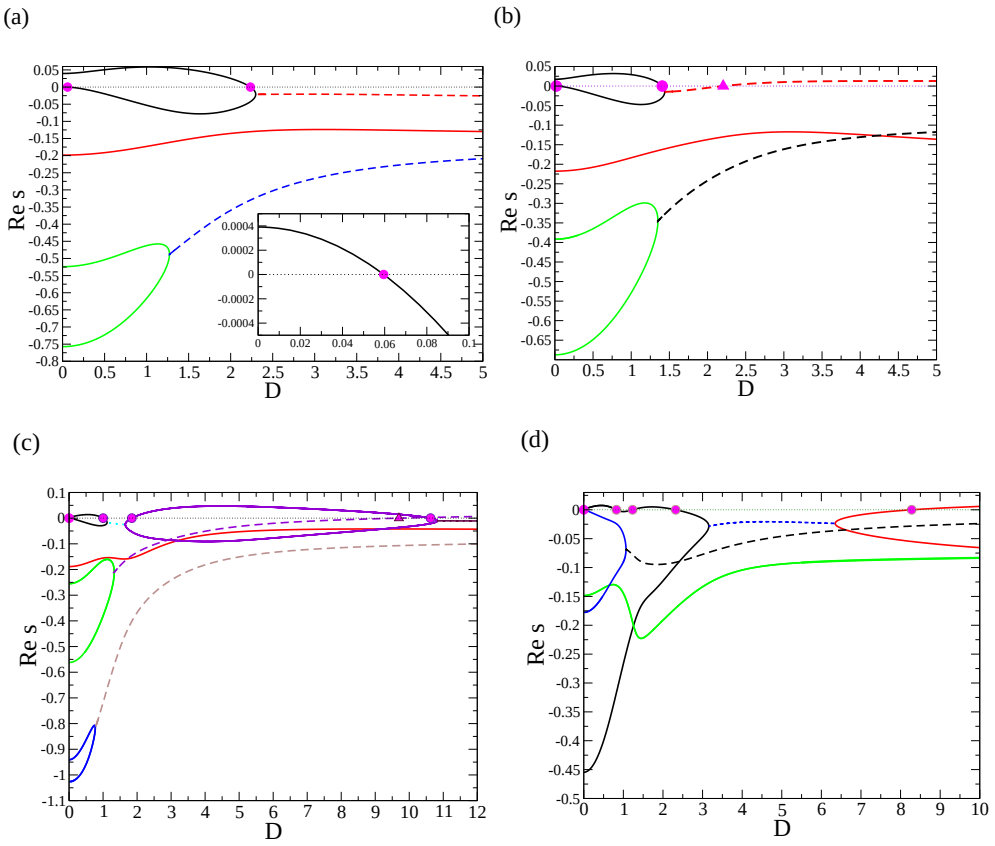

Figure 5.26: The dependence of the real parts of the dominant eigenvalues s on the driving force D along the 2-mode primary branch when $L = 22, 25, 30$ and 35 (panels (a), (b), (c) and (d), respectively) at $\bar{u} = 0.4$ (Fig. 5.9). The solid lines correspond to the eigenvalues with zero imaginary part. The dashed lines correspond to the eigenvalues with non-zero imaginary part. The red circles indicate pitchfork bifurcations to side branches and the red triangles indicate Hopf bifurcations to branches of time-periodic solutions.

strong driving destabilises 1-mode solutions, although for $\bar{u} = 0.55$ and $L = 35$ we find that there is only a bounded instability interval.

5.4.2.3 Linear stability of 2-mode primary branches and coarsening

Figs. 5.26 and 5.36 show the real parts of the dominant eigenvalues along the 2-mode primary branches presented in Figs. 5.9 and 5.14, respectively. The solid lines correspond to the real eigenvalues. The dashed lines correspond to the eigenvalues with non-zero imaginary parts. The solid red circles correspond to the bifurcation points to secondary branches, the solid red squares correspond the saddle-node bifurcations, and the solid red triangles correspond to the Hopf bifurcations to time-periodic solutions.

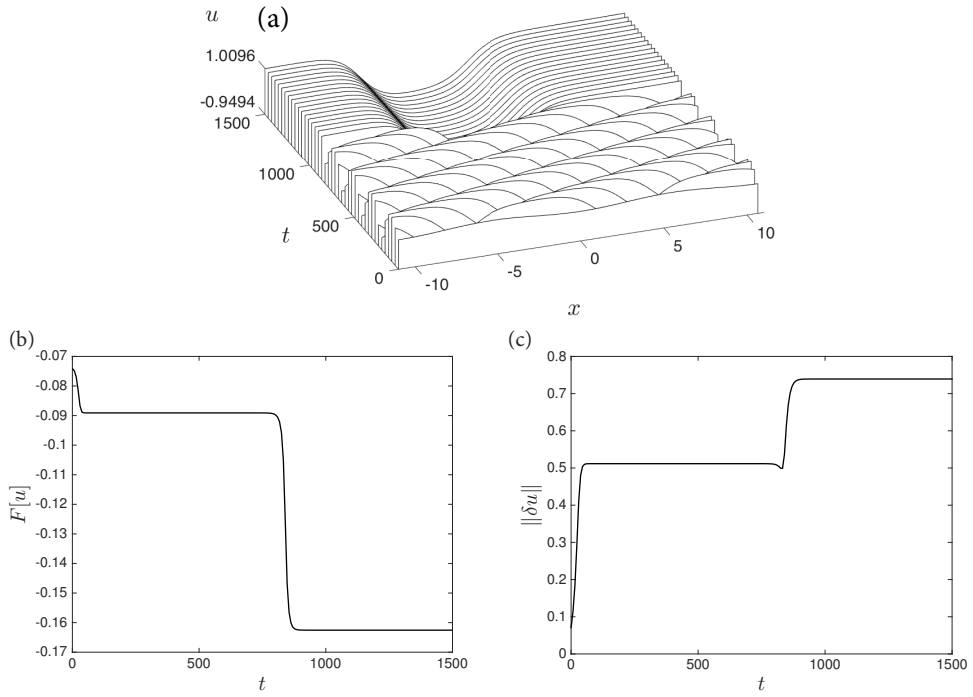

Figure 5.27: Numerical solution of the convective Cahn-Hilliard equation (2.28) on the periodic domain of length $L = 22$ for $\bar{u} = 0.4$ and $D = 0.3$, with the initial condition $u(x,0) = \bar{u} - 0.1\cos(2\pi x/L)$. Panel (a) shows the time evolution of the solution for $t \in [0, 1500]$ in a frame moving at velocity 0.026 (for presentational purposes). Panel (b) shows the time evolution of the energy of the solution. Panel (c) shows the time evolution of the norm of the solution. Note that for this value of D the 2-mode solution is unstable with respect to coarsening, see Fig. 5.26(a).

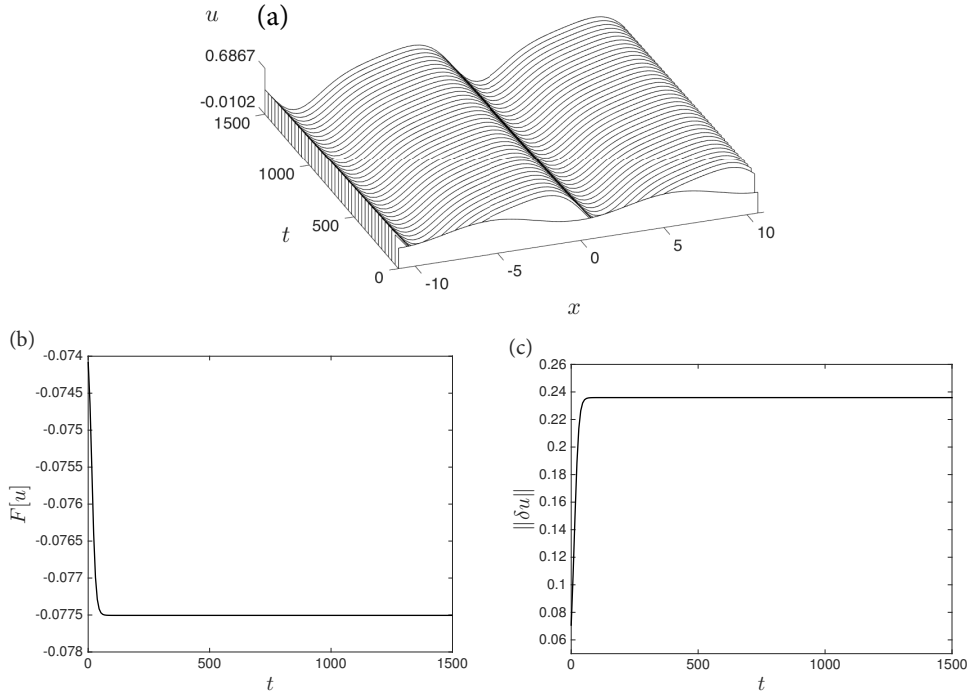

Figure 5.28: Numerical solution of the convective Cahn-Hilliard equation (2.28) on the periodic domain of length $L = 22$ for $\bar{u} = 0.4$ and $D = 3$, with the initial condition $u(x,0) = \bar{u} - 0.1\cos(2\pi x/L)$. Panel (a) shows the time evolution of the solution for $t \in [0, 1500]$ in a frame moving at velocity 1.05 (for presentational purposes). Panel (b) shows the time evolution of the energy of the solution. Panel (c) shows the time evolution of the norm of the solution. Note that for this value of D the 2-mode solution is stable with respect to coarsening, see Fig. 5.26(a).

Figs. 5.26(a)–(d) correspond to $L = 22$, 25, 30 and 35, respectively, at $\bar{u} = 0.4$ (see Figs. 5.9 (a), (b), (c) and (d), respectively). In Fig. 5.26(a), we see that for $L = 22$ there are two bifurcation points to side branches, there are no Hopf bifurcations and there is a stable interval for $D \gtrsim 2.24$. Interestingly, this means that coarsening can be prevented by sufficiently strong driving force. This effect is demonstrated in time-dependent simulations (obtained by using the spectral method described in Section 2.5) shown in Figs. 5.27 and 5.28 that show the results for $\bar{u} = 0.4$, $L = 22$ and $D = 0.3$ and 3, respectively. The initial condition for the simulations was chosen to be

$$u(x, 0) = \bar{u} - 0.1 \cos(2\pi x/L). \tag{5.74}$$

Panels (a) of the figures show the time evolution of the solution for t changing from 0 to 1500. Panels (b) shows the time evolution of the energies of the solutions. (We use the same energy functional $F[u]$ here as for the standard Cahn-Hilliard equation, although it should be pointed out that for $D \neq 0$ this functional is not anymore a Lyapunov functional and should not necessarily be minimised in the time evolution.) Panels (c) show the time evolution of the norms of the solutions. We can observe that for $D = 0.3$, the solution initially evolves into a two-droplet travelling-wave solution that at $t \approx 850$ starts to coarsen and transforms into a stable single-droplet solution moving at a slower speed (a single-droplet solution is linearly stable for this value of D, see Fig. 5.24(a)). However, for stronger driving, when $D = 3.0$, we can observe that the solution evolves into a two-droplet solution and remains bimodal during the course of the evolution, i.e., coarsening does not happen. This is in agreement with the theoretical prediction indicating that the bimodal solutions become linearly stable for $D \gtrsim 2.24$. (We note that for $D = 3.0$ the 1-mode solution is also linearly stable. So the long-time dynamics of solutions depends on an initial conditions.)

The most unstable eigenmode u_1 superimposed with the primary 2-mode solution u_0 is shown in Fig. 5.29 for $\bar{u} = 0.4$ and $L = 22$. The black solid lines in this figure shows the two-droplet solutions, u_0, the blue dotted line show the eigenmode u_1 and the red dashed line shows the two-droplet solution superimposed with the eigenmode, $U = u_0 + \epsilon u_1$ for sufficiently small ϵ. The arrows indicate the directions in which the fronts are shifted (in the same way as in Figs. 5.5, 5.7 and 5.8 for the standard Cahn-Hilliard equation). Panels (a) and (b) correspond to $D = 0.1$ and 0.5, respectively.

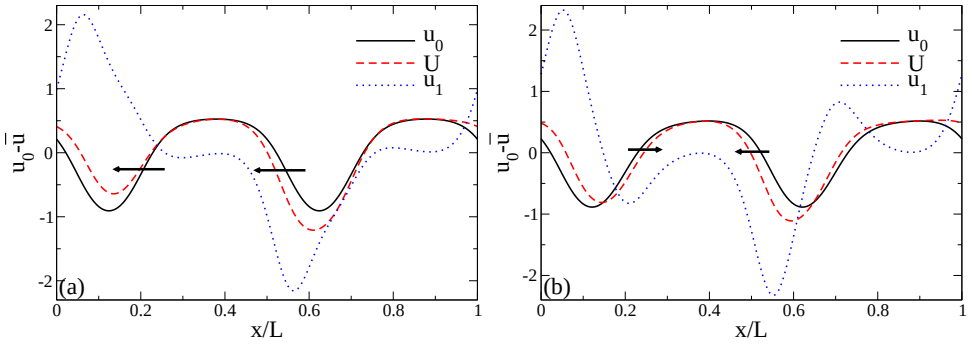

Figure 5.29: Shown are the most unstable eigenfunctions for two-droplet solutions at $\bar{u} = 0.4$ and $L = 22$. Panel (a) represents the translational mode for $D = 0.1$ and panel (b) represent the volume mode for $D = 0.5$. The solid lines correspond to the solutions $u_0(x)$.The dotted lines correspond to the eigenfunctions $u_1(x)$. The dashed lines correspond to the solutions $u_0(x)$ superimposed with eigenfunction $u_1(x)$ multiplied by a small coefficient ϵ, i.e., $U(x) = u_0(x) + \epsilon u_1(x)$. The arrows indicate the directions where the fronts of the droplets shift after the eigenfunctions are added.

An interesting observation is that for, the smaller value of D, the most unstable mode appears to be translational (in agreement with the $D = 0$ case), whereas for larger values of D the mode seems to change into a volume mode.

Fig. 5.26(b) shows that for $L = 25$ there two pitchfork bifurcation points to side branches, one Hopf bifurcation to a branch of time-periodic solutions, and there is a stable interval between the second bifurcation point to a side branch and the Hopf bifurcation point, i.e., between $D \approx 1.41$ and $D \approx 2.21$. The observations are corroborated by the time-dependent simulations shown in Figs. 5.30, 5.31 and 5.32 for $\bar{u} = 0.4$, $L = 25$ and $D = 0.3$, 2 and 5, respectively. The initial conditions are $u(x,0) = \bar{u} - 0.1\cos(2\pi x/L)$ for Figs. 5.30, 5.31 and $u(x,0) = \bar{u} - 0.1\cos(2\pi x/L) + 0.001\cos(\pi x/L)$. It can be observed that for $D = 0.3$, the solution initially evolves into a two-droplet solution, but around $t = 1500$ the droplets coarsen and a one-droplet solution is obtained (a single-droplet solution is linearly stable for this value of D, see Fig. 5.24(b)). In contrast, for $D = 3$, a two-droplet solution remains stable during the course of evolution, which agrees with the theoretical prediction (a single-droplet solution is also linearly stable for this value of D, see Fig. 5.24(b), so the long-time evolution of the solutions should depend on initial conditions). For $D = 5$, the solution again initially tends to evolve into a two-droplet solution. But as is evident from the energy and norm plots, around $t = 150$, the droplets start to oscillate, and the solution eventually evolves into a time-periodic state resembling two droplets periodically exchanging mass. We note that a single-droplet solution is also linearly stable for this value of D, see Fig. 5.24(b). So we expect that different initial conditions can lead to

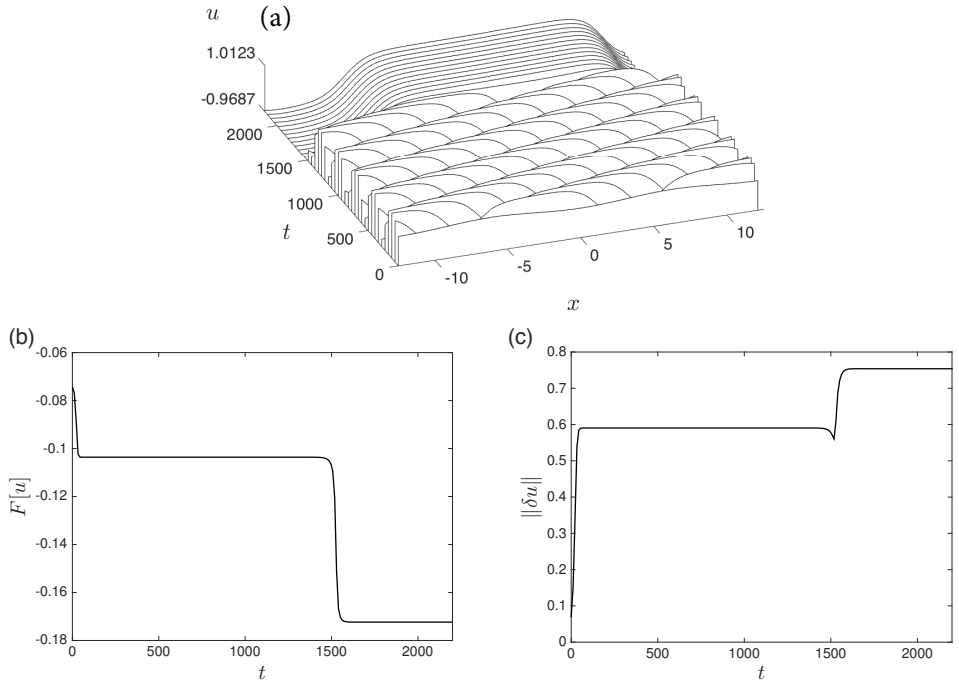

Figure 5.30: Numerical solution of the convective Cahn-Hilliard equation (2.28) on the periodic domain of length $L = 25$ for $\bar{u} = 0.4$ and $D = 0.3$, with the initial condition $u(x,0) = \bar{u} - 0.1\cos(2\pi x/L)$. Panel (a) shows the time evolution of the solution for $t \in [0, 2200]$ in a frame moving at velocity 0.02 (for presentational purposes). Panel (b) shows the time evolution of the energy of the solution. Panel (c) shows the time evolution of the norm of the solution. Note that for this value of D the 2-mode solution is unstable with respect to coarsening, see Fig. 5.26(b).

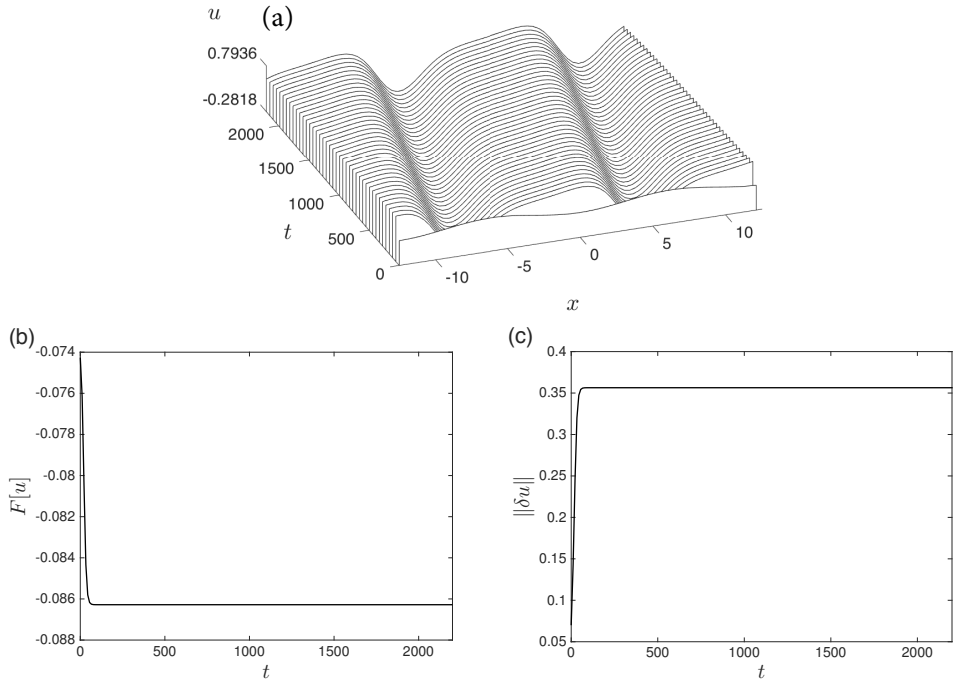

Figure 5.31: Numerical solution of the convective Cahn-Hilliard equation (2.28) on the periodic domain of length $L = 25$ for $\bar{u} = 0.4$ and $D = 2$, with the initial condition $u(x,0) = \bar{u} - 0.1\cos(2\pi x/L)$. Panel (a) shows the time evolution of the solution for $t \in [0, 2200]$ in a frame moving at velocity 0.555 (for presentational purposes). Panel (b) shows the time evolution of the energy of the solution. Panel (c) shows the time evolution of the norm of the solution. Note that for this value of D the 2-mode solution is stable with respect to coarsening, see Fig. 5.26(b).

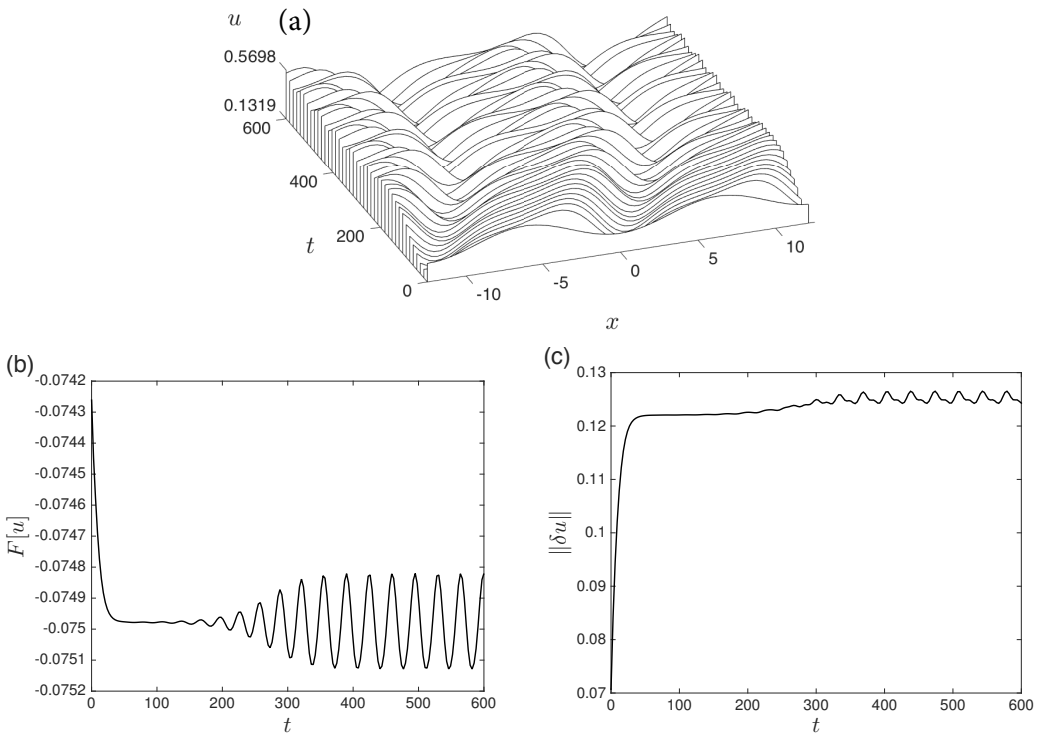

Figure 5.32: Numerical solution of the convective Cahn-Hilliard equation (2.28) on the periodic domain of length $L = 25$ for $\bar{u} = 0.4$ and $D = 5$, with the initial condition $u(x,0) = \bar{u} - 0.1\cos(2\pi x/L) + 0.001\cos(\pi x/L)$. Panel (a) shows the time evolution of the solution for $t \in [0, 600]$ in a frame moving at velocity 1.86 (for presentational purposes). Panel (b) shows the time evolution of the energy of the solution. Panel (c) shows the time evolution of the norm of the solution. Note that for this value of D the 2-mode solution Hopf is unstable with respect to coarsening, see Fig. 5.26(b).

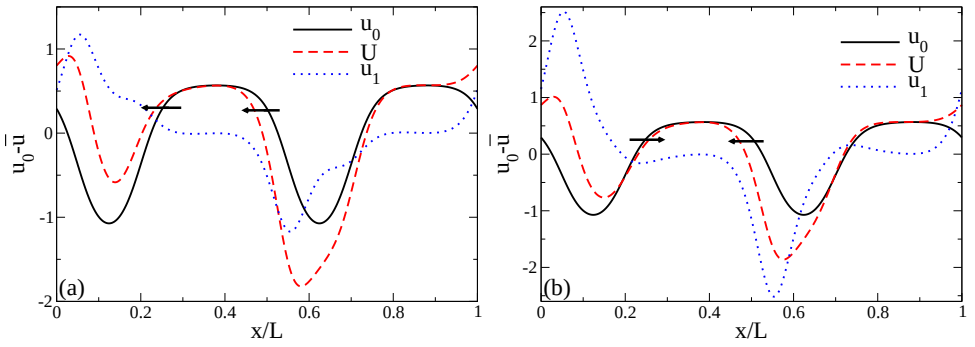

Figure 5.33: Shown are the most unstable eigenfunctions for two-droplet solutions at $\bar{u} = 0.4$ and $L = 25$. Panel (a) represents the translational mode for $D = 0.005$ and panel (b) represent the volume mode for $D = 0.1$. The solid lines correspond to the solutions $u_0(x)$. The dotted lines correspond to the eigenfunctions $u_1(x)$. The dashed lines correspond to the solutions $u_0(x)$ superimposed with eigenfunction $u_1(x)$ multiplied by a small coefficient ϵ, i.e., $U(x) = u_0(x) + \epsilon u_1(x)$. The arrows indicate the directions where the fronts of the droplets shift after the eigenfunctions are added.

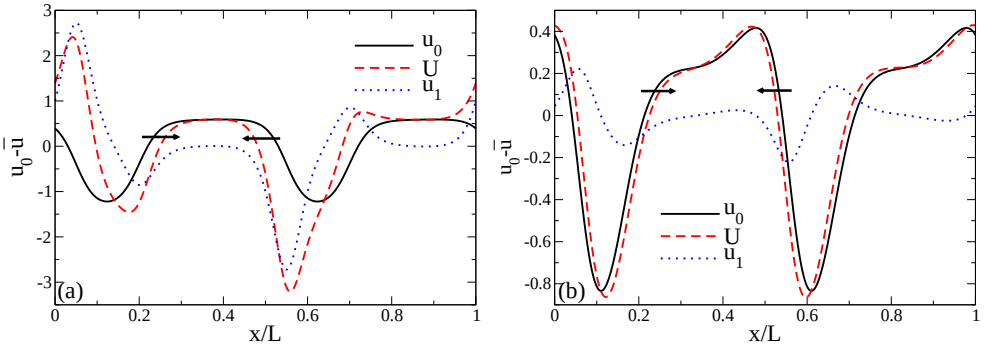

Figure 5.34: Shown are the most unstable eigenfunctions for two-droplet solutions at $\bar{u} = 0.4$ and $L = 30$. Panels (a) and (b) represent volume modes for $D = 0.1$ and $D = 1.8$, respectively. The solid lines correspond to the solutions $u_0(x)$. The dotted lines correspond to the eigenfunctions $u_1(x)$. The dashed lines correspond to the solutions $u_0(x)$ superimposed with eigenfunction $u_1(x)$ multiplied by a small coefficient ϵ, i.e., $U(x) = u_0(x) + \epsilon u_1(x)$. The arrows indicate the directions where the fronts of the droplets shift after the eigenfunctions are added.

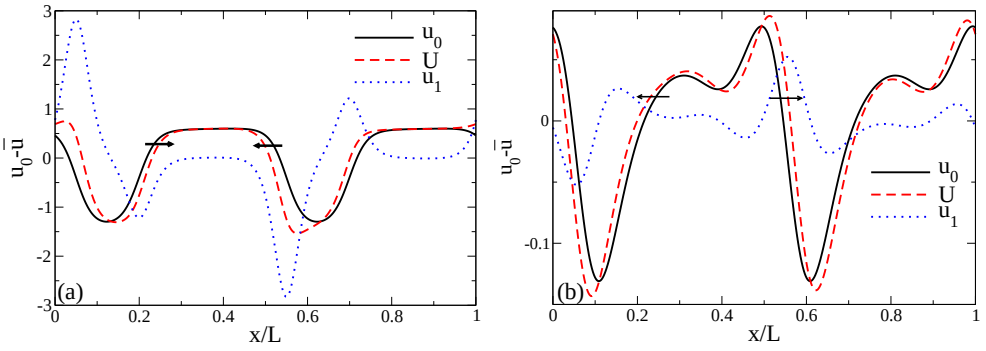

Figure 5.35: Shown are the most unstable eigenfunctions for two-droplet solutions at $\bar{u} = 0.4$ and $L = 35$. Panels (a) and (b) represent volume modes for $D = 0.1$ and $D = 9$, respectively. The solid lines correspond to the solutions $u_0(x)$. The dotted lines correspond to the eigenfunctions $u_1(x)$. The dashed lines correspond to the solutions $u_0(x)$ superimposed with eigenfunction $u_1(x)$ multiplied by a small coefficient ϵ, i.e., $U(x) = u_0(x) + \epsilon u_1(x)$. The arrows indicate the directions where the fronts of the droplets shift after the eigenfunctions are added.

time-periodic solutions or travelling single-droplet solutions. Fig. 5.33 shows the most unstable eigenmode u_1 superimposed with the primary 2-mode solution u_0 for $\bar{u} = 0.4$ and $L = 25$. Panels (a) and (b) correspond to $D = 0.005$ and 0.1. As for the case of $L = 22$ we observe that for, the smaller value of D, the most unstable mode appears to be translational (in agreement with the $D = 0$ case), whereas for larger values of D the mode seems to change into a volume mode.

Fig. 5.26(c) shows that for $L = 30$ there are four pitchfork bifurcation points to side branches, one Hopf bifurcation and there is a stable interval between two of the bifurcation points, i.e., between $D \approx 1.003$ and $D \approx 1.845$. As for the cases of $L = 22$ and $L = 25$, time-dependent simulations support the theoretical predictions, and we have decided not to show such simulations here. Fig. 5.34 shows the most unstable eigenmode u_1 superimposed with the primary 2-mode solution u_0 for $\bar{u} = 0.4$ and $L = 30$. Panels (a) and (b) correspond to $D = 0.1$ and 1.8. These two values are from two different instability regions and are separated by a stability regions. In both cases, we observe that the modes seems to be volume modes.

In Fig. 5.26(d), we can see that for $L = 35$ there are five pitchfork bifurcation points to side branches and no Hopf bifurcations. We also see that there are two stable intervals in D, namely, $0.82 \leq D \leq 1.23$ and $2.32 \leq D \leq 8.28$. As for the cases of $L = 22$ and $L = 25$, time-dependent simulations support the theoretical predictions, and we have decided not to show such simulations here. Fig. 5.35 shows the most unstable eigenmode u_1 superimposed with the primary 2-mode solution u_0 for $\bar{u} = 0.4$ and $L = 35$. Panels (a) and (b) correspond to $D = 0.1$ and 9. As for the previous case, we observe that both modes seem to be volume modes.

Figs. 5.36(a) and (b) correspond to $L = 35$ and 50, respectively, at $\bar{u} = 0.55$ (see Figs. 5.14 (a) and (b), respectively). In Fig. 5.36(a), the solid and dashed lines correspond to the real and complex (having non-zero imaginary parts) eigenvalues, respectively, for part a (the upper part) of the bifurcation curve shown in Fig. 5.14(a). However, we additionally introduce the dot-dashed lines that correspond to the real eigenvalues for part b (the lower part) of the bifurcation curve shown in Fig. 5.14(a). Note that for part b there are no eigenvalues with non-zero imaginary parts. Also, note that the green dot-dashed line corresponds to the unstable eigenvalue that is inherited from the 1-mode primary branch (that is unstable). We can see in Fig. 5.36(a) that for $L = 35$ there are four pitchfork bifurcations to side branches, two for part a and two for part

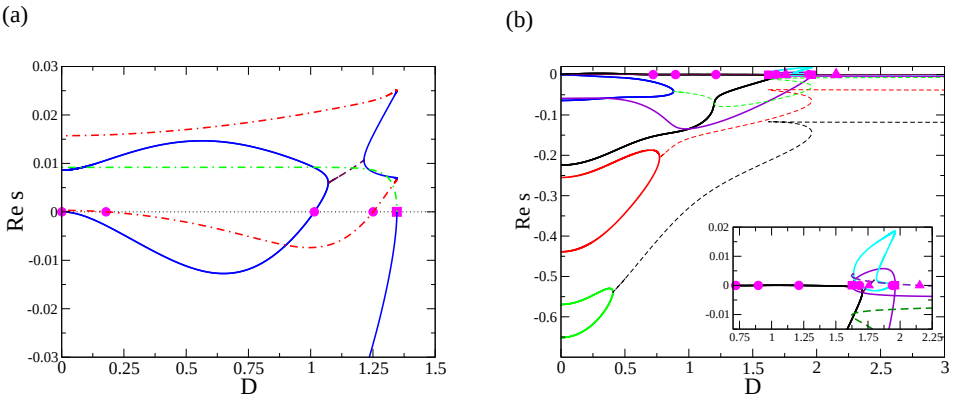

Figure 5.36: The dependence of the real parts of the dominant eigenvalues s on the driving force D along the 2-mode primary branch when $L = 35$ and 50 (panels (a) and (b), respectively) at $\bar{u} = 0.55$ (Fig. 5.14). In panel (a), the solid lines correspond to the eigenvalues with zero imaginary part for part a (the upper part) of the bifurcation diagram and the dot-dashed lines correspond to the eigenvalues with zero imaginary part for part b (the lower part) of the bifurcation diagram. The dashed lines correspond to the eigenvalues with non-zero imaginary part. In panel (b), the solid lines correspond to the eigenvalues with zero imaginary part. The dashed lines correspond to the eigenvalues with non-zero imaginary part. The red circles indicate pitchfork bifurcations to side branches, the red squares indicate the saddle-node bifurcations, and the red triangles indicate Hopf bifurcations to branches of time-periodic solutions.

b. In addition, there is one saddle-node bifurcation and there are no Hopf bifurcations. Also, we note that there are no stable intervals at any value of D. Fig. 5.37 shows the unstable symmetry-breaking eigenmodes u_1 superimposed with the primary 2-mode solutions u_0 for $\bar{u} = 0.55$ and $L = 35$ at $D = 0.05$. Panels (a) and (b) correspond to two unstable symmetry breaking modes for part b (lower part) of the bifurcation curve shown in Fig. 5.14(a). Note that for the lower part of the bifurcation diagram there is always one unstable symmetry breaking mode that is shown in panel (a) at $D = 0.05$ (and it turns out to be a translational mode for this value of D). For the lower part of the bifurcation diagram, there is also another symmetry-breaking mode that remains unstable up to $D \approx 0.18$. Note that this mode is stabilised for $0.18 \lesssim D \lesssim 1.25$ and becomes unstable again for $D \gtrsim 1.25$. It is shown in panel (b) at $D = 0.05$ (it turns out to be a volume mode). We also note that for the lower part of the bifurcation diagram shown in Fig. 5.14(a) there is an unstable symmetry-preserving mode (shown by the green dot-dashed line), but it is less unstable than the symmetry breaking mode shown in Fig. 5.37(a). Panel (c) of Fig. 5.37 shows the unstable symmetry breaking mode for part a (the upper part) of the bifurcation diagram shown in Fig. 5.14(a). This mode appears to be a volume mode.

Fig. 5.36(b) shows that for $L = 50$ there five bifurcation points to side branches, two

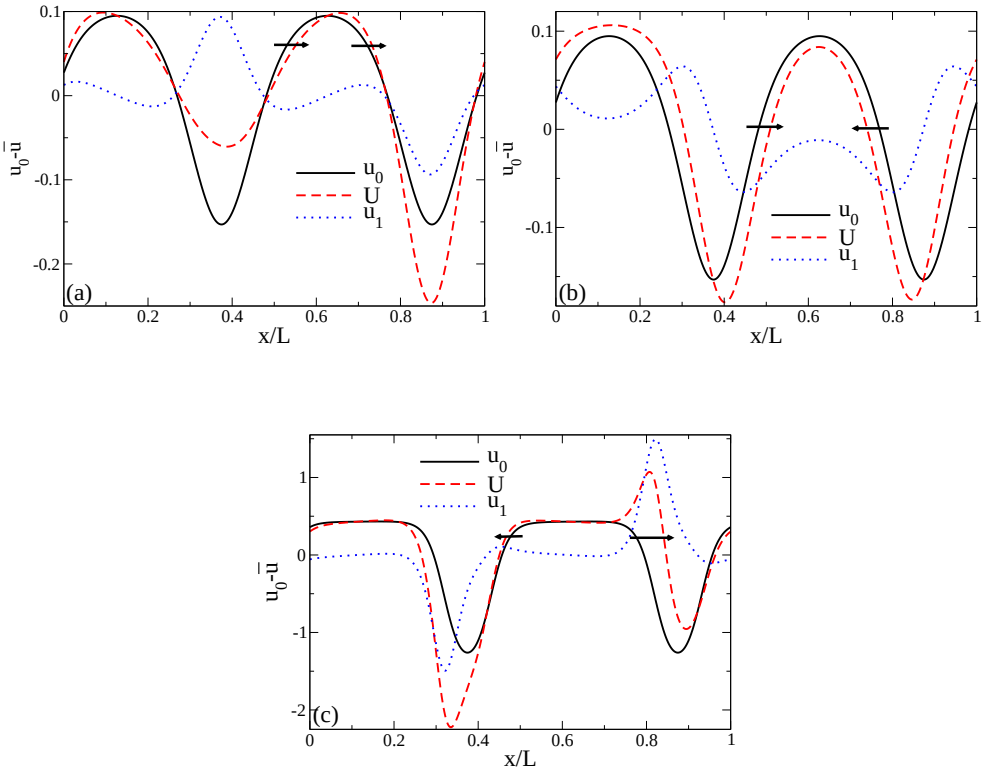

Figure 5.37: Shown are unstable symmetry-breaking modes for two-droplet solutions at $\bar{u} = 0.55$ and $L = 35$ at $D = 0.05$. Panels (a) and (b) represent the modes for part b (the lower part) of the bifurcation diagram shown in Fig. 5.14(a) (with the mode shown in panel (a) being more unstable). Panel (c) represents the mode for part a (the upper part) of the bifurcation diagram shown in Fig. 5.14(a). The solid lines correspond to the solutions $u_0(x)$. The dotted lines correspond to the eigenfunctions $u_1(x)$. The dashed lines correspond to the solutions $u_0(x)$ superimposed with eigenfunction $u_1(x)$ multiplied by a small coefficient ϵ, i.e., $U(x) = u_0(x) + \epsilon u_1(x)$. The arrows indicate the directions where the fronts of the droplets shift after the eigenfunctions are added.

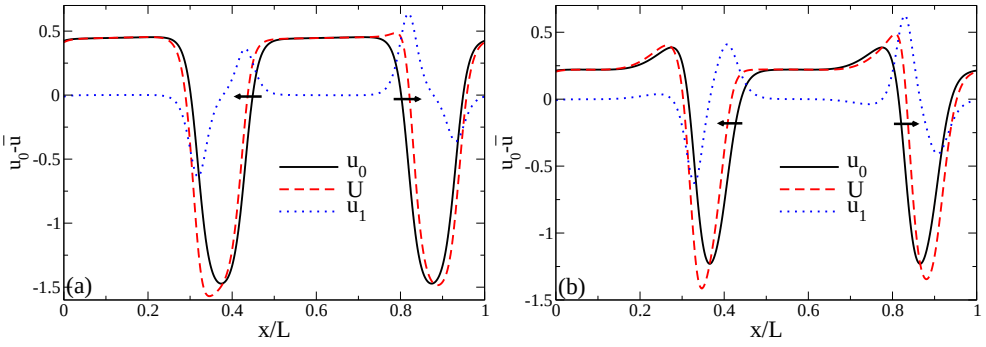

Figure 5.38: Shown are symmetry modes for two-droplet solutions at $\bar{u} = 0.55$ and $L = 50$. Panels (a) and (b) represent volume mode for $D = 0.05$ and $D = 1$, respectively. The solid lines correspond to the solutions $u_0(x)$. The dotted lines correspond to the eigenfunctions $u_1(x)$. The dashed lines correspond to the solution $U(x)$ superimposed with eigenfunction $u_1(x)$ multiplied by a small coefficient ϵ. The arrows indicate the directions where the fronts of the droplets shift after a the eigenfunctions are added.

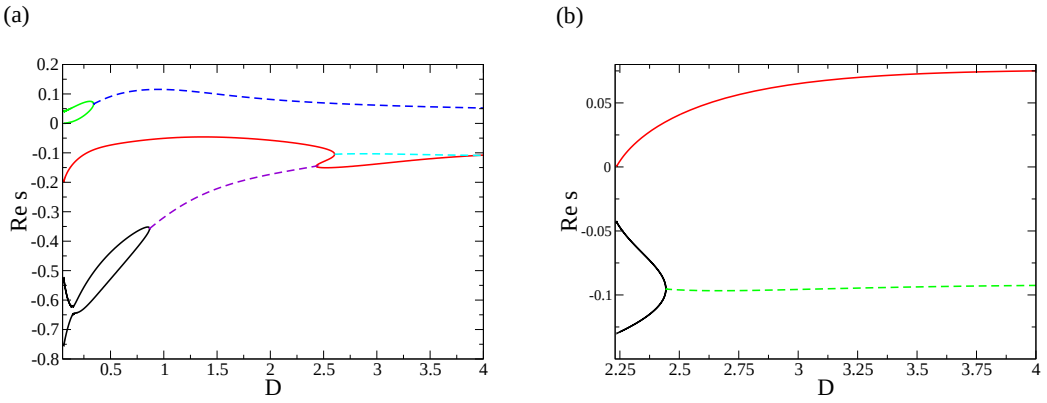

Figure 5.39: The real parts of the dominant eigenvalues s along the $n = 2$ secondary branch when $L = 22$ at $\bar{u} = 0.4$ (Fig. 5.9(a)). Panel (a) corresponds to the first secondary branch in Fig. 5.9(a) starting at $D \approx 0.06$ (see the red dashed line), while panel (b) corresponds to the second secondary branch in Fig. 5.9(a) starting at $D \approx 2.24$ (see the green dashed line). The solid lines correspond to the eigenvalues with zero imaginary part. The dashed lines correspond to the eigenvalues with non-zero imaginary part.

saddle-node bifurcation and two Hopf bifurcations. Also, we note that there are two stable intervals on part a (the upper part) of the bifurcation diagram shown in Fig. 5.14(b), namely, $0.72 \lesssim D \lesssim 0.90$ and $1.21 \lesssim D \lesssim 1.76$. Part c (the middle part of the bifurcation diagram) is unstable, and there is a stable interval on part c (the lower part) of the bifurcation diagram, namely, $D \gtrsim 2.15$. Fig. 5.38 shows the most unstable symmetry-breaking eigenmodes u_1 superimposed with the primary 2-mode solutions u_0 for $\bar{u} = 0.55$ and $L = 50$ at $D = 0.05$ and $D = 1$ (panels (a) and (b), respectively). Note that both panels correspond to the upper part of the bifurcation diagram shown in Fig. 5.14(b). In both cases, we can observe that the symmetry-breaking modes appear to be volume modes. We note that time-dependent simulations support the theoretical predictions following from Fig. 5.36(a) and (b), and we have decided not to show such simulations here.

5.4.2.4 Linear stability of secondary branches

In this section, we analyse the linear stability of the secondary branches. Figs. 5.39–5.52 show the real parts of the dominant eigenvalues s along the secondary branches presented in Figs. 5.9 and 5.14. As before, the solid lines correspond to real eigenvalues (i.e., eigenvalues with zero imaginary parts), the dashed lines correspond to eigenvalues with non-zero imaginary parts, the solid red squares represent saddle-node bifurcations, and the solid red triangles represent Hopf bifurcations.

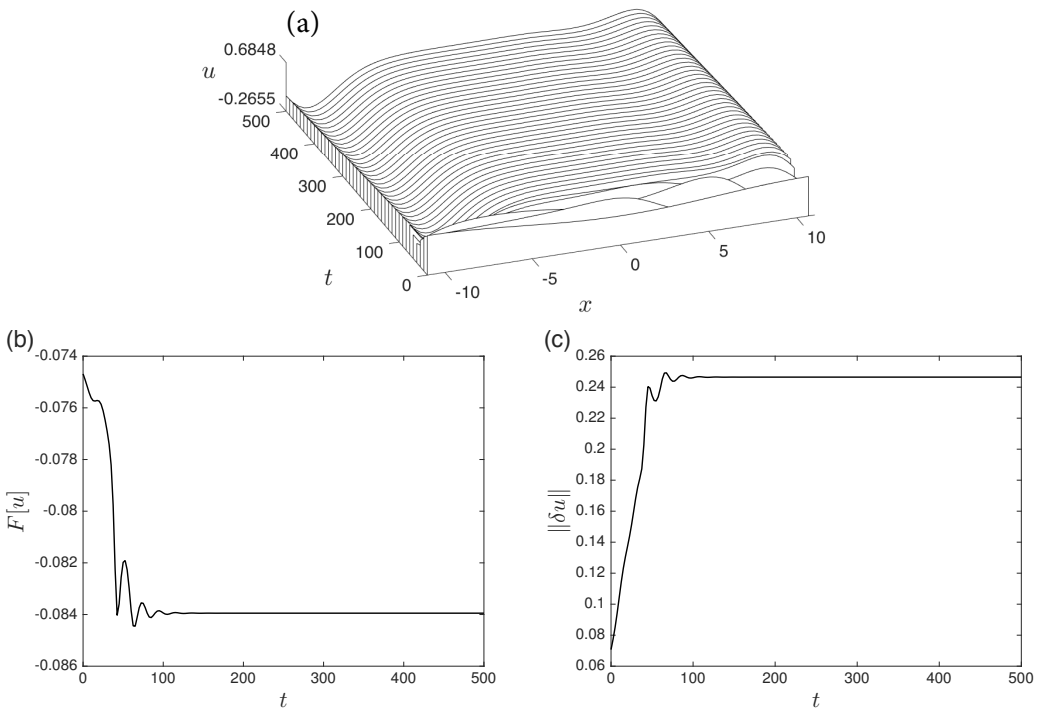

Figure 5.40: Numerical solution of the convective Cahn-Hilliard equation (2.28) on the periodic domain of length $L = 22$ for $\bar{u} = 0.4$ and $D = 3$, with the initial condition $u(x,0) = \bar{u} - 0.1\cos(\pi x/L)$. Panel (a) shows the time evolution of the solution for $t \in [0, 1500]$ in a frame moving at velocity 0.625 (for presentational purposes). Panel (b) shows the time evolution of the energy of the solution. Panel (c) shows the time evolution of the norm of the solution.

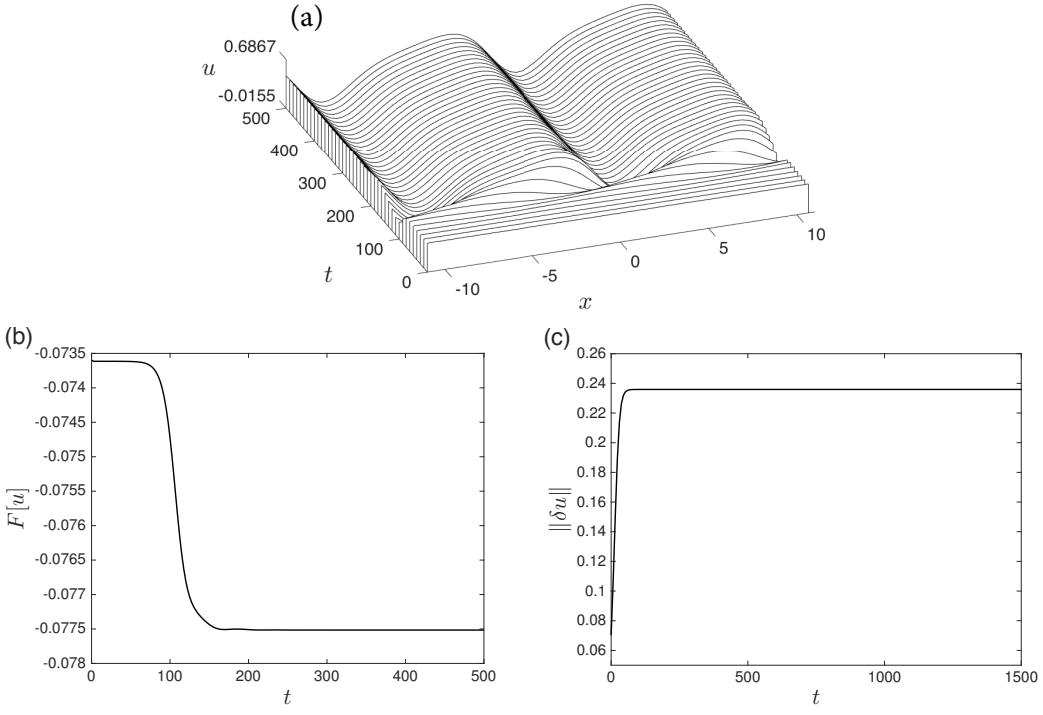

Figure 5.41: Numerical solution of the convective Cahn-Hilliard equation (2.28) on the periodic domain of length $L = 22$ for $\bar{u} = 0.4$ and $D = 3$, with the initial condition equal to $\bar{u}$ superimposed with a small-amplitude random noise. Panel (a) shows the time evolution of the solution for $t \in [0, 1500]$ in a frame moving at velocity 1.05 (for presentational purposes). Panel (b) shows the time evolution of the energy of the solution. Panel (c) shows the time evolution of the norm of the solution.

Figs. 5.39(a) and (b) correspond to $L = 22$ at $\bar{u} = 0.4$ (see Fig. 5.9 (a)). Panel (a) corresponds to the first secondary branch shown by the red dashed line in Fig. 5.9(a), while panel (b) corresponds to the second secondary branch shown by the green dashed line in Fig. 5.9(a). We can observe that for both secondary branches there is at least one eigenvalue with a positive real part for all the values of the driving force, D, i.e., both branches are unstable for all D values. Taking into account the fact that the 2-mode primary branch is also unstable for $D \lesssim 2.24$ (see Fig. 5.26(a)), we can conclude that in a time evolution, a solution will not evolve into either a solution of the 2-mode primary branch or a solution of the secondary branch. In fact, for these values of D the solution eventually evolves into a single-droplet solution of period $L = 22$, and this is confirmed in the time-dependent simulations presented in Fig. 5.27. For $D \gtrsim 2.24$, the solution of the 2-mode primary branch is linearly stable, and this is confirmed in the time-dependent simulations presented in Fig. 5.28. We note, however, that a single-droplet solution of period $L = 22$ also turns out to be linearly stable for $D = 3.0$, and so for some initial conditions the solution may evolve into a single-droplet solution. An example of such a time-dependent simulation is given in Fig. 5.40, where the initial condition is $u(x, 0) = \bar{u} - 0.1\cos(\pi x/L)$. It can be observed that after an initial transient period, the solution evolves into a single-droplet solution. Note, however, that for a uniform solution on the domain of length $L = 22$, the growth rate of a 1-mode disturbance of period $L = 22$ is 0.036, while the growth rate for a 2-mode disturbance (i.e., a disturbance of period $L = 11$) is 0.063 (with the higher modes being stable). Therefore, in time-dependent simulations with the initial condition equal to $\bar{u} = 0.4$ superimposed with a small random noise, we expect the long-time dynamics to converge to a 2-mode solution. This is confirmed in the time-dependent simulation given in Fig. 5.41. It is interesting to note that, although the energy of the one-droplet turns out to be lower than the energy on the two-droplet solution, the two-droplet solution is still selected in time dependent simulations and does not coarsen. As expected, "energy" is not a good measure for out-of-equilibrium solutions.

Figs. 5.42(a) and (b) correspond to $L = 25$ at $\bar{u} = 0.4$ (see Fig. 5.9 (b)). Panel (a) corresponds to the first secondary branch shown by the red dashed line in Fig. 5.9(b), while panel (b) corresponds to the second secondary branch shown by the green dashed line in Fig. 5.9(b). For the first secondary branch, there are two saddle-node bifurcations, while for the second secondary branch there are no saddle-node bifurcations. Also, in

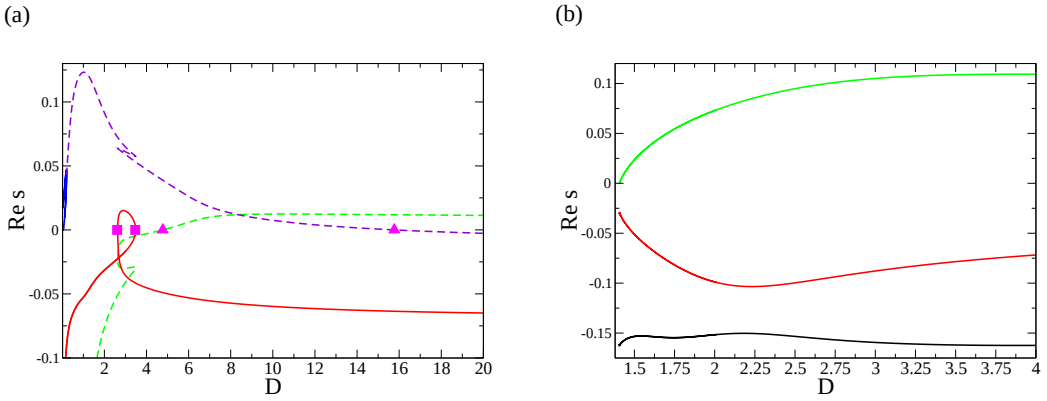

Figure 5.42: The real parts of the dominant eigenvalues s along the $n = 2$ secondary branch when $L = 25$ at $\bar{u} = 0.4$ (Fig. 5.9(b)). Panel (a) corresponds to the first secondary branch in Fig. 5.9(b) starting $D \approx 0.019$ (see the red dashed line), while panel (b) corresponds to second secondary branch in Fig. 5.9(b) starting $D \approx 1.41$ (see the green dashed line). The solid lines correspond to the eigenvalues with zero imaginary part. The dashed lines correspond to the eigenvalues with non-zero imaginary part. The solid red squares represent the saddle-node bifurcations and the solid red triangles represent the Hopf bifurcations.

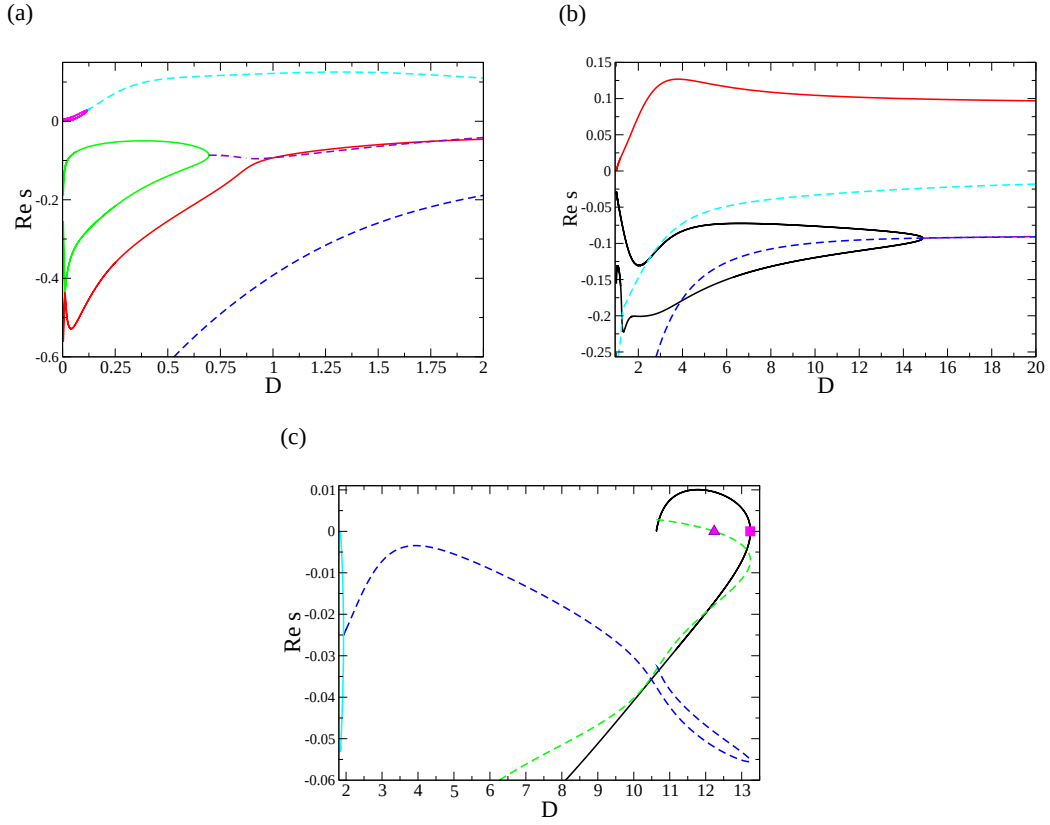

Figure 5.43: The real parts of the dominant eigenvalues s along the $n = 2$ secondary branch when $L = 30$ at $\bar{u} = 0.4$ (Fig. 5.9(c)). Panel (a) corresponds to the first secondary branch starting $D \approx 0.0032$ (see the red dashed line), while panel (b) corresponds to second secondary branch starting $D \approx 1.003$ (see the green dashed line). Panel (c) corresponds to the third secondary branch starting at $D \approx 1.85$ and terminating at $D \approx 10.63$. The solid lines correspond to the eigenvalues with zero imaginary part. The dashed lines correspond to the eigenvalues with non-zero imaginary part. The solid red squares represent the saddle-node bifurcations and the solid red triangles represent the Hopf bifurcations.

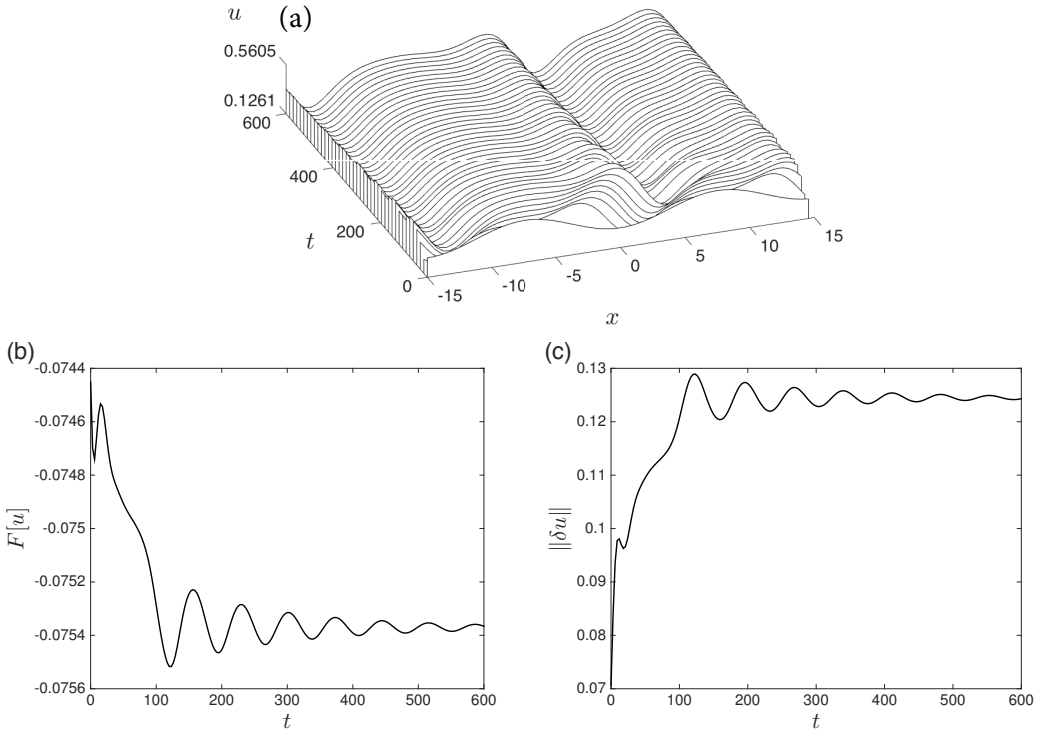

Figure 5.44: Numerical solution of the convective Cahn-Hilliard equation (2.28) on the periodic domain of length $L = 30$ for $\bar{u} = 0.4$ and $D = 5$, with the initial condition $u(x,0) = \bar{u} - 0.1\cos(2\pi x/L) + 0.001\cos(\pi x/L)$. Panel (a) shows the time evolution of the solution for $t \in [0, 600]$ in a frame moving at velocity 1.765 (for presentational purposes). Panel (b) shows the time evolution of the energy of the solution. Panel (c) shows the time evolution of the norm of the solution.

Fig. 5.42(a) can we see that two eigenvalues with non-zero real parts cross the imaginary axis. Therefore, there are two Hopf bifurcation on the first secondary branch, while Fig. 5.42(b) implies that there are no Hopf bifurcations on the second secondary branch. In addition, we can observe that for both secondary branches there is at least one eigenvalue with a positive real part for all the values of the driving force, D. Therefore, as for $L = 22$, both branches are unstable for all D values. So, in a time evolution, a solution will not evolve into a solution of the secondary branch. Instead, it can evolve into a 2-mode solution (if D belongs to the stable interval), or a single-mode solution, or a time-periodic solution – such time evolutions are shown in Figs. 5.30–5.32.

Fig. 5.43 corresponds to $L = 30$ at $\bar{u} = 0.4$ (see Fig. 5.9(c)). Panels (a), (b) and (c) correspond to the first, second and third secondary branches shown by the red, green and blue dashed lines, respectively, in Fig. 5.9(c). The first and the second secondary

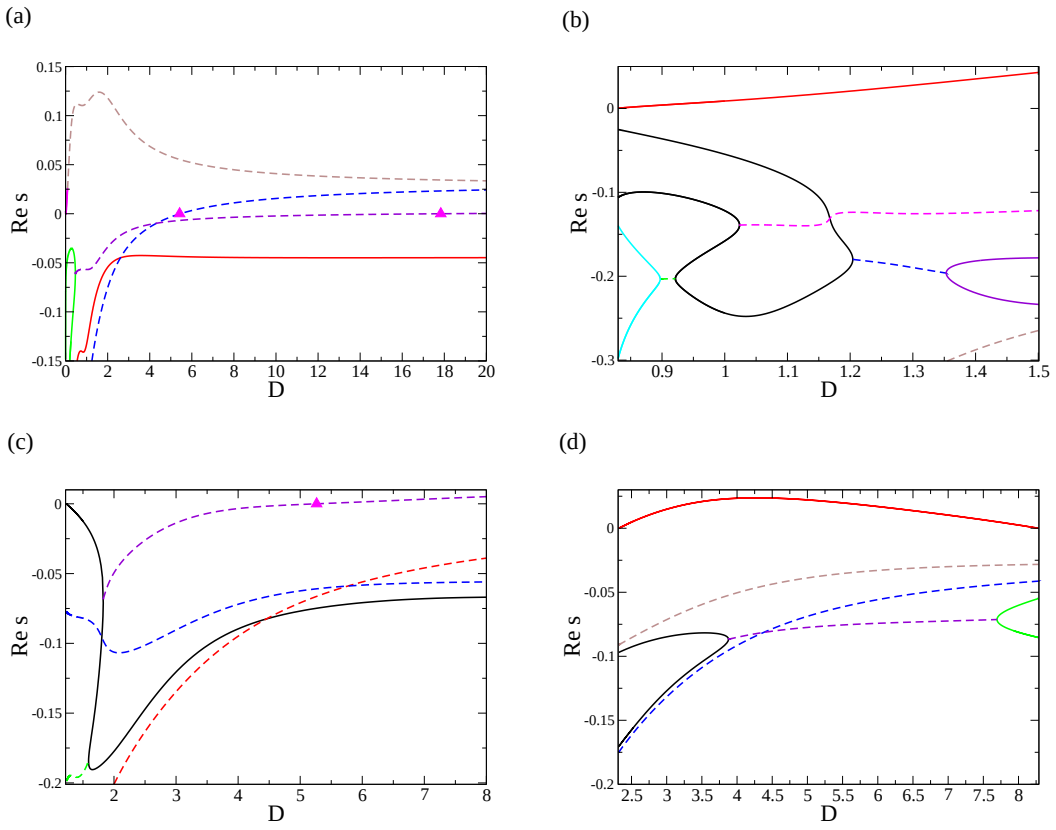

Figure 5.45: The real parts of the dominant eigenvalues s along the $n = 2$ secondary branch when $L = 35$ at $\bar{u} = 0.4$ (Fig. 5.9(d)). Panel (a) corresponds to the first secondary branch starting $D \approx 0.0006$ (see the red dashed line), while panel (b) corresponds to second secondary branch starting $D \approx 0.82$ (see the green dashed line). Panel (c) corresponds to the third secondary branch starting $D \approx 1.23$ (see the blue dashed line). Panel (d) corresponds to the fourth secondary branch between $D \approx 2.32$ and $D \approx 8.28$ (see the yellow dashed line). The solid lines correspond to the eigenvalues with zero imaginary part. The dashed lines correspond to the eigenvalues with non-zero imaginary part. The solid red triangles represent the Hopf bifurcations.

branches go off to infinity and appear to be linearly unstable for all D values. There are no saddle nodes or Hopf bifurcations on these branches. The third side branch does not go off to infinity. Instead, it is reconnected to the 2-mode primary branch (at point 4 in Fig. 5.9(c)). In addition, this branch exhibits a saddle-node bifurcation and has one Hopf bifurcation to time-periodic solutions. Interestingly, we can observe that the part of this branch connecting point 3 (in Fig. 5.9(c)), for which $D = 1.845$, to the saddle-node, for which $D = 13.238$, appears to be linearly stable. This means that in a time-dependent simulation a numerical solution may evolve into a symmetry-broken solution of this secondary branch. An example of such a time-dependent solution is shown in Fig. 5.44 where $D = 5$ and the initial condition is chosen to be $u(x, 0) = \bar{u} - 0.1\cos(2\pi x/L) + 0.001\cos(\pi x/L)$. It can be observed that the solution initially tends to evolve into a symmetric 2-mode solution (up to approximately $t = 70$), but

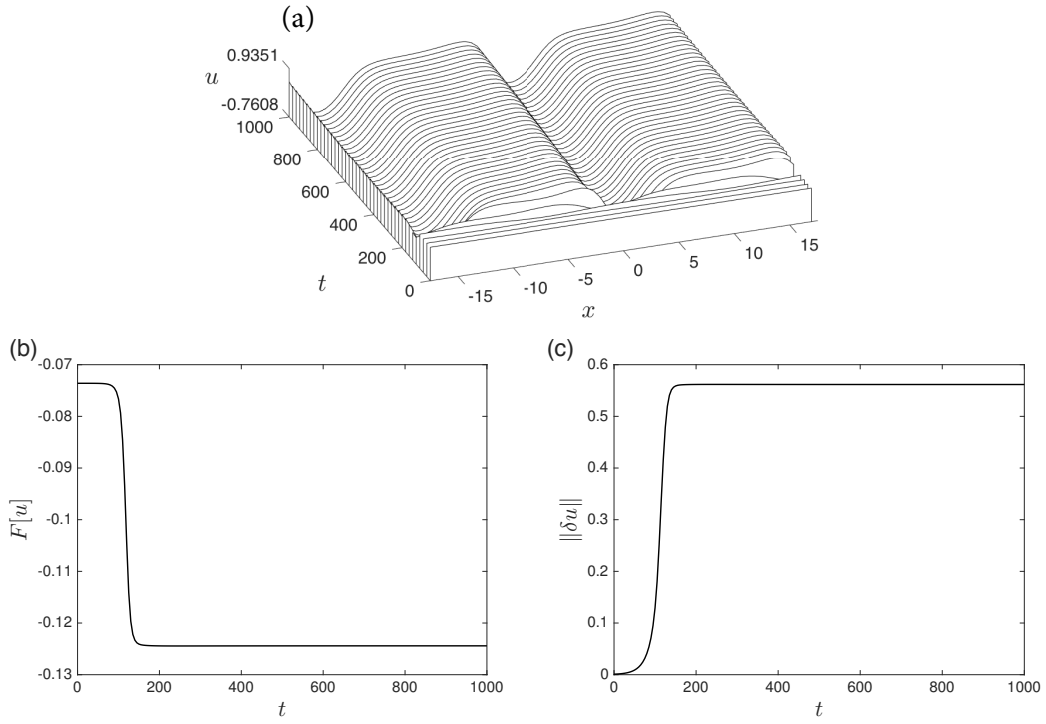

Figure 5.46: Numerical solution of the convective Cahn-Hilliard equation (2.28) on the periodic domain of length $L = 35$ for $\bar{u} = 0.4$ and $D = 1$, with the initial condition $u(x,0) = \bar{u} + 0.001\cos(2\pi x/L) + 0.001\cos(\pi x/L)$. Panel (a) shows the time evolution of the solution for $t \in [0, 1000]$ in a frame moving at velocity 0.13 (for presentational purposes). Panel (b) shows the time evolution of the energy of the solution. Panel (c) shows the time evolution of the norm of the solution.

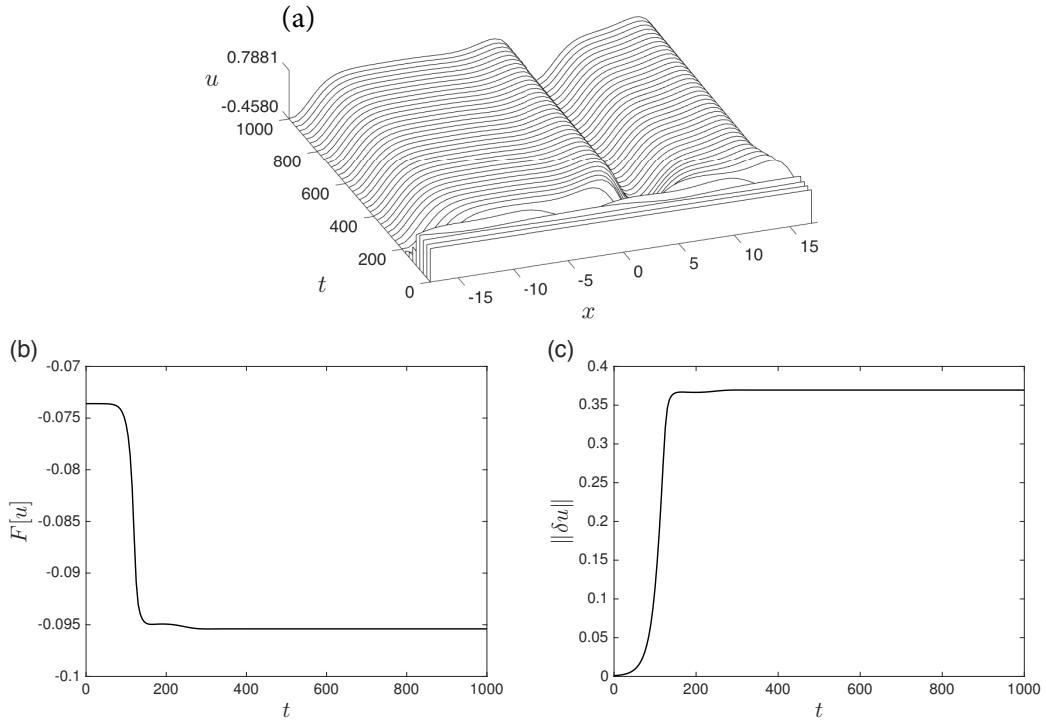

Figure 5.47: Numerical solution of the convective Cahn-Hilliard equation (2.28) on the periodic domain of length $L = 35$ for $\bar{u} = 0.4$ and $D = 2$, with the initial condition $u(x,0) = \bar{u} + 0.001\cos(2\pi x/L) + 0.001\cos(\pi x/L)$. Panel (a) shows the time evolution of the solution for $t \in [0, 1000]$ in a frame moving at velocity 0.371 (for presentational purposes). Panel (b) shows the time evolution of the energy of the solution. Panel (c) shows the time evolution of the norm of the solution.

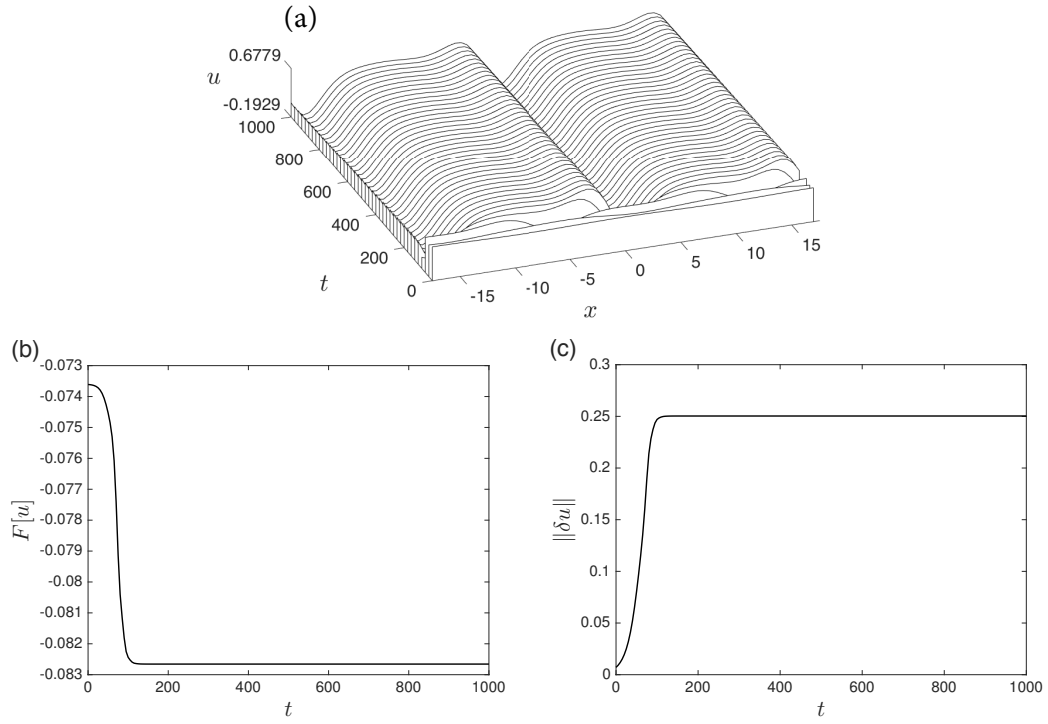

Figure 5.48: Numerical solution of the convective Cahn-Hilliard equation (2.28) on the periodic domain of length $L = 35$ for $\bar{u} = 0.4$ and $D = 3$, with the initial condition $u(x,0) = \bar{u} + 0.01\cos(2\pi x/L)$. Panel (a) shows the time evolution of the solution for $t \in [0, 1000]$ in a frame moving at velocity 0.748 (for presentational purposes). Panel (b) shows the time evolution of the energy of the solution. Panel (c) shows the time evolution of the norm of the solution.

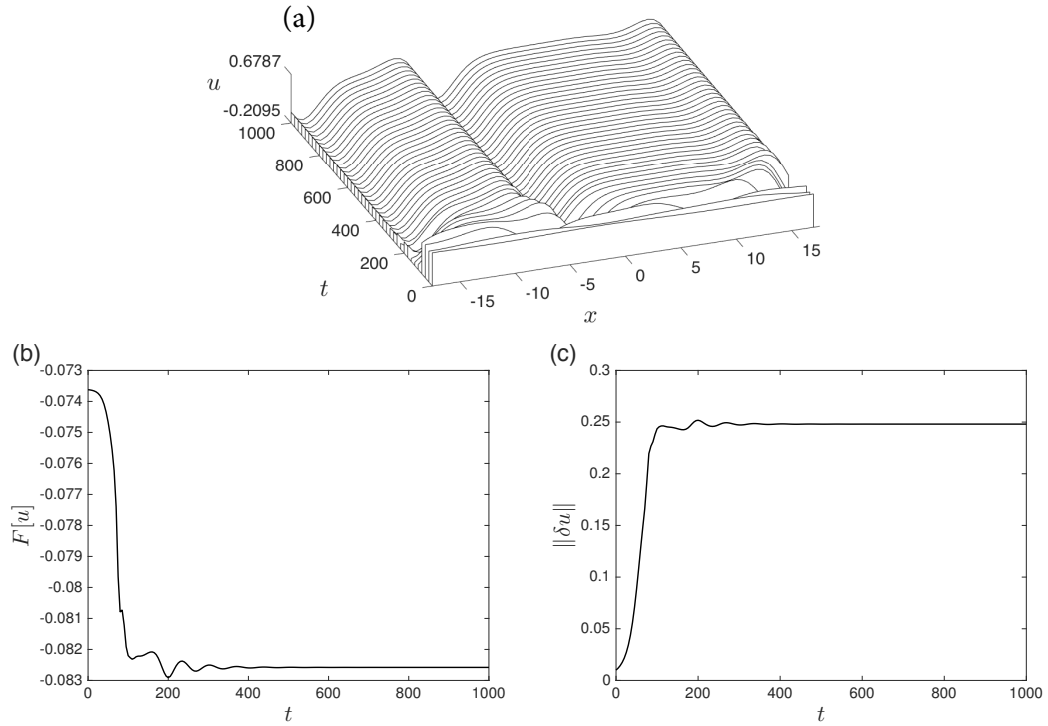

Figure 5.49: Numerical solution of the convective Cahn-Hilliard equation (2.28) on the periodic domain of length $L = 35$ for $\bar{u} = 0.4$ and $D = 3$, with the initial condition $u(x,0) = \bar{u} + 0.01\cos(2\pi(x+2)/L) + 0.01\cos(\pi(x+2)/L)$. Panel (a) shows the time evolution of the solution for $t \in [0, 1000]$ in a frame moving at velocity 0.761 (for presentational purposes). Panel (b) shows the time evolution of the energy of the solution. Panel (c) shows the time evolution of the norm of the solution.

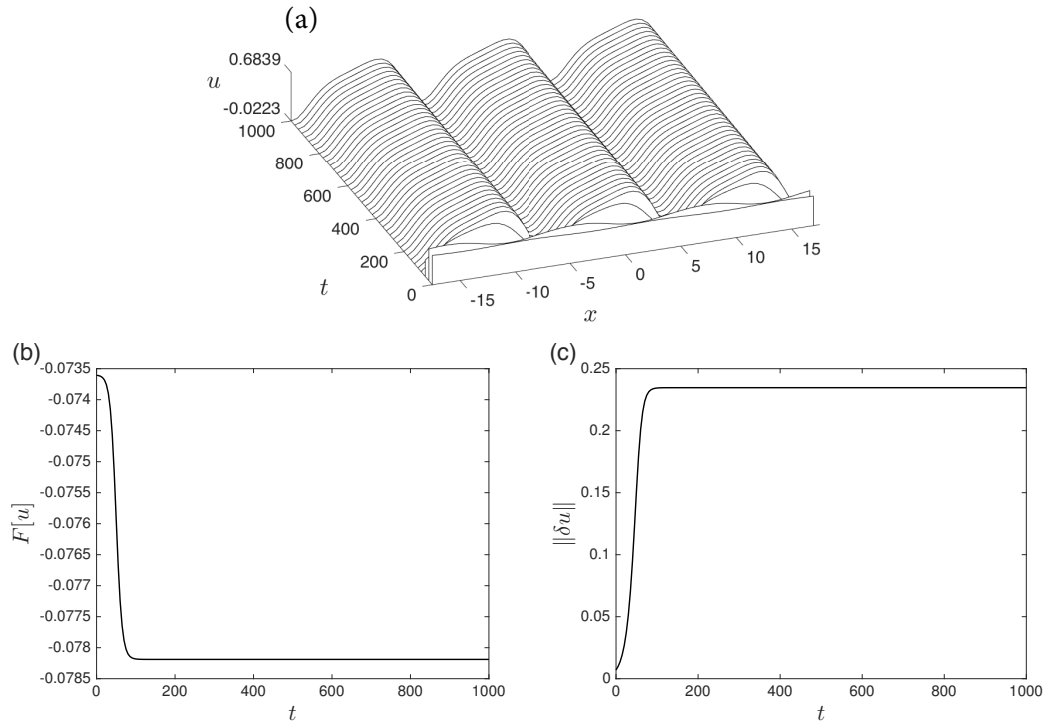

Figure 5.50: Numerical solution of the convective Cahn-Hilliard equation (2.28) on the periodic domain of length $L = 35$ for $\bar{u} = 0.4$ and $D = 3$, with the initial condition $u(x,0) = \bar{u} + 0.01\cos(3\pi(x-3)/L)$. Panel (a) shows the time evolution of the solution for $t \in [0, 1000]$ in a frame moving at velocity 1.026 (for presentational purposes). Panel (b) shows the time evolution of the energy of the solution. Panel (c) shows the time evolution of the norm of the solution.

then the symmetry of the solution breaks, and the solution evolves (through oscillations of a decaying amplitude) into a symmetry-broken solution consisting of two droplets of different sizes.

Fig. 5.45 corresponds to $L = 35$ at $\bar{u} = 0.4$ (see Fig. 5.9(d)). Panels (a), (b), (c) and (d) correspond to the first, second, third and fourth secondary branches shown by the red, green, blue and yellow dashed lines, respectively, in Fig. 5.9(d). Figs. 5.45(a) and (c) have two and one Hopf bifurcations, respectively, while there are no Hopf bifurcations in Figs. 5.45(b) and (d). Figs. 5.45 (a), (b) and (d) imply that there are no stable intervals for the first, second and fourth secondary branches, while Fig. 5.45(c) implies that there is a stable interval for the third secondary branch between $D \approx 1.23$ and $D \approx 5.26$. Taking into account the fact that for the 2-mode primary branch the stable intervals are $0.82 \lesssim D \lesssim 1.23$ and $2.32 \lesssim D \lesssim 8.28$, we can conclude that for $D \in (0.82, 1.23)$ a 2-mode solution is stable, for $D \in (1.23, 2.32)$ a symmetry-broken solution is stable, for $D \in (2.32, 5.26)$ both a 2-mode solution and a symmetry-broken solution are stable, for $D \in (5.26, 8.28)$ a 2-mode solution is stable. Of course, there may exist other branches of solutions that are stable for these values of D, e.g., solutions of the 1-mode primary

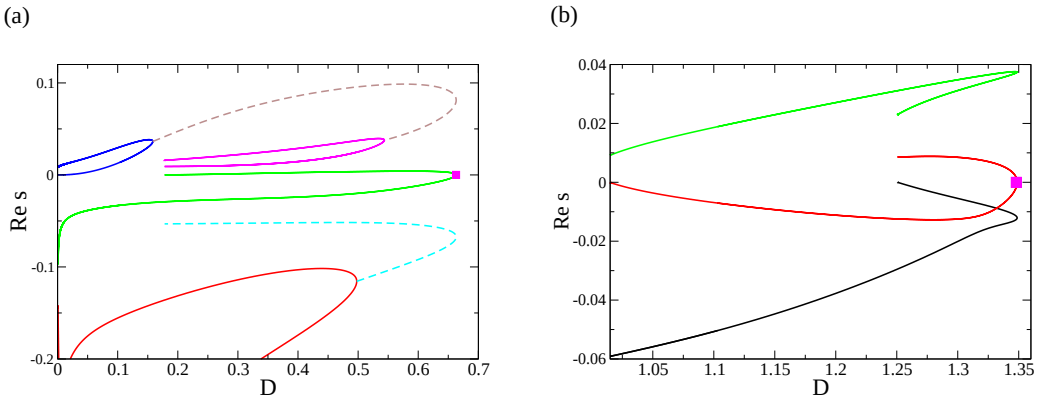

Figure 5.51: The real parts of the dominant eigenvalues s along the $n = 2$ secondary branch when $L = 35$ at $\bar{u} = 0.55$ (Fig. 5.14(a)). Panel (a) corresponds to the first secondary branch between $D \approx 0.0007$ and $D \approx 0.18$ (see the red dashed line). Panel (b) corresponds to the second secondary branch between $D \approx 1.01$ and $D \approx 1.25$ (see the green dashed line). The solid lines correspond to the eigenvalues with zero imaginary part. The dashed lines correspond to the eigenvalues with non-zero imaginary part. The solid red squares represent the saddle-node bifurcations.

branch with $L = 35$ are stable for $D \lesssim 7.28$, or there may exist some time-periodic solutions (or even quasi-periodic or chaotic solutions). For relatively large values of L there can also exist n-mode branches with $n > 2$ (see, e.g., Fig. 5.9), and there can of course also exist other symmetry-broken solutions bifurcating from n-mode branches with $n > 2$. For example, for $L = 35$, the first four modes are linearly unstable for $\bar{u} = 0.4$, and, therefore, in time-dependent simulations we may also observe 3- and 4-mode solutions. For other values of D, neither a 1-mode nor 2-mode nor a symmetry-broken solution are stable. Then, a time-dependent solution can evolve, for example, into a time-periodic solution or a multi-mode solution (or a quasi-periodic or chaotic solution).

Some of these predictions are confirmed in the time-dependent simulations presented in Figs. 5.46–5.50 for $\bar{u} = 0.55$ and $L = 35$ and for various values of D and various initial conditions. Fig. 5.46 corresponds to $D = 1$ for which we expect a 2-mode solution to be stable. Indeed, choosing $u(x, 0) = \bar{u} + 0.001\cos(2\pi x/L) + 0.001\cos(\pi x/L)$, we can observe the time-dependent solution evolves into an apparently stable 2-mode solution. Fig. 5.47 corresponds to $D = 2$ for which a symmetry-broken solution is stable. Indeed, choosing the same initial condition as for Fig. 5.46, we observe the time-dependent solution evolves into a symmetry-broken solution consisting of two droplets of different sizes. Figs. 5.48, 5.49 and 5.50 correspond to $D = 3$ with the initial conditions $u(x, 0) = \bar{u} + 0.01\cos(2\pi x/L)$, $u(x, 0) = \bar{u} + 0.01\cos(2\pi(x + 2)/L)$ and

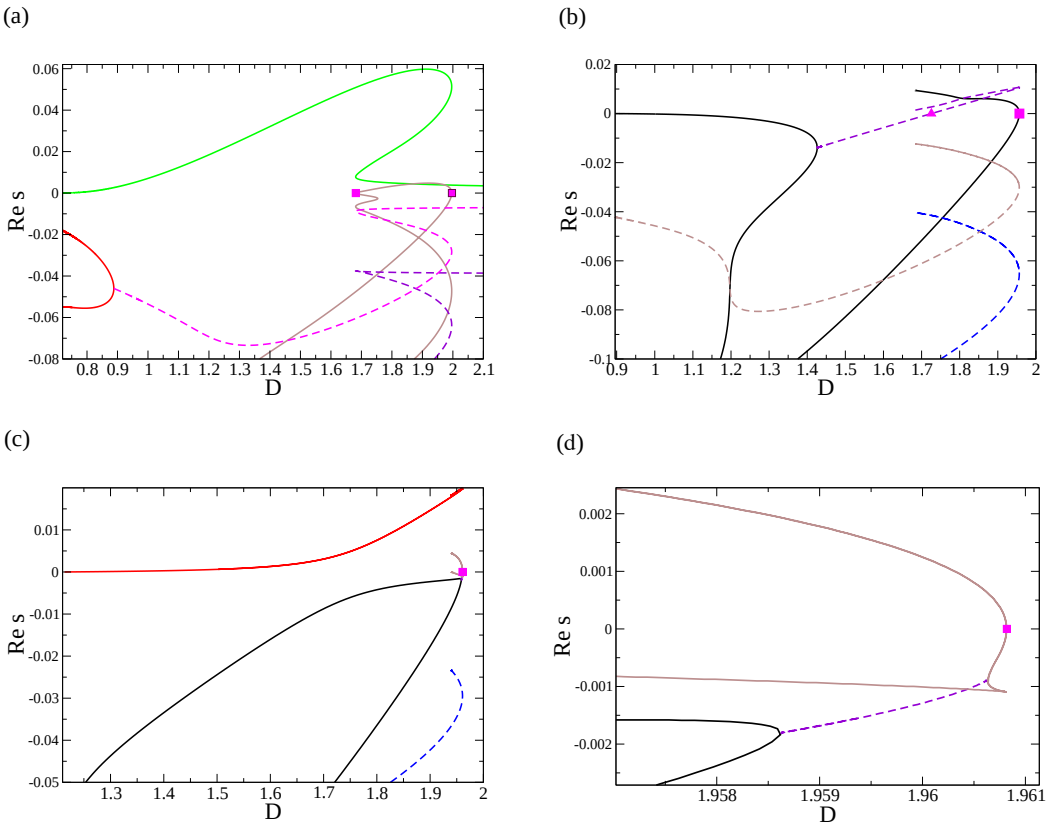

Figure 5.52: The real parts of the dominant eigenvalues s along the $n = 2$ secondary branch when $L = 50$ at $\bar{u} = 0.55$ (Fig. 5.14(b)). Panel (a) corresponds to the first secondary branch starting $D \approx 0.72$ (see the red dashed line). Panel (b) corresponds to the second secondary branch between $D \approx 0.90$ and $D \approx 1.68$ (see the green dashed line). Panel (c) corresponds to the third secondary branch between $D \approx 1.21$ and $D \approx 1.94$ (see the blue dashed line). Panel (d) shows a zoom of panel (c) around the region of the saddle-node bifurcation. The solid lines correspond to the eigenvalues with zero imaginary part. The dashed lines correspond to the eigenvalues with non-zero imaginary part. The solid red squares represent the saddle-node bifurcations and the solid red triangles represent the Hopf bifurcations.

$u(x,0) = \bar{u} + 0.01\cos(3\pi(x-3)/L)$, respectively. For this value of D, we expect both a 2-mode solution and a symmetry-broken solution to be stable. Indeed, the results presented in Fig. 5.48 indicate that the solution converges to a 2-mode solution, whereas the results presented in Fig. 5.49 indicate that the solution evolves into a symmetry-broken solution consisting of two droplets of different sizes. It is interesting to note that there may exist other stable solutions, and, in particular, for the initial condition chosen for Fig. 5.50, we observe that the solution evolves into a 3-mode solution (that appears to be stable, at least in the time interval presented in Fig. 5.50). In this thesis, we do not investigate in detail branches of n-mode solutions with $n > 2$.

Figs. 5.51(a) and (b) correspond to $L = 35$ at $\bar{u} = 0.55$ (see Fig. 5.14 (a)). Panel (a) corresponds to the first secondary branch shown by the red dashed line in Fig. 5.14(a), while panel (b) corresponds to the second secondary branch shown by the green dashed

line in Fig. 5.14(a). In Figs. 5.51(a) and (b), looking at the real parts of eigenvalues of the secondary branches, we can see that for both branches there are no branch points, no Hopf bifurcations, and there are no stable intervals. These observations can be corroborated by time-dependent simulations, however, we decided not to present such calculations here, as the results agree with the expectations.

Figs. 5.52(a), (b) and (c) correspond to $L = 50$ at $\bar{u} = 0.55$ (see Fig. 5.14(b)). Panels (a), (b) and (c) correspond to the first, second and third secondary branches shown by the red, green and blue dashed lines, respectively, in Fig. 5.14(b). Panel (d) additionally shows a zoom of panel (c) around the region of the saddle-node bifurcation. There are two saddle-node bifurcation on the first secondary branch and one saddle-node bifurcation on the second and the third secondary branches. In Figs. 5.52(a) and (c), we can see that both for the first and the third branches there are no branch points and no Hopf bifurcations, and there are no stable intervals, while Fig. 5.52(b) shows that the second branch has one Hopf bifurcation and there is a stable interval between $D \approx 0.90$ and $D \approx 1.68$. Taking into account the fact that for the 2-mode primary branch the stable intervals are $0.72 \lesssim D \lesssim 0.90$ and $D \gtrsim 2.12$, we can conclude that for $D \in (0.72, 0.90)$ a 2-mode solution is stable, for $D \in (0.9, 1.68)$ a symmetry-broken solution is stable, for $D \in (1.68, 2.12)$ both a 2-mode solution and a symmetry-broken solution are stable, for $D \gtrsim 2.12$ a 2-mode solution is stable. For other values of D, neither a 2-mode solution nor a symmetry-broken solution are stable. Then, as also discussed above for other cases, a time-dependent solution can, for example, evolve into a one-droplet solution (that is stable for $D \lesssim 7.13$), a time-periodic or multi-mode or quasi-periodic or chaotic solution. These observations can be corroborated by time-dependent simulations, however, we decided not to present such calculations here, as the results agree with the expectations and are generally qualitatively similar to the already presented time-dependent simulations.

5.4.2.5 Regions of linear stability of 2-mode solutions in the (D, L)- and $(D, \bar{u})$-planes.

In the previous Section, we have found that the driving force can have an interesting and non-trivial effect on coarsening behaviour, namely, we found that for a fixed value of $\bar{u}$, there can exist stability intervals for the driving force D, i.e., a carefully chosen driving force can be used to prevent coarsening. We also found that there can exist intervals for the driving force D, where solutions evolve into time-periodic solutions that resemble

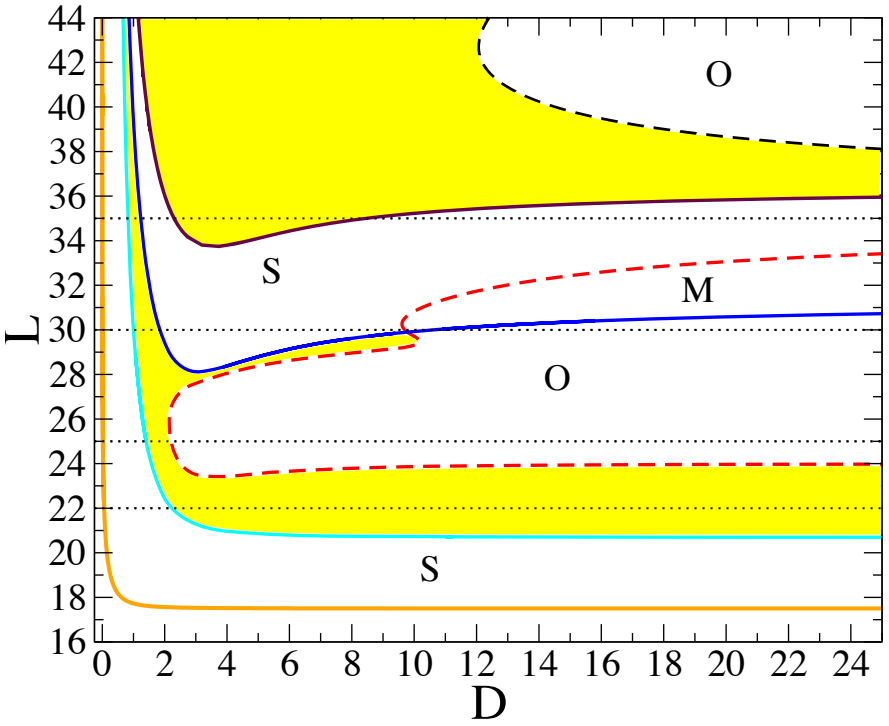

Figure 5.53: Loci of the bifurcation points on the 2-mode primary branch in the (D, L)-plane for $\bar{u} = 0.4$. The solid lines correspond to the real eigenvalues (having zero imaginary parts). The dashed lines correspond to the eigenvalues with non-zero imaginary parts. The regions filled with yellow colour indicate linear stability regions. The instability types in various instability regions are indicated by letters S (to indicate the regions of existence of other stable steady solutions), O (to indicate the regions of existence of stable oscillatory solutions) and M (to indicate the regions of existence of stable steady and oscillatory solutions, i.e., stable solutions of mixed type).

superpositions of two droplets of different sizes that periodically exchange mass. In this Section, we construct bifurcation diagrams showing the locations of the bifurcation points on the 2-mode primary branches and obtain the stability regions (i.e., the regions where coarsening is prevented) in the (D, L)- and $(D, \bar{u})$-planes. The solid lines in the diagrams will correspond to the real eigenvalues (having zero imaginary parts). The dashed lines will correspond to the eigenvalues with non-zero imaginary parts.

Fig. 5.53 shows the loci of the bifurcation points on the 2-mode primary branch in the (D, L)-plane for $\bar{u} = 0.4$. The dotted lines correspond to $L = 22$, 25, 30 and 35. These are the values that were chosen in Figs. 5.9 and 5.26, so the dotted lines make the comparison with these figures easier. As expected, for $L = 22$ we have two bifurcation points to secondary branches. For $L = 25$ we have two bifurcation points to secondary branches and one Hopf bifurcation to a time-periodic branch. Also, for

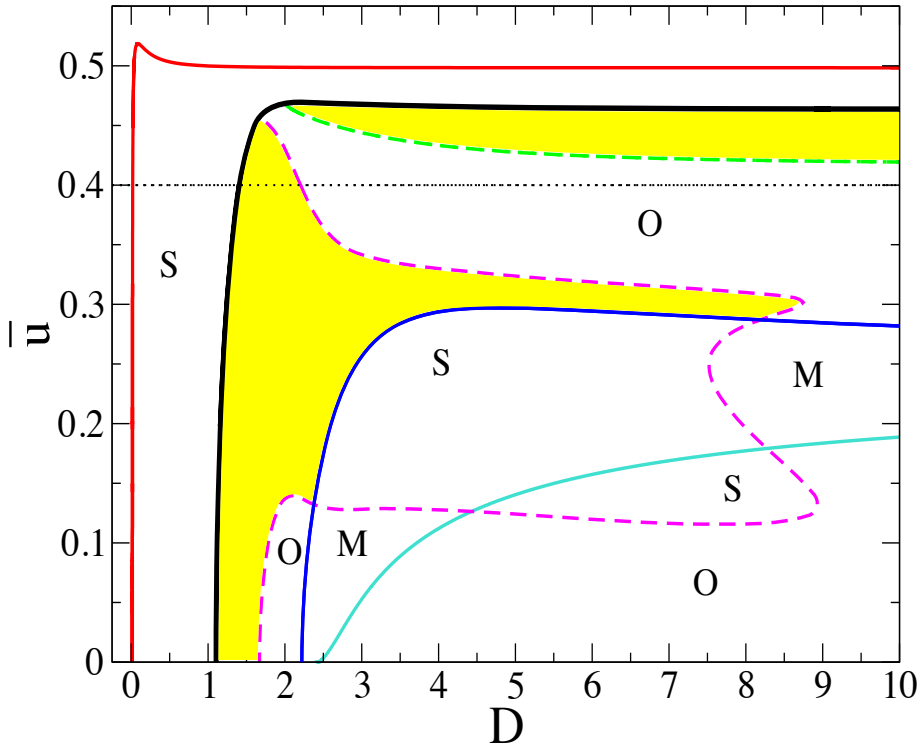

Figure 5.54: Loci of the bifurcation points on the 2-mode primary branch in the $(D, \bar{u})$-plane for $L = 25$. The solid lines correspond to the real eigenvalues (having zero imaginary parts). The dashed lines correspond to the eigenvalues with non-zero imaginary parts. The regions filled with yellow colour indicate linear stability regions. The instability types in various instability regions are indicated by letters S (to indicate the regions of existence of other stable steady solutions), O (to indicate the regions of existence of stable oscillatory solutions) and M (to indicate the regions of existence of stable steady and oscillatory solutions, i.e., stable solutions of mixed type).

$L = 30$ we have four bifurcation points to secondary branches and one Hopf bifurcation to a time-periodic branch. Finally, for $L = 35$ we have five bifurcation points to secondary branches. We can now clearly see how the various bifurcation points move as either D or L changes, and we can also obtain stability regions, which are shown by yellow colour in the diagram. In this diagram and in the other diagrams in this Section, the instability types in various instability regions are indicated by letters S (to indicate the regions of existence of other stable steady solutions), O (to indicate the regions of existence of stable oscillatory solutions) and M (to indicate the regions of existence of stable steady and oscillatory solutions, i.e., stable solutions of mixed type).

Fig. 5.54 shows the loci of the bifurcation points on the 2-mode primary branch in the $(D, \bar{u})$-plane for $L = 25$. The dotted line corresponds to $\bar{u} = 0.4$. Note we can have various numbers of bifurcation points to side branches and time-periodic solutions for smaller values of $\bar{u}$. However, for larger value of $\bar{u}$, we first loose bifurcations to time-periodic solutions, and then, we loose bifurcations to side branches.

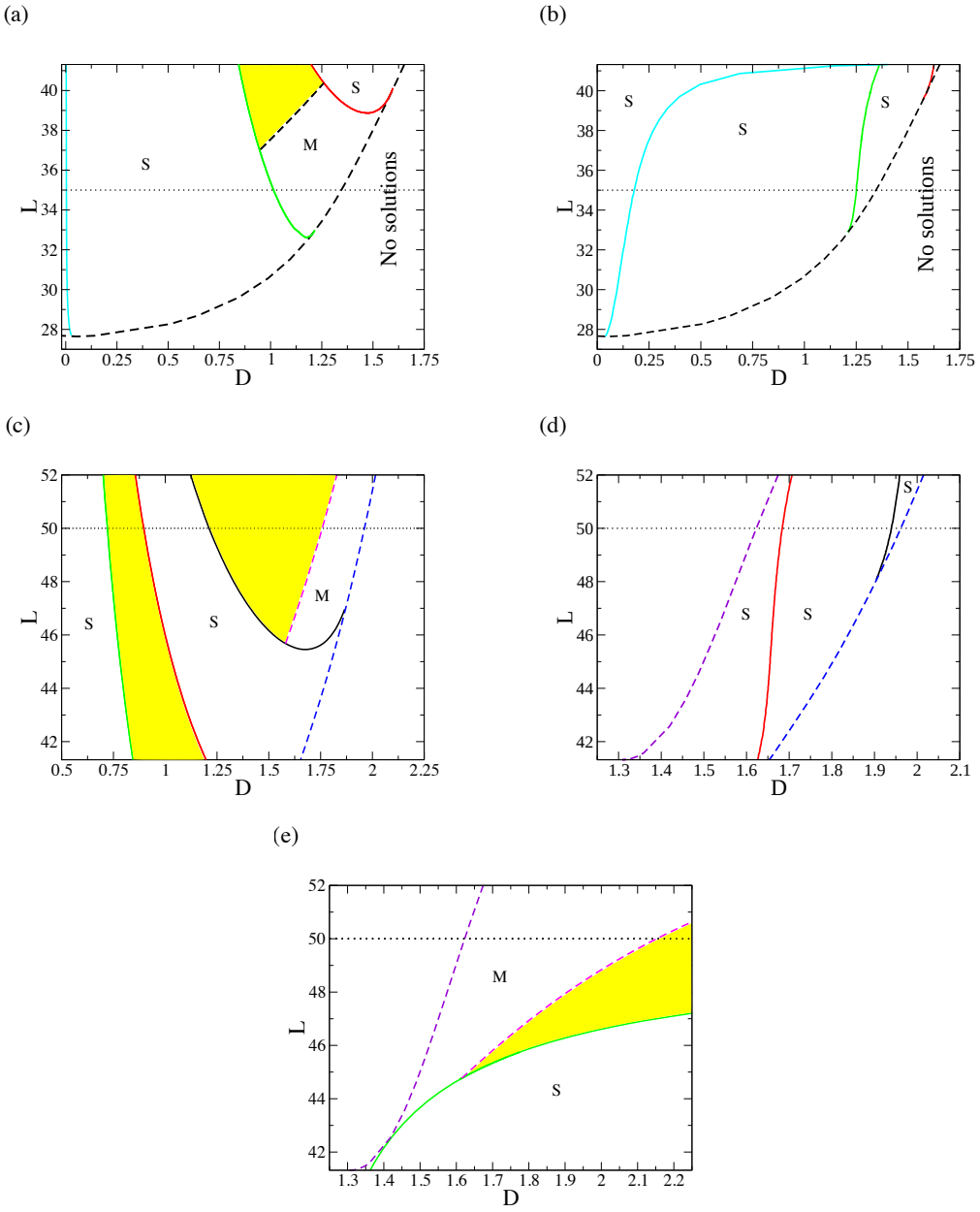

Figure 5.55: Loci of the bifurcation points on the 2-mode primary branch in the (D, L)-plane for $\bar{u} = 0.55$. The solid lines correspond to the real eigenvalues (having zero imaginary parts). The dashed lines correspond to the eigenvalues with non-zero imaginary parts. The regions filled with yellow colour indicate linear stability regions. Panels (a) and (b) correspond to the values of L that are less than $L_c = 41.32$. For these values of L, the primary branch has a single saddle-node bifurcation (when D is used as the principle bifurcation parameter, see Fig. 5.14(a)), and consists of two parts, the upper one and the lower one, that we denote by parts (a) and (b) in Fig. 5.14(a). Panels (a) and (b) correspond to parts (a) and (b) of the primary branch, respectively. Panels (c), (d) and (e) correspond to the values of L that are greater than $L_c = 41.32$. For these values of L, the primary branch has two saddle-node bifurcations (when D is used as the principle bifurcation parameter, see Fig. 5.14(b)), and consists of three parts, the upper one, the middle one, connecting the two saddle-nodes, and the lower one, starting from the second saddle-node and extending to infinity. These parts of the primary branch were denoted by parts (a), (b) and (c) in Fig. 5.14(d), and panels (c), (d) and (e) correspond these parts, respectively. The instability types in various instability regions are indicated by letters S (to indicate the regions of existence of other stable steady solutions), O (to indicate the regions of existence of stable oscillatory solutions) and M (to indicate the regions of existence of stable steady and oscillatory solutions, i.e., stable solutions of mixed type).

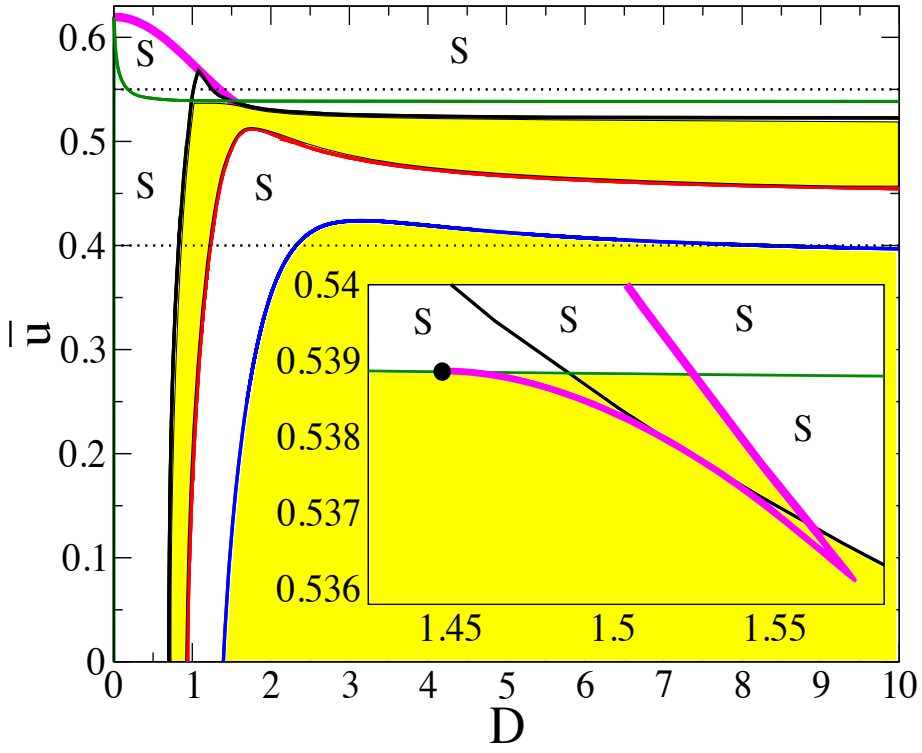

Figure 5.56: Loci of bifurcation points on the $n = 2$ primary branch in the $(D, \bar{u})$-plane for $L = 35$. The solid lines correspond to the eigenvalues with zero imaginary part. The letter S in the instability regions indicates the existence of other stable steady solutions.

Fig. 5.55 shows the loci of the bifurcation points on the 2-mode primary branch in the (D, L)-plane for $\bar{u} = 0.55$. We have split this figure in several parts. Panels (a) and (b) show correspond to $L < L_c \approx 41.32$. For these values of L, the primary branch has one saddle-node bifurcation, when D is used as the principle bifurcation parameter, see Fig. 5.14(a), and the branch returns to $D = 0$. Thus, the bifurcation branch consists of two parts, the upper and lower parts, that we denote by parts (a) and (b), respectively, in Fig. 5.14(a). Panels (a) and (b) of Fig. 5.55 correspond to parts (a) and (b) of the primary branch, respectively. Panels (c), (d) and (e) correspond to $L > L_c \approx 41.32$. For these values of L, the primary branch has a pair of saddle-node bifurcations, when D is used as the principle bifurcation parameter, see Fig. 5.14(b), and consists of three parts, the upper one denoted by letter (a), the middle one (connecting the two saddle-nodes) denoted by letter (b), and the lower one (starting from the second saddle-node and extending to infinity) denoted by letter (c). Panels (c), (d) and (e) of Fig. 5.55 correspond these parts (a), (b) and (c), respectively.

Fig. 5.56 shows the loci of the bifurcation points on the 2-mode primary branch in the $(D, \bar{u})$-plane for $L = 35$. The dotted lines correspond to $\bar{u} = 0.4$ and 0.55. Note that the thick solid line in this figure show the locations of the saddle-node bifurcations. We note that for $\bar{u} = 0.4$ we have five bifurcation points, while for $\bar{u} = 0.55$ we have

four bifurcation points and one saddle-node bifurcation, in agreement with Fig. 5.26(d). Note also that the line showing the locations of the saddle-node bifurcations seems to emerge from one of the branches showing the location of a bifurcation point (see the inset in the figure). This is in agreement with the theoretical consideration presented in Sect. 4.5. For the given domain size L for a 2-mode solution, we can find the value $\bar{u}_c$ of $\bar{u}$ at which the spatially-uniform solution changes its stability and a single-mode non-uniform solution emerges. This value is given by the formula

$$\bar{u}_c = \sqrt{\frac{1-k^2}{3}}, \tag{5.75}$$

where $k = 4\pi/L$ (the wavenumber is equal to $4\pi/L$ but not to $2\pi/L$, since the value of L that we consider corresponds to a 2-mode solution). For this value of $\bar{u}$, we can then find the value D_c by formula (4.97) which gives the value of the driving force at which the nature of the primary bifurcation changes (between subcritical and supercritical). Thus, we expect (and, in fact, observe in our numerical results, that we decided not to show here) that when L is fixed and D is used as the principal continuation parameter, we will find that for $\bar{u} > \bar{u}_c$ the primary branch has a single saddle-node bifurcation and returns to $D = 0$, for $\bar{u} = \bar{u}_c$, the primary branch has a single saddle-node bifurcation but it does not return to $D = 0$, but instead hits the D axis at $D = D_c$. For $\bar{u}$ is increased slightly beyond $\bar{u}_c$, there appears one more saddle-node bifurcation out of point (D_c, u_c), and the branch now extend to infinity. For $L = 35$, we find that $k = 0.3590$, $\bar{u}_c = 0.5389$ and $D_c = 1.4480$. This is in agreement with the results presented in Fig. 5.56 (see the inset showing point (1.4480,0.5389) by a black circle – it appears that the branch showing the locations of saddle-node bifurcations appears exactly from this point).

We note that for a more complete picture, it would be of benefit to indicate more precisely which non-2-mode solutions (e.g., droplet-mode, symmetry-broken or time-periodic solutions) are stable in the various regions where 2-mode solutions are unstable. However, we do not present such a 'morphological phase diagram' in the present thesis and leave this as a topic for future investigation.

Chapter 6

Two-dimensional solutions of the standard and convective Cahn-Hilliard equations

6.1 Introduction

In this chapter, we present some preliminary computations of bifurcation diagrams for single- and double-droplet solutions (or rather single- and double-hole solution for $\bar{u} > 0$) for the following two-dimensional convective Cahn-Hilliard equation:

$$u_t = -Duu_x - \nabla^2(u - u^3 + \nabla^2 u) \tag{6.1}$$

on a domain $(x, y) \in [-L_x, L_x] \times [-L_y, L_y]$ that is periodic both in the x- and y-direction. Note that for $D = 0$, we obtain the two-dimensional standard Cahn-Hilliard equation. For the computations, we use a numerical continuation procedure implemented in the continuation and bifurcation package Matcont [28] for Matlab. The details of the computational procedure are explained in Section 6.2. The case of the standard Cahn-Hilliard equation ($D = 0$) is analysed in Section 6.3 and the case of the convective Cahn-Hilliard equation is analysed in Section 6.4. We start the computations on a domain that is narrow in the y-direction and from neutrally stable small-amplitude sinusoidal waves in the x-direction, and perform first continuations in the domain-size parameter L_x (that is the half-domain size in the x-direction). This leads to

one-dimensional droplet/hole solutions. We then perform continuation in the domain-size parameter L_y (that is the half-domain size in the y-direction) obtaining bifurcations to side branches of two-dimensional droplet/hole solutions. We can then extend these droplet/hole solutions periodically either in the x- or y-direction and study the effect of driving on such double-droplet/hole solutions. In the present thesis, we restrict our attention to double-droplet/hole solutions extended in the x-direction. We additionally compute side branches of symmetry-broken solutions. We note that our numerical continuation code is capable of computing branches of time-periodic solutions. However, for two-dimensional equations, computation of branches of time-periodic solutions is time-consuming, and therefore this is left for future investigation. We also note that none of the computed branches of double-droplet/hole solutions extends to infinity in D. This means that there may exist additional branches of solutions that we have not computed yet. This is as well left as a topic for future investigation. In the future, we also plan to perform time-dependent simulations to verify the theoretical predictions and to better understand the behaviour of the solutions of two-dimensional standard and convective Cahn-Hilliard equations.

6.2 Numerical procedure

In this section, we discuss how continuation techniques can be used to compute branches of stationary and travelling periodic solutions and branches of time-periodic solutions of the two-dimensional standard ($D = 0$) and convective ($D \neq 0$) Cahn-Hilliard equations (6.1). Introducing a generalised moving coordinate $x \to x - a(t)$ in equation (6.1), we obtain

$$u_t = \dot{a}u_x - Duu_x - \nabla^2(u - u^3 + \nabla^2 u), \tag{6.2}$$

where the dot denotes differentiation with respect to time. As in Section 5.3.2.3, we assume that the speed of the moving frame, $\dot{a}$, is not necessarily a constant, but can vary in time. This will allow us to compute not only stationary and travelling periodic solutions but also time-periodic solutions. We consider this equation on a domain $(x, y) \in [-L_x, L_x] \times [-L_y, L_y]$ that is periodic both in the x- and y-direction.

Solution u can be represented by the following Fourier series:

$$u = \sum_{k_x, k_y \in \mathbb{Z}} \hat{u}_{k_y, k_x}(t) \exp(ik_x q_x x + ik_y q_y y), \tag{6.3}$$

where $q_x = \pi/L_x$, $q_y = \pi/L_y$. Also, since u is a real-valued function, the Fourier coefficients satisfy $\hat{u}_{-k_y,-k_x} = (\hat{u}_{k_y,k_x})^*$, where the asterisk denotes complex conjugation. Therefore, from all the Fourier coefficients only those with $k_x \in \mathbb{Z}$ and $k_y > 0$ and those with $k_x \geq 0$ and $k_y = 0$ are independent. The remaining coefficients can be obtained by complex conjugations.

As usual, we impose the condition fixing the mean value of the solution over the domain,

$$\frac{1}{4L_xL_y}\int_{-L_y}^{L_y}\int_{-L_x}^{L_x} u\,dxdy = \bar{u}. \tag{6.4}$$

To break the translational symmetry due to periodic boundary conditions in the x- and y-directions, we can impose, for example, the following integral constraints:

$$\int_{-L_y}^{L_y}\int_{-L_x}^{L_x} u\sin(n_xq_xx)\,dxdy = 0, \qquad \int_{-L_y}^{L_y}\int_{-L_x}^{L_x} u\sin(n_yq_yy)\,dxdy = 0, \tag{6.5}$$

where n_x and n_y are some chosen positive integers. These conditions are equivalent to requiring that

$$\mathrm{Im}(\hat{u}_{0,n_x}) = 0, \qquad \mathrm{Im}(\hat{u}_{n_y,0}) = 0, \tag{6.6}$$

where Im is used to denote imaginary parts.

Next, we truncate the Fourier series for u so that $k_x = -M_x, -M_x+1, \ldots, M_x$ and $k_y = -M_y, -M_y+1, \ldots, M_y$ for sufficiently large integers M_x and M_y and substitute in (6.2) obtaining a dynamical system for the real and imaginary parts of the Fourier coefficients $\hat{u}_{k_y,k_x}$ with

$$\begin{aligned}(k_x,k_y) \;\in\; & \big(\{-M_x,\ldots,M_x\}\times\{1,\ldots,M_y\}\big)\\ & \cup\big(\{0,\ldots,M_x\}\times\{0\}\big).\end{aligned} \tag{6.7}$$

Note that due to (6.4)

$$\hat{u}_{0,0} = (2M_x+1)(2M_y+1)\bar{u}, \tag{6.8}$$

and also that $\mathrm{Im}(\hat{u}_{0,n_x}) = \mathrm{Im}(\hat{u}_{n_y,0}) = 0$. Thus, it can be easily verified that we obtain a system of $(2M_x+1)(2M_y+1) - 3$ ODEs.

Note that since $\mathrm{Im}(\hat{u}_{0,n_x}) = 0$, we obtain $d\big(\mathrm{Im}(\hat{u}_{0,n_x})\big)/dt = 0$, and, thus, the right-hand side of the equation for $d\big(\mathrm{Im}(\hat{u}_{0,n_x})\big)/dt$ can be used to express the speed $\dot{a}(t)$.

In our numerical implementation, we use fast Fourier transforms to obtain the right-hand sides for the dynamical system for the real and imaginary parts of the Fourier coefficients. Stationary and travelling periodic solutions of (6.1) correspond to steady-state solutions of the dynamical system. We use the Matlab package Matcont [28] to perform continuation with respect to the domain-size parameter in the x-direction, L_x, or the domain-size parameter in the y-direction, L_y, (note that L_x and L_y are actually half-domain sizes in the corresponding directions, as the computational domain is $[-L_x, L_x] \times [-L_y, L_y]$), or the driving force D, or the mean value of the solution, $\bar{u}$. We can obtain branches of stationary and travelling periodic solutions. In addition to branch points that may appear on the solution branches and that correspond to bifurcations to side branches, our formulation allows for the detection of Hopf bifurcation points that correspond bifurcations to time-periodic solutions. The computation of branches of time-periodic solutions for two-dimensional equations is quite time-consuming, and, therefore, in the present thesis we have not computed such branches. This is left as a topic for future investigation.

6.3 The case of the standard Cahn-Hilliard equation

In this section, we compute solutions to the standard Cahn-Hilliard equation, when $D = 0$, for the case when the average value of the solution is $\bar{u} = 0.4$ and 0.55. The steady solutions u_0 are characterised by the norm

$$\|\delta u_0\| = \sqrt{\frac{1}{4L_xL_y}\int_{-L_y}^{L_y}\int_{-L_x}^{L_x} u_0^2\, dxdy}. \tag{6.9}$$

We use the half-domain size in the x-direction, L_x, as the control parameter. To initiate the continuation procedure, we choose a sufficiently small L_y (the half-domain size in the y-direction) and a small amplitude sinusoidal wave of a cutoff wavelength L_c in the x-direction that is obtained from the linear stability analysis discussed in Section 3.2, i.e.,

$$L_x = L_c/2 = \frac{\pi}{k_c}, \quad \text{where} \quad k_c = \sqrt{1 - 3\bar{u}^2}. \tag{6.10}$$

For the case when $\bar{u} = 0.4$, we find $L_c \approx 4.357$. By choosing this value of L_c, we can obtain one-dimensional solutions that we characterise as one-hole solutions (rather

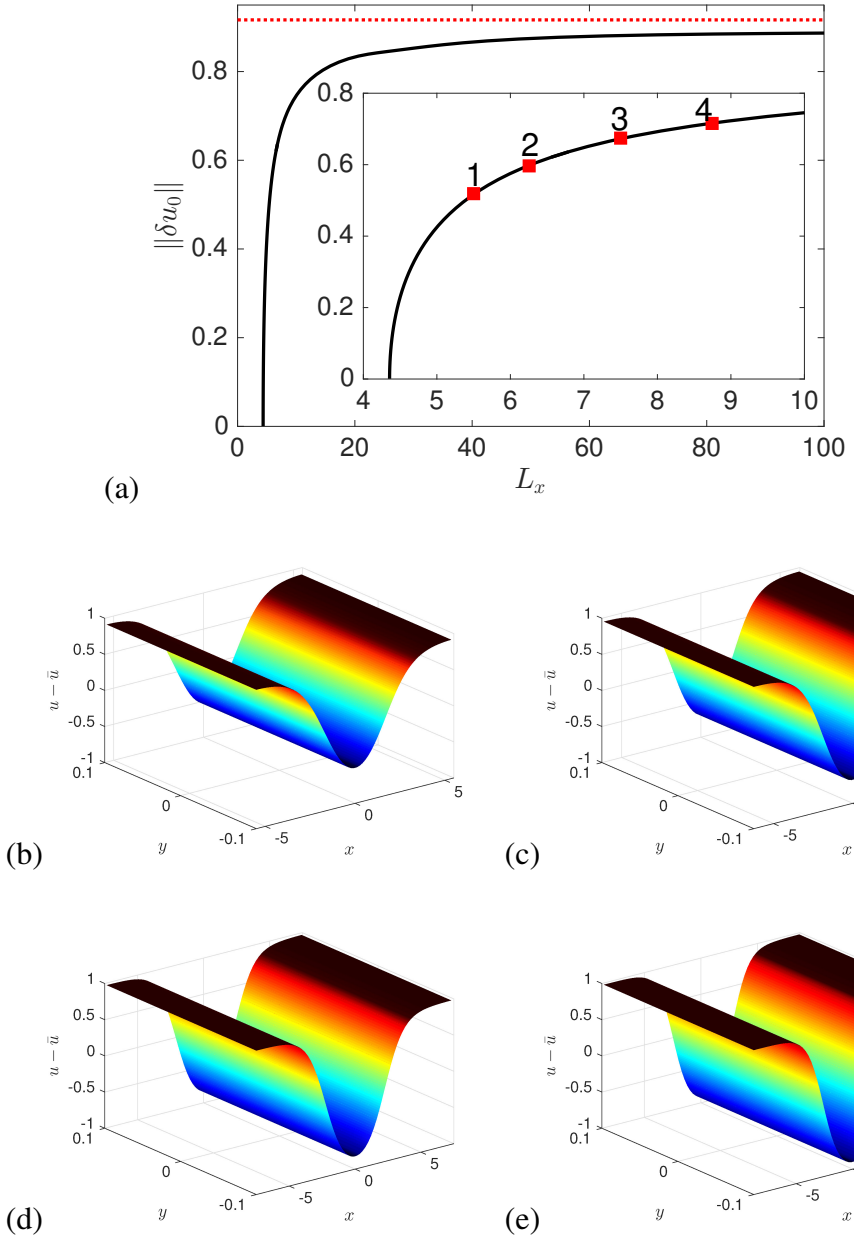

Figure 6.1: (a) The bifurcation diagram of one-dimensional (without y-dependence) steady solutions of the two-dimensional standard Cahn-Hilliard equation (6.1), when $D = 0$, for the case when $\bar{u} = 0.4$, showing the dependence of the norm $\|\delta u_0\|$ on the domain-size parameter L_x (that is the half-domain size in the x-direction) (cf. Fig. 4.3(a)). The dotted line corresponds to the value $\sqrt{1-\bar{u}^2} \approx 0.9165$ towards which the norm converges as L_x increases. The inset gives a zoom at small values of L_x. The red squares correspond to $L_x = 5.5$, 6.25, 7.5 and 8.75 and the corresponding solution profiles $u_0(x, y)$ are shown in panels (b), (c), (d) and (e), respectively.

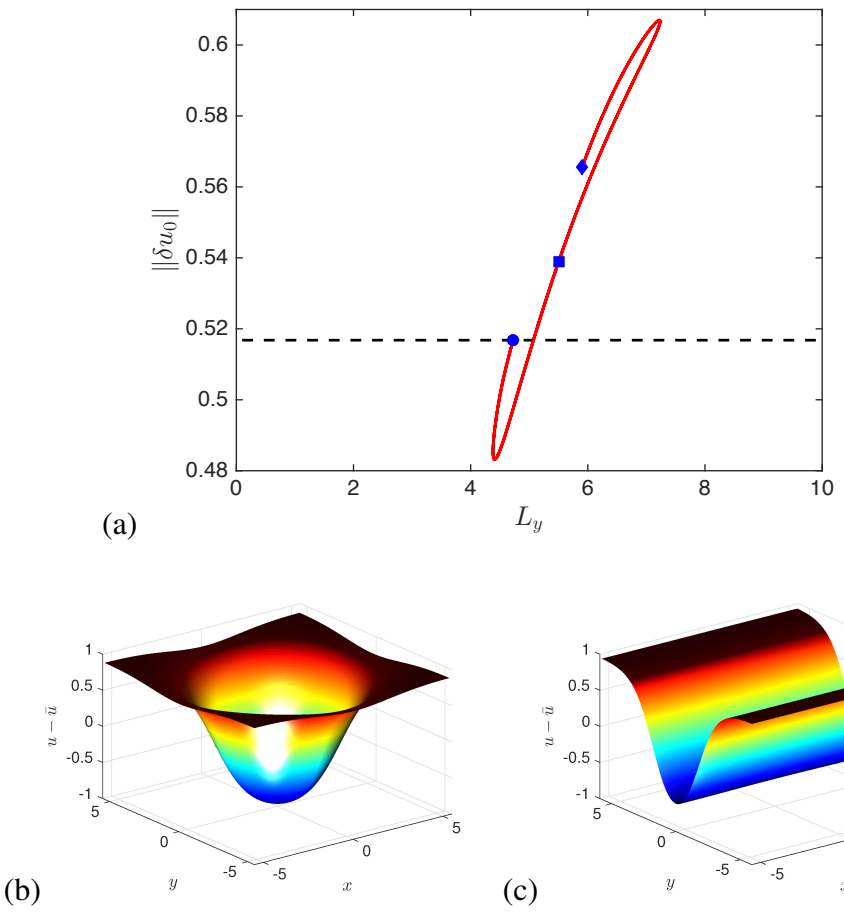

Figure 6.2: (a) The bifurcation diagram of one-hole steady solutions of the two-dimensional standard Cahn-Hilliard equation (6.1), when $D = 0$, for the case when $\bar{u} = 0.4$, showing the dependence of the norm $\|\delta u_0\|$ on the domain-size parameter L_y (that is the half-domain size in the y-direction) when $L_x = 5.5$. The black dashed line corresponds to one-dimensional solutions without dependence on y, starting from the solution shown in Fig. 6.1(b). The circle on this line shows a bifurcation point to a side branch of fully two-dimensional solutions that is shown by the red solid line. The diamond shows the point at which the branch terminates and the corresponding solution profile is shown in panel (c). The square corresponds to the point where $L_y = 5.5$ (and, therefore, $L_x = L_y$). The corresponding solution profile is shown in panel (b).

than one-droplet solutions) – as we will see later, for $\bar{u} > 0$ it is more appropriate to characterise such solutions as hole solutions rather than droplet solutions.

Fig. 6.1 shows the results of the calculations for $\bar{u} = 0.4$, where panel (a) shows the bifurcation diagram and panels (b-e) show solution profiles $u_0(x, y)$ for the values of the half-domain size in the x-direction $L_x = 5.5$, 6.25, 7.5 and 8.75. In Fig. 6.1(a), the dependence of the norm $\|\delta u_0\|$ on the half-domain size in the x-direction, L_x, is shown. The branch of spatially non-uniform solutions bifurcates supercritically from the homogeneous branch at $L_x = L_c/2$. We can see that the norm increases monotonically and tends to 0.9165 as L_x increases, in the same way as in Fig. 4.3(a). The dotted line corresponds to the value $\sqrt{1-\bar{u}^2} \approx 0.9165$, and we can see that the norm approaches this value as L increases, in agreement with (4.35).

After performing the continuation with respect to L_x, we next perform continuation with respect to L_y starting from solutions corresponding to $L_x = 5.5, 6.25, 7.5$ and 8.75. The corresponding results are shown in Figs. 6.2, 6.3, 6.4 and 6.5. Panels (a) in these figures show the bifurcation diagrams where the norm $\|\delta u_0\|$ is plotted over L_y. The (black) dashed lines correspond to one-dimensional solutions without dependence on y. For all such branches, we find bifurcation points (shown by blue circles) from which branches of two-dimensional solutions emanate. Such branches are shown by (red) solid lines. Interestingly, all these branches terminate at points (shown with diamonds) which correspond to one-dimensional solutions without x-dependence (we note that for solutions without x-dependence, the convective term vanishes, so these solutions are, in fact, one-dimensional solutions of the standard Cahn-Hilliard equation). So, these branches connect y-translation-invariant branches of solutions to x-translation-invariant branches of solutions, but the solutions on the branches themselves have none of these translational symmetries. We note that similar branches of solution have been found by Bribesh [14] in the study of free-surface films of binary liquid mixtures for the case of flat films without energetic bias. Apparently, these points belong to branches of such one-dimensional solutions, which are not shown in the bifurcation diagrams. The solution profiles corresponding to these points are shown in Figs. 6.2(b), 6.3(d), 6.4(d) and 6.5(d) for $L_x = 5.5, 6.25, 7.5$ and 8.75, respectively. The squares in the bifurcation diagrams correspond to points where $L_x = L_y$. For $L_x = 5.5$, we find that there exists only one such solution, shown in Figs. 6.2(a). However, for $L_x = 6.25$, 7.5 and 8.75, there exist two such solutions for each L_x. Such solutions are indicated by symbols 1 and 2 in the bifurcation diagrams, and the corresponding solution profiles are shown in panels (b) and (c) of Figs. 6.3, 6.4 and 6.5, respectively. We can observe that the

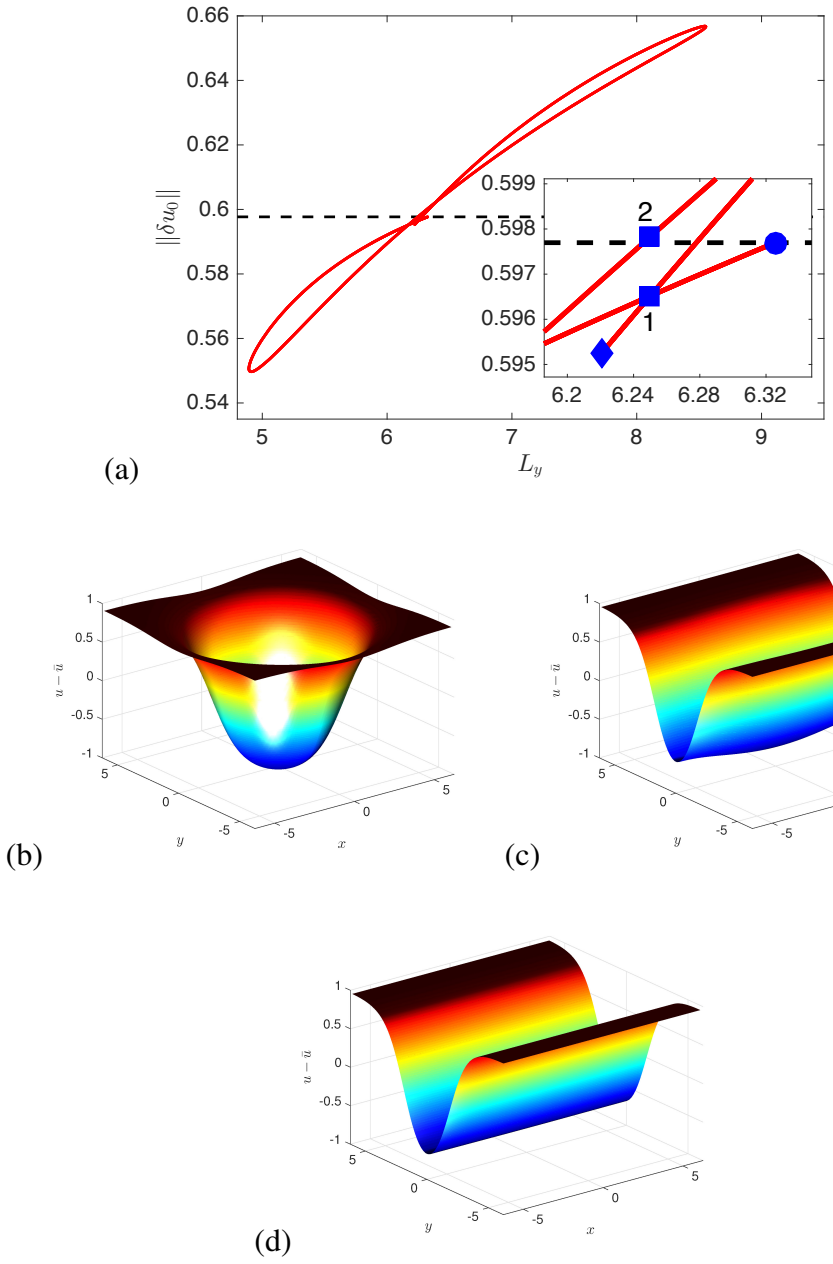

Figure 6.3: (a) The bifurcation diagram of one-hole steady solutions of the two-dimensional standard Cahn-Hilliard equation (6.1), when $D = 0$, for the case when $\bar{u} = 0.4$, showing the dependence of the norm $\|\delta u_0\|$ on the domain-size parameter L_y (that is the half-domain size in the y-direction) when $L_x = 6.25$. The black dashed line corresponds to one-dimensional solutions without dependence on y, starting from the solution shown in Fig. 6.1(c). The circle on this line (see the inset) shows a bifurcation point to a side branch of fully two-dimensional solutions that is shown by the red solid line. The diamond (see the inset) shows the point at which the branch terminates and the corresponding solution profile is shown in panel (d). Squares 1 and 2 corresponds to the points where $L_y = 6.25$ (and, therefore, $L_x = L_y$). The corresponding solution profiles are shown in panels (b) and (c).

solution profiles shown in Figs. 6.3(b), 6.4(c) and 6.5(c), for $L_x = 6.25$, 7.5 and 8.75, respectively, are one-hole solutions. We will use the points that correspond to these solution profiles to start continuation in the driving force parameter D, which will be discussed in Section 6.4.

The results analogous to those given in Figs. 6.1–6.5 but for $\bar{u} = 0.55$ are presented in Figs. 6.6–6.8. Fig. 6.6 corresponds to continuation with respect to L_x from a small-amplitude sinusoidal wave of a cutoff wavelength that is $L_c \approx 5.33$ for $\bar{u} = 0.55$. Fig. 6.6(a) shows the dependence of the norm $\|\delta u_0\|$ on L_x, and we can see that the branch of spatially non-uniform solutions bifurcates subcritically from $L_x = L_c/2$, as expected for this value of $\bar{u}$ (see Fig. 4.5(a)). The dotted line corresponds to the value $\sqrt{1-\bar{u}^2} \approx 0.8352$, and we can see that the branch tends to this value, as expected (see the discussion of Fig. 4.5(a)). Panels (b) and (c) show the solution profiles for $L_x = 8.75$, were panel (b) corresponds to the solution on the lower part of the bifurcation diagram (point 1 in the inset of Fig. 6.6(a)) and panel (c) corresponds to the solution on the upper part of the bifurcation diagram (point 2 in the inset of Fig. 6.6(a)). Panel (d) show the solution profile for $L_x = 12.5$ (which corresponds to point 3 in the inset of Fig. 6.6(a)).

The results of continuation with respect to L_y starting from solutions given in Figs. 6.6(c) and (d) are presented in Figs. 6.7 and 6.8 that correspond to $L_x = 8.75$ and 12.5, respectively. As in Figs. 6.2–6.5 corresponding to $\bar{u} = 0.4$, panels (a) show the bifurcation diagrams where the norm $\|\delta u_0\|$ is plotted over L_y. The (black) dashed lines correspond to one-dimensional solutions without dependence on y, and (red) solid lines correspond to side branches of two-dimensional solutions (the bifurcation points are shown by circles). As for $\bar{u} = 0.4$, these branches terminate at points (shown with diamonds) which correspond to one-dimensional solutions without x-dependence. So, as for $\bar{u} = 0.4$, these branches connect y-translation-invariant branches of solutions to x-translation-invariant branches of solutions, but the solutions on the branches themselves have none of these translational symmetries. The solution profiles corresponding to the points at which the branches terminate are shown in Figs. 6.7(c) and 6.8(d) for $L_x = 8.75$ and 12.5, respectively. The squares in the bifurcation diagrams correspond to points where $L_x = L_y$. For $L_x = 8.75$, we find that there exists only one such solution, shown in Figs. 6.7(a). However, for $L_x = 12.5$, there exist two such solutions for each L_x. Such

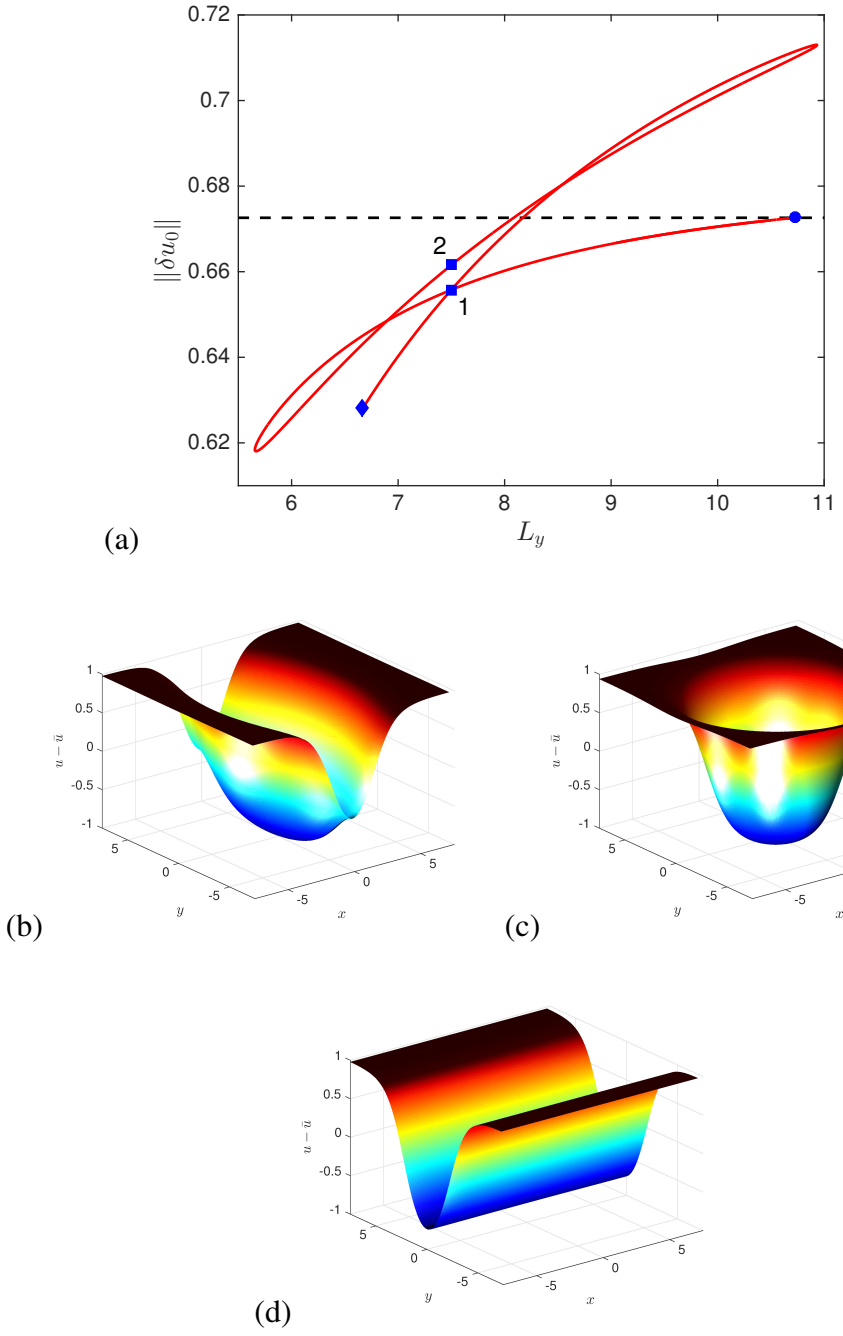

Figure 6.4: (a) The bifurcation diagram of one-hole steady solutions of the two-dimensional standard Cahn-Hilliard equation (6.1), when $D = 0$, for the case when $\bar{u} = 0.4$, showing the dependence of the norm $\|\delta u_0\|$ on the domain-size parameter L_y (that is the half-domain size in the y-direction) when $L_x = 7.5$. The black dashed line corresponds to one-dimensional solutions without dependence on y, starting from the solution shown in Fig. 6.1(d). The circle on this line shows a bifurcation point to a side branch of fully two-dimensional solutions that is shown by the red solid line. The diamond shows the point at which the branch terminates and the corresponding solution profile is shown in panel (d). Squares 1 and 2 corresponds to the points where $L_y = 7.5$ (and, therefore, $L_x = L_y$). The corresponding solution profiles are shown in panels (b) and (c).

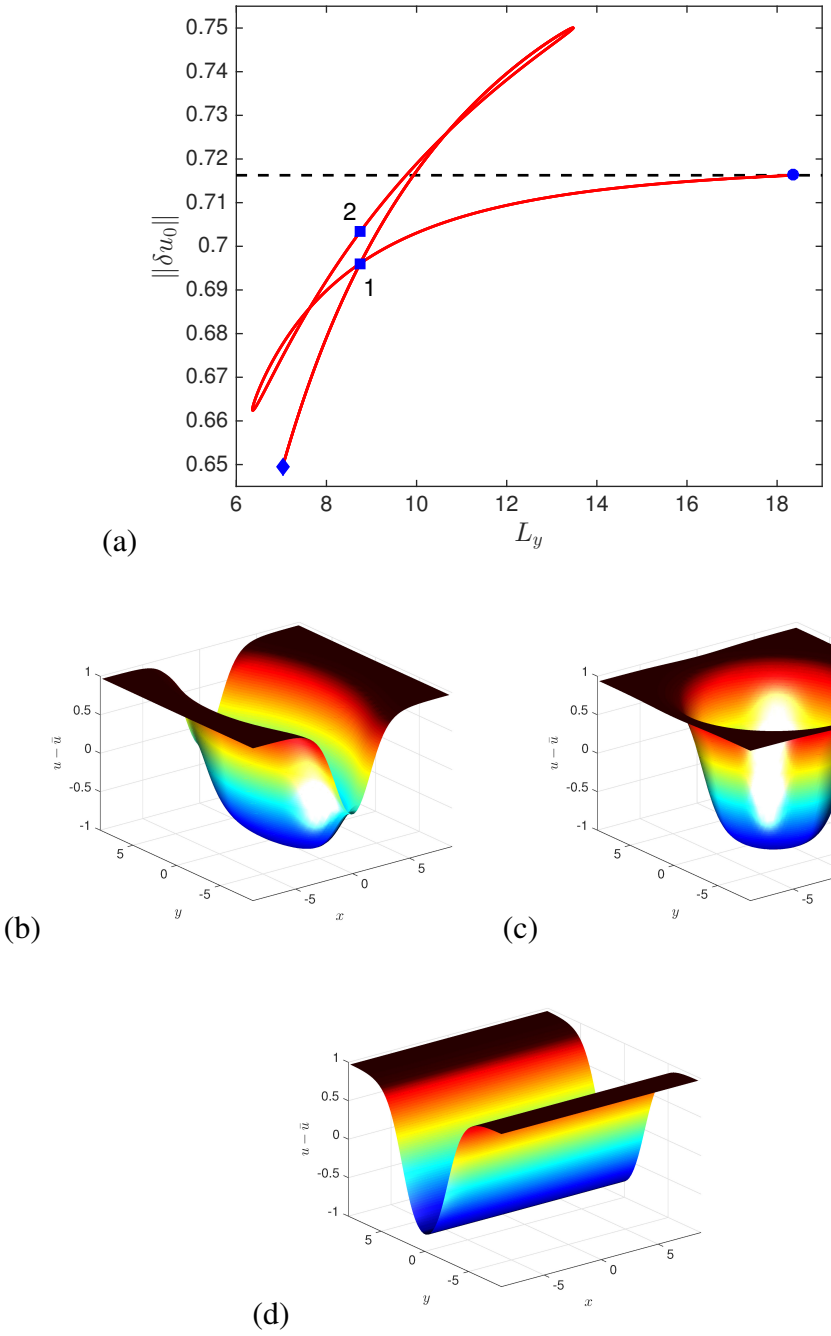

Figure 6.5: (a) The bifurcation diagram of one-hole steady solutions of the two-dimensional standard Cahn-Hilliard equation (6.1), when $D = 0$, for the case when $\bar{u} = 0.4$, showing the dependence of the norm $\|\delta u_0\|$ on the domain-size parameter L_y (that is the half-domain size in the y-direction) when $L_x = 8.75$. The black dashed line corresponds to one-dimensional solutions without dependence on y, starting from the solution shown in Fig. 6.1(e). The circle on this line shows a bifurcation point to a side branch of fully two-dimensional solutions that is shown by the red solid line. The diamond shows the point at which the branch terminates and the corresponding solution profile is shown in panel (d). Squares 1 and 2 corresponds to the points where $L_y = 8.75$ (and, therefore, $L_x = L_y$). The corresponding solution profiles are shown in panels (b) and (c).

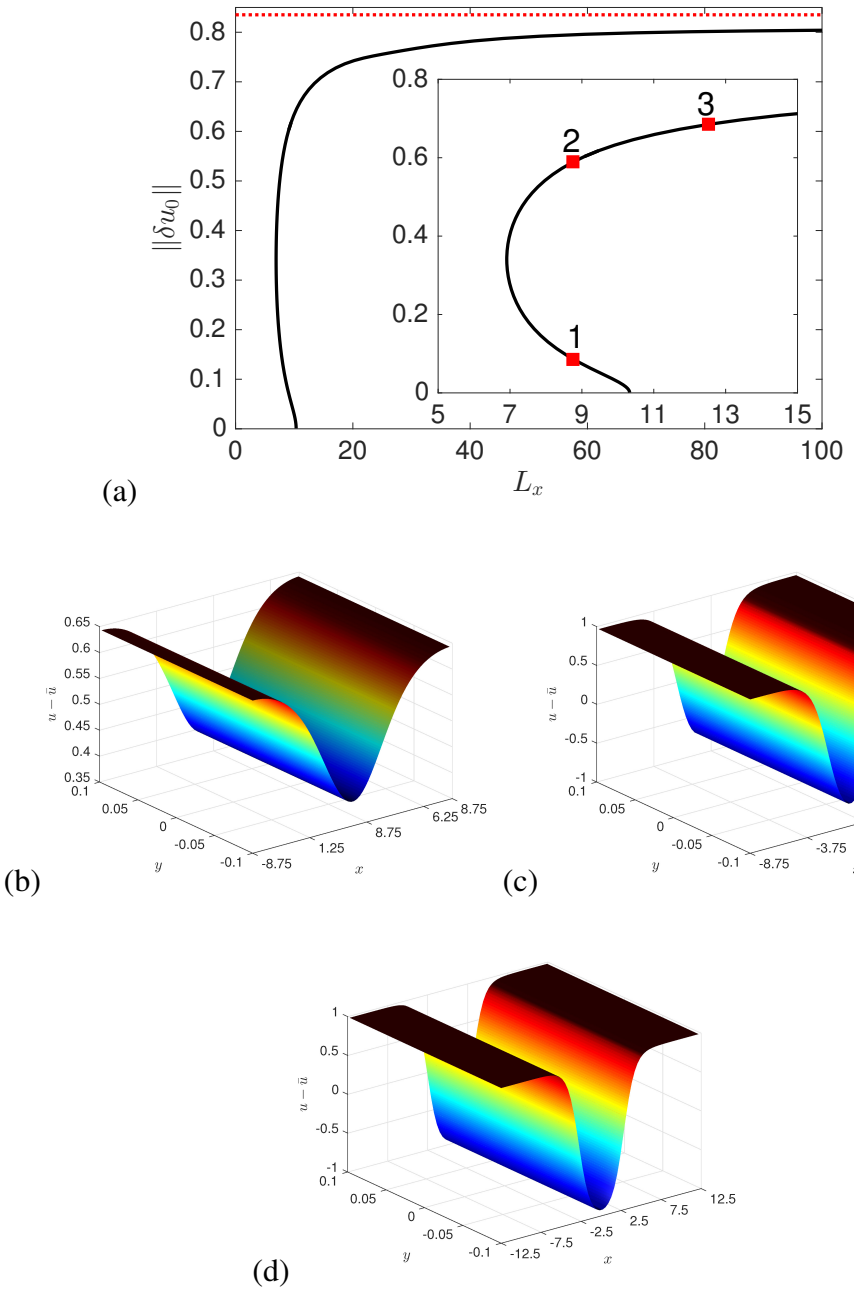

Figure 6.6: (a) The bifurcation diagram of one-dimensional (without y-dependence) steady solutions of the two-dimensional standard Cahn-Hilliard equation (6.1), when $D = 0$, for the case when $\bar{u} = 0.55$, showing the dependence of the norm $\|\delta u_0\|$ on the domain-size parameter L_x (that is the half-domain size in the x-direction) (cf. Fig. 4.5(a)). The dotted line corresponds to the value $\sqrt{1-\bar{u}^2} \approx 0.8352$ towards which the norm converges as L_x increases. The inset gives a zoom at small values of L_x. The red squares 1 and 2 correspond to $L_x = 8.75$ and the red square 3 corresponds to 12.5. The solution profiles $u_0(x, y)$ corresponding to the red squares 1, 2 and 3 are shown in panels (b), (c) and (d), respectively.

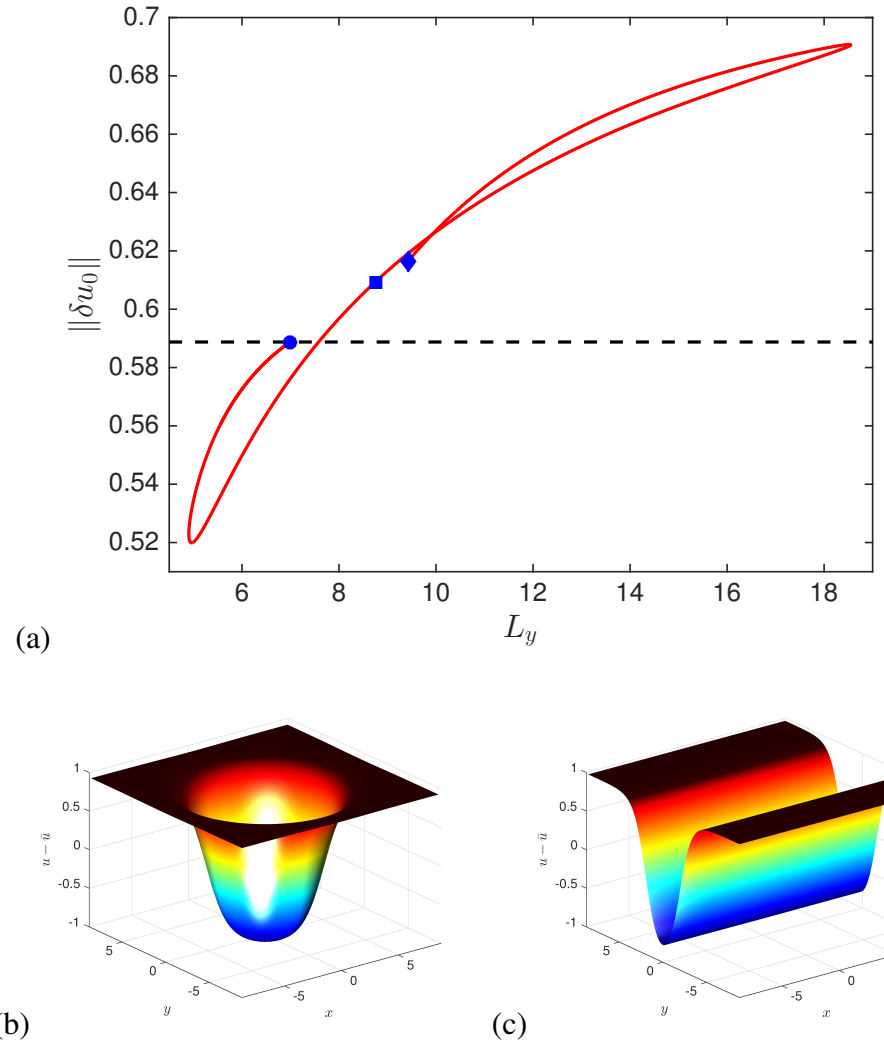

Figure 6.7: (a) The bifurcation diagram of one-hole steady solutions of the two-dimensional standard Cahn-Hilliard equation (6.1), when $D = 0$, for the case when $\bar{u} = 0.55$, showing the dependence of the norm $\|\delta u_0\|$ on the domain-size parameter L_y (that is the half-domain size in the y-direction) when $L_x = 8.75$. The black dashed line corresponds to one-dimensional solutions without dependence on y, starting from the solution shown in Fig. 6.6(c). The circle on this line shows a bifurcation point to a side branch of fully two-dimensional solutions that is shown by the red solid line. The diamond shows the point at which the branch terminates and the corresponding solution profile is shown in panel (c). The square corresponds to the point where $L_y = 8.75$ (and, therefore, $L_x = L_y$). The corresponding solution profile is shown in panel (b).

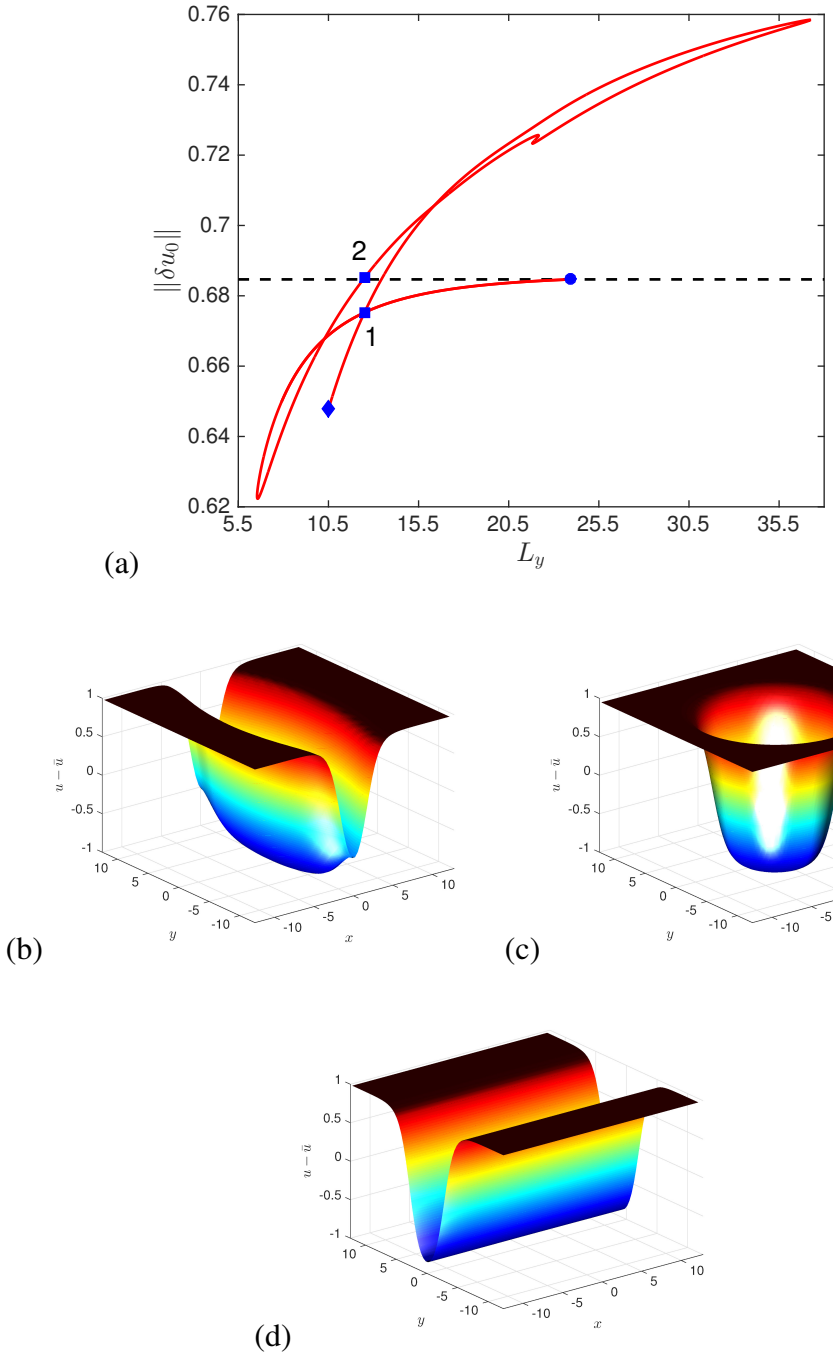

Figure 6.8: (a) The bifurcation diagram of one-hole steady solutions of the two-dimensional standard Cahn-Hilliard equation (6.1), when $D = 0$, for the case when $\bar{u} = 0.55$, showing the dependence of the norm $\|\delta u_0\|$ on the domain-size parameter L_y (that is the half-domain size in the y-direction) when $L_x = 12.5$. The black dashed line corresponds to one-dimensional solutions without dependence on y, starting from the solution shown in Fig. 6.6(d). The circle on this line shows a bifurcation point to a side branch of fully two-dimensional solutions that is shown by the red solid line. The diamond shows the point at which the branch terminates and the corresponding solution profile is shown in panel (d). Squares 1 and 2 corresponds to the points where $L_y = 12.5$ (and, therefore, $L_x = L_y$). The corresponding solution profiles are shown in panels (b) and (c).

solutions are indicated by symbols 1 and 2 in the bifurcation diagram, Fig. 6.8(a), and the corresponding solution profiles are shown in panels (b) and (c) of Fig. 6.8. We can observe that the solution profile shown in Fig. 6.8(c) is a one-hole solution. We will use the point corresponding to this solution profile to start continuation in the driving force parameter D. This will be discussed in Section 6.4.

6.4 The case of the convective Cahn-Hilliard equation

In this section, we present some preliminary results on the effect of the driving force on the one-hole solutions computed in the previous section.

First, we consider the case of $\bar{u} = 0.4$ and take the one-hole solutions presented in Figs. 6.2(b), 6.3(b), 6.4(c), 6.5(c) that correspond to $L_x = L_y = 5.5$, 6.25, 7.5 and 8.75, respectively, and extend them periodically in the x-direction to obtain two-hole solutions on the domain $[-2L_x, 2L_x] \times [-L_y, L_y]$. We then perform continuation with respect to the driving force parameter D.

In Fig. 6.9(a), the dependence of the norm $\|\delta u_0\|$ on the driving force parameter D is shown for $L_x = L_y = 5.5$. The black solid line shows the branch of solutions with discrete translational symmetry in the x-direction. The red circles on this branch indicate bifurcation points to branches of symmetry-broken solutions, and the (blue and red) dashed lines emanating from these points show these side branches of symmetry-broken solutions. The blue squares show the points at which these branches terminate. The solution profile shown in panel (b) corresponds to the point at which the primary branch terminates. The solution profile shown in panel (c) corresponds to the point at which the side branch emanating from the first bifurcation point terminates. Apparently, these solution profiles are one-dimensional without x-dependence, and the profiles are exactly the same and belong to the same horizontal line of such one-dimensional solutions. This branch is shown by the dot-dashed horizontal line. The solution profile shown in panel (d) corresponds to the point at which the side branch emanating from the second bifurcation point terminates. Apparently, this solution is one-dimensional without y-dependence, and it belongs to a branch of such one-dimensional one-droplet solutions. This branch was already computed in Fig. 5.9(a) (see the thick blue line), and part of this branch is shown in Fig. 6.9(a) by a non-horizontal (pink) dot-dashed line. Fig. 6.10 shows solution profiles from all of the branches in Fig. 6.9(a) that correspond

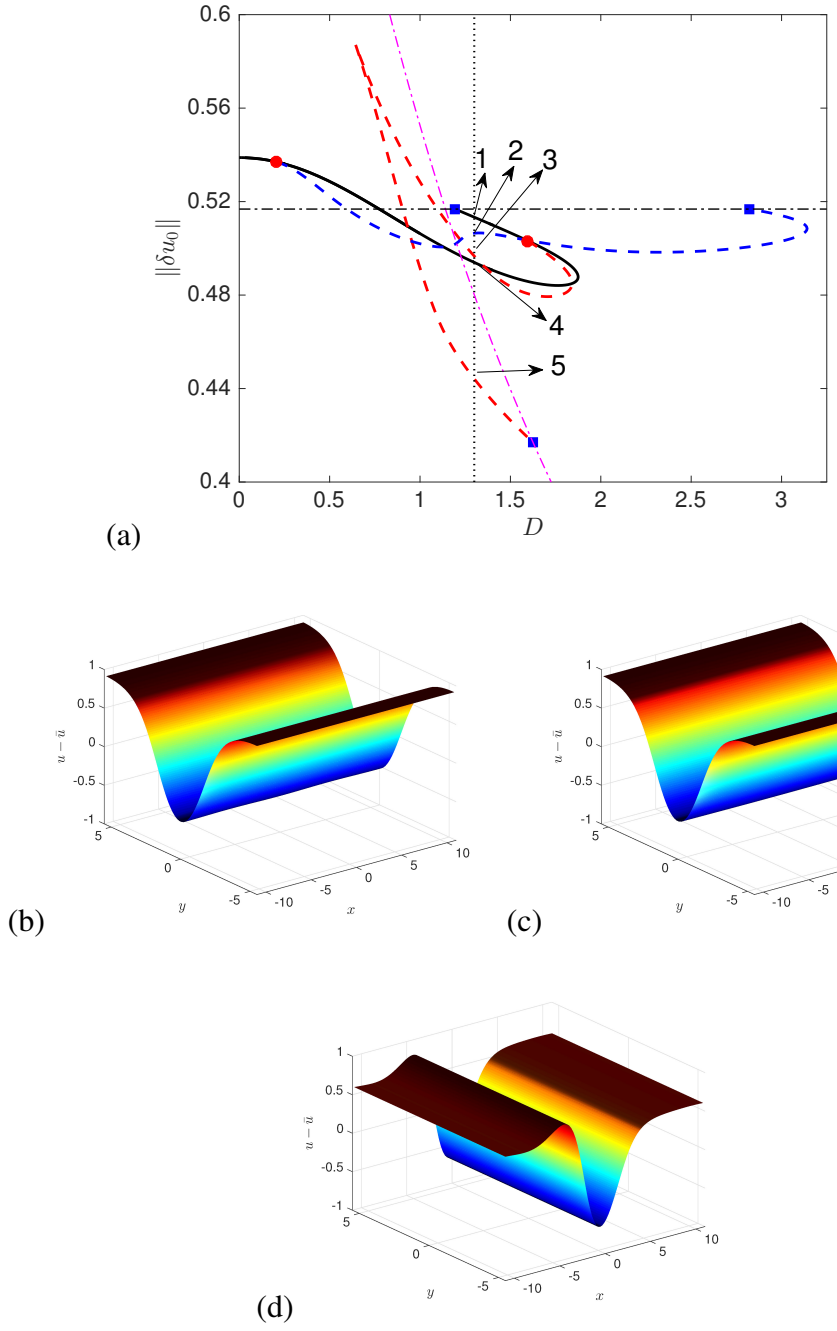

Figure 6.9: (a) The bifurcation diagram of two-hole solutions of the two-dimensional convective Cahn-Hilliard equation (6.1), for the case when $\bar{u} = 0.4$ and $L_x = L_y = 5.5$, showing the dependence of the norm $\|\delta u_0\|$ on the driving force parameter D. The solid line corresponds to the primary branch of solutions with discrete translational symmetry in the x-direction. The dashed lines show side branches of symmetry-broken solutions. The red circles indicate pitchfork bifurcations to the side branches. The blue squares show the points at which the branches terminate, and the profiles corresponding to these points are shown in panels (b), (c) and (d) for the primary and the first and second side branches, respectively, on the domain $[-2L_x, 2L_x] \times [-L_y, L_y]$. In addition, the horizontal dot-dashed line shows the branch of one-dimensional solutions without x-dependence on which the primary branch (black solid line) and the first side branch (blue dashed line) terminate. The other (pink) dot-dashed line shows the branch of one-dimensional (without y-dependence) one-droplet solutions on which the second side branch (red dashed line) terminates. The vertical dotted line corresponds to $D = 1.3$. Points 1–5 on the primary and side branches correspond to $D = 1.3$, and the corresponding solution profiles are shown in Figs. 6.10(a)–(e), respectively.

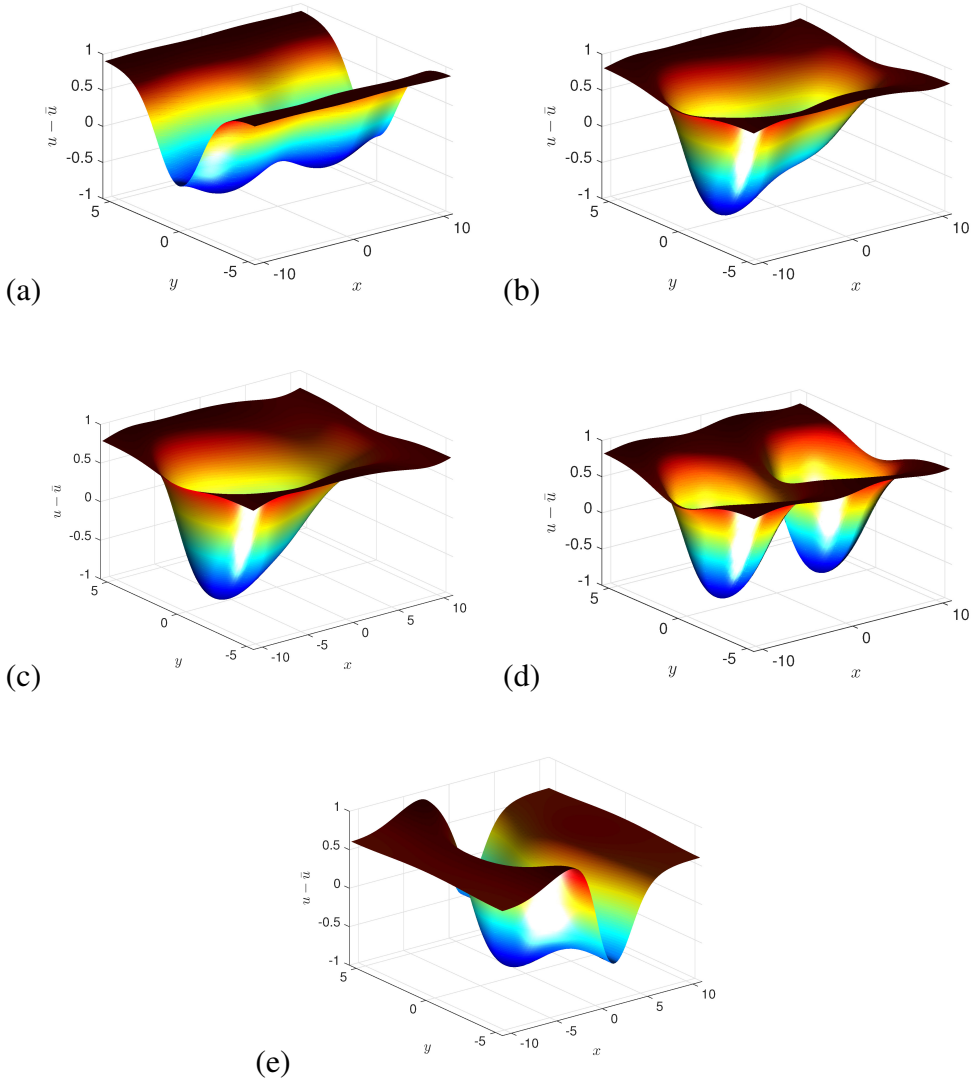

Figure 6.10: Solution profiles of the two-dimensional convective Cahn-Hilliard equation (6.1) shown on the domain $[-2L_x, 2L_x] \times [-L_y, L_y]$, for the case when $\bar{u} = 0.4$, $L_x = L_y = 5.5$ and $D = 1.3$. Panels (a)–(e) correspond to points 1–5, respectively, in the bifurcation diagram shown in Fig. 6.9(a).

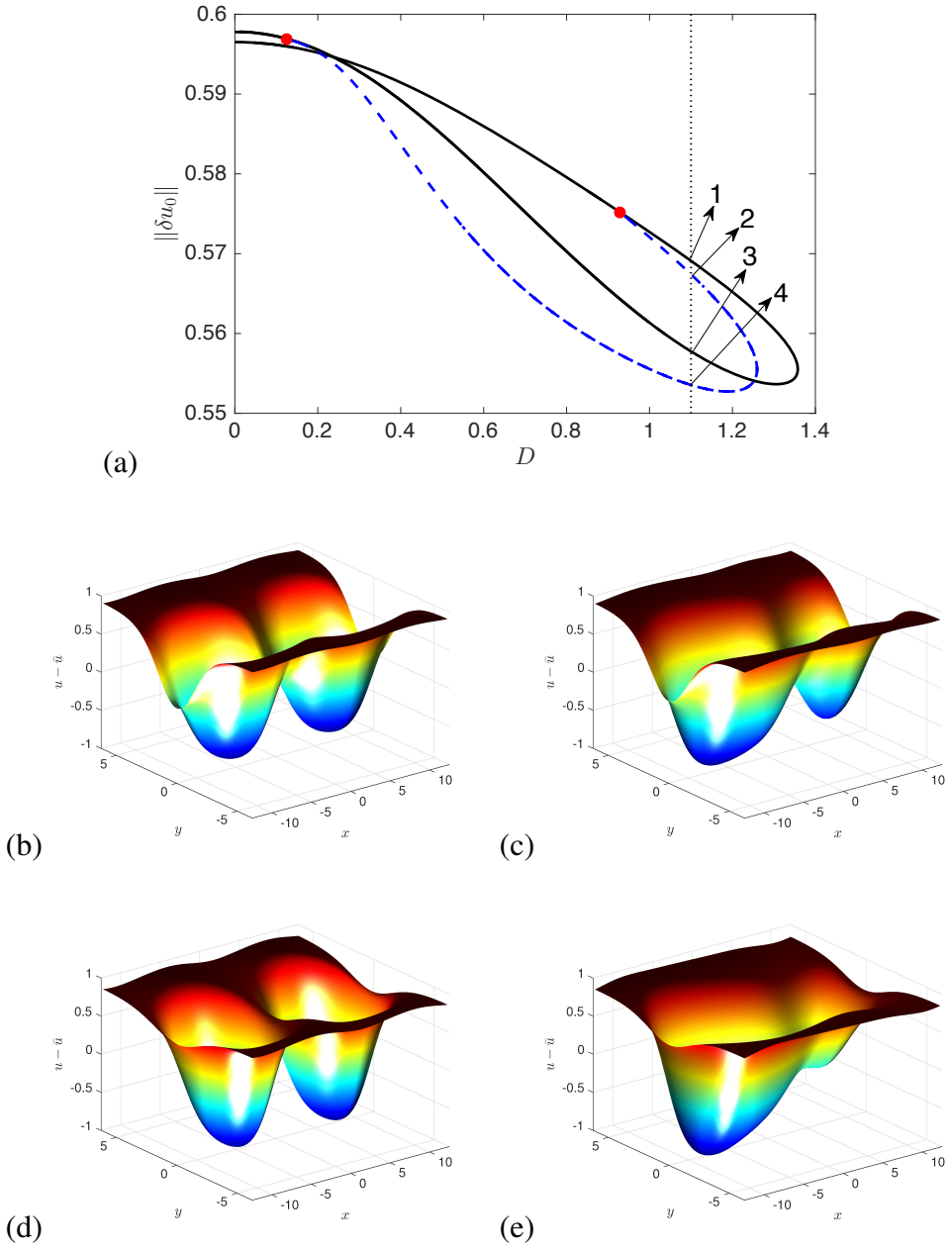

Figure 6.11: (a) The bifurcation diagram of two-hole solutions of the two-dimensional convective Cahn-Hilliard equation (6.1), for the case when $\bar{u} = 0.4$ and $L_x = L_y = 6.25$, showing the dependence of the norm $\|\delta u_0\|$ on the driving force parameter D. The solid line corresponds to the primary branch of solutions with discrete translational symmetry in the x-direction. The dashed line shows a side branch of symmetry-broken solutions and it connects two pitchfork bifurcations on the primary branch (shown by the red circles). The vertical dotted line corresponds to $D = 1.1$. Points 1–4 on the branches correspond to $D = 1.1$ and the corresponding solution profiles are shown in panels (b)–(e), respectively, on the domain $[-2L_x, 2L_x] \times [-L_y, L_y]$.

to $D = 1.3$ (see a vertical dotted line in Fig. 6.9(a)). Panels (a)–(e) show the solution profiles corresponding to points 1–5, respectively, indicated in Fig. 6.9(a).

In Fig. 6.11(a), the dependence of the norm $\|\delta u_0\|$ on the driving force parameter D is shown for $\bar{u} = 0.4$ and $L_x = L_y = 6.25$. The black solid line shows the branch of solutions with discrete translational symmetry in the x-direction. This branch starts at $D = 0$, but then has a turning point (saddle-node) and returns to $D = 0$. The red circles on this branch indicate bifurcation points, and we find that there is a single side branch of symmetry-broken solutions that connects these two points shown by the blue dashed line. Apparently, the there are certain transitions in the bifurcation diagrams are involved as L_x, L_y vary from 5.5 to 6.25. However, we do not investigate this further in this thesis. Panels (b)–(e) show the solution profiles corresponding to points 1–4, respectively, indicated in Fig. 6.11(a) for $D = 1.1$.

In Fig. 6.12(a), the dependence of the norm $\|\delta u_0\|$ on the driving force parameter D is shown for $\bar{u} = 0.4$ and $L_x = L_y = 7.5$. The black solid line shows the branch of solutions with discrete translational symmetry in the x-direction. This branch starts at $D = 0$, but then has a turning point (saddle-node) and returns to $D = 0$. The red circles on this branch indicate bifurcation points, and, as for the case of $L_x = L_y = 6.25$, we find that there is a single side branch of symmetry-broken solutions that connects these two points shown by the red dashed line. Panels (b)–(e) show the solution profiles corresponding to points 1–4, respectively, indicated in Fig. 6.12(a) for $D = 0.85$.

In Fig. 6.13(a), the dependence of the norm $\|\delta u_0\|$ on the driving force parameter D is shown for $\bar{u} = 0.4$ and $L_x = L_y = 8.75$. The black solid line shows the branch of solutions with discrete translational symmetry in the x-direction. This branch starts at $D = 0$, but then has a turning point (saddle-node) and returns to $D = 0$. The red circles on this branch indicate bifurcation points, and, as for the cases of $L_x = L_y = 6.25$ and $L_x = L_y = 8.75$, we find that there is a single side branch of symmetry-broken solutions that connects these two points shown by the red dashed line. Panels (b)–(e) show the solution profiles corresponding to points 1–4, respectively, indicated in Fig. 6.13(a) for $D = 0.85$.

Next, we consider the case of $\bar{u} = 0.55$ and take the one-hole solutions presented in Figs. 6.7(b) and 6.8(b) that correspond to $L_x = L_y = 8.75$ and 12.5, respectively, and extend them periodically in the x-direction to obtain two-hole solutions, and perform continuation with respect to the driving force parameter D.

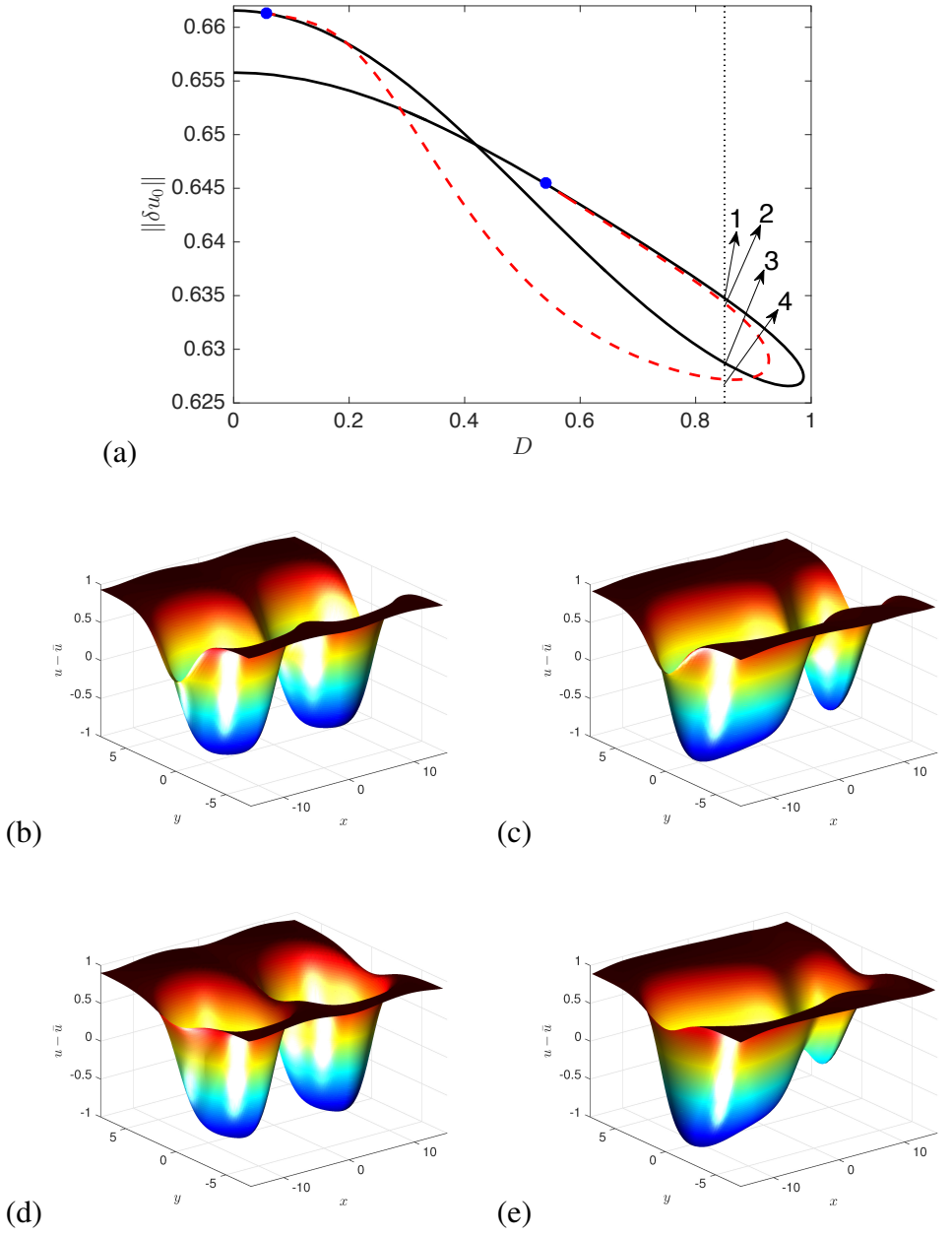

Figure 6.12: (a) The bifurcation diagram of two-hole solutions of the two-dimensional convective Cahn-Hilliard equation (6.1), for the case when $\bar{u} = 0.4$ and $L_x = L_y = 7.5$, showing the dependence of the norm $\|\delta u_0\|$ on the driving force parameter D. The solid line corresponds to the primary branch of solutions with discrete translational symmetry in the x-direction. The dashed line shows a side branch of symmetry-broken solutions and it connects two pitchfork bifurcations on the primary branch (shown by the blue circles). The vertical dotted line corresponds to $D = 0.85$. Points 1–4 on the branches correspond to $D = 0.85$ and the corresponding solution profiles are shown in panels (b)–(e), respectively, on the domain $[-2L_x, 2L_x] \times [-L_y, L_y]$.

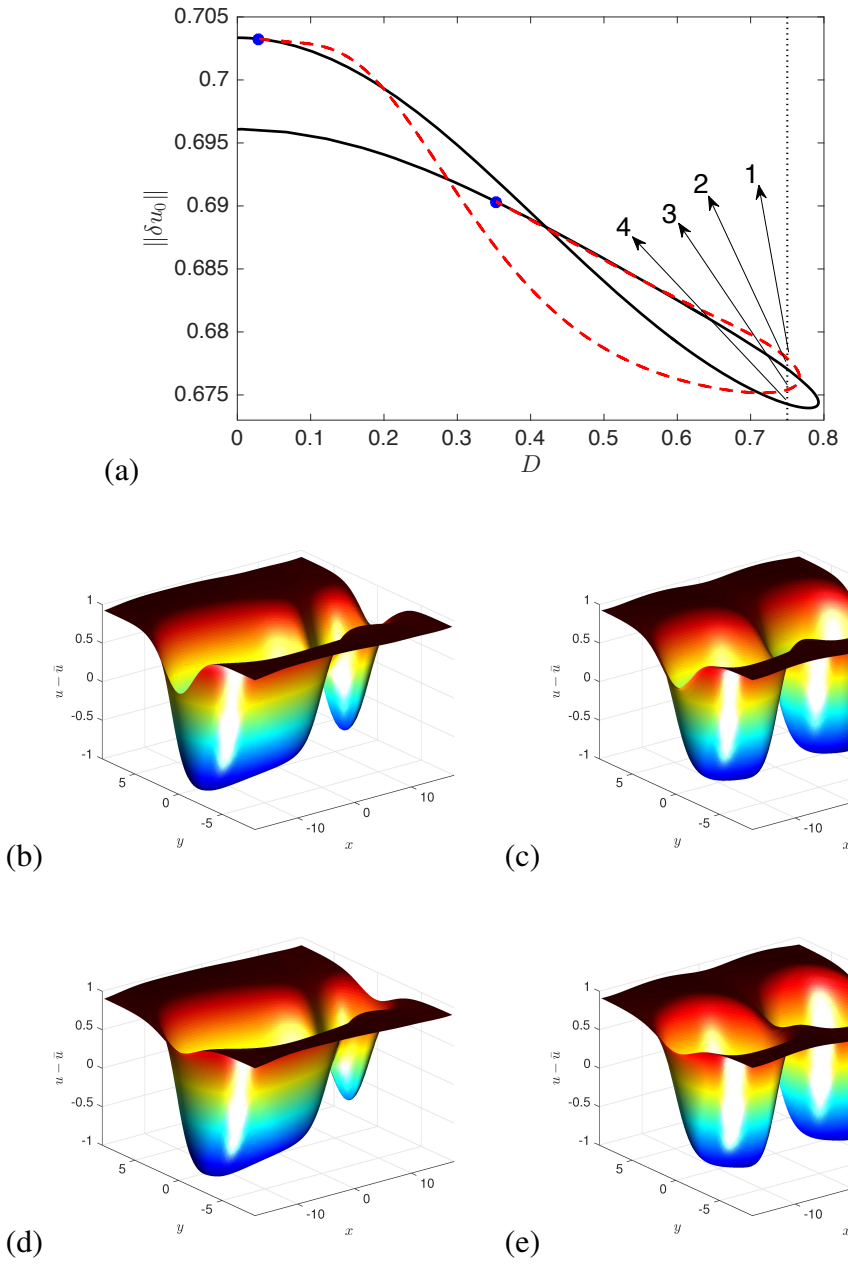

Figure 6.13: (a) The bifurcation diagram of two-hole solutions of the two-dimensional convective Cahn-Hilliard equation (6.1), for the case when $\bar{u} = 0.4$ and $L_x = L_y = 8.75$, showing the dependence of the norm $\|\delta u_0\|$ on the driving force parameter D. The solid line corresponds to the primary branch of solutions with discrete translational symmetry in the x-direction. The dashed line shows a side branch of symmetry-broken solutions and it connects two pitchfork bifurcations on the primary branch (shown by the blue circles). The vertical dotted line corresponds to $D = 0.75$. Points 1–4 on the branches correspond to $D = 0.85$ and the corresponding solution profiles are shown in panels (b)–(e), respectively, on the domain $[-2L_x, 2L_x] \times [-L_y, L_y]$.

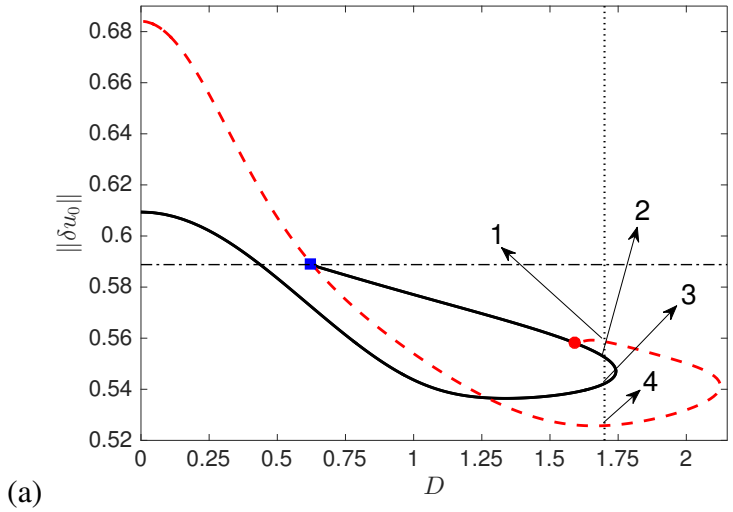

(a)

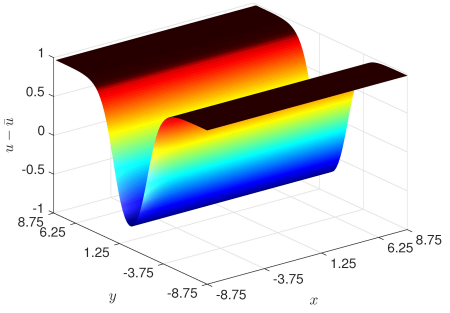

(b)

Figure 6.14: (a) The bifurcation diagram of two-hole solutions of the two-dimensional convective Cahn-Hilliard equation (6.1), for the case when $\bar{u} = 0.55$ and $L_x = L_y = 8.75$, showing the dependence of the norm $\|\delta u_0\|$ on the driving force parameter D. The solid line corresponds to the primary branch of solutions with discrete translational symmetry in the x-direction. The blue square shows the point at which this branches terminates, and the profile corresponding to this point is shown in panel (b) on the domain $[-2L_x, 2L_x] \times [-L_y, L_y]$. The dashed line shows a side branch of symmetry-broken solutions that starts at a pitchfork bifurcation on the primary branch shown by the red circle and continues to $D = 0$. In addition, the horizontal dot-dashed line shows the branch of one-dimensional solutions without x-dependence on which the primary branch (black solid line) terminates. The vertical dotted line corresponds to $D = 1.7$. Points 1–4 on the branches correspond to $D = 1.7$ and the corresponding solution profiles are shown in Figs. 6.15(a)–(d), respectively.

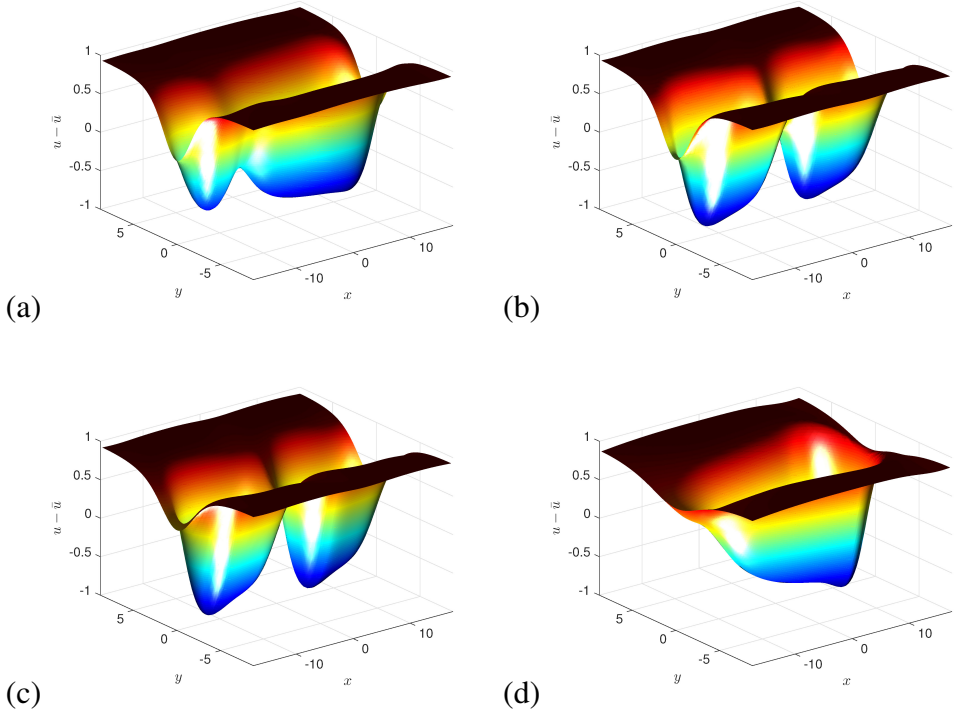

Figure 6.15: Solution profiles of the two-dimensional convective Cahn-Hilliard equation (6.1) shown on the domain $[-2L_x, 2L_x]\times[-L_y, L_y]$, for the case when $\bar{u} = 0.55$, $L_x = L_y = 8.75$ and $D = 1.7$. Panels (a)–(d) correspond to points 1–4, respectively, in the bifurcation diagram shown in Fig. 6.14(a).

In Fig. 6.14(a), the dependence of the norm $\|\delta u_0\|$ on the driving force parameter D is shown for $\bar{u} = 0.55$ and $L_x = L_y = 8.75$. The black solid line shows the branch of solutions with discrete translational symmetry in the x-direction, and it terminates at a point (shown by a blue square) that corresponds to a one-dimensional solution without x-dependence shown in Fig. 6.14(b). This point belongs to a branch of such solutions without x-dependence shown by the horizontal dot-dashed line. The red circle on the primary branch indicates the bifurcation point to a side branch of symmetry-broken solutions shown by the red dashed line. This branch has a turning point (saddle-node) at goes to $D = 0$. Panels (b)–(e) show the solution profiles corresponding to points 1–4, respectively, indicated in Fig. 6.14(a) for $D = 1.7$. We note that it may seem from Fig. 6.14(a) that the primary branch (black solid line) terminates at a point that belongs to the the side branch (red dashed line). However, it has been verified that this is not the case.

In Fig. 6.16(a), the dependence of the norm $\|\delta u_0\|$ on the driving force parameter D is shown for $\bar{u} = 0.55$ and $L_x = L_y = 12.5$. The black solid line shows the branch of solutions with discrete translational symmetry in the x-direction. This branch starts at

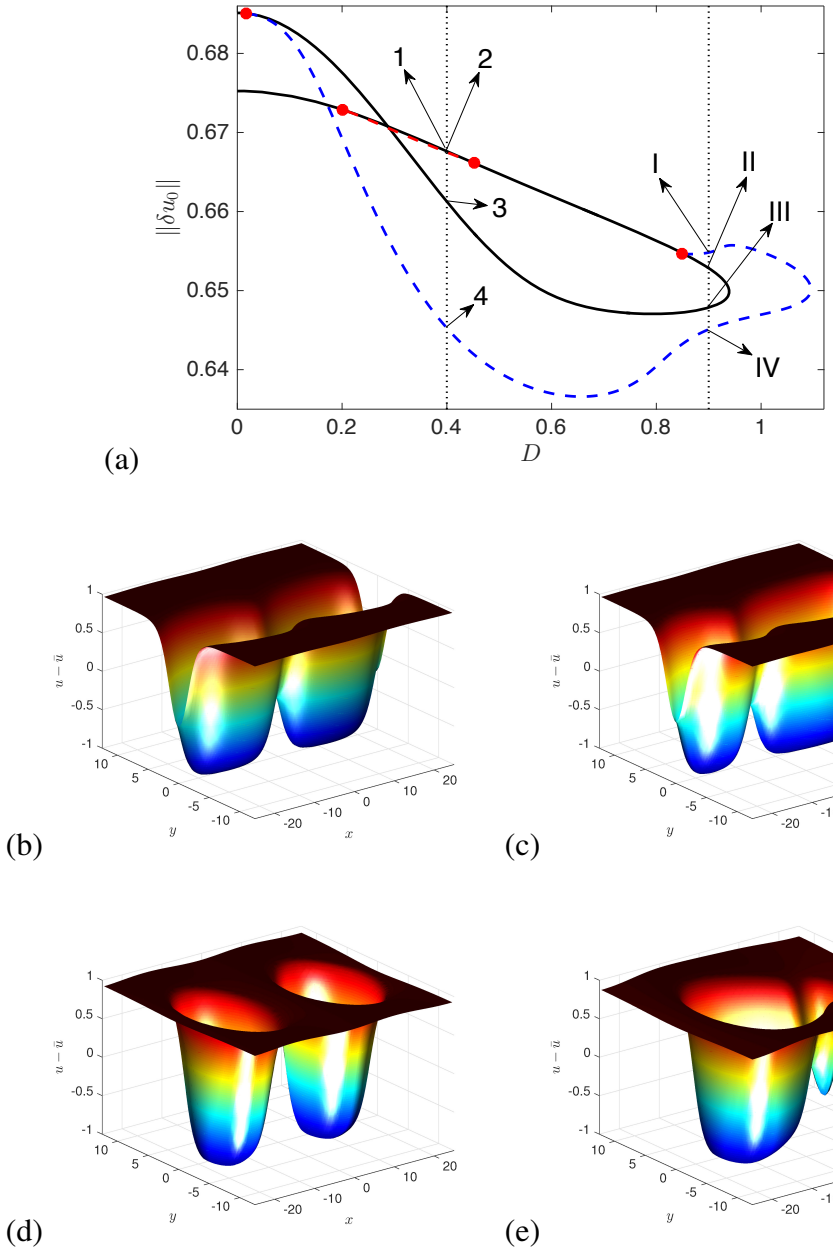

Figure 6.16: (a) The bifurcation diagram of two-hole solutions of the two-dimensional convective Cahn-Hilliard equation (6.1), for the case when $\bar{u} = 0.55$ and $L_x = L_y = 12.5$, showing the dependence of the norm $\|\delta u_0\|$ on the driving force parameter D. The solid line corresponds to the primary branch of solutions with discrete translational symmetry in the x-direction. The dashed lines show side branches of symmetry-broken solutions that start at pitchfork bifurcation on the primary branch (shown by the red circles). The vertical dotted lines correspond to $D = 0.4$ and 0.9. Points 1–4 on the branches correspond to $D = 0.4$ and the corresponding solution profiles are shown in panels (b)–(e), respectively. Points I–IV on the branches correspond to $D = 0.9$ and the corresponding solution profiles are shown in Figs. 6.17(a)–(d), respectively, on the domain $[-2L_x, 2L_x] \times [-L_y, L_y]$.

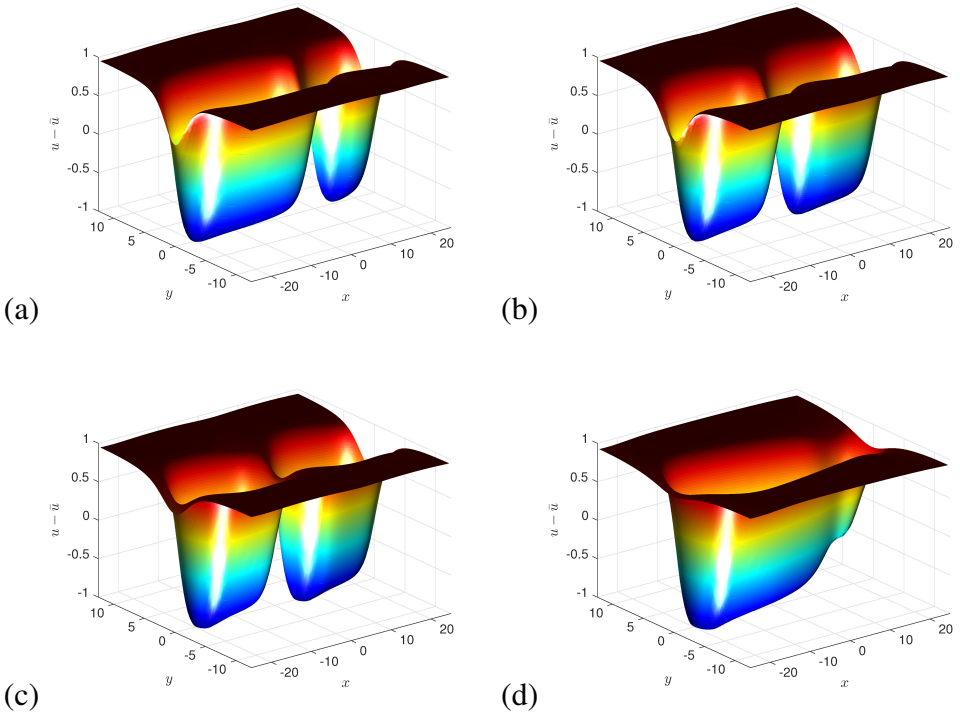

Figure 6.17: Solution profiles of the two-dimensional convective Cahn-Hilliard equation (6.1) show on the domain $[-2L_x, 2L_x] \times [-L_y, L_y]$, for the case when $\bar{u} = 0.55$, $L_x = L_y = 12.5$ and $D = 0.9$. Panels (a)–(d) correspond to points I–IV, respectively, in the bifurcation diagram shown in Fig. 6.16(a).

$D = 0$, but then has a turning point (saddle-node) and returns to $D = 0$. The red circles on this branch indicate the bifurcation points to a side branches of symmetry-broken solutions. For these values of L_x and L_y, we find that there are four bifurcation points and pairs of them are connected by side branches shown by the (red and blue) dashed line. Panels (b)–(e) show the solution profiles corresponding to points 1–4 indicated on all the branches in Fig. 6.16(a) for $D = 0.4$. Additional profiles from the main branch and one of the side branches that correspond to points I–IV for $D = 0.9$ in Fig. 6.16(a) are shown in Figs. 6.17(a)–(d), respectively.

Chapter 7

Conclusion and outlook

In the present thesis, we have analysed the effect of the driving force on the solutions of the convective Cahn-Hilliard equation. We first introduced in Chapter 2 the standard Cahn-Hilliard equation in a general gradient-dynamics formulation involving a general free-energy functional, and we reviewed some of the important concepts and ideas for this equation. Namely, we showed that the free-energy functional is a Lyapunov functional so that the dynamics aims to minimise it, we discussed stability of homogeneous solutions and introduced the concepts of spinodal and binodal lines, and we discussed the two mechanisms of coarsening for the standard Cahn-Hilliard equation – coarsening due to volume and translational modes. We then introduced the convective Cahn-Hilliard equation. After that, we reviewed the numerical techniques used in the thesis, namely, time-dependent solution by Fourier spectral methods and numerical continuation and bifurcation techniques.

Next, in Chapter 3, we discussed in detail both temporal and spatial linear stability analyses of homogenous solutions of the one-dimensional standard and convective Cahn-Hilliard equations. We also discussed the connection of the spatial linear stability analysis to the existence of single- and double-interface solutions (i.e., fronts and droplets/holes) of the standard and convective Cahn-Hilliard equations. An interesting observation was that for the driving force parameter D in the interval $[0, \sqrt{2}/3)$ the "horizontal" parts of the fronts and droplets/holes are expected to be monotonic, for $D \in (\sqrt{2}/3, \sqrt{2})$ we expect to observe oscillations on top of the "horizontal" parts of the fronts and droplets/holes. For $D > \sqrt{2}$ we do not expect to see "true" droplet/hole solutions. Instead, we expect to observe, for example, positive/negative-pulse solutions. In addition, for $D \in (2\sqrt{2}/3, \sqrt{2})$, "horizontal" parts of front- or droplet/hole-solutions

are linearly unstable, and thus, we expect the solutions on large spatial domains to break up into smaller structures. All these observation have been confirmed by time-dependent computations.

Next, in Chapter 4, we presented the results of numerical continuation of single- and double-interface solutions (i.e., fronts and droplets/holes). We first discussed the results of numerical continuation with respect to the domain size L for the standard Cahn-Hilliard equation for several values of the mean solution thickness $\bar{u}$ and showed that for smaller values of $\bar{u}$ the primary bifurcation from the branch of homogeneous solutions is supercritical, whereas at some value of $\bar{u}$ the primary bifurcation changes to subcritical. (The value of $\bar{u}$ at which this change happens can be found by the weakly nonlinear analysis, and such analysis was given at the end of Chapter 4 for the convective Cahn-Hilliard equation in a general form.) At some even larger value of $\bar{u}$ (that, in fact, can be found by the linear stability analysis), the primary bifurcation disappears, and beyond a certain value of the domain size, we obtain a coexistence of linearly stable homogeneous and inhomogeneous solutions and a linearly unstable inhomogeneous solution. After that, we analysed how the driving force affects inhomogeneous solutions of the Cahn-Hilliard equation. For smaller values of $\bar{u}$, we found that when continuation is performed in the driving force parameter D, branches of solutions extend to infinity for all sufficiently large values of the domain size. Whereas for larger values of $\bar{u}$ the branches of solutions exhibit saddle-nodes and return to $D = 0$ if L is sufficiently small. For larger values of L, the branches exhibit an additional saddle-node and extend to infinity. The transition from one type of the bifurcation diagram to the other type of the bifurcation diagram happens at $L = L_c$, where L_c is the wavelength of a small-amplitude neutrally stable sinusoidal wave. For this value of L, the branch of solutions terminates at the horizontal axis at $D = D_c$, where D_c can be found by the weakly nonlinear analysis. So, for $L > L_c$ (but not too large), there is a range of D values for which we obtain coexistence of two different stable spatially inhomogeneous solutions and one unstable inhomogeneous solution. For even larger values of L, the saddle-nodes annihilate each other, and the branches extend to infinity. Also, if $\bar{u}$ becomes sufficiently large, the branches of inhomogeneous solutions exhibit a saddle-node and return to $D = 0$ for all sufficiently large values of L. In Chapter 4, we also analysed the effect of driving on single-interface solutions (i.e., kinks and anti-kinks). As expected from theoretical considerations, kink solutions only exist for $D < \sqrt{2}$, unlike anti-kink solutions. However, for a fixed value of L, numerical continuation in D shows that the branch of "kink" solutions extends to infinity exhibiting a sharp transition around $D = \sqrt{2}$, indicating that the branch of kink solutions is connected to a

branch of other-type solutions for each sufficiently large value of the domain size L.

In Chapter 5, we studied in detail the linear stability properties of the various possible spatially periodic traveling solutions of the convective Cahn-Hilliard equation. For this, we implemented numerical procedures for continuation of inhomogeneous solutions along with real and non-real eigenvalues. To obtain more complete bifurcation diagrams, we also implemented a numerical procedure for continuation of time-periodic solutions. Our primary interest was in the study of the stability of double-droplet/hole solutions, and coarsening of such solutions in particular. In the absence of the driving force, two-droplet/hole solutions have two positive (unstable) eigenvalues that correspond to two coarsening modes – volume and translational modes. For the volume mode, the corresponding eigenfunction tends to increase the volume of one of the droplets and decrease the volume of the other one. For the translational mode, the corresponding eigenfunction tends shift both droplets in the opposite directions, so that they move towards each other. When driving is introduced, we found that one of the coarsening modes is stabilised at relatively small values of D. In addition, our results indicate that the type of a coarsening mode can change as D increases. We also found that there may be intervals in the driving force D, where there are no unstable eigenvalues, and, therefore, driving can be used to prevent coarsening. We, in addition, computed side branches of symmetry-broken solutions and analysed the stability of such solutions. We also computed branches of time-periodic solutions. Finally, in Chapter 5, we presented detailed stability diagrams in the (D, L)- and $(D, \bar{u})$-planes. The predictions from the numerical continuation results have been confirmed by time-dependent simulations for the convective Cahn-Hilliard equation.

In the final Chapter 6, we presented some preliminary results on the computation of solutions of the two-dimensional standard and convective Cahn-Hilliard equations. To compute such solutions, we developed a numerical continuation procedure based on the Fourier spectral representation of the equation. We first computed one-dimensional solutions for the standard Cahn-Hilliard equation with no y-dependence, by considering a narrow domain in the y-direction (so that L_y is small, where L_y denotes the half-domain size in the y-direction) and by performing a numerical continuation in the half-domain size parameter, L_x, starting from a neutrally stable small-amplitude wave in the x-direction. We then performed continuation in the parameter L_y for several values of L_x obtaining bifurcations to side branches of fully two-dimensional solutions. This allowed us to compute fully two-dimensional solutions for the standard Cahn-Hilliard equation, which for positive values of $\bar{u}$ turned out to be one-hole solutions

rather than one-droplet solutions (we would obtain one-droplet solutions for negative values of $\bar{u}$). Our next aim was to analyse the effect of driving on such solutions, and the effect on coarsening of such solutions in particular. In the present thesis, we only provided some preliminary results on the effect of driving on coarsening of fully two-dimensional two-hole solutions that are obtained by periodically extending one-hole solutions in the x-direction. In the future, it would be interesting to analyse how the coarsening of fully two-dimensional droplet/hole solutions depends on the co-location of the droplets/holes in space. We found that for the case of fully two-dimensional double-hole solutions that are obtained by periodically extending one-hole solutions in the x-direction, all the computed branches of solutions (both of solutions with a discrete translational symmetry in the x-direction and of symmetry-broken solutions) either terminate at some positive values of D (on some other branches of solutions, for example, branches of solutions without x- or y-dependence) or exhibit turning points and return back to $D = 0$. Although our numerical continuation procedure is capable of computing branches of fully two-dimensional time-periodic solutions, computation of such branches is time-consuming, and, therefore, this is left as topic for future investigation. We can conclude that the bifurcation diagrams for the two-dimensional convective Cahn-Hilliard equation that we have computed are not complete yet, and detailed understanding of the behaviour of solutions for larger values of D is still missing. Moreover, in the present thesis, we have not analysed yet the stability of the various computed branches for the two-dimensional convective Cahn-Hilliard equation. This is also left as a topic for future research. In the future, it would also be of benefit to perform time-dependent simulations for the full two-dimensional convective Cahn-Hilliard equation in order to verify the theoretical predictions and to better understand the effect of driving on two-dimensional solutions. Finally, in the future, it will be of interest to undertake similar studies for related equations, such as, for example, the Kuramoto-Sivashinsky equation and various thin-film models.

Bibliography

[1] FFTW webpage. Available at http://www.fftw.org. Accessed: 5 January, 2016.

[2] E. L. Allgower and K. Georg. Introduction to Numerical Continuation Methods. Classics in Applied Mathematics. Society for Industrial and Applied Mathematics, 2003.

[3] H. W. Alt and I. Pawlow. A mathematical model of dynamics of non-isothermal phase separation. Physica D: Nonlinear Phenomena, 59:389–416, 1992.

[4] D. Anders and K. Weinberg. Numerical simulation of diffusion induced phase separation and coarsening in binary alloys. Computational Materials Science, 50:1359–1364, 2011.

[5] D. G. Aronson, E. J. Doedel, and H. G. Othmer. The dynamics of coupled current-biased Josephson junctions – Part II. International Journal of Bifurcation and Chaos, 1:51–66, 1991.

[6] A. L. Bertozzi, A. Münch, X. Fanton, and A. M. Cazabat. Contact line stability and "undercompressive shocks" in driven thin film flow. Physical Review Letters, 81:5169–5172, 1998.

[7] A. L. Bertozzi, A. Münch, and M. Shearer. Undercompressive shocks in thin film flows. Physica D: Nonlinear Phenomena, 134:431–464, 1999.

[8] A. L. Bertozzi, A. Münch, M. Shearer, and K. Zumbrun. Stability of compressive and undercompressive thin film travelling waves. European Journal of Applied Mathematics, 12:253–291, 2001.

[9] A. L. Bertozzi and M. Shearer. Existence of undercompressive traveling waves in thin film equations. SIAM Journal on Mathematical Analysis, 32:194–213, 2000.

[10] G. Bordyugov and H. Engel. Continuation of spiral waves. Physica D: Nonlinear Phenomena, 228:49–58, 2007.

[11] J. P. Boyd. Chebyshev and Fourier Spectral Methods. Dover Books on Mathematics. Dover Publications, 2001.

[12] F. Boyer. A theoretical and numerical model for the study of incompressible mixture flows. Computers & fluids, 31:41–68, 2002.

[13] A. J. Bray. Theory of phase-ordering kinetics. Advances in Physics, 43:357–459, 1994.

[14] F. A. M. Bribesh. Free surface films of binary liquid mixtures. PhD thesis, Loughborough University, 2013.

[15] J. M. Burgers. A mathematical model illustrating the theory of turbulence. In R. von Mises and T. von Kármán, editors, Advances in Applied Mechanics, volume 1, pages 171–199. Academic Press Inc., New York, N. Y., 1948.

[16] J. W. Cahn. On spinodal decomposition. Acta Metallurgica, 9:795–801, 1961.

[17] J. W. Cahn. On spinodal decomposition in cubic crystals. Acta Metallurgica, 10:179–183, 1962.

[18] J. W. Cahn. Spinodal decomposition. Transaction of the Metallurgical Society of AIME, 242:166–180, 1968.

[19] J. W. Cahn and J. E. Hilliard. Free energy of a nonuniform system. I. interfacial free energy. The Journal of Chemical Physics, 28:258–267, 1958.

[20] J. W. Cahn and J. E. Hilliard. Spinodal decomposition: A reprise. Acta Metallurgica, 19:151–161, 1971.

[21] H. Chang and E. A. Demekhin. Complex Wave Dynamics on Thin Films. Studies in Interface Science. Elsevier Science, 2002.

[22] J. D. Cole. On a quasilinear parabolic equations occurring in aerodynamics. Quarterly of Applied Mathematics, 9:225–236, 1951.

[23] P. Collet, J.-P. Eckmann, H. Epstein, and J. Stubbe. Analyticity for the Kuramoto-Sivashinsky equation. Physica D: Nonlinear Phenomena, 67:321–326, 1993.

[24] P. Collet, J.-P. Eckmann, H. Epstein, and J. Stubbe. A global attracting set for the Kuramoto-Sivashinsky equation. Communications in Mathematical Physics, 152:203–214, 1993.

[25] H. E. Cook. Brownian motion in spinodal decomposition. Acta Metallurgica, 18:297–306, 1970.

[26] V. Cristini, X. Li, J. S. Lowengrub, and S. M. Wise. Nonlinear simulations of solid tumor growth using a mixture model: invasion and branching. Journal of mathematical biology, 58:723–763, 2009.

[27] R. C. Desai and R. Kapral. Dynamics of Self-organized and Self-assembled Structures. Cambridge University Press, 2009.

[28] A. Dhooge, W. Govaerts, Yu. A. Kuznetsov, W. Mestrom, A. M. Riet, and B. Sautois. MATCONT and CL_MATCONT: Continuation toolboxes in Matlab. Available at http://www.matcont.ugent.be/manual.pdf, 2006. Accessed: 5 January, 2016.

[29] A. Di Carlo, M. E. Gurtin, and P. Podio-Guidugli. A regularized equation for anisotropic motion-by-curvature. SIAM Journal on Applied Mathematics, 52:1111–1119, 1992.

[30] H. A. Dijkstra, F. W. Wubs, A. K. Cliffe, E. Doedel, I. F. Dragomirescu, B. Eckhardt, A. Yu. Gelfgat, A. L. Hazel, V. Lucarini, A. G. Salinger, E. T. Phipps, J. Sanchez-Umbria, H. Schuttelaars, L. S. Tuckerman, and U. Thiele. Numerical bifurcation methods and their application to fluid dynamics: analysis beyond simulation. Communications in Computational Physics, 15:1–45, 2014.

[31] E. J. Doedel, R. C. Paffenroth, A. R. Champneys, T. F. Fairgrieve, Y. A. Kuznetsov, B. E. Oldeman, B. Sandstede, and X. J. Wang. Auto-07p: Continuation and bifurcation software for ordinary differential equations (2007). Available for download from http://indy.cs.concordia.ca/auto.

[32] E. J. Doedel, R. C. Paffenroth, H. B. Keller, D. J. Dichmann, J. Galán-Vioque, and A. Vanderbauwhede. Computation of periodic solutions of conservative systems with application to the 3-body problem. International Journal of Bifurcation and Chaos, 13:1353–1381, 2003.

[33] A. Eden and V. K. Kalantarov. The convective Cahn-Hilliard equation. Applied Mathematics Letters, 20:455–461, 2007.

[34] V. Egorov and M. A. Shubin. Partial Differential Equations I: Foundations of the Classical Theory. Encyclopaedia of mathematical sciences. Springer-Verlag, 1994.

[35] C. M. Elliott and D. A. French. Numerical studies of the Cahn-Hilliard equation for phase separation. IMA Journal of Applied Mathematics, 38:97–128, 1987.

[36] C. L. Emmott and A. J. Bray. Coarsening dynamics of a one-dimensional driven Cahn-Hilliard system. Physical Review E, 54:4568–4575, 1996.

[37] T. Erneux and S. Davis. Nonlinear rupture of free films. Physics of Fluids A: Fluid Dynamics, 5:1117–1122, 1993.

[38] L. C. Evans. Partial Differential Equations. Graduate studies in mathematics. American Mathematical Society, 1998.

[39] M. Frigo and S. G. Johnson. The design and implementation of FFTW3. Proceedings of the IEEE, 93:216–231, 2005.

[40] D. R. Gaskell. Introduction to the Thermodynamics of Materials. CRC Press, 2008.

[41] K. B. Glasner and T. P. Witelski. Coarsening dynamics of dewetting films. Physical review E, 67:016302, 2003.

[42] K. B. Glasner and T. P. Witelski. Collision versus collapse of droplets in coarsening of dewetting thin films. Physica D: Nonlinear Phenomena, 209:80–104, 2005.

[43] P. Glendinning and C. Sparrow. Local and global behavior near homoclinic orbits. Journal of Statistical Physics, 35:645–696, 1984.

[44] N. Goldenfeld. Lectures on Phase Transitions and the Renormalization Group. Frontiers in physics. Addison-Wesley, Advanced Book Program, 1992.

[45] A. A. Golovin, S. H. Davis, and A. A. Nepomnyashchy. A convective Cahn-Hilliard model for the formation of facets and corners in crystal growth. Physica D: Nonlinear Phenomena, 122:202–230, 1998.

[46] A. A. Golovin, S. H. Davis, and A. A. Nepomnyashchy. Model for faceting in a kinetically controlled crystal growth. Physical Review E, 59:803–825, 1999.

[47] A. A. Golovin, A. A. Nepomnyashchy, S. H. Davis, and M. A. Zaks. Convective Cahn-Hilliard models: From coarsening to roughening. Physical Review Letters, 86:1550–1553, 2001.

[48] A. A. Golovin, B. Y. Rubinstein, and L. M. Pismen. Effect of van der Waals interactions on the fingering instability of thermally driven thin wetting films. Langmuir, 17:3930–3936, 2001.

[49] J. Goodman. Stability of the Kuramoto-Sivashinsky and related systems. Communications on Pure and Applied Mathematics, 47:293–306, 1994.

[50] J. Guckenheimer and P. Holmes. Nonlinear oscillations, dynamical systems, and bifurcations of vector fields, volume 42. Springer, 1983.

[51] M. E. Gurtin. Thermomechanics of Evolving Phase Boundaries in the Plane. Oxford mathematical monographs. Clarendon Press, 1993.

[52] B. Gustafsson, H. O. Kreiss, and J. Oliger. Time dependent problems and difference methods, volume 67. Wiley New York, 1995.

[53] B. T. Hayes and P. G. LeFloch. Non-classical shocks and kinetic relations: Scalar conservation laws. Archive for Rational Mechanics and Analysis, 139:1–56, 1997.

[54] M. Hillert. A solid-solution model for inhomogeneous systems. Acta Metallurgica, 9:525–535, 1961.

[55] J. E. Hilliard. In phase transformation. edited by H. I. Aronson (American Society for Metals, Metals Park, Ohio, 1970).

[56] E. Hopf. The partial differential equation $u_t + uu_x = \mu u_{xx}$. Communications on Pure and Applied Mathematics, 3:201–230, 1950.

[57] J. M. Hyman, B. Nikolaenko, and S. Zaleski. Order and complexity in the Kuramoto-Sivashinsky model of turbulent interfaces. Physica D: Nonlinear Phenomena, 23:265–292, 1986.

[58] P. Šmilauer, M. Rost, and J. Krug. Fast coarsening in unstable epitaxy with desorption. Physical Review E, 59:R6263–R6266, 1999.

[59] J. S. Il'yashenko. Global analysis of the phase portrait for the Kuramoto-Sivashinsky equation. Journal of Dynamics and Differential Equations, 4:585–615, 1992.

[60] R. S. Johnson. A Modern Introduction to the Mathematical Theory of Water Waves. Cambridge Texts in Applied Mathematics. Cambridge University Press, 1997.

[61] M. Jolly, R. Rosa, and R. Temam. Evaluating the dimension of an inertial manifold for the Kuramoto-Sivashinsky equation. Advances in Differential Equations, 5:31–66, 2000.

[62] R. A. L. Jones. Soft condensed matter, volume 6. Oxford University Press, 2002.

[63] I. G. Kevrekidis, B. Nikolaenko, and C. Scovel. Back in the saddle again: a computer assisted study of the Kuramoto-Sivashinsky equation. SIAM Journal on Applied Mathematics, 50:760–790, 1990.

[64] V. V. Khatavkar, P. D. Anderson, and H. E. H. Meijer. On scaling of diffuse–interface models. Chemical engineering science, 61:2364–2378, 2006.

[65] J. Kim. A continuous surface tension force formulation for diffuse-interface models. Journal of Computational Physics, 204:784–804, 2005.

[66] J. Knobloch and T. Wagenknecht. Homoclinic snaking near a heteroclinic cycle in reversible systems. Physica D: Nonlinear Phenomena, 206:82–93, 2005.

[67] M. H. Köpf and U. Thiele. Emergence of the bifurcation structure of a Langmuir–Blodgett transfer model. Nonlinearity, 27:2711–2734, 2014.

[68] M. D. Korzec, P. L. Evans, A. Münch, and B. Wagner. Stationary solutions of driven fourth-and sixth-order cahn-hilliard-type equations. SIAM Journal on Applied Mathematics, 69:348–374, 2008.

[69] B. Krauskopf, H. M. Osinga, and J. Galán-Vioque. Numerical Continuation Methods for Dynamical Systems: Path Following and Boundary Value Problems. Understanding Complex Systems. Springer, 2007.

[70] Y. Kuramoto. Chemical Oscillations, Waves, and Turbulence. Dover books on chemistry. Dover Publications, 2003.

[71] Y. A. Kuznetsov. Elements of applied bifurcation theory, volume 112. Springer, 2013.

[72] P. D. Lax. Hyperbolic Systems of Conservation Laws and the Mathematical Theory of Shock Waves. Number nos. 11-16 in CBMS-NSF Regional Conference Series in Applied Mathematics. Society for Industrial and Applied Mathematics, 1973.

[73] D. Lee, J.-Y. Huh, D. Jeong, J. Shin, A. Yun, and J. Kim. Physical, mathematical, and numerical derivations of the Cahn-Hilliard equation. Computational Materials Science, 81:216–225, 2014.

[74] I. M. Lifshitz and V. V. Slyozov. The kinetics of precipitation from supersaturated solid solutions. Journal of Physics and Chemistry of Solids, 19:35–50, 1961.

[75] T.-S. Lin, M. G. Blyth, S. Kalliadasis, and D. Tseluiko. Coherent-structure theory and bound-state formation in electrified falling films. In preparation, 2016.

[76] T.-S. Lin, S. Rogers, D. Tseluiko, and U. Thiele. Bifurcation analysis of the behavior of partially wetting liquids on a rotating cylinder. Submitted, 2016.

[77] F. Liu and H. Metiu. Dynamics of phase separation of crystal surfaces. Physical Review B, 48:5808–5817, 1993.

[78] J. A. Marqusee and J. Ross. Theory of ostwald ripening: Competitive growth and its dependence on volume fraction. The Journal of chemical physics, 80:536–543, 1984.

[79] A. Mielke. Instability and stability of rolls in the Swift-Hohenberg equation. Communications in Mathematical Physics, 189:829–853, 1997.

[80] A. Münch. Shock transitions in Marangoni gravity-driven thin-film flow. Nonlinearity, 13:731–746, 2000.

[81] F. J. Muñoz-Almaraz, E. Freire, J. Galán, E. Doedel, and A. Vanderbauwhede. Continuation of periodic orbits in conservative and hamiltonian systems. Physica D: Nonlinear Phenomena, 181:1–38, 2003.

[82] F. J. Muñoz-Almaraz, E. Freire, J. Galan-Vioque, and A. Vanderbauwhede. Continuation of normal doubly symmetric orbits in conservative reversible systems. Celestial Mechanics and Dynamical Astronomy, 97:17–47, 2007.

[83] A. Onuki. Phase transition dynamics. Cambridge University Press, 2002.

[84] W. Ostwald. Studien über die bildung und umwandlung fester körper (Studies on the formation and transformation of solid bodies). Zeitschrift für Physikalische Chemie, 22:289–330, 1897.

[85] F. Otto. Optimal bounds on the Kuramoto-Sivashinsky equation. Journal of Functional Analysis, 257:2188–2245, 2009.

[86] D. T. Papageorgiou and Y. S. Smyrlis. The route to chaos for the Kuramoto-Sivashinsky equation. Theoretical and Computational Fluid Dynamics, 3:15–42, 1991.

[87] J. M. Park, R. Mauri, and P. D. Anderson. Phase separation of viscous ternary liquid mixtures. Chemical engineering science, 80:270–278, 2012.

[88] L. M. Pismen and Y. Pomeau. Mobility and interactions of weakly nonwetting droplets. Physics of Fluids, 16:2604–2612, 2004.

[89] D. A. Porter and K. E. Easterling. Phase transformations in metals and alloys, van nostrnad reinhold co. Ltd., UK, 204, 1991.

[90] A. Pototsky, A. J. Archer, S. E. Savel'ev, U. Thiele, and F. Marchesoni. Ratcheting of driven attracting colloidal particles: Temporal density oscillations and current multiplicity. Physical Review E, 83:061401, 2011.

[91] A. Pototsky, U. Thiele, and A. J. Archer. Coarsening modes of clusters of aggregating particles. Physical Review E, 89:032144, 2014.

[92] B. Sandstede. Stability of travelling waves. In B. Fiedler, editor, Handbook of Dynamical Systems, volume 2, pages 983–1055. Elsevier, 2002.

[93] D. G. Schaeffer and M. Shearer. The classification of 2×2 systems of non-strictly hyperbolic conservation laws, with application to oil recovery. Communications on Pure and Applied Mathematics, 40:141–178, 1987.

[94] M. R. Schulze and M. Shearer. Undercompressive shocks for a system of hyperbolic conservation laws with cubic nonlinearity. Journal of Mathematical Analysis and Applications, 229:344–362, 1999.

[95] T. M. Segin, B. S. Tilley, and L. Kondic. On undercompressive shocks and flooding in countercurrent two-layer flows. Journal of Fluid Mechanics, 532:217–242, 2005.

[96] M. Shearer, D. G. Schaeffer, D. Marchesin, and P. L. Paes-Leme. Solution of the riemann problem for a prototype 2×2 system of non-strictly hyperbolic conservation laws. Archive for Rational Mechanics and Analysis, 97:299–320, 1987.

[97] Y. S. Smyrlis and D. T. Papageorgiou. Predicting chaos for the infinite dimensional dynamical systems: the Kuramoto-Sivashinsky equation, a case study. Proceedings of the National Academy of Sciences of the United States of America, 88:11129–11132, 1991.

[98] M. Spiegel, S. Lipschutz, and J. Liu. Schaum's Outline of Mathematical Handbook of Formulas and Tables, 3ed. Schaum's Outline Series. McGraw-Hill Education, 2008.

[99] S. H. Strogatz. Nonlinear Dynamics and Chaos: With Applications to Physics, Biology, Chemistry, and Engineering. Advanced Book Program. Westview Press, 1994.

[100] J. Sur, A. L. Bertozzi, and R. P. Behringer. Reverse undercompressive shock structures in driven thin film flow. Physical Review Letters, 90:126105, 2003.

[101] R. Temam. Infinite-Dimensional Dynamical Systems in Mechanics and Physics. Applied Mathematical Sciences. Springer New York, 1997.

[102] U. Thiele. Thin Films of Soft Matter, chapter Structure Formation in Thin Liquid Films, pages 25–93. Springer Vienna, 2007.

[103] U. Thiele. Thin film evolution equations from (evaporating) dewetting liquid layers to epitaxial growth. Journal of Physics: Condensed Matter, 22:084019, 2010.

[104] U. Thiele, L. Brusch, M. Bestehorn, and M. Bär. Modelling thin-film dewetting on structured substrates and templates: Bifurcation analysis and numerical simulations. The European Physical Journal E, 11:255–271, 2003.

[105] U. Thiele and E. Knobloch. Front and back instability of a liquid film on a slightly inclined plate. Physics of Fluids, 15:892–907, 2003.

[106] U. Thiele and E. Knobloch. Thin liquid films on a slightly inclined heated plate. Physica D: Nonlinear Phenomena, 190:213–248, 2004.

[107] U. Thiele, C. Schelte, and F. Ehebrecht. Münsteranian Tutorials on Nonlinear Science. Continuation DROP: steady drop and film states on a horizontal homogeneous substrate. Available at http://pauli.uni-muenster.de/tutorials/continuationAuto/04LINDROP.pdf, 2015. Accessed: 5 January, 2016.

[108] U. Thiele, C. Schelte, and F. Ehebrecht. Münsteranian Tutorials on Nonlinear Science. Continuation LINDROP: linear stability of steady solutions of a thin film equation for a horizontal homogeneous substrate. Available at http://pauli.uni-muenster.de/tutorials/continuationAuto/01DROP.pdf, 2015. Accessed: 5 January, 2016.

[109] U. Thiele, J. M. Vega, and E. Knobloch. Long-wave Marangoni instability with vibration. Journal of Fluid Mechanics, 546:61–87, 2006.

[110] U. Thiele, M. G. Velarde, K. Neuffer, M. Bestehorn, and Y. Pomeau. Sliding drops in the diffuse interface model coupled to hydrodynamics. Physical Review E, 64:061601, 2001.

[111] U. Thiele, M. G. Velarde, K. Neuffer, and Y. Pomeau. Film rupture in the diffuse interface model coupled to hydrodynamics. Physical Review E, 64:031602, 2001.

[112] L. N. Trefethen. Spectral Methods in MATLAB. Software, Environments, and Tools. Society for Industrial and Applied Mathematics, 2000.

[113] D. Tseluiko, M. G. Blyth, and D. T. Papageorgiou. Stability of film flow over inclined topography based on a long-wave nonlinear model. Journal of Fluid Mechanics, 729:638–671, 2013.

[114] D. Tseluiko, M. Galvagno, and U. Thiele. Collapsed heteroclinic snaking near a heteroclinic chain in dragged meniscus problems. The European Physical Journal E, 37:1–17, 2014.

[115] P. W. Voorhees. The theory of ostwald ripening. Journal of Statistical Physics, 38:231–252, 1985.

[116] C. Wagner. Theory of precipitate change by redissolution. Z. Elektrochem, 65:581–591, 1961.

[117] S. J. Watson. Crystal growth, coarsening and the convective Cahn-Hilliard equation. International Series of Numerical Mathematics, 147:329–341, 2003.

[118] S. J. Watson. Free Boundary Problems: Theory and Applications, chapter Crystal Growth, Coarsening and the Convective Cahn-Hilliard Equation, pages 329–341. Birkhäuser Basel, Basel, 2004.

[119] S. J. Watson, F. Otto, B. Y. Rubinstein, and S. H. Davis. Coarsening dynamics of the convective Cahn-Hilliard equation. Physica D: Nonlinear Phenomena, 178:127–148, 2003.

[120] G. B. Whitham. Linear and Nonlinear Waves. Pure and Applied Mathematics: A Wiley Series of Texts, Monographs and Tracts. Wiley, 2011.

[121] S. M. Wise, J. S. Lowengrub, H. B. Frieboes, and V. Cristini. Three-dimensional multispecies nonlinear tumor growthi: model and numerical method. Journal of theoretical biology, 253:524–543, 2008.

[122] J. H. Yao, K.R. Elder, H. Guo, and M. Grant. Theory and simulation of ostwald ripening. Physical review B, 47:14110, 1993.

[123] M. A. Zaks, A. Podolny, A. A. Nepomnyashchy, and A. A. Golovin. Periodic stationary patterns governed by a convective Cahn–Hilliard equation. SIAM Journal on Applied Mathematics, 66:700–720, 2005.

[124] C. Zhou and S. Kumar. Two-dimensional two-layer channel flow near a step. Chemical engineering science, 81:38–45, 2012.